Complex Charge Compensation Mechanisms in Lithium-Rich Chalcogenide Cathodes

Thesis by
Joshua Joseph Zak

In Partial Fulfillment of the Requirements for the
Degree of
Doctor of Philosophy

CALIFORNIA INSTITUTE OF TECHNOLOGY
Pasadena, California

2023
Defended September 20, 2022

Joshua Joseph Zak
ORCID: 0000-0003-3793-7254

ACKNOWLEDGEMENTS

Please bear with me during the likely long-winded acknowledgements that follow this statement, but, as they say, it really does take a village.

If one were to read any of my graduate school application essays or fellowship personal statements, they would find right at the beginning an anecdote about how my passion for science began. It would say something about a trip I took with my middle school agriculture class to Kangaroo Island when my family lived in Adelaide, Australia and how helping with environmental surveys at the field station there first sparked my interest. While that is certainly true and I definitely did not lie to the funding agencies for a nice, neat story, the process has been a bit less linear than I have made it seem under word count constraints. That being said, I have to express my gratitude towards my teachers at Scotch College in Adelaide and Australia as a whole for opening my eyes to the true beauty of the natural world and inspiring me to want to find ways to protect it.

Back stateside at Allderdice High School, my ever-evolving interest in many fields of science was honed by Sally Martin, whom I am convinced is the best chemistry teacher in the country if not the world. She, coincidentally, is Australian. I will forever be grateful to her for going above and beyond in recognizing my aptitude for the physical sciences and giving me every opportunity under the sun to explore and learn. I owe much of my success to her for helping me build the foundation upon which all of my chemistry knowledge rests.

I must also extend my deepest thanks to the other teachers at Allderdice that had a profound impact on me including, but not limited to, Lesley Britton (math), Dr. Jan Waldeck (physics), and Dr. Isabel Espino de Valdivia (Japanese). Your encouragement meant the world to a dazed and confused teenager.

I would be remiss in thanking my teachers at my own high school without thanking my Latin teacher, and my aunt, Dr. Victoria Jordan. For some reason, she humored my desire to learn Latin, something that was not offered at Allderdice, and took the time to teach me privately. My writing and grasp on language is what it is today because of her. Scientists write a lot it turns out.

Upon matriculating down the street to Carnegie Mellon University, I was lucky enough to find support everywhere I looked.

Thank you to Prof. Karen Stump, Prof. Gizelle Sherwood, and Carolyn Neiderlander. As the Director of Undergraduate Studies in chemistry, Karen provided deeply insightful advice and endless snacks in her office, and even invited us into her home during holidays (her Halloween parties will always be the standard for me, LA party planners take notes). Gizelle and Carolyn rounded out a group of truly inspiring women leading and fostering a close-knit department.

Thank you to Prof. Stefan Bernhard, who gave me my first opportunity to do chemistry research at the academic level. I spent three years in his group learning the ins and out of organometallic chemistry and pranking him with the other undergrads. Big thanks to Dr. Jonathan Porras, my graduate student mentor, who was the first to teach me what it means to do research. I am grateful to everyone in the Bernhard group over the years that made it such a fun place to do science, showing me that a healthy work-life balance in graduate school is possible in the process.

Outside of chemistry, I want to thank Prof. William Alba, the director of the Science and Humanities Scholars Program, who has curated an amazing program that afforded me the freedom to explore my wide breadth of interests. When I said I wanted to take courses in materials science and engineering, he made a call with me sitting in his office to get me into the introductory course during my freshman year. My coursework in materials science is how I narrowed the scope of my scientific interest even further. Prof. Maggie Braun, the Dean of Undergraduate Studies for the Mellon College of Science, was also a huge advocate for me in this area and I thank her for her continued support.

I would like to thank all the faculty in humanities, especially my sensei in the Japanese department. To this day, I will shout from the rooftops the importance of a balanced education for STEM professionals. In my opinion, success in science becomes less about what to learn and more about how to think.

Thank you to all the faculty and administrators I worked closely with during my leadership roles with Spring Carnival Committee and First-Year Orientation. I learned everything I know about long-term, large-scale organization and planning from these experiences, which has been invaluable in keeping track of all the balls a graduate student has to keep in the air.

Speaking of graduate school, absolutely none of this would have been possible without my advisor Prof. Kim See. We essentially joined Caltech at the same time five years ago, and I have had the privilege of joining Kim on the journey to

developing what is now a thriving research program. It all started with a glovebox in what is essentially a storage closet where all we had for cable management were the drawer handles of the filing cabinet upon which our only potentiostat sat. It has been an honor to learn from Kim. She has taught me what it means to do thorough, hypothesis-driven science, manage research projects from start to finish, and truly think outside the box. In addition, unbeknownst to me I have adopted many of her idiosyncrasies with respect to figure-making: square figures are superior, redundant coding is equitable and important, and green basically always looks bad. Finding an advisor that will act as an unwavering supporter of your science, your DEI work, and your dumb jokes is not easy. I must have had a buildup of good karma or something. I cannot wait to watch her career continue to flourish as we transition to colleagues and friends in and outside the battery field.

A huge thanks is due to the See Group members that have come and gone along the way. The OG crew, Dr. Andy Martinolich, Sarah Bevilacqua, and Charlie Hansen, were a huge source of support in the early days, and I learned so much from and with each of them. Since then, the group has grown to almost twenty and it has been a highlight of my experience to work with everyone. Special thanks is owed to my partners in crime and at the beamline on the anion redox team, Steve Kim and Eshaan Patheria. It has been so much fun bouncing ideas off of each other the past few years and I am excited to see where you take the research with the new folks that have joined the team recently. Watching the See Group grow into what it is today and working with new members every year has been a huge honor and I thank you all for continuing to foster such a positive lab environment.

Now, I truly would not have made it to this point without the help of my friends and family. Despite the rigors of being a PhD student at Caltech, I was intentional about making time and space for myself outside of lab and, as a result, had some amazing experiences with amazing people. Music has been a huge avenue of release for me so I have to thank my festival/concert family. Just to name a few in a totally non-exhaustive list: Jacob and Kaitlin Brooks, Phil Massey, Aubrey Higginson, Hunter Rideout, and Jack Funari. It has been a joy watching people from different stages of my life come together to laugh and dance, I love you all. At Caltech, I could not have asked for a better cohort of chemistry colleagues. I want to specifically call out Axl Levan, Patricia Nance, and Madeline Meier for being the best, most supportive friends. Suffice it to say, we have been through a lot together. I cherish each and every one of those memories and I am so excited to continue making more

as lifelong friends. Big thanks also go to my other roomies, Anna Scott and Dirk Schild, and my friends and teammates with Cold Fusion softball and VGL beach volleyball. And to my CISV Southern California family, it's true that no matter where in the world you are you can find CISVers. Thank you for always believing in me and excusing me when school got a little too crazy. There's no one else with whom I would rather start a new CISV chapter.

I would be remiss if I didn't mention another loving home I found at Caltech in the form of the Center for Inclusion and Diversity and PRISM. I need to thank Taso Dimitriadis in particular for being an amazing mentor and friend over the years. He has done so much for Caltech and its students, and I am no exception. A giant rainbow thank you also goes to my PRISM co-leaders over the years–Dr. Sean Mullin, Prashant Bhat, Abigail Jiang, Levi Palmer, Natasha Reich, and David Oliveira–for helping me connect with my queer identity and learn about myself through supporting the community at Caltech. Some of my proudest moments over the last five years have been working with you inspiring people.

Last but almost certainly the most, I need to express my deepest gratitude to my family. To my grandparents, who have encouraged my every curiosity from day one and made me feel like no matter what happened I could rely on them for anything. To my two brothers, Justin and Malik, who have been constant company throughout this journey and long before. It has gotten to the point where our "shared braincell" moments actually freak me out. Jokes aside, our hours-long phone calls have sustained me during my time at Caltech, and I can always rest easy knowing you two are behind me whether it's to catch me when I fall or back me up when times are tough. I cannot wait to continue to live and grow with you two. To my future sister-in-law Stephanie, I'm so excited to be family come next September, even though we have been in my heart for years. And, finally, to my parents, Leslie and Tim. I am tearing up trying to find the words to express how much you have given and continue to give me everyday. From piano to karate, from tennis to CISV, from acting to science, no matter what I have wanted to do or try, you supported me with your whole hearts. You are my most ardent supporters and my guiding lights. I am able to be proud of the person I have become because you led by example and taught me how. Thank you. Now, enough mushy stuff, on with the science.

ABSTRACT

Lithium-ion batteries have revolutionized the world by enabling long-lasting portable electronics, electrified transportation, and grid storage solutions for renewable energy implementation. However, current commercialized technologies are limited by the one electron transfer per transition metal paradigm utilized by cathode materials that operate with an intercalation-based charge storage mechanism. Finding ways to increase the charge storage capabilities of the cathode into the multielectron regime has long been a focus of research efforts, and involvement of structural anions in the redox has been demonstrated as a promising way to accomplish multielectron storage. Layered lithium-rich oxide materials have been shown to afford dramatic improvements to overall storage capacity but are plagued by complex mechanisms and unwanted side reactions that lead to poor cycling stability and characterization difficulties. This thesis expands upon previous understanding of oxide-based anion redox materials and extends the exploration into sulfide and selenide systems, which allow the study of anion redox without the side processes that affect oxides. First, a dynamic charge compensation mechanism of late group metal-poor, lithium-rich oxide, $Li_2Ru_{0.3}Mn_{0.7}O_3$, is uncovered and found to involve an irreversible anion oxidation that leads to involvement of redox states on transition metals previously thought to be unavailable. Second, active electrolyte additives are explored as a method of stabilizing the cathode-electrolyte interface of anion redox material, Li_2RuO_3. Third, reversible anion redox is demonstrated in alkali-rich sulfides, Li_2FeS_2 and $LiNaFeS_2$, and proven to occur through oxidation of sulfides (S^{2-}) to persulfides (S_2^{2-}). Understanding of the structural ramifications of anion oxidation in Li_2FeS_2 is further expanded through computational and experimental methods. Fourth, the role of metal-anion covalency is systematically investigated through anion substitution of Li_2FeS_2 with Se^{2-}, highlighting the importance of a holistic understanding of changes to the electronic and physical structure of anion redox materials to predict long-term performance. Finally, detailed perspectives and future outlooks on sulfur redox in lithium battery systems are offered with an exhaustive survey of thermodynamically stable binary and ternary persulfide materials.

PUBLISHED CONTENT AND CONTRIBUTIONS

Portions of this thesis have been drawn from the following publications:

Hansen, C. J.*; Zak, J. J.*; Martinolich, A. J.; Ko, J. S.; Bashian, N. H.; Kaboudvand, F.; Van der Ven, A.; Melot, B. C.; Nelson Weker, J.; See, K. A. Multielectron, Cation and Anion Redox in Lithium-Rich Iron Sulfide Cathodes. *J. Am. Chem. Soc.* **2020**, *142*, 6737–6749. DOI: 10.1021/jacs.0c00909. ©2020 American Chemical Society.

> J.J.Z. performed, and analyzed spectroscopic data, contributed to discussions on project direction, and helped prepare the manuscript (**equal author contribution*.)

Bashian, N. H.; Preefer, M. B.; Milam-Guerrero, J.; Zak, J. J.; Sendi, C.; Ahsan, S. A.; Vincent, R. C.; Haiges, R.; See, K. A.; Seshadri, R.; Melot, B. C. Understanding the role of crystallographic shear on the electrochemical behavior of niobium oxyfluorides. *J. Mater. Chem. A* **2020**, *8*, 12623–12632. DOI: 10.1032/D0TA01406K. ©2020 Royal Society of Chemistry.

> J.J.Z. performed Raman spectroscopy and helped write manuscript section about results.

Martinolich, A. J.*; Zak, J. J.*; Agyeman-Budu, D. N.; Kim, S. S.; Bashian, N. H.; Irshad, A.; Narayan, S. R.; Melot, B. C.; Nelson Weker, J.; See, K. A. Controlling Covalency and Anion Redox Potentials through Anion Substitution in Li-Rich Chalcogenides. *Chem. Mater.* **2021**, *33*, 378–391. DOI: 10.1021/acs.chemmater.0c04164. ©2021 American Chemical Society.

> J.J.Z. performed and analyzed spectroscopic data, contributed to discussions on project direction, and helped prepare the manuscript (**equal author contribution*).

Wyckoff, K. E.; Kaufman, J. L.; Baek, S. W.; Dolle, C.; Zak, J. J.; Bienz, J.; Kautzsch, L.; Vincent, R. C.; Zohar, A.; See, K. A.; Eggeler, Y. M.; Pilon, L.; Van der Ven, A.; Seshadri, R. Metal–Metal Bonding as an Electrode Design Principle in the Low-Strain Cluster Compound $LiScMo_3O_8$. *J. Am. Chem. Soc.* **2022**, *144*, 5841-–5854. DOI: 10.1021/jacs.1c12070. ©2022 American Chemical Society.

J.J.Z. performed Raman spectroscopy and helped write manuscript section about results.

Kim, S. S.; Agyeman-Budu, D. N.; Zak, J. J.; Dawson, A.; Yan, Q.; Cában-Acevedo, M.; Wiaderek, K. M.; Yakovenko, A. A.; Yao, Y.; Irshad, A.; Narayan, S. R.; Luo, J.; Nelson Weker, J.; Tolbert, S. H.; See, K. A. Promoting Reversibility of Multielectron Redox in Alkali-Rich Sulfide Cathodes through Cryomilling. *Chem. Mater.* **2022**, *34*, 3236-–3245. DOI: 10.1021/acs.chemmater.2c00030. ©2022 American Chemical Society.

J.J.Z. performed *operando* X-ray diffraction experiments with K.M.W and A.A.Y. and processed the data.

Zak, J. J.; Kim, S. S.; Laskowski, F. A. L.; See, K. A. An Exploration of Sulfur Redox in Lithium Battery Cathodes. *J. Am. Chem. Soc.* **2022**, *144*, 10119—10132. DOI: 10.1021/jacs.2c02668. ©2022 American Chemical Society.

J.J.Z. led discussions for perspective content, conducted materials survey, and prepared the manuscript.

Zak, J. J.; Zuba, M.; Lebens-Higgins, Z. W.; Huang, H.; Crafton, M. J.; Dalleska, N. F.; McCloskey, B. D.; Piper, L. F. J.; See, K. A. Irreversible Anion Oxidation Leads to a Dynamic Charge Compensation Mechanism in Ru-poor, Li-rich Cathode $Li_2Ru_{0.3}Mn_{0.7}O_3$. *Submitted*.

J.J.Z. designed and performed experiments, analyzed the data, and prepared the manuscript.

Zak, J. J.; Skærvø, S. H.; Patheria, E.; Baek, S. W.; Harper, A. F.; Tao, S.; Kwon, G.; Wiaderek, K. M.; Borkiewicz, O.; Ko, J. S.; Nelson Weker, J.; Morris, A. J.; Pilon, L.; Billinge, S. J. L.; See, K. A. Complex Structural Response of Multielectron Cathode Li_2FeS_2 to Mixed Cation and Anion Oxidation. *In preparation*.

J.J.Z. designed and performed experiments, analyzed the data, and prepared the manuscript.

TABLE OF CONTENTS

LIST OF ILLUSTRATIONS

LIST OF TABLES

LIST OF ABBREVIATIONS

CEI	cathode electrolyte interphase
CV	cyclic voltammetry
DEMS	differential electrochemical mass spectrometry
DFT	density functional theory
DMC	dimethyl carbonate
EC	ethylene carbonate
EDX	electron dispersive X-ray spectroscopy
EIS	electrochemical impedance spectroscopy
EXAFS	extended X-ray absorption fine structure
GITT	galvanostatic intermittant titration technique
HAXPES	hard X-ray photoelectron spectroscopy
HMDS	hexamethyldisilizane
ICP-MS	inductively coupled plasma mass spectrometry
ICSD	Inorganic Crystal Structure Database
LCO	$LiCoO_2$, lithium cobalt(III) oxide
LFP	$LiFePO_4$, lithium iron(II) phosphate
LIB	lithium-ion battery
NCA	$LiNi_xCo_yAl_zO_2$ ($x + y + z = 1$)
NMC	$LiNi_xMn_yCo_zO_2$ ($x + y + z = 1$)
O_h	octahedral coordination
PC	propylene carbonate
PDF	pair distribution function
pDOS	partial density of states
RIXS	resonant inelastic X-ray scattering
SEI	solid electrolyte interphase
SEM	scanning electron microscope
SOC	state of charge
SSE	solid state electrolyte
sXAS	soft X-ray absorption spectroscopy
T_d	tetrahedral coordination
TBA	tetra-n-butylammonium
TBP	tributylphosphate
TEM	transmission electron microscopy

TEY	total electron yield
TFSI	bis(trifluoromethane)sulfonimide
TMP	trimethylphosphate
TMPi	trimethylphosphite
TPP	triphenylphosphate
U_{OCV}	open circuit potential
XANES	X-ray absorption near-edge structure
XAS	X-ray absorption spectroscopy
XES	X-ray emission spectroscopy
XPS	X-ray photoelectron spectroscopy
XRD	X-ray diffraction

Chapter 1

INTRODUCTION

Partially adapted from: Zak, J. J.; Kim, S. S.; Laskowski, F. A. L.; See, K. A. An Exploration of Sulfur Redox in Lithium Battery Cathodes. *J. Am. Chem. Soc.* **2022**, *144*, 10119—10132.

Climate change associated with the warming of the planet has had, and will continue to have, adverse effects including extreme weather events, rising sea levels, ecosystem collapse, and ocean acidification.[2] As a result, electrification has emerged as a central effort in the push towards a more sustainable energy landscape[3, 4] driven by new technological developments and policy objectives.[5] To meet rising energy demands while lowering dependence on fossil fuels, the widespread implementation of electrified transportation and integration of renewable energy sources like wind and solar into the grid must be realized.[6] Just as electric vehicles require energy storage systems, wind and solar are intermittent sources of energy, which necessitates storage systems such that the grid can maintain power when the wind is not blowing and the sun is not shining.

One such technology, the Li-ion battery (LIB), is a contender for many electrification applications and has already revolutionized the world of portable electronics and, in recent years, personal and public transportation.[7, 8] Broadly, this thesis is focused on gaining a fundamental understanding of next-generation cathode materials for LIBs within a interdisciplinary framework of chemistry, electrochemistry, and materials science. The following section will provide a brief, big picture view of the motivations for the work described herein, and each chapter will provide additional background and specifics relevant to the individual projects.

1.1 Lithium-Ion Batteries in Brief

Electrochemical battery systems, in general, are two-electrode systems with an anode, cathode, and an electrolyte between them. The anode and cathode are most often a mixture of the electrochemically active material, a conductive additive (often a form of high-surface area carbon), and a binder to hold the mixture together adhered to a metal foil current collector. The electrodes are separated by a thin sheet

of porous material and electrolyte that are ionically conductive but electronically insulating. Batteries operate by storing charge in the form of electrons at a high energy state in the anode as shown in Figure 1.1, and this energy is defined by the electrochemical potential, $\bar{\mu}$, of Li ions, Li^+, and electrons in the host lattice. The electrochemical potential is measured as the chemical potential, μ, taking into account the energy contribution of electrostatics, or electrical potential, ϕ. In other words, the electrochemical potential is the partial molar Gibbs free energy of a given species in a given phase at the specified electric potential. The difference in the chemical potential of the anode and cathode is the driving force for mass transfer, which is the basis of battery function.

In more detail, when a battery is fully discharged, the anode and cathode active materials are at their thermodynamically most stable states. To charge the cell, external energy must be applied to force Li^+ out of the cathode where it has low chemical potential to the anode where it has high chemical potential. To maintain charge neutrality, electrons flow in the same direction as Li^+ through the external circuit connecting the two electrodes, thereby oxidizing the cathode and reducing the anode. The cell is now in the charged state as shown in Figure 1.1. When electrons are allowed to flow through the external circuit, the cell will spontaneously discharge to minimize the chemical potential and, by extension, the electrochemical potential of Li^+ in the system and lower the overall energy. This process converts the chemical energy of the motion of Li^+ from the anode and cathode to electrical energy that can do useful work and power devices. In this process, the anode is oxidized and the cathode is reduced. Since, and even before, commercialization of the LIB in the early 1990s, researchers have had great interest in understanding the fundamental properties governing performance of all components of the cell. Particular fervor has surrounded cathode development as the cathode is the capacity-limiting component in modern LIB systems.

Conventional positive electrode (i.e. cathode) materials for Li-ion technology utilize a Li^+ intercalation mechanism charge-balanced by redox on transition metals within an oxide host lattice. Current state-of-the-art LIBs use a transition metal oxide cathode of the general form $LiMO_2$, where M can be a mixture of metals, that relies on topotactic Li^+ intercalation during discharge and deintercalation during charge. One of the first commercialized materials was $LiCoO_2$ (LCO), reported by Goodenough and coworkers in 1980.[9] LCO can reversibly cycle up to 50% of the stoichiometric Li^+ before undergoing an irreversible phase change.[9] Delithiation of LCO causes

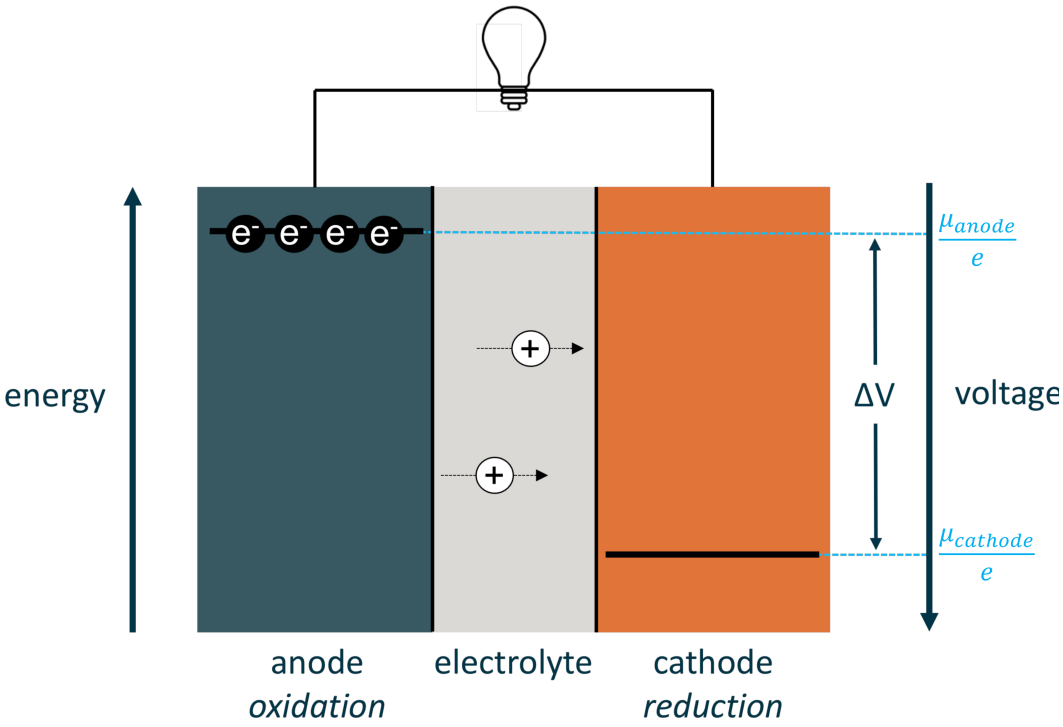

Figure 1.1: Graphical representation of a traditional LIB system in the charged state.

oxidation of the formally Co^{3+} to mixed $Co^{3+/4+}$. To overcome the 50% capacity limitation and stabilize the structure at higher degrees of delithiation, other metals have been partially substituted onto the Co site. Common substitutions include Mn and Ni, yielding the so-called NMC materials, or Ni and Al, yielding the so-called NCA materials. The energy density and average operating voltage of the most common forms of NMC and NCA ($LiNi_{1/3}Mn_{1/3}Co_{1/3}O_2$ and $LiNi_{0.8}Co_{0.15}Al_{0.05}O_2$) are comparable, while the experimental gravimetric capacity of NCA is higher (200 mAh g^{-1} vs. 170 mAh g^{-1} for NMC).[10–12] Additionally, olivine $LiFePO_4$ (LFP) has been widely employed as a cathode for applications prioritizing safety and long life cycle. LFP cathodes are increasingly considered for use in electric vehicles but they exhibit a lower energy density and operating voltage than NMC and NCA cathodes.[13] NMC, NCA, and LFP all store charge via intercalation chemistry and are limited to storing one Li^+ per transition metal.

Expanding beyond the one electron per transition metal paradigm set by conventional intercalation materials to achieve so-called multielectron storage allows access to higher theoretical capacities. In this thesis, one mechanism to achieve multielectron charge storage is investigated: anion redox. Materials that leverage both cation and anion redox while maintaining similar structures and composition to the tradi-

tional cathode materials display increased specific capacity and energy density.[14] Such materials often incorporate the desirable elements of intercalation-based redox chemistry like high reversibility while overcoming the capacity limitations of traditional transition metal-based redox. Observed multielectron energy storage has been attributed to anion redox in a wide range of oxides as well as some Li-rich metal sulfides.

1.2 Thesis Summary

The following chapters of this thesis detail four main studies of layered lithium metal chalcogenides as battery cathode materials that exhibit complex redox behavior that goes beyond the traditional one electron per transition metal paradigm represented in commercialized materials today.

Chapter 2 focuses on $Li_2Ru_{0.3}Mn_{0.7}O_3$, a material in the solid solution between Li_2RuO_3 and Li_2MnO_3, which have both generated significant interest in the field of anion redox cathodes for lithium-ion batteries. We show that this material does not exhibit reversible anion redox as previously implied in the literature. We characterize the charge compensation mechanism on and after the first cycle through extensive spectroscopic and local structure analysis and reveal a dynamically changing mechanism that evolves with cycling.

Chapter 3 focuses on attempts to modify the particle surface of anion redox cathode Li_2RuO_3 to stabilize high-energy defect sites and prevent structure changes detrimental to cell performance. We utilize several parallel approaches centered around soluble additives to the electrolyte that may either adsorb, coordinate, or electrochemically decompose onto the cathode surface and investigate the effects on capacity, cyclability, and mechanism.

Chapter 4 details the first work from the See Group on alkali-rich metal sulfides, which has become a principle area of research for us. Specifically, we report detailed electrochemical and spectroscopic characterization of previously reported phase Li_2FeS_2 and new structural analogue $LiNaFeS_2$ and show that both are capable of highly reversible multielectron redox enabled by both Fe and S contributions with S oxidation resulting in the formation of persulfides (i.e. S–S bonds). The S–S bonds are hypothesized to form via a coordinated tilting of corner-sharing Fes_4 tetrahedra around Li^+ vacancies. This work is published.

Chapter 5 is an extension of the work described in Chapter 4 and aims at further investigating the structural ramifications of persulfide formation in Li_2FeS_2. The

material undergoes different charge and discharge pathways yet is highly reversible from cycle to cycle. We find that the hypothesis of tetrahedral tilting is consistent with theoretical and experimental results, but the system is complex from a structural standpoint, bringing to light additional challenges associated with this type of anion redox behavior. This work is in preparation for publication.

Chapter 6 focuses on understanding the role of metal-anion covalency in dictating the anion redox behavior in lithium-rich iron chalcogenides. We report the synthesis and characterization of materials across the anion solid solution, $Li_2FeS_{2-y}Se_y$, wherein we can directly control the anion redox potential through anion substitution. Metal-anion covalency is highest in the selenium-rich materials as evidenced by the co-oxidation of Fe and Se throughout charging, but the capacity retention suffers due to the irreversible formation of a new, high-impedance phase, highlighting the importance of a holistic picture of the electronic and structural implications to anion-anion bond formation. This work is published.

Finally, Chapter 7 contains a detailed perspective on sulfur redox in lithium-ion battery materials framed in the context of the magnitude of change to the cathode material structure. This chapter provides a detailed summary of S redox in materials with intercalation- and conversion-type mechanisms as well as what we call hybrid-type mechanisms that take the advantages of both types while overcoming some of the greatest pitfalls. At the end, a survey of candidate hybrid-type materials is reported along with outlooks for the future of S-based redox in high-capacity batteries. This perspective is published.

Chapter 2

IRREVERSIBLE ANION OXIDATION LEADS TO DYNAMIC CHARGE COMPENSATION IN Ru-POOR, Li-RICH CATHODE $Li_2Ru_{0.3}Mn_{0.7}O_3$

Adapted from: Zak, J. J.; Zuba, M.; Lebens-Higgins, Z. W.; Huang, H.; Crafton, M. J.; Dalleska, N. F.; McCloskey, B. D.; Piper, L. F. J.; See, K. A. Irreversible Anion Oxidation Leads to a Dynamic Charge Compensation Mechanism in Ru-poor, Li-rich Cathode $Li_2Ru_{0.3}Mn_{0.7}O_3$. *Submitted*.

Chapter Abstract

Conventional cathodes for Li-ion batteries are layered transition metal oxides that support Li^+ intercalation charge-balanced by redox on the transition metals. Oxidation beyond one electron per transition metal can be achieved in Li-rich layered oxides by involving structural anions, which necessitates high voltages and complex charge compensation mechanisms convoluted by degradation reactions. We report a detailed structural and spectroscopic analysis of the multielectron material $Li_2Ru_{0.3}Mn_{0.7}O_3$, chosen due to low Ru content. *Ex situ* and *operando* spectroscopic data over multiple cycles highlight the dynamically changing charge compensation mechanism. Notably, over half of the first cycle capacity is attributed to O_2 gas evolution and reversible O redox is minimal. Instead, reduced Ru and Mn species are detected in the bulk and on the surface, which then increasingly contribute to charge compensation as more metal reduction occurs with cycling. Permanent structural changes linked to metal migration are observed with EXAFS and Raman analysis.

2.1 Introduction

In recent years, Li-rich oxides have been the subject of fervent investigation as high-capacity cathodes for LIBs.[14–19] Many examples take advantage of high-voltage processes most often attributed to oxidation of structural anions, going beyond the one electron per transition metal paradigm under which virtually all commercial LIB cathode materials operate.[12] The Li-rich material Li_2MnO_3, which is a component of Li-rich NMC materials,[20] was once thought to be electrochemically inactive.[21] Activation of Li_2MnO_3 can be achieved by nanoscaling the particles,[22] but the capacity was attributed primarily to irreversible side reactions involving the electrolyte, native surface carbonates, and gas evolution.[23] Thus, other materials in the Li_2MO_3 materials family have been explored to leverage the high Li to metal ratio. In particular, the focus has been on tuning the metal-anion covalency to access both cation and anion redox by changing the transition metal to 4d and 5d metals.[24–27]

One such 5d metal oxide is Li_2RuO_3, first reported by Goodenough and coworkers.[28] Li_2RuO_3 shows high gravimetric capacity with charge compensation suggested from both Ru and O redox.[29] However, Ru is a prohibitively expensive metal, which led to substitution of Ru in Li_2RuO_3 with less precious metals like Sn[25], Ti[30], and Mn[24, 31]. The solid solution between Li_2RuO_3 and Li_2MnO_3 is of interest due to the body of knowledge already accummulated on the electrochemical behavior of Li_2MnO_3, both on its own and as a component of Li-rich NMC materials. Sathiya *et al.* first reported the $Li_2Ru_{1-y}Mn_yO_3$ solid solution and more deeply characterized the $y = 0.4$ member, $Li_2Ru_{0.6}Mn_{0.4}O_3$.[24] Similarly, Lyu *et al.* focused on the $Li_2Ru_{0.5}Mn_{0.5}O_3$ material and examined the redox behavior and structural response to (de)lithiation over a wide voltage window.[31] These analyses of the $Li_2Ru_{1-y}Mn_yO_3$ solid solution focus on the more Ru-rich materials. Also, exploring the materials with a significantly lower voltage cutoff as in Lyu *et al.* make comparisons between materials and reports difficult.[31] Reducing the amount of Ru in the structure is important for cost reasons, and exploring if the same rules apply to Ru-poor materials is imperative to understand the role of Ru and probe the effects on anion redox mechanisms. Here, we aim to address several questions: (1) What are the contributions of each redox-active component? (2) Are the bulk and surface processes the same or different? (3) How does the structural response to redox influence reversibility? As such, we report the detailed characterization of the charge compensation mechanism and consequent structural response to (de)lithiation for Ru-poor material $Li_2Ru_{0.3}Mn_{0.7}O_3$. We find a complex and dynamically changing

redox mechanism, the deconvolution of which provides insight into anion redox mechanisms in similar Li-rich layered oxide cathodes.

2.2 Results and Discussion

Synthesis and Structure

As-synthesized Li_2RuO_3 and Li_2MnO_3 are black and bright orange, respectively, due to the intrinsic differences in electronic structure dictated by the transition metal. Li_2RuO_3 is a semimetal[32] and Li_2MnO_3 is a wide-bandgap semiconductor.[33] Detailed characterization is conducted on $Li_2Ru_{0.3}Mn_{0.7}O_3$ as a low-Ru material that exhibits multielectron storage capabilities with respect to the transition metal content yielding over 250 mAh g^{-1} on the first charge (1.2 mol e^- per f.u.). $Li_2Ru_{0.3}Mn_{0.7}O_3$ is a dark brown powder, a visual sign that the material is well-mixed. The X-ray diffraction (XRD) pattern with quantitative Rietveld refinement is shown in Figure 2.1a. Sathiya *et al.* previously reported the structure and refined lattice parameters of several materials in the solid solution[24] but did not report the Ru = 0.7 material. Here, we find that $Li_2Ru_{0.3}Mn_{0.7}O_3$ crystallizes in the C2/*m* space group of Li_2MnO_3. Like in previous reports of similar materials,[24, 31] the XRD pattern was fit by allowing intraplanar site mixing in the LiM_2 layers between the 4g and 2b sites occupied by a transition metal and Li, respectively. Intralayer mixing from the 4g onto the 2b site was held constant at 0.1 Mn, 0.1 Ru, and 0.2 Li. Improvements to the fit are possible but the quality of data and X-ray source prevented rigorous refinement of mixing involving Li. The refinement is adequate to show that the phase is formed but it does not describe the peaks between 20 and 34° 2θ attributed to Li/transition metal ordering in the layers, thus signifying significant disorder in the assumed O3 stacking of $Li_2Ru_{0.3}Mn_{0.7}O_3$.[34, 35] This is likely due to mixing on the 4g and 2b sites by Li, Ru, and Mn. If intralayer mixing is not allowed, the refinement fits slightly worse as evidenced by a higher residual value. The stoichiometry is supported by a comparison of *ex situ* Raman spectra of various materials in the $Li_2Ru_{1-y}Mn_yO_3$ ($y > 0.4$) solid solution (Figure 2.1b) in which there are systematic changes to the spectra as Ru content is increased, highlighting the facile synthetic control over transition metal ratios. The peaks broaden as disorder increases and two new Ru-related modes appear around 680 and 720 cm^{-1}.

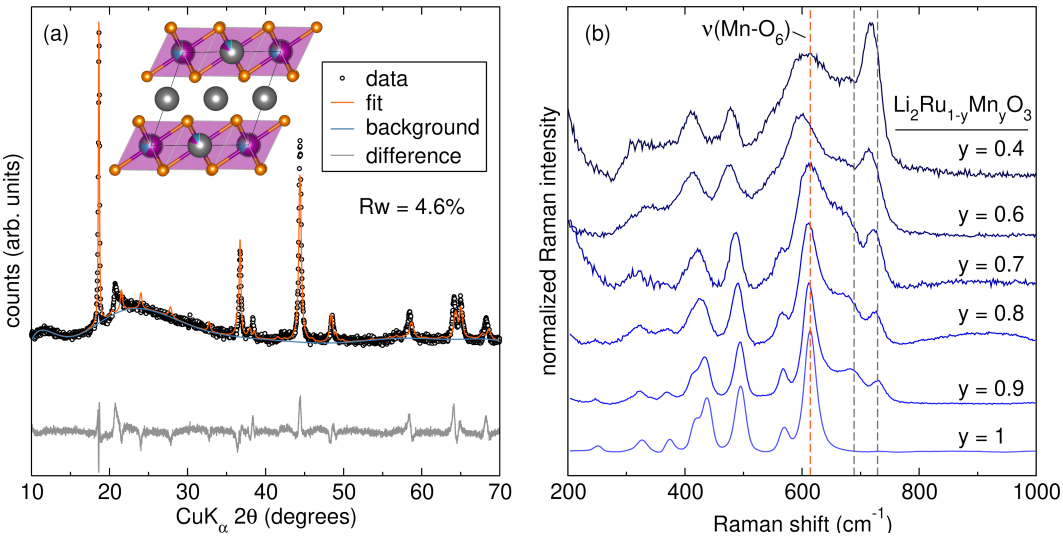

Figure 2.1: Structural confirmation and analysis of $Li_2Ru_{0.3}Mn_{0.7}O_3$. (a) Powder XRD with quantitative fit using the Rietveld method. (b) *Ex situ* Raman spectroscopy with comparison to other materials in the $Li_2Ru_{1-y}Mn_yO_3$ ($y > 0.4$) family highlighting the onset of Ru-related modes.

Electrochemical Characterization

The galvanostatic cycling data is shown in Figure 2.2a. $Li_2Ru_{0.3}Mn_{0.7}O_3$ exhibits charge storage capabilities greater than that afforded by $Ru^{4+/5+}$ redox alone, which would give only approximately 62 mAh g^{-1}. However, the extent to which the extra capacity is contributed by redox on the oxide anions or by side reactions is an important distinction. We assert that the redox mechanisms in this material are complex and change dynamically, and a detailed account of the charge compensation mechanism is laid out in the following discussion. The voltage profile shows an initial sloping region with an inflection around 3.75 V followed by a more gently sloping plateau centered around 4.2 V. The subsequent discharge is S-shaped with a significant voltage hysteresis and an irreversible capacity loss of approximately 82 mAh g^{-1}, consistent with previous reports.[24, 31] After extended cycling, the voltage profile shows evidence of two more distinct sloping regions centered around 3.2 V and 4.3 V and greater voltage hysteresis. The evolution of the voltage profile with cycling suggests significant changes to the charge compensation mechanism over time. The long-term cycling performance of $Li_2Ru_{0.3}Mn_{0.7}O_3$ is shown in Figure 2.2b. Interestingly, the capacity upon charging increases steadily from 186 mAh g^{-1} to 206 mAh g^{-1} between cycles 2 and 18 before beginning to decrease. While the capacity during charge increases, the capacity during discharge does not indicating some irreversibility in the charging mechanism during oxidation.

Furthermore, when the charge capacity starts decreasing after cycle 18 the discharge capacity decreases as well, suggesting that the irreversible processes contributing to the initial increase of the capacity during charge are self-terminating.

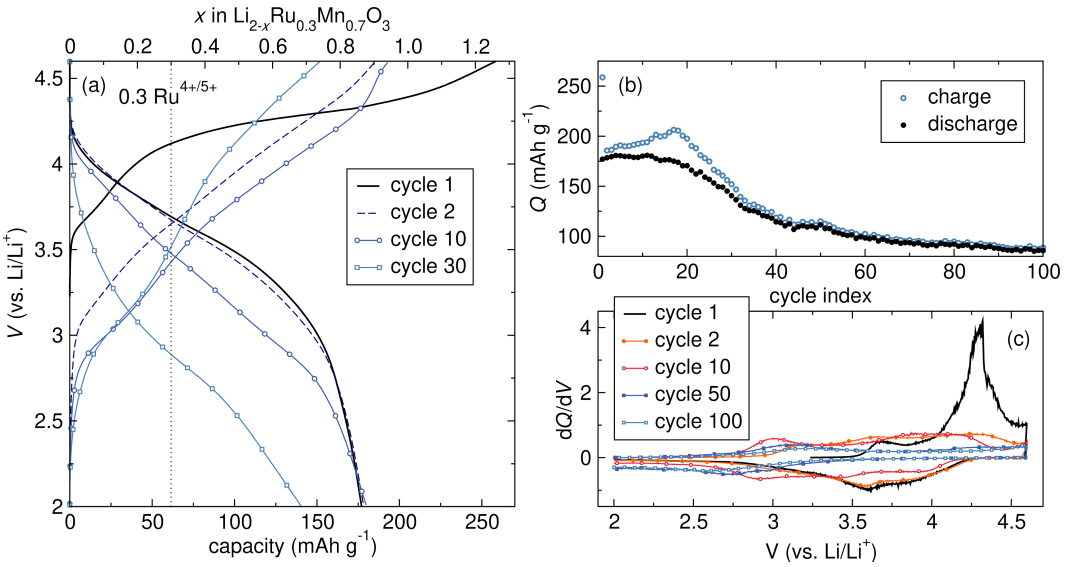

Figure 2.2: (a) Charge and discharge profiles from cycles 1, 2, and 10, (b) long-term cycling performance of $Li_2Ru_{0.3}Mn_{0.7}O_3$ at a rate of C/10 based on 1 e^- per formula unit, and (c) differential capacity (dQ/dV) plot of $Li_2Ru_{0.3}Mn_{0.7}O_3$ from selected cycles.

The differential capacity curves shown in Figure 2.2c begin to shed light on potential reasons for the odd cycling behavior. The first charge is characterized by a large feature centered around 4.3 V that is not reproduced on later cycles, and the reduction features on discharge are distinctly different than those on charge highlighting the change in mechanism. On later cycles, a new, low-voltage redox couple around 2.8 V (reduction) and 3.2 V (oxidation) appears, and a similar feature in analogous materials has been attributed to Mn redox.[24, 36–38] Reduction of surface Mn that then contributes to redox on subsequent cycles could explain the rise in capacity from cycle 2 to 18. In later cycles, the Mn redox feature begins to disappear along with the higher voltage features, which explains the more rapid decrease in capacity after cycle 18 and corroborates a dynamically changing charge compensation mechanism.

Charge Compensation Mechanism

To explore the origins of the excess capacity beyond $Ru^{4+/5+}$, we first employ a variety of bulk characterization techniques on extracted electrodes at different states of charge (SOCs) in cycles 1, 2, and 10. First, evidence of the changes to the oxidation state of Ru and Mn are elucidated through K-edge X-ray absorption spectroscopy

(XAS). Cycle 1 and cycle 2 are hereafter compared due to the significant change in the electrochemistry after the first charge, and data from cycle 10 is used to probe for changes that evolve with cycling.

The Ru K-edge spectra of $Li_2Ru_{0.3}Mn_{0.7}O_3$ are shown in Figure 2.3a-d. The rising edge position, here defined as the energy at half the height of the main absorption edge, is 22129.5 eV corresponding to bulk Ru^{4+} in reasonable agreement with that reported for $Li_2Ru_{0.5}Mn_{0.5}O_3$.[31] Compared to reports of similar materials like $Li_{1.2}Ni_{0.2}Ru_{0.6}O_2$, which adopts the $R\bar{3}m$ structure like $LiCoO_2$,[9] the rising edge position of $Li_2Ru_{0.3}Mn_{0.7}O_3$ is approximately 1 eV higher, suggesting that the Ru–O interaction is more ionic.[39] The lower proportion of Ru compared to the 3d metal causes greater isolation of Ru, likely contributing to the greater degree of charge localization in $Li_2Ru_{0.3}Mn_{0.7}O_3$. Upon charging to 4.15 V, the rising edge position shifts to higher energy by 0.5 eV, which indicates oxidation of bulk Ru^{4+} to Ru^{5+}. At 4.15 V, the charge passed as measured by the electrochemistry equates to almost exactly that required to oxidize all Ru to Ru^{5+} (61.5 mAh g^{-1}). Upon fully charging to 4.6 V, the rising edge does not shift further, suggesting oxidation of Ru does not proceed past Ru^{5+}. At full SOC, the pre-edge region around 22120 eV exhibits an intensity increase, indicating a distortion in the octahedral symmetry, which leads to more efficient d-p mixing.[40] Upon discharging to 2 V, a significant shift (2.2 eV) of the rising edge to lower energy is observed. The shift to lower energies relative to the as-prepared sample indicates an over-reduction of Ru and the presence of Ru^{3+}. Near-edge scattering features differ slightly in their position and intensity, which points to irreversible changes in the local structure around Ru. The Ru K-edge X-ray absorption near-edge structure (XANES) spectra for the second and tenth cycles display similar trends as the first. Notably, the edge position never recovers to that of the as-prepared material, suggesting that either the average oxidation state of Ru stays lower than 4+ or structural changes lead to new Ru environments. Figure 2.3d shows relative changes of the edge position, making apparent the over-reduction of Ru after the first charge process. On later cycles, the edge position never recovers the original value but continues to shift as evidence of Ru involvement in the redox.

Mn K-edge XAS (Figure 2.3e-h is also measured to investigate redox non-innocence as suggested by the new low-voltage redox couple observed in the dQ/dV plots. The pre-edge features arise from a 1s to 3d transition for Mn in an octahedral geometry and represent the partially filled t_{2g} (6541 eV) and e_g (6543 eV) states. The edge position of $Li_2Ru_{0.3}Mn_{0.7}O_3$ is 6557 eV, which is in good agreement with reports

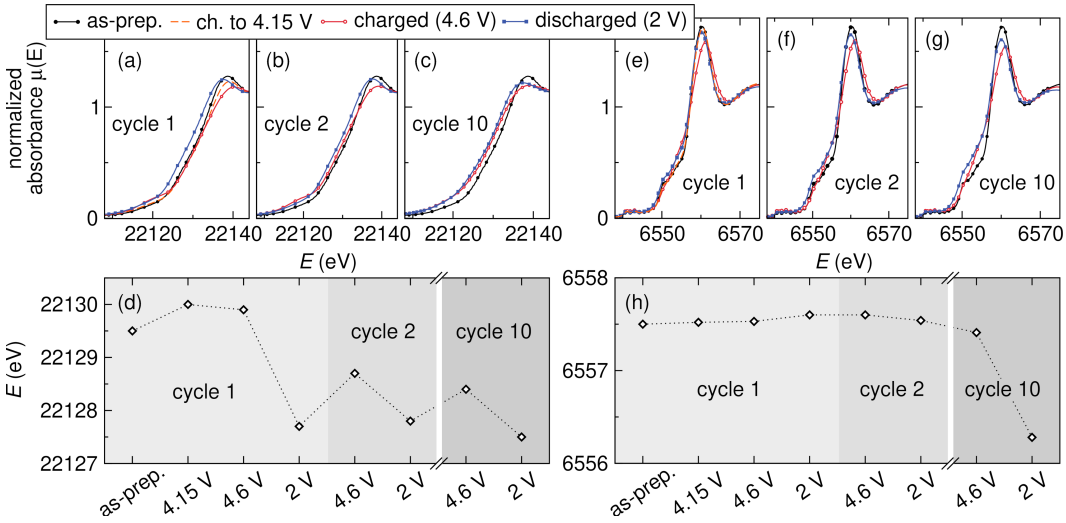

Figure 2.3: (a-c) *Ex situ* Ru K-edge XANES of $Li_2Ru_{0.3}Mn_{0.7}O_3$ at various SOCs: as-prepared, charged to 4.15 V, charged to 4.6 V, fully charged then discharged to 2 V, charged to 4.6 V on cycle 2, discharged on cycle 2, charged to 4.6 V on cycle 10, and discharged on cycle 10. (d) The change in the Ru K-edge position with cycling highlighting redox involvement and over-reduction upon discharge. (e-g) *Ex situ* Mn K-edge XANES at the same SOC with arrows highlighting reduced Mn. (h) The change in the Mn K-edge position showing minimal changes until later cycles. Collected by M. Zuba.

of Mn K-edge XANES of $Li_2Ru_{0.5}Mn_{0.5}O_3$[31] and Li_2MnO_3[23] signifying that Mn is formally Mn^{4+}. The K-edge white line arises from the 1s to 4p transition and is especially sharp and intense due, in part, to the negatively charged neighboring anions and the localization of the excited electron on Mn, suggesting a fairly ionic Mn-O interaction. The rising edge in the Mn K-edge XANES does not shift upon oxidation, which is more easily observed in Figure 2.3h, indicating no oxidation of Mn past Mn^{4+}. Irreversible changes to the spectral shape and pre-edge may be due to changes to the local environment around Mn that persist after the first oxidation. After discharging to 2 V, extra spectral weight near the edge at lower energies indicates reduction of Mn below Mn^{4+}. The trends are essentially identical in cycle 2. By cycle 10, the edge position decreases by over 1 eV upon discharge, indicating significant Mn involvement to the redox and corroborating the dQ/dV results.

On the first charge, XAS shows that Ru^{4+} is oxidized and the Mn^{4+} is largely redox innocent. However, the charge expected from full oxidation of Ru^{4+} to Ru^{5+} is insufficient to explain the high capacities observed. The possible explanations for the excess capacity are lattice O redox and decomposition reactions, both of

which have been reported extensively.[24, 31, 41, 42] To explore the possibility of reversible lattice O redox, O K-edge resonant inelastic X-ray scattering (RIXS) studies are performed. RIXS acts as a sensitive probe of the electronic structure of lattice O by combining XAS and X-ray emission spectroscopy (XES), allowing filled states to be probed and introducing a higher dimensionality than either technique alone.[40] The RIXS maps for $Li_2Ru_{0.3}Mn_{0.7}O_3$ on the first charge are shown in Figure 2.4a-c. Two pre-edge features are observed and attributed to hybridized Mn 3d–O 2p orbitals split into t_{2g} and e_g states by the octahedral crystal field.[43] The appearance of a RIXS loss feature at 523.5 eV from an excitation at 531 eV has been attributed to bulk O redox contributions in several Li-rich layered oxide systems.[39, 44–46] However, this spectroscopic signature is not observed in the RIXS maps of $Li_2Ru_{0.3}Mn_{0.7}O_3$, indicating the lack of bulk O redox activity, a different O oxidation mechanism, or the prevalence of oxidized O being lower than the detection limit in the RIXS measurements. Bruce and coworkers have shown in several closely related systems that high-resolution RIXS is necessary to detect the presence of holes on O or trapped molecular O_2.[47–49]

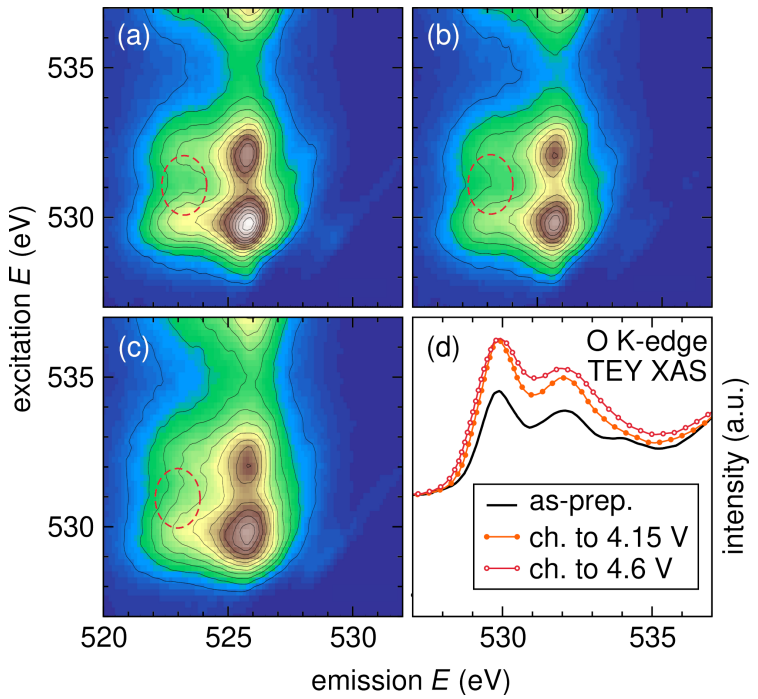

Figure 2.4: *Ex situ* (a-c) RIXS and (d) O K-edge TEY XAS of $Li_2Ru_{0.3}Mn_{0.7}O_3$ during the first charge cycle. Notably, no new features are observed that would indicate oxidized lattice O, highlighting the irreversibility of O redox processes in this material. Collected by Z. W. Lebens-Higgins, H. Huang, and M. Zuba.

To determine if irreversible decomposition reactions are occuring, we turn to differ-

ential electrochemical mass spectrometry (DEMS) to characterize gaseous products during cycling. The *operando* DEMS data for the first three cycles are shown in Figure 2.5a. During the first charge cycle, a significant feature from O_2 gas release is observed starting at the onset of the high-voltage plateau. O_2 release can come from oxidation of lattice O followed by gas release[25, 50, 51] since electrolyte degradation and oxidation of surface carbonates produces exclusively CO_2.[41, 52, 53] A comparatively small amount of CO_2 is observed at the top of charge (>4.4 V). By integrating the DEMS data, the charge contributions of the decomposition reactions resulting in gaseous products to the total capacity are calculated. The capacity from oxidation to O_2 alone during the first charge assuming a four-electron oxidation process is 122 mAh g^{-1}, or 45.7% of the total charge capacity. Comparatively, CO_2 only contributes approximately 2 mAh g^{-1}. As such, about half of the first charge capacity can be attributed to irreversible degradation reactions. Upon discharging, the gas release drops precipitously, confirming that the gases detected are a result of oxidative decomposition reactions at high voltages. The O_2 gas release on subsequent cycles sequentially decreases. The gas release likely on the first cycle likely triggers a structural change and consequent change to the redox mechanism, which is corroborated by the change in the shape of the voltage profile.

Surface Characterization

In the absence of evidence of bulk O redox, we turned to more surface sensitive methods. Figure 2.4d shows the O K-edge XAS spectra in surface-sensitive total electron yield (TEY) mode. The two pre-edge features at 529.9 and 532.1 eV correspond with the Mn–O hybridized states as observed in the RIXS. An additional feature in the as-prepared sample around 534 eV is attributed to surface carbonates.[54, 55] The carbonate feature disappears upon charging suggesting that the carbonates are oxidized off the surface. The changes upon charging consist solely of broadening of the pre-edge features, as is also observed in the RIXS maps, and do not indicate significant oxidation of lattice O that stays near the surface.

The release of O_2 from the cathode suggests O^{2-} oxidation and necessitates charge compensation and/or densification near the surface where O vacancies are known to form.[56, 57] To probe the effects of gas release on $Li_2Ru_{0.3}Mn_{0.7}O_3$, surface-sensitive probes of the electronic structure including hard X-ray photoelectron spectroscopy (HAXPES) and XAS in TEY mode are used (Figure 2.5). In the O 1s region of the HAXPES, the as-prepared $Li_2Ru_{0.3}Mn_{0.7}O_3$ cathode has two main features: a narrow peak around 529.5 eV and a broader feature centered around

532.5 eV attributed to bulk O^{2-} and surface carbonates, respectively.[14, 24, 58, 59] Upon charging to 4.15 V, the feature at 532.5 eV largely disappears as native surface carbonates are oxidized. Then, at full charge, a new feature around 531 eV grows along with additional spectral weight between 532 and 535 eV. The new feature at 531 eV has historically been used as a direct indicator of bulk O oxidation.[24–26, 58] In fact, Lebens-Higgins *et al.* recently performed a systematic study on several common Li-ion cathode materials and observed the new feature, but it is instead attributed to transition metal reduction and electrolyte decomposition near the surface.[60] The same concepts are invoked here and are supported by HAXPES in the Ru 3p and Mn 2p region and XAS (TEY) at the Mn L-edge (Figure 2.5c-g). HAXPES results in the Ru 3p region closely mirror the K-edge XAS data with an initial positive shift at 4.15 V (Ru^{4+} to Ru^{5+}) and no further shift at 4.6 V. However, additional spectral weight arises at low binding energies in the fully charged vs. partially charged samples, suggesting a small proportion of reduced Ru near the surface upon oxidation. The Mn 2p HAXPES data, specifically comparing cathodes charged to 4.15 and 4.6 V (Figure 2.5f), show additional spectral weight (more substantial than the Ru case) at low binding energies in the fully charged sample as illustrated by the difference curve. This result indicates reduction of Mn near the surface at high voltages. Greater amounts of reduced Mn are also observed at high voltages in the Mn L-edge XAS (Figure 2.5g). Reduced Mn near the surface has been observed in a variety of Li-rich NMC materials,[56, 57, 61, 62] which are structurally similar to $Li_2Ru_{0.3}Mn_{0.7}O_3$. O_2 gas release from the lattice near the surface has been shown to be accompanied by transition metal reduction and sometimes densification.[56, 57, 63–66]

The signs of reduced transition metals near the surface in $Li_2Ru_{0.3}Mn_{0.7}O_3$ from HAXPES are not maintained upon discharge. To determine if the reduced metals are lost to the electrolyte, inductively coupled plasma mass spectrometry (ICP-MS) is performed for the electrolyte before and after cycling. Mn is observed in the electrolyte after cycling, pointing to Mn dissolution, which has been observed in Mn-rich materials with low-valent Mn.[67–70] The Mn L-edge XAS (TEY) results show the most significant quantity of reduced Mn in the fully discharged sample. As such, we assert that transition metals are reduced past the formal charge state of the prisinte material on both the surface and in the bulk upon discharge. This result is consistent with the nucleation and growth model for spinel formation reported by Gu *et al.* in C2/*m* $Li_{1.2}Ni_{0.1}Mn_{0.525}Co_{0.175}O_2$,[56] where here we consider spinel formation as a proxy for reduction of transition metals.

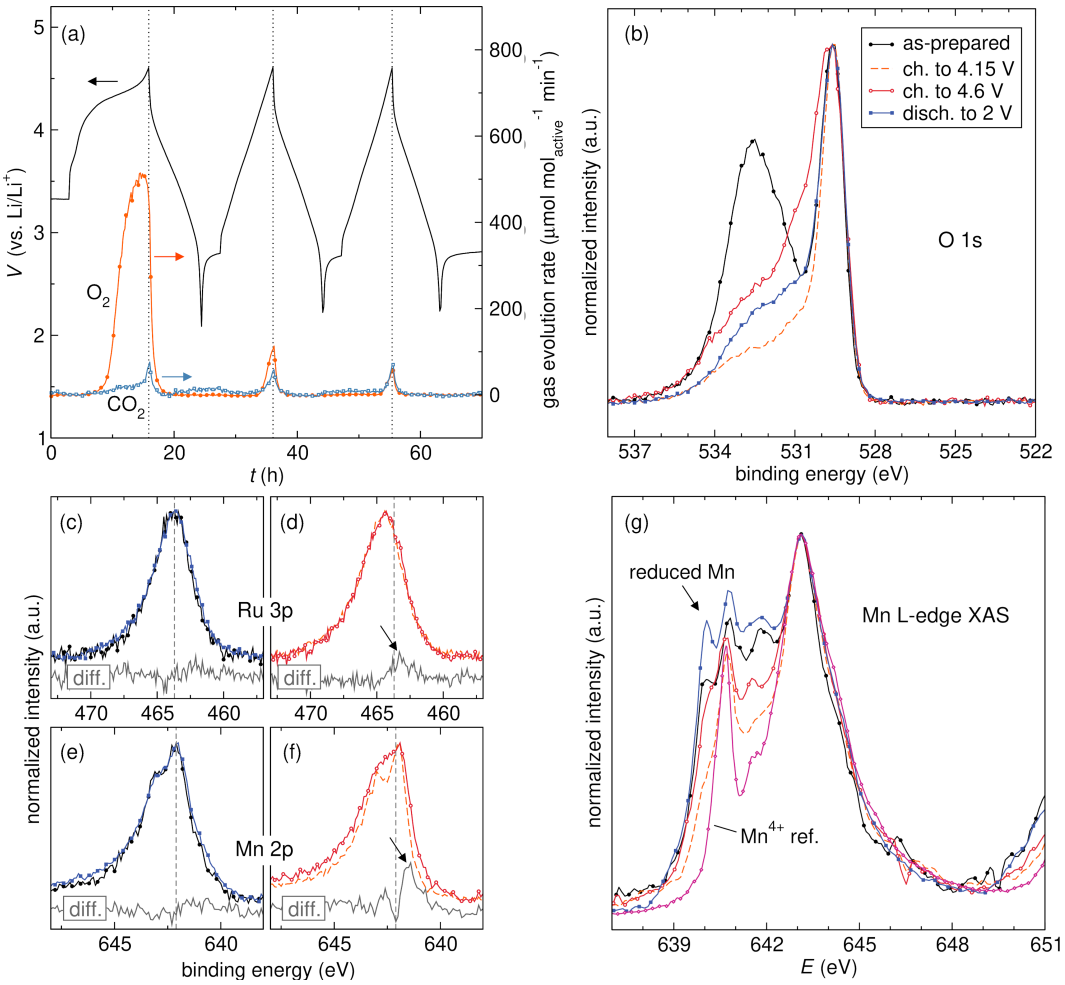

Figure 2.5: (a) *Operando* DEMS of $Li_2Ru_{0.3}Mn_{0.7}O_3$ for the first three cycles. DEMS collected by M. J. Crafton. (b) HAXPES at various SOC in the (b) O 1s, (c, d) Ru 3p, and (e, f) Mn 2p regions. (g) Mn L-edge XAS collected in total electron yield mode. HAXPES and L-edge XAS collected by Z. Lebens-Higgins and M. Zuba and analyzed by J. Zak.

Local Structure Evolution

To understand how the dynamically changing charge compensation and gas release affects local structure, extended X-ray absorption fine structure (EXAFS) analysis is performed and first- and second-shell bond lengths and correlation distances are extracted from fits. A summary of the fits of the EXAFS data is shown in Figure 2.6a-b. Overall, the amplitude of the EXAFS decreases during charge and is not fully recovered upon discharge, indicating permanent increases in disorder.[23, 31] The first-shell correlations correspond to *M*–O bonds (Figure 2.6a). Here, the *M*–O distance can be thought of as a proxy for redox involvement; that is, a shortening indicates oxidation and a lengthening indicates reduction. As expected,

the Ru–O bond length shortens with oxidation at 4.15 V and lengthens slightly at 4.6 V, corroborating HAXPES results suggesting slightly reduced Ru when fully charged. After discharge, Ru–O has increased beyond that in the as-prepared sample, consistent with reduction beyond the formal oxidation state in the pristine phase. The Mn–O bond length does not change much with cycling, which highlights the relative redox inactivity in early cycles. A slight decrease in the Mn–O bond length is observed at 4.6 V, however, which supports the presence of reduced Mn as indicated by the XANES and HAXPES.

The second-shell coordination sphere is dominated by metal-metal scattering events. Li correlations are ignored in the model due to the small X-ray scattering cross section. The multi-structure model allows for metal-metal correlation lengths to be extracted for Ru and Mn back-scatterers from both Ru and Mn absorbers. For ease of understanding, correlations will be discussed with a M_1–M_2 convention where M_1 is the absorber and M_2 is the back-scatterer. The Ru–Ru correlation length decreases during the first oxidation, consistent with an overall lattice contraction (Figure 2.6b). Upon discharging, the Ru–Ru distance returns to the same value as in the as-prepared sample (approximately 3.03 Å). On cycle 2, Ru–Ru correlations contract during oxidation and expand again during reduction to comparable values as in the first cycle. However, by cycle 10, the correlation length at fully charged dips to 2.89 Å, a 0.14 Ådecrease, and only lengthens slightly to 2.92 Åduring discharge. Additionally, the model fits Ru–Ru correlations worse as $Li_2Ru_{0.3}Mn_{0.7}O_3$ is cycled (see relative errors), suggesting significant changes to the Ru network with cycling. Ru–Mn correlations show less change overall due to the majority of Mn being redox inactive Mn^{4+}. However, as K-edge XAS and HAXPES show, more Mn is reduced with cycling. The redox involvement of Mn is supported by shorter Ru–Mn correlation lengths on cycle 10. Interestingly, on cycles 1 and 2, Ru–Ru and Ru–Mn correlation lengths converge at full charge, and by cycle 10 are almost identical. One possible explanation for this behavior is mobile Mn as has been observed in similar Li-rich NMC materials.[56, 57, 66, 71]

The trends observed in the Mn–Mn correlations are similar to those with a Ru absorber (Figure 2.6b). The Mn–Mn correlation distance does not noticeably change during cycling, which is attributed to the large amount of Mn relative to Ru and a large proportion of the Mn being surrounded only by Mn and remaining relatively inert during cycling. Mn–Ru correlation distances trend the same as the fit Ru-Mn distances from the Ru K-edge EXAFS as expected. The errors are much larger

due to Mn-Ru scattering events being a much smaller proportion of the overall scattering than Ru-Mn scattering events are to the Ru EXAFS. The changes suggest a reordering of Mn in the lattice during the first cycle, supporting the mobility of Mn during oxidation. These results also indicate that most changes to Mn are occurring in those that have redox active Ru next-nearest neighbors.

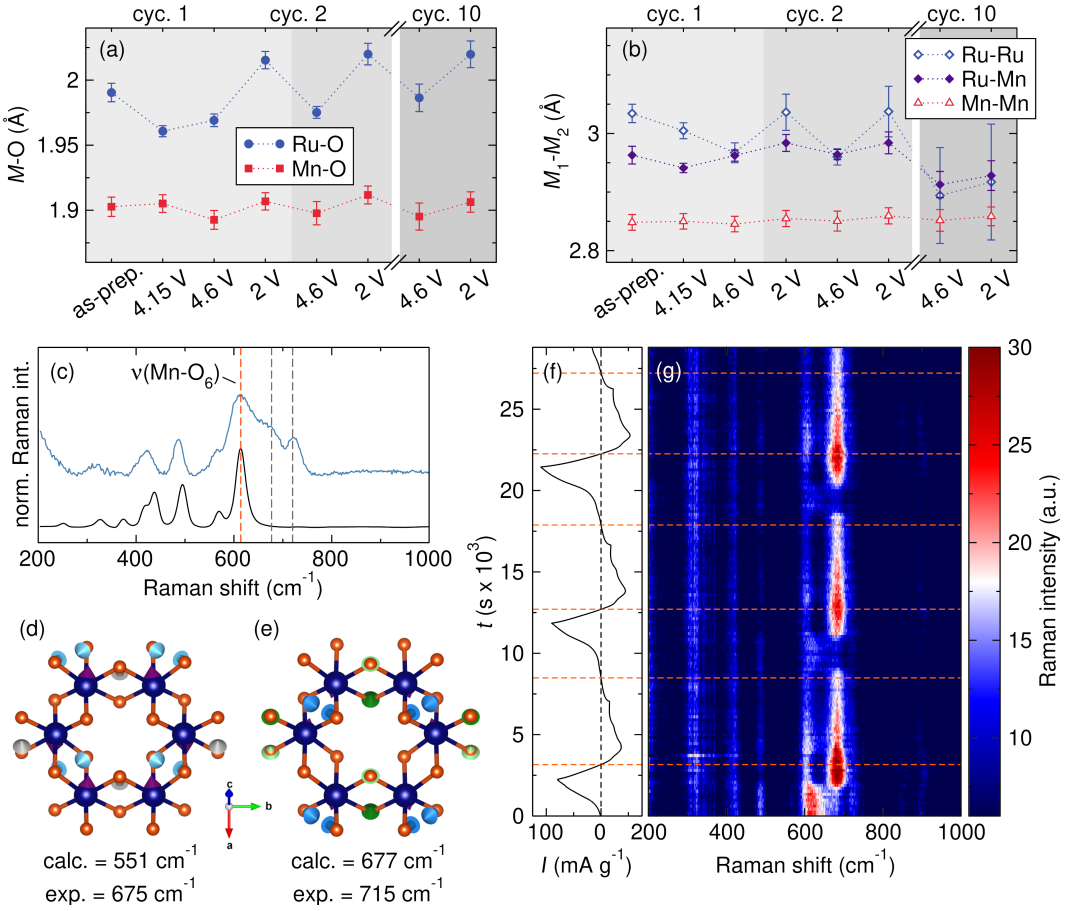

Figure 2.6: (a) First shell metal-O bond lengths and (b) second shell metal-metal coordination distances as a function of cycling from EXAFS fits. EXAFS collected by M. Zuba. (c) *Ex situ* Raman spectroscopy of $Li_2Ru_{0.3}Mn_{0.7}O_3$ as compared to Li_2MnO_3 with the Mn-O A_{1g} mode and two new modes in $Li_2Ru_{0.3}Mn_{0.7}O_3$ highlighted. Calculated Raman modes in Li_2RuO_3 with translation vectors scaled up by a factor of 2, provided by authors from Ref. 62, at (d) 551 cm^{-1} (predicted)/675 cm^{-1} (experimental) and (e) 677 cm^{-1} (predicted)/715 cm^{-1} (experimental). (f, g) *Operando* Raman spectroscopy of $Li_2Ru_{0.3}Mn_{0.7}O_3$ over three CV cycles with the zero current points marked with dotted lines to separate oxidative and reductive current regions.

Significant changes to the Ru environments and Mn network in $Li_2Ru_{0.3}Mn_{0.7}O_3$ as evidenced by EXAFS are also observed by Raman spectroscopy. The *ex situ* Raman spectra of $Li_2Ru_{0.3}Mn_{0.7}O_3$ and Li_2MnO_3 are shown in Figure 2.6d. The

spectrum of Li_2MnO_3 is reported and the mode at 612 cm^{-1} is attributed to the MnO_6 A_{1g} symmetric stretch.[72] The lower frequency peaks are attributed to various Mn–O and Li–O modes. The spectrum of $Li_2Ru_{0.3}Mn_{0.7}O_3$ shows modes at similar frequencies with several key differences. First, the MnO_6 A_{1g} mode is significantly broader, which is attributed to a variety of different next nearest neighbor Mn environments. Two notable new modes at 678 and 718 cm^{-1} are observed and we attribute them to Ru–O related vibrations. *Ex situ* Raman spectra of several members of the $Li_2Ru_{1-y}Mn_yO_3$ ($y > 0.4$) solid solution further support the assignment as these modes increase in intensity relative to the Mn–O A_{1g} mode with increasing Ru content (Figure 2.1b). Phonon modes calculated by Ponosov *et al.* for Li_2RuO_3 have good agreement with the two new modes in $Li_2Ru_{0.3}Mn_{0.7}O_3$, specifically those calculated at 551 cm^{-1} (A_g) and 677 cm^{-1} (A_g) were observed experimentally at 675 cm^{-1} and 715 cm^{-1}, respectively.[73] The atom displacement vectors associated with the calculated modes by Ponosov *et al.* are shown in Figure 2.6e-f.[73] Both new modes in $Li_2Ru_{0.3}Mn_{0.7}O_3$ have components of O translation that shortens one RuO_6 octahedral edge and brings two adjacent O closer together, and the lower frequency mode has a larger component of Ru motion. The presence of these modes and good agreement of the observed frequencies with Li_2RuO_3 may indicate Ru clustering.

Operando Raman spectroscopy is collected during a cyclic voltammetry (CV) measurement for three cycles to observe how these modes change with oxidation adn reduction (Figure 2.6g-h). Galvanostatic cycling is not used due to the long times spent at high voltages that result in significant O_2 release and side reactions, which block Raman signal from the bulk material. Results show significant changes to the local structure with cycling. Upon oxidation, the Mn-related modes lose intensity and red-shift to lower frequencies, which supports the reduction of Mn as a result of O_2 release at high voltages. Additionally, a new potential-dependent mode at 682 cm^{-1} appears on the first negative scan. The mode is likely a sharp increase in intensity and blue-shift of the Ru–O related mode due to Ru oxidation because the Ru–O related mode decreases in intensity. The high-frequency Ru–O related mode also blue-shifts but to a lesser degree, which tracks with Ru motion being of lesser magnitude as shown in the calculated phonon mode. When the voltammogram reaches reduction, i.e. negative current, the changes begin to reverse. The point at which the CV switches from oxidation to reduction, and vice versa, are indicated with dashed lines in Figure 2.6g-h. However, the Mn-related modes do not recover their original intensity, indicating permanent changes to the Mn network. On subse-

quent cycles, the Ru-related modes display similar behavior to that observed on the first cycle, indicating some reversibility with respect to the Ru local environment.

2.3 Conclusions

$Li_2Ru_{0.3}Mn_{0.7}O_3$ shows a complex charge compensation mechanism that changes dynamically with cycling. On the first charge, XAS confirms that Ru is oxidized to Ru^{5+} and no further, which only accounts for 0.3 of the >1 Li that appears to be removed. Excess charge is accomodated by lattice O oxidation, but most of the anion oxidation is irreversible and results in significant O_2 gas release as shown by DEMS. O loss causes reduction of Mn even in the charged mateiral. Upon discharge, both Mn and Ru are educed beyond the formal oxidation state of the pristine material. In subsequent cycles, the majority of the capacity is attributed to Ru and Mn redox alone, though the contributions from each change with time. This dynamic redox behavior can give a false impression of good cyclability based on anion redox when, in fact, $Li_2Ru_{0.3}Mn_{0.7}O_3$ only exhibits significant contributions from O on the first charge cycle despite being within a solid solution ($Li_2Ru_{1-y}Mn_yO_3$) reported to have reversible anion redox.[24] Therefore, it is prudent to consider each material across a solid solution separately, especially when the end members have different structures and electrochemical behaviors. Considering $Li_2Ru_{0.3}Mn_{0.7}O_3$ with respect to Li_2MnO_3, this work shows that a small amount of a redox active metal activates semi-reversible Li removal and insertion (approximately 0.8 Li reversibly in this case) whereas all observed capacity in Li_2MnO_3 is from decomposition reactions and not Li cycling.[23] Nevertheless, the charge compensation mechanism is convoluted and changes with cycling, which highlights the difficulty of characterizing the long-term viability of anion redox materials based on Li-rich layered structures.

2.4 Experimental Methods

Materials Preparation. $Li_2Ru_{1-y}Mn_yO_3$ was synthesized according to the procedure provided by Sathiya *et al*.[24] Powders of Li_2CO_3 (Sigma-Aldrich, 99.99%), RuO_2 (Acros Organics, 99.5%, anhydrous) and $MnCO_2$ (Sigma-Aldrich, 99.9%) were ground in stoichiometric quantities (a 10% by weight excess of Li_2CO_3 was used to combat Li volatilization during heating) and pressed into pellets of 200-300 mg with a hand-operated arbor press. Pellets were heated in alumina crucibles in air at 2 °C min^{-1} to 900 °C with a dwell time of 15 h and cooled ambiently to room temperature. After an intermediate grinding step, the powder was again pressed

into pellets and heated at 2 °C min^{-1} to 950 °C followed by a dwell time of 15 h before being cooled ambiently to room temperature. The pellets were ground into fine powders for further characterization.

Electrode Fabrication. Electrode slurries were prepared by suspending 80/10/10 (wt%) active material, conductive carbon (SuperP, Alfa Aesar, > 99%), and PVDF binder (MTI) in *N*-methyl-2-pyrrolidone (ca. 2 times by mass of total solids) (Sigma-Aldrich, 99.5%) with a centrifugal mixer (Thinky USA). Electrode films were prepared by doctor blading onto carbon-coated Al foil (MTI) at a 20 μm thickness. The films were dried in air and 1/2" diameter electrodes were punched from the film. The electrodes were dried in a vacuum oven at 110 °C for at least 12 h, yielding an active material loading of 4-6 mg.

Electrochemical Testing. All electrochemical cells were assembled inside an Ar-filled glovebox (H_2O and O_2 < 1 ppm). Electrochemistry with slurry-cast electrodes was performed in 2032 coin cells (MTI) with a Li foil anode (Alfa Aesar, > 99.9%, 0.75 mm, mechanically cleaned immediately before cell assembly), polypropylene separator (Celgard 2400), c.a. 4 drops of LP100 electrolyte, and a working electrode of 80 wt% active material as described above. The LP100 electrolyte was prepared as a 1 M solution of $LiPF_6$ (Oakwood Chemical, Battery Grade) in a 1:1:3 (by volume) mixture of ethylene carbonate (EC), propylene carbonate (PC), and dimethyl carbonate (DMC) (all Sigma, > 99%, anhydrous). The solution was prepared in a dried HDPE bottle. The liquid carbonates (DMC and PC) were stored over activated molecular sieves (3 Å, Beantown Chemical) prior to use. All materials were charged (oxidized) at the rate indicated (based on one electron per formula unit) to 4.6 V and discharged at the rate indicated to 2 V. All voltages are *vs.* Li/Li^+. Electrochemical experiments were performed with a BCS 805 battery cycler (Bio-Logic) unless otherwise specified.

Powder X-ray Diffraction. Lab powder X-ray diffraction (PXRD) was collected on samples in air using a PANalytical X'Pert Pro diffractometer. The diffraction patterns were fit with the Rietveld method using the General Structure Analysis System II (GSAS-II),[74, 75] and visualization of the crystal structures was aided by VESTA.[76]

Raman Spectroscopy. Raman spectra were collected on a Horiba XploRA One confocal Raman microscope. All spectra were collected with a 638 nm diode laser, a grating with groove density 1200 g mm^{-1}, and 10% laser power (c.a. 2.9 mW) to minimize laser damage to the samples. The hole and slit were fixed at 500 and

200 μm, respectively. The laser was focused using a 10× (numerical aperature 0.25) objective, which yielded a lateral resolution of ca. 1.5 μm and an axial resolution of ca. 10.2 μm.

Operando measurements were performed in a front-side configuration in a custom spectroelectrochemical cell (Figure 2.7) with a slurry cast electrode as described above, a lithium metal anode with a 5/32" hole punched out, Celgard 2400 separator with a 3/32" hole punched out, and LP100 electrolyte diluted 10× (0.1 M $LiPF_6$ to limit fluorescence background. Spectra were collected with a 3 s acquisition time and 60 accumulations throughout the course of the experiment. The accompanying electrochemical experiment was cyclic voltammetry between 4.4 V and 2 V at a rate of 0.5 mV s^{-1} for three cycles. The lower voltage cutoff was used to avoid long times spent at high voltages where electrolyte can decompose onto the cathode surface and disrupt the focus of the Raman microscope on the surface of the cathode.

X-ray Absorption Spectroscopy and Resonant Inelastic X-ray Scattering. Samples for *ex situ* X-ray absorption spectroscopy (XAS) were prepared in 2032 coin cells with a Li foil anode as described above. Electrodes were measured in the following states for Li_2RuO_3: pristine, charged to 3.75 V, charged to 3.85 V, fully charged to 4.6 V, fully charged then fully discharged to 2 V, fully charged to 4.6 V on the second cycle, and fully discharged to 2 V on the second cycle. For $Li_2Ru_{0.3}Mn_{0.7}O_3$, electrodes were measured in the following states: pristine, charged to 4.15 V, fully charged to 4.6 V, fully charged then fully discharged to 2 V, fully charged to 4.6 V on the second cycle, and fully discharged to 2 V on the second cycle. For Li_2MnO_3, electrodes were measured at the following states: pristine, charged to 4.15 V, charged to 4.6 V, and charged then discharged to 2 V. After oxidizing or reducing the material galvanostatically to a defined cutoff, the samples were extracted, rinsed with DMC, dried under vacuum overnight, and sealed in Kapton tape. All Ru K-edge samples were measured from three sweeps in transmission mode. Mn K-edge samples were measured from three sweeps (APS) in transmission mode or one sweep (SSRL) in fluorescence and transmission modes, where the Samples for Ru and Mn K-edge XAS were measured at beamline 20-BM-B at the Advanced Photon Source at Argonne National Laboratory and beamline 4-1 at the Stanford Synchrotron Radiation Lightsource at SLAC National Accelerator Laboratory, respectively. Calibration, background correction, and data processing of X-ray absorption near edge structure (XANES) and EXAFS was performed using Athena.[77] Standards were prepared by diluting 20-30 mg of material with 60 mg of carbon and pressed into 3/8" pellets

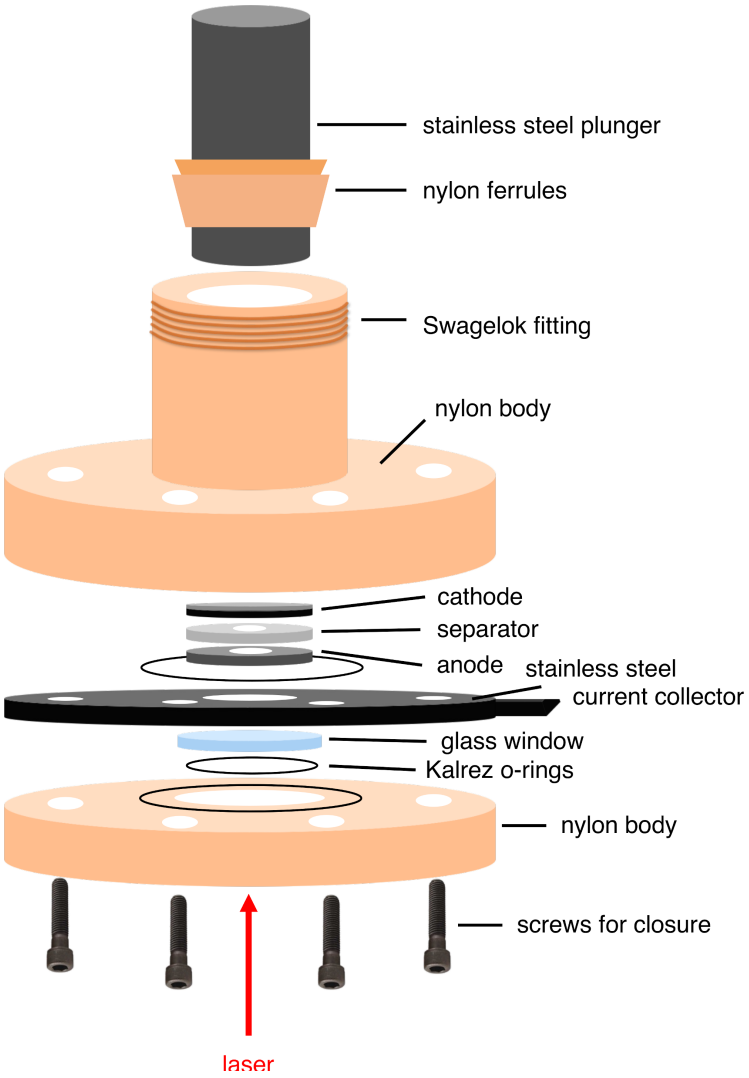

Figure 2.7: Schematic of the custom spectroelectrochemical cell used for *operando* Raman measurements.

under approximately 1 ton of force.

Soft X-ray absorption spectroscopy (sXAS) measurements at the Mn L-edge were collected in total electron yield (TEY) mode at beamline I09 at the Diamond Light Source Ltd., UK. sXAS and resonant inelastic X-ray scattering (RIXS) measurements at the O K-edge were collected at beamline 8.0.1 (iRIXS endstation) at the Advanced Light Source. The sXAS spectra were calibrated using the Ti L-edge and O K-edge for a TiO_2 reference. The emission energy axis in RIXS measurements were calibrated from the elastic peak in the RIXS map. All samples were mounted on conductive tape in an Ar-filled glovebox and transferred to the beamline using a vacuum suitcase to avoid air exposure.

Differential Electrochemical Mass Spectrometry. The custom-built DEMS instrument and its operation was described in previous publications.[78–80] Cathodes were made under an Ar atmosphere by casting a slurry of $Li_2Ru_{0.3}Mn_{0.7}O_3$ active material, conductive carbon (carbon black, acetylene, 50% compressed, 99.9+%, Alfa Aesar), polyvinylidene fluoride (PVDF, Solef 6010/1001, SOLVAY), and N-methyl-2-pyrrolidone solvent (anhydrous, 99.5%, Sigma Aldrich) onto 1/2-inch stainless steel mesh discs. The ratio of active:carbon:PVDF in the slurry was approximately 70:20:10, by weight. After the slurry was cast, the cathodes were dried under vacuum at 120 °C overnight. The cathode active material loading was approximately 5 mg cm^{-2}. Lithium metal discs of 11 mm diameter cut from Li foil were used as anodes. Hermetically-sealed, custom-built Swagelok cells containing a $Li_2Ru_{0.3}Mn_{0.7}O_3$ cathode and Li metal anode were assembled with LP100 electrolyte (1 M $LiPF_6$ in 1:1:3 (v/v) EC/PC/DMC) and a dual layered separator consisting of a polypropylene sheet (cathode side, Celgard 2500) and quartz filter paper (anode side, Whatman QMA). The electrolyte loading was approximately 60 μL cm^{-2}. The cells were assembled in an Ar atmosphere glovebox and appropriately attached to the DEMS apparatus to avoid air exposure. The cells were cycled on a Bio-Logic VSP-series potentiostat under positive Ar pressure (approximately 1.2 bar). For all experiments, the cells were cycled at a constant rate of C/10 based on one electron per formula unit (20.512 mA g^{-1}) with an upper cutoff voltage of 4.6 V and a lower cutoff voltage of 2.0 V. After each discharge, the cell was allowed to rest on open circuit for 3 hours before the subsequent charge to improve the resolution of cycle-to-cycle gas evolution measurements. Throughout the experiment, the cell headspace was purged with 500 μL of Ar by the DEMS instrument every 10 minutes and any accumulated gases were swept to the mass spectrometer chamber for analysis. The apparatus is calibrated O_2 and CO_2 in Ar, allowing for the determination of the partial pressures of each analyte. The amount of each gas evolved was then quantified using the volume and temperature of the gas sample.

X-ray Photoelectron Spectroscopy. Hard X-ray photoelectron spectroscopy (HAXPES) measurements at $h\nu \approx 5940$ eV were conducted at beamline I09 at the Diamond Light Source Ltd., UK. The experimental chamber is equipped with a Scienta Electron Analyzer set to a pass energy of 200 eV operating in angular mode. Calibration of all materials was done using the C 1s peak of carbon black (C-C) at 284.5 eV.

Inductively-Coupled Mass Spectrometry. Three samples were prepared. The first consisted of a coin cell assembled as described above and allowed to sit without

electrochemical cycling for 24 hours. The others were cycled for 10 cycles with one being stopped after a full charge and the second being allowed to discharge completely. Coin cells were opened and components were washed with 2 mL of DMC, which was collected. Each sample was quantitatively transferred to a 50 mL digestion tube to which 1 mL conc. nitric acid was added and all were heated to 100 °C for 2 h. This process was repeated twice. For analysis, the samples were diluted to a total volume of 20 mL.

Chapter 3

STABILIZING MULTIELECTRON REDOX IN LITHIUM-RICH OXIDE CATHODES WITH ACTIVE ELECTROLYTE ADDITIVES

Chapter Abstract

Electrolyte additives with tailored chemistry can be an efficient and cost-effective way to stabilize surface transformations and promote reversible cycling in battery cathodes. Electrolyte additives have been employed for Li-ion systems as a method of increasing safety and ionic conductivity as well as controlling the interaction of the electrolyte with the electrodes by scavenging trace contaminants and mitigating unwanted side reactions. Li-rich layered metal oxides that can invoke anion redox (i.e. charge compensation by the structural lattice anions) present the opportunity to substantially increase the practical charge storage capacity of the cathode, but are often plagued by side reactions like gas release and electrolyte decomposition. Such parasitic side reactions can lead to surface reorganization and densification, which strains the cathode material particles in addition to being detrimental for Li^+ diffusion. As such, the ability of active electrolyte additives to stabilize the cathode surface against irreversible transformations is evaluated. In particular, Li^+ and O^{2-} vacancies destabilize the surface and can act as nucleation sites for structural distortions and side reactions. Here, the ability of oxophilic additives to coordinate preferentially to undercoordinated O atoms surrounding Li^+ vacancies is explored using Li_2RuO_3 as the cathode. Similarly, we evaluate highly oxidized additives to adsorb to surface O^{2-} vacancies in addition to interphase-forming additives oxidized onto the cathode *in situ* to protect the high-energy defects against causing further decomposition. Of the additives investigated, organophosphite compounds oxidized onto the surface *in situ* have the most promising effects, slightly increasing capacity and improving capacity retention. The other additives tested had either no effect or a detrimental effect on the electrochemical performance.

3.1 Introduction

The role of conventional electrolytes is simply to enable Li^+ transport between the electrodes and remain inert with respect to the cathode material while preventing electron transfer directly between the electrodes. Organic carbonate electrolytes with lithium hexafluorophosphate $LiPF_6$ supporting electrolyte are commonly used to this end.[81] The electrolytes do react at the anode, however, forming a self-passivating decomposition layer at low potentials commonly referred to as the solid electrolyte interphase (SEI). The SEI allows Li^+ transport to the anode while blocking the anode surface and preventing further undesirable electrolyte decomposition.[82] Understanding the SEI and its stabilization effects has been a focus of research in the field for years, but less attention has been paid to analogs on the cathode side of a cell, the cathode electrolyte interphase (CEI).

As stated in Chapter 2, Li-rich layered oxide materials are capable of storing more than one Li^+ per transition metal, overcoming a limitation of the current paradigm in commercialized cathode active materials. Of particular interest is Li_2RuO_3, due to its ability to accommodate high degrees of Li^+ removal leading to high gravimetric capacities.[24, 25, 29] Such multielectron materials are highly desirable for energy-dense Li-ion cathodes. However, Li_2RuO_3 was also shown to have a significant irreversible capacity loss specifically after the first charge in addition to O_2 and CO_2 gas release upon oxidation, pointing to oxidative decomposition of the material itself and incompatibilities with the electrolyte at high voltages.[83] We hypothesized that the poor reversibility from the first charge to the first discharge could be attributed to structural distortions at or near the surface of the material at high states of charge as Li^+ is removed, and, further, that this issue could be addressed through active electrolyte additives, specifically through soluble additives that target surface defects.

3.2 Methodology

Recent work on electrolyte additives for cathode stabilization has focused on high-voltage materials like Ni-rich NMCs and primarily report fluorinated, organosilane, and thioether compounds that can form thin, uniform, and stable films on the cathode surface.[84, 85] This work encompasses several parallel approaches that are both centered around the idea of stabilizing vacancies on the surface of the cathode material by introducing additives that reversibly adsorb, coordinate, or otherwise interact with the defect sites. The first approach aims to stabilize Li^+ vacancies, which are introduced upon oxidation (i.e. charging). O atoms at the surface of the cathode are

inherently undercoordinated and the state of undercoordination is worsened upon removing Li^+. To alleviate the reactivity of undercoordinated O and stabilize the surface, simple ionic salts with various cations are added to the electrolyte such that the cation can coordinate to the O surrounding the vacancy as shown in Figure 3.1a. Cations of interest are selected based on the normalized oxophilicity relative to those of Ru^{4+} (0.4) as calculated from tabulated thermochemical data.[86] Cations with higher values will coordinate preferentially to O, but, if the coordination is too strong, the cathode material could dissolve into the electrolyte. Metals with lower oxophilicity values are expected to coordinate to O without the risk of dissolution. However, the interaction between the cation and the O could be too weak to stabilize the extra charge density on the O. With this in mind, several cations are evaluated.

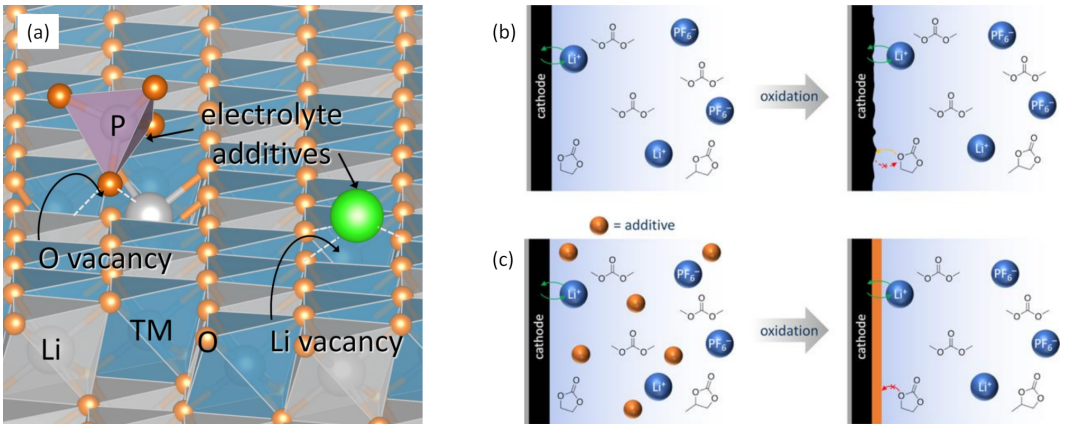

Figure 3.1: The three parallel approaches to surface stabilization in Li_2RuO_3. (a) Graphical representation of how electrolyte additives might stabilize surface defects formed during charge to promote reversible cycling. Oxophilic cations could coordinate preferentially to Li^+ vacancies formed upon removing Li^+ during charge. Highly oxidized additives with available lone pairs could adsorb on to the surface at O^{2-} vacancies, inhibiting parasitic side reactions. Alternatively, additives could prevent (b) electrolyte degradation by (c) being oxidized onto the cathode surface *in situ*.

The second approach is focused on O^{2-} vacancies, which are present throughout metal oxides due to entropy. Importantly, the concentration of vacancies at the surface is high as diffusion of vacancies from the surface into the bulk is not favored due to surface tension effects.[87, 88] O^{2-} vacancies can increase the activity of the oxygen reduction reaction (ORR), and thereby the release of O_2 gas, in mixed metal oxides.[89] O^{2-} vacancies on the surface of the cathode material could affect similar behavior, however, in batteries, evolution of O_2 is a parasitic side reaction that compromises reversibility. To passivate such surface instabilities, highly oxidized

species are added to the electrolyte to stabilize reactive sites by adsorbing to the vacancies as shown in Figure 3.1a. Specifically, ionic and alkyl phosphates are investigated as oxidatively stable additives with available lone pairs. Phosphates have been shown to adsorb onto metal oxide surfaces[90] and have also been used as solid-state films to stabilize Li_2RuO_3.[91]

The third and final approach is to use an additive that can be electrochemically oxidized onto the cathode surface *in situ* to create a CEI layer analogous to the SEI traditionally considered to form on the anode side of a cell. Organophosphites have been used to this end in traditional layered oxides like LCO[92] and Li-rich NMC materials.[93, 94] Li-rich materials like Li_2RuO_3 are cycled to highly oxidizing voltages to access anion redox, which results in significant electrolyte decomposition at the interface as represented in Figure 3.1b. To alleviate this reactivity, we target a variety of organophosphite additives due to their ability to be oxidized as well as the lone pair of electrons on the phosphorus that may facilitate coordination to the defects on the cathode surface. We hypothesize that organophosphite additives could be electrooxidized onto the cathode surface to form a protecting layer that stabilizes structure transformations and prevents further electrolyte degradation (Figure 3.1c).

All three approaches to surface stabilization are tested in parallel via extensive electrochemical studies to understand each additive's effects on performance metrics like voltage hysteresis, Coulombic efficiency, and cycle life/capacity retention. We find that the third approach, electrooxidation of the additive to form a CEI, is the only one that has a significant impact on the electrochemical performance of Li_2RuO_3, though not significant enough to pursue to the point of publication. A summary of results from the different additives investigated and potential future work in this area can be found at the end of this chapter.

3.3 Results and Discussion

Approach 1: Stabilize Li^+ vacancies by coordination of a cation to undercoordinated O on the surface

Where available, hexafluorophosphate (PF_6^-) salts are used to avoid introducing another variable, the additive anion, into the system, which may convolute the interpretation of electrochemical results. PF_6^- salts are commercially available for all monovalent ions investigated, but soluble bis(trifluoromethane)sulfonimide ($TFSI^-$) salts are used for divalent ions like Mg^{2+}. The oxophilicity values for different monoatomic cations and the commercial availability of PF_6^- salts dictate

Table 3.1: Additives used based on stabilizing undercoordinated O around Li^+ vacanacies with corresponding oxophilicity of each cation. Selected experimental metrics are also compared where "Charge Plateau" refers to galvanostatic cycling experiments.

Additive	**Cation oxophilicity[86]**	**Charge Plateau 1 (V)**	**Charge Plateau 2 (V)**	Other observations
None	n/a	3.8	4.1	
$NaPF_6$	0.4	3.7	4.2	Plateau 2 has an earlier onset, features observed on discharge in cases of additive concentration approaching LiPF6
KPF_6	0.4	3.7	4.1	Features observed on discharge in cases of additive concentration approaching LiPF6
$Mg(TFSI)_2$	0.6	3.8	4.1	Current in CV significantly lowered, peak at 4.1 V absent
LiTFSI	0.3	3.8	4.1	No change to current density in CV but peak potentials increased

the starting point for the work described herein. Table 3.1 describes the additives investigated based on this approach.

$NaPF_6$ and KPF_6 are added to the electrolyte at various concentrations to observe any concentration dependence of the additives relative to the $LiPF_6$ salt (Figure 3.2). If the anionic redox were stabilized by the electrolyte additives, we expect the voltage associated with those processes to decrease. In the case of adding $NaPF_6$, the first redox plateau is lowered in voltage and the second is increased, suggesting that the first redox process may be stabilized but the second is slightly destabilized. Additionally, the onset of the second plateau is earlier in all but the lowest concentration of additive. Since there is kinetic control in galvanostatic experiments, a change in the contributions to the capacity of different redox events implies that the additive is having some effect on the electronic states of the redox centers, which could be an indication of coordination of Na^+ to surface O^{2-}. Upon discharging the cells, the step-like feature observed only in cells with additive increases in magnitude with concentration, suggesting changes to the redox behavior that are linked to the additive. Similar results are observed in KPF_6 upon discharge,

but the voltage profile of the first charge is relatively unchanged. In both cases, cells with additives at concentrations approaching that of $LiPF_6$ display activation barriers on the first charge, which could indicate that the Na^+ and K^+ are interfering with the diffusion of Li^+ to the anode. The only marked difference in capacity is observed in the cell with 0.05 M $NaPF_6$ added. The voltage profile does not differ significantly from the other cells with $NaPF_6$, which means 0.05 M may be the ideal concentration for some favorable interaction between the Na^+ and the cathode material. The nature of the interaction could be coordination-based, but it could also be due to more substantial interaction of the bulk material with Na^+ or K^+.

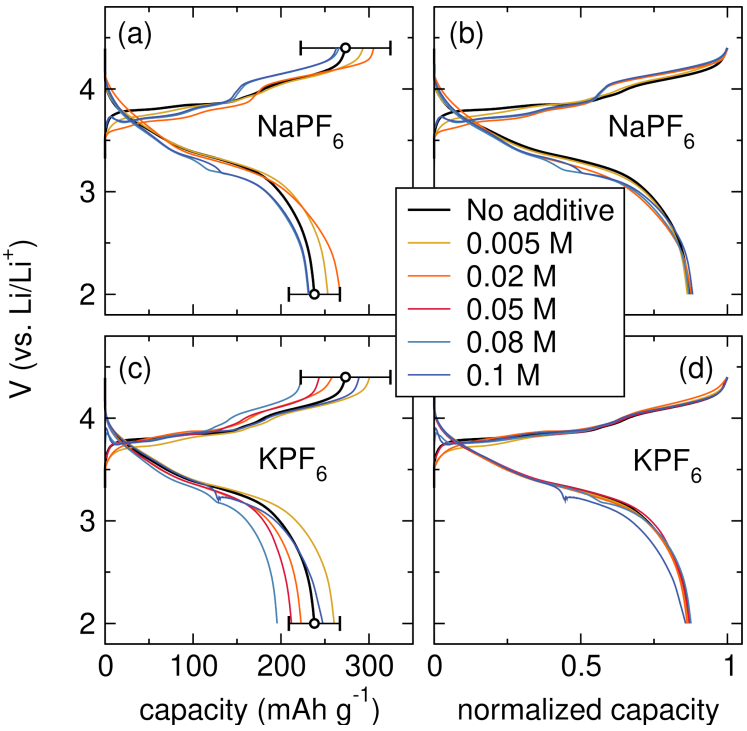

Figure 3.2: Galvanostatic charge and discharge profiles of Li_2RuO_3 half-cells with various concentrations of (a,b) $NaPF_6$ and (c,d) KPF_6 added. (b) and (d) show normalized profiles to allow for easy comparison of the profile shapes. The points on the "No additive" trace represent the average capacity calculated from three replicate cells, and the error bars signify one standard deviation from the average. The base electrolyte contains only 1 M $LiPF_6$.

To try other ions of interest, particularly Mg^{2+} as a more oxophilic cation of similar size to Li^+, we move to $(TFSI)^-$ salts. LiTFSI is used as an additive to determine the effects of adding $(TFSI)^-$ into the electrolyte without convolution with the effects of a new cationic species. There are little to no changes observed in both the galvanostatic cycling and the cyclic voltammetry when comparing the cell with LiTFSI to that with no additive (Figure 3.3). In the cyclic voltammogram, addition

of LiTFSI to the electrolyte does not impact the magnitude of the current, but slightly alters the shape of the oxidation waves. Peak voltages are shifting to higher potentials in both cases, suggesting slightly increased thermodynamic (i.e. destabilization of the redox processes) or kinetic barriers. However, addition of $Mg(TFSI)_2$ to the electrolyte causes drastic changes in the cyclic voltammogram as shown in Figure 3.3a. The magnitude of the current decreases drastically while also changing the shape of all redox waves. In particular, the oxidative wave around 4.1 V, which is attributed to redox involving the structural oxide lattice, is absent.[25] Interestingly, the detrimental effects of Mg^{2+} are not observed in the galvanostatic experiment, which might suggest kinetic limitations are being imposed.

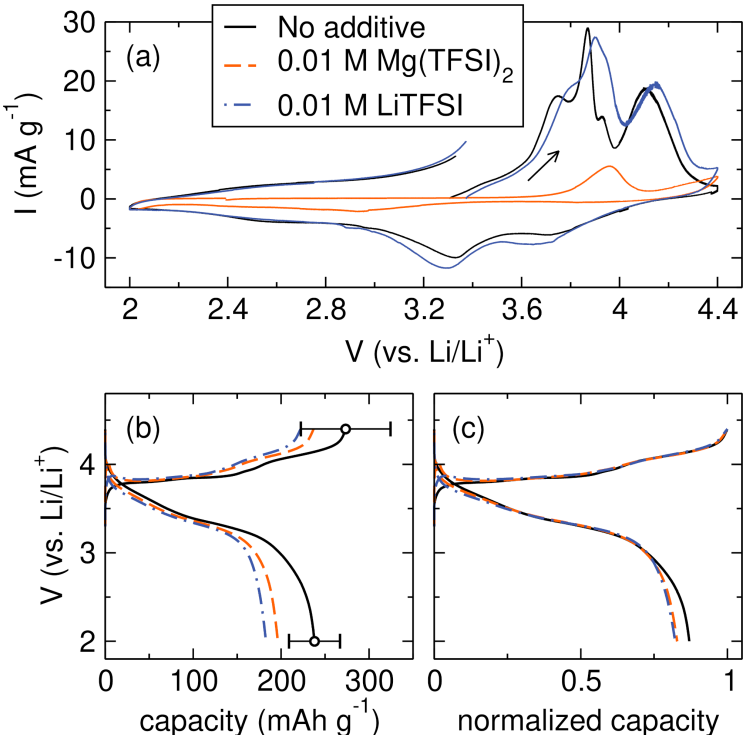

Figure 3.3: First cycle of Li_2RuO_3 by (a) cyclic voltammetry at 0.01 mV/s and (b, c) galvanostatic cycling at C/10 with 0.01 M $Mg(TFSI)_2$ or LiTFSI electrolyte additives. Little difference was observed in the galvanostatic experiments, but the CVs showed drastic negative changes upon introducing Mg^{2+} to the system. The base electrolyte contains only 1 M $LiPF_6$.

Approach 2: Stabilize O^{2-} vacancies by adsorption of a highly oxidized species on the surface

For the second approach aimed at stabilizing O^{2-} vacancies, ionic and alkyl phosphates are investigated as additives. Ionic phosphates (Li_3PO_4 and $Mg_3(PO_4)_2$) are sparingly soluble in the carbonate-based electrolyte solution and do not have any

Table 3.2: Additives used based on stabilizing O^{2-} vacancies on the surface.

Additive	**Soluble?**	**Charge Plateau 1 (V)**	**Charge Plateau 2 (V)**	**Other Observations**
None	n/a	3.8	4.1	No significant changes
$Mg_3(PO_4)_2$	N	3.8	4.1	No significant changes
Li_3PO_4	N	3.8	4.1	Incorporation into cathode yielded negative effects
$TBAH_2PO_4$	N	3.8	4.1	No change on charge, first discharge capacity significantly decreased
TMP	Y		3.8	4.1
No significant changes				
TBP	Y	3.7	4.2	Features upon discharge resulting in slightly lower voltage
TPP	Y	3.7	4.2	Features upon discharge resulting in slightly lower voltage
HMDS	Y	3.7	4.1	No significant changes to shape

notable impact on cell performance. In an attempt to solubilize the phosphate anion in the electrolyte, a salt with a larger cation is used, tetrabutylammonium (TBA^+). Phosphate salts of TBA^+ are only available with protonated phosphate anions, which still show low solubility. Additionally, the presence of protons complicates the electrochemistry and may have additional negative effects given the tendency of PF_6^- to accept protons and make HF.[95, 95] Alkyl phosphates ($R_3(PO_4)_3$; R = CH_3, $CH_2CH_2CH_2CH_3$, and Ph) are soluble and result in a decrease in the voltage of the first redox plateau, again suggesting stabilization. The additives with more sterically bulky groups (i.e. butyl and phenyl) cause similar changes to the electrochemical behavior while the effects of those with less bulky groups (i.e. methyl) behaved more like cells without additives. Hexamethyldisilizane (HMDS) was also used due to the lone pair of electrons on the N atom, and the electrochemistry looked like that exhibited by cells with sterically large alkyl phosphates indicating that perhaps sterics around the central heteroatom impacts surface chemistry on the cathode material. Results are summarized in Table 1.

Approach 3: Stabilize the surface by tuning the CEI composition through *in situ* electrooxidation of electrolyte additives

Armed with the hypothesis that sterics may play a role in additive interactions with the cathode material, additional additives with less bulky groups are explored. Organophosphite compounds are targeted due to their ability to be oxidized as well as the lone pair of electrons on the P that may facilitate coordination to defects on the cathode surface. Phosphites of this type have been utilized as electrolyte additives for layered oxides in the NMC and Li-rich NMC materials families with success noted in cyclability and rate performance.[96–98] Here, we investigate the effects of one such additives, trimethyl phosphite (TMPi) on Li-rich oxide Li_2RuO_3. For context, when cycling Li_2RuO_3, the first charge displays a step-like voltage profile where the lower voltage plateau is attributed to $Ru^{4+/5+}$ redox and the higher voltage plateau is attributed to contributions from the anionic oxide lattice.[24, 25, 99]

TMPi is first explored as an additive for Li_2RuO_3 under normal operating conditions, i.e. in the usual voltage window of 2 V to 4.4 V. Little to no change is observed in the first several cycles, and the discharge capacity decayed in the same fashion as control cells with no TMPi. The upper cutoff voltage is then increased to 4.8 V (Figure 3.4) and an additional plateau is observed at 4.7 V, which we attribute to oxidation of the TMPi onto the cathode surface. The plateau is not observed on subsequent cycles and the charge passed is not sufficient to oxidize all of the TMPi present in the electrolyte, suggesting that the oxidation of the additive is self-terminating. Interestingly, after the high voltage oxidation process, the discharge capacity is retained extremely well over 40 cycles with virtually no loss and significantly higher capacities than the control cases.

To further explore the phenomenon observed, TMPi is intentionally oxidized on the first charge of the Li_2RuO_3 cells. Cyclic voltammetry is performed on cells with various concentrations of TMPi to more easily deconvolute the effect of the additive on different redox processes occurring in the material during the first oxidation. Addition of the TMPi additive stabilizes oxidation of Li_2RuO_3 as evidenced by the decrease in peak potential of the high voltage wave near 4.5 V (Figure 3.5). The potential shifts successively from 0.02 M to 0.05 M but does not shift further upon increasing to 0.1 M TMPi. The peak potential then increases slightly with 0.2 M TMPi, which suggests that there is an optimum concentration of the additive. Oxidation of the additive itself occurs around 4.9 V vs. Li/Li^+, and seemingly suppresses current associated with electrolyte degradation seen around 5.1 V. It is

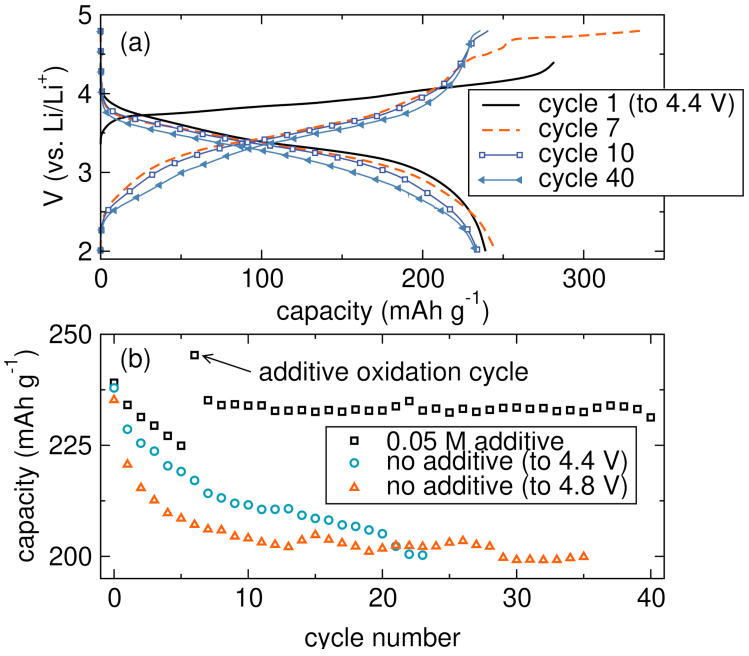

Figure 3.4: (a) Galvanostatic charge/discharge curves at a rate of C/10 given one electron of a Li_2RuO_3 cell with TMPi additive cycled to 4.4 V upper cutoff for six cycles then to 4.8 V. (b) Discharge capacity vs. cycle number of the cell with TMPi additive and two control cells cycled to 4.4 V and 4.8 V.

apparent from galvanostatic cycling data that Li_2RuO_3 undergoes an irreversible transformation on the first charge, and therefore the cathode material is different structurally on subsequent cycles. The differences between the pristine cathode and the cathode after the first charge explain the difference in oxidation potential of the additive, which occurs at lower potentials when first oxidized after the first charge. At such highly oxidizing potentials, it is likely that the electrolyte solvent is oxidizing in conjunction with the electrolyte additive but, based on control experiments, the additive is the primary contributor to the long plateau observed at approximately 4.9 V. Allowing the additive to oxidize to depletion on the first charge results in decreased discharge capacities, likely due to the extent of electrolyte solvent decomposition and the surface layer being thick enough to noticeably start impeding ionic transport. Based on some preliminary results, the beneficial effects on capacity retention occur to a greater degree when the additive is oxidized after the first cycle, i.e. after the structural transformations occur.

Scanning electron microscopy with electron dispersive X-ray spectroscopy (SEM/EDX) was used to look directly at the surface of the cathode material particles (Figure 3.6). The samples imaged include a pristine electrode and electrodes removed from coin

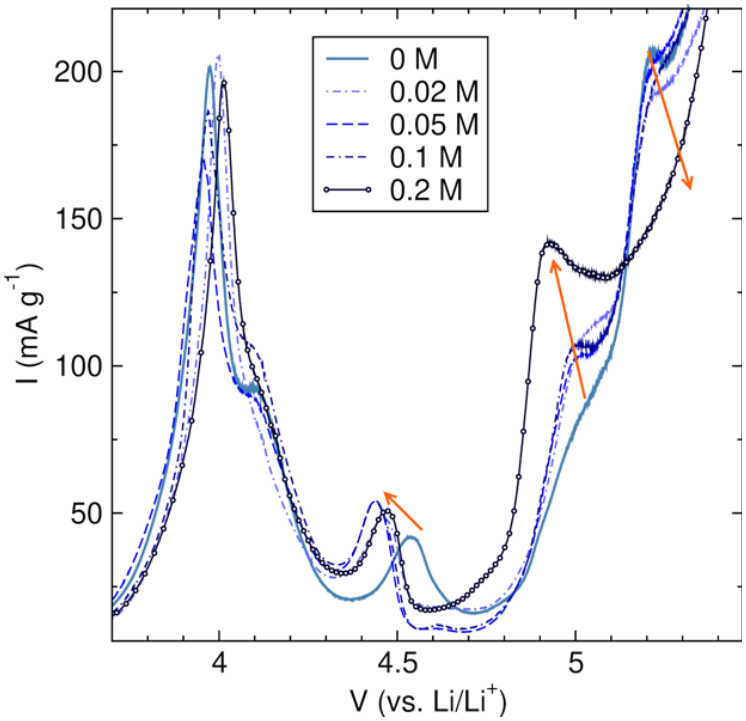

Figure 3.5: (a) Galvanostatic charge/discharge curves at a rate of C/10 given one electron of a Li_2RuO_3 cell with TMPi additive cycled to 4.4 V upper cutoff for six cycles then to 4.8 V. (b) Discharge capacity vs. cycle number of the cell with TMPi additive and two control cells cycled to 4.4 V and 4.8 V.

cells having been soaked in the electrolyte, fully charged, or fully charged and discharged. Aside from the pristine sample, all electrodes are thoroughly washed with DMC to remove all traces of unreacted TMPi additive and $LiPF_6$ supporting electrolyte. The particles of Li_2RuO_3 in the pristine electrode are 1 to 10 µm in diameter. EDX mapping shows no detectable P on the surface of the pristine electrode. Upon soaking the cathode in the electrolyte with TMPi added for several hours, there is no observable change in the particle morphology. The EDX map shows a small peak corresponding to <1% P in the cathode. Upon fully charging the cell and allowing for oxidation of TMPi as evidenced by a long plateau at high potentials, many of the larger particles are cracked but no obvious surface film is observed. EDX mapping of charged and discharged electrodes show an increased amount of P in the electrode after electrooxidation, which suggests that the phosphite additive is oxidizing onto the cathode surface irreversibly. However, the phosphorus is highly dispersed across the surface of the electrodes, implying that the TMPi does not oxidize preferentially onto the cathode material and instead oxidizes indiscriminately on Li_2RuO_3 and conductive carbon in the composite electrode, which is expected

for an electrooxidation process.

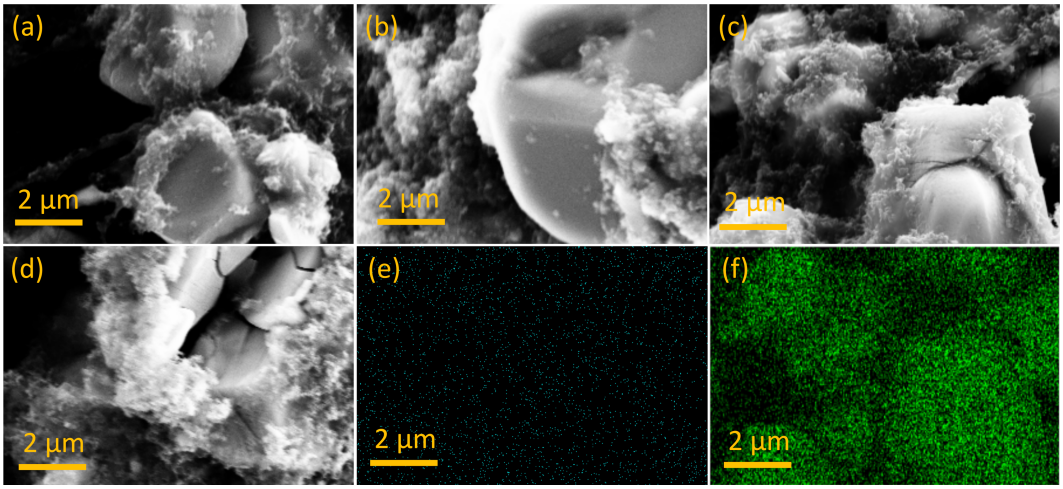

Figure 3.6: *Ex situ* scanning electron microscope images of a Li2RuO3 cathode (a) pristine; (b) soaked in electrolyte; (c) fully charged; and (d) fully discharged. Electron dispersive X-ray spectroscopy (EDX) maps of (e) P and (f) Ru of the fully charged sample.

3.4 Potential Future Directions

If one were to expand upon the results described herein, the focus should be on advancing understanding of the effects of TMPi on the cycling of Li_2RuO_3. First, the electrochemistry associated with the *in situ* oxidation should be optimized for the duration of the additive oxidation and the ideal point during cycling for the oxidation to take place. Once the electrochemistry is optimized, characterization of the film on the cathode surface should be performed using a variety of spectroscopic and imaging techniques. *Ex situ* Raman spectroscopy may allow for the characterization of amorphous species in the protective layer. X-ray photoelectron spectroscopy (XPS) may be used to observe elemental composition of the surface and provide information about the electronic states of those elements, including P and O. Comparisons should be made with cells cycled without the additive to look at any changes to the behavior of Ru at various states of charge. With respect to imaging, SEM/EDX should continue to be used to look at particle morphology and P content. Transmission electron microscopy (TEM) may also be used to look more closely at the thickness and homogeneity of the surface layer. Upon fully optimizing the experimental conditions for TMPi, similar additives with different functional groups should be explored to tune the oxidation potential of the additive, ideally shifting it to lower potentials such that the additive can be oxidized onto the cathode surface before the first charge.

3.5 Conclusions

The research described in this chapter lays the groundwork for additional exploration into ways to stabilize the high-energy surfaces of Li-rich oxide cathodes that act as active sites for unwanted side reactions like electrolyte decomposition at high voltages. From the work in Sections 3.3 and 3.3 detailing the two approaches to stabilizing surface defects, we know that these types of adsorbable additives do not necessarily have a significant impact on the structural transformations taking place in Li_2RuO_3. As such, targeting specific surface defects with electrolyte additives may not be a viable approach to preventing large-scale structural changes that result from high degrees of delithiation and anion involvement in the redox. However, the work described in Section 3.3 indicates that preventing the structural distortions may not be necessary if the goal is high capacities and improved cycle life. Instead, *in situ* oxidation of additives with specific chemical properties onto the cathode composite surface, specifically after the first-charge structural changes have already taken place, may be the key to improved performance in layered Li-rich oxide materials. This work and any future work in this area will inform the design of new cathode materials and electrolytes, providing access to Li-ion batteries with capacities over twice that of current industry standards (e.g. LCO).

3.6 Experimental Methods

Electrode Fabrication. Electrode slurries were prepared by suspending 80/10/10 (wt%) active material, conductive carbon (SuperP, Alfa Aesar, > 99%), and PVDF binder (MTI) in *N*-methyl-2-pyrrolidone (ca. 2 times by mass of total solids) (Sigma-Aldrich, 99.5%) with a centrifugal mixer (Thinky USA). Electrode films were prepared by doctor blading onto carbon-coated Al foil (MTI) at a 20 μm thickness. The films were dried in air and 1/2" diameter electrodes were punched from the film. The electrodes were dried in a vacuum oven at 110 °C for at least 12 h, yielding an active material loading of 4-6 mg.

Electrochemical Testing. All electrochemical cells were assembled inside an Ar-filled glovebox (H_2O and O_2 < 1 ppm). Electrochemistry with slurry-cast electrodes was performed in 2032 coin cells (MTI) with a Li foil anode (Alfa Aesar, > 99.9%, 0.75 mm, mechanically cleaned immediately before cell assembly), polypropylene separator (Celgard 2400), c.a. 4 drops of LP100 electrolyte, and a working electrode of 80 wt% active material as described above. The LP100 electrolyte was prepared as a 1 M solution of $LiPF_6$ (Oakwood Chemical, Battery Grade) in a 1:1:3 (by volume) mixture of ethylene carbonate (EC), propylene carbonate (PC), and dimethyl

carbonate (DMC) (all Sigma, > 99%, anhydrous). The solution was prepared in a dried HDPE bottle. The liquid carbonates (DMC and PC) were stored over activated molecular sieves (3 Å, Beantown Chemical) prior to use. All solid electrolyte additives were dried on a Schlenk line prior to use, and all liquid electrolyte additives were freeze-pump-thawed to remove any residual water. All materials were charged (oxidized) and discharged at the rate indicated (based on one electron per formula unit). All voltages are *vs.* Li/Li^+. Electrochemical experiments were performed with a BCS 805 battery cycler (Bio-Logic) unless otherwise specified. Cyclic voltammograms were collected at a rate of 0.05 mV s^{-1} with a VMP3 potentiostat (Bio-Logic).

Imaging. Scanning electron microscopy of cathode composites was performed using a ZEISS 1550VP field emission SEM with an acceleration voltage of 10 kV. EDX mapping was performed with an Oxford X-Max SDD X-ray Energy Dispersive Spectrometer system attached to the SEM at an acceleration voltage of 15 kV.

Chapter 4

MULTIELECTRON, CATION AND ANION REDOX IN LITHIUM-RICH IRON SULFIDE CATHODES

Adapted from: Hansen, C. J.; Zak, J. J.; Martinolich, A. J.; Ko, J. S.; Bashian, N. H.; Kaboudvand, F.; Van der Ven, A.; Melot, B. C.; Nelson Weker, J.; See, K. A. Multielectron, Cation and Anion Redox in Lithium-Rich Iron Sulfide Cathodes. *J. Am. Chem. Soc.* **2020**, *142*, 6737–6749.

Chapter Abstract

Conventional Li-ion cathodes store charge by reversible intercalation of Li^+ coupled to metal cation redox. There has been increasing interest in new materials capable of accommodating greater than one Li^+ per transition metal center, thereby yielding higher charge storage capacities. We demonstrate here that the lithium-rich layered iron sulfide, Li_2FeS_2, as well as a new structural analog, $LiNaFeS_2$, reversibly store ≥ 1.5 electrons per formula unit and support extended cycling. *Ex situ* and *operando* structural and spectroscopic data indicate that delithiation results in reversible oxidation of Fe^{2+} concurrently with an increase in the covalency of the Fe-S interactions, followed by reversible anion redox: $2\,S^{2-}/(S_2)^{2-}$. S K-edge spectroscopy unequivocally proves the contribution of the anions to the redox processes. The structural response to the oxidation processes is found to be different in Li_2FeS_2 in contrast to that in $LiNaFeS_2$, which we suggest is the cause for capacity fade in the early cycles of $LiNaFeS_2$. The materials presented here have the added benefit of avoiding resource-sensitive transition metals such as Co or Ni. In contrast to Li-rich oxide materials that have been the subject of so much recent study, and that suffer capacity fade and electrolyte degradation issues, the materials presented here operate within the stable potential window of the electrolyte, permitting clearer understanding of the underlying processes.

4.1 Introduction

Li-rich metal oxides, such as Li_2RuO_3 originally studied by Goodenough and coworkers in 1988,[28] have attributed redox at high states of charge to oxidation of the oxide anions to form peroxo-like moieties.[16, 24, 25, 51, 100–102] Such a mechanism is termed "anion redox" but the covalency of the Li-rich metal oxides makes it difficult to determine exactly where the oxidation is originating. Oxide cathodes can also irreversibly evolve O_2[50, 51, 103, 104], CO_2, and CO[41] upon oxidation at high voltages as demonstrated in Chapter 2. The nature of structural distortions, and even direct oxygen-related characterization, in Li-rich oxide materials at high states of charge is unclear and difficult, in part due to convolution of the data from electrolyte decomposition at high potentials.

Because of the complications associated with the high potentials required to access anion redox in oxides, we aim to study anion redox in Li-rich materials within conventional carbonate electrolyte stability windows. Sulfides are excellent candidates as sulfide oxidation occurs at much lower potentials than oxide oxidation. Layered metal-sulfides, such as the canonical TiS_2 identified by Whittingham in 1976,[105] have been studied at length as intercalation hosts.[106–113] Li-rich sulfides have gained interest in the community to study anion redox very recently. A few new alkali-rich sulfides have been reported including Li_2TiS_3,[114–116] $Li_{1.2}Ti_{0.6}S_2$,[117] and $Li_{1.33-2x/3}Ti_{0.67-x/3}S_2$.[118] Data to support anion redox in $Li_{1.33-2x/3}Ti_{0.67-x/3}S_2$ includes shifts in the S L-edge and S K-edge along with the appearance of a new feature in the S 2s region of the X-ray photoelectron spectra upon charging.[118] Saha *et al.* mention that the sulfide oxidation does not necessarily cause persulfide bond formation and leave the existence of S_2^{2-} vs. S^{n-} ($n <$ 2) open for debate.[118]

To study anion redox in sulfides, we turn to the original Li-rich sulfide material: Li_2FeS_2. Li_2FeS_2 was reported by Sharma *et al.* in 1976.[119] Li_2FeS_2 crystallizes as a layered material. Li occupies a layer of edge-sharing octahedral sites separated by a layer of mixed Li/Fe edge-sharing tetrahedral sites.[120] Early reports suggested that Fe occupies the octahedral sites,[121] but Batchelor *et al.* reported definitive single crystal diffraction data to confirm the Fe is in fact in shared tetrahedral sites,[120] which is supported by Mössbauer spectroscopy, infrared spectroscopy,[122] and extended X-ray absorption fine structure (EXAFS) data (see Figure 4.1).[123]

Early studies of the redox behavior of Li_2FeS_2 were largely separated into elec-

trochemical experiments[124–126] and characterization of chemically oxidized material.[122, 124, 127] The theoretical capacity of Li_2FeS_2 is 400 mAh g^{-1} assuming a 2 e^- oxidation per formula unit. Previous studies have shown electrochemical oxidation between 1.5-2 mol e^- per formula unit[126, 128] making Li_2FeS_2 a good material system to study multielectron redox. Li_2FeS_2 has also been used as cathodes in full cell geometries with graphite anodes.[128] The oxidation mechanism has been suggested to involve first a single-phase deintercalation of Li^+ resulting in some Fe^{2+} oxidation to Fe^{3+} followed by a two-phase oxidation resulting in S^{2-} oxidation to S_2^{2-}. Infrared spectroscopy on chemically delithiated samples suggests persulfide moieties form with oxidation of greater than one electron per formula unit.[122] Assignments of the Mössbauer spectra suggest that chemical oxidation by < 1 e^- (i.e. in the range $0 \leq x \leq 1$ in $Li_{2-x}FeS_2$) proceeds through the $Fe^{2+/3+}$ couple, with no further oxidation to Fe^{4+} even up to removal of 2 electrons.[125, 127] More recent work on the material has focused on varied syntheses of Li_2FeS_2 aiming to utilize lower temperatures or different precursors.[128, 129]

Along with Li_2FeS_2, we report a new isostructural phase $LiNaFeS_2$. Na^+ is a larger monovalent cation compared to Li^+ and therefore preferentially occupies the octahedral site. Both materials support oxidation at > one electron per Fe providing a basis to study the possibility of anion redox. By correlating the electrochemical performance with detailed structural and spectroscopy data, we demonstrate that the multielectron redox involves reversible cation and anion redox in both materials.

4.2 Results and Discussion

Structural Characterization

Preparation of Li_2FeS_2 produces a dense, polycrystalline boule with large hexagonal facets visible on the surface suggesting solidification from the melt (T_m *ca.* 885 °C).[119] The boule was subsequently ground to yield a dark grey/black powder with particles having facets still visible to some extent. $LiNaFeS_2$ was prepared at a lower temperature and did not melt, thus retaining the pellet morphology. The as-prepared $LiNaFeS_2$ pellet is black and the color is retained upon grinding.

The structure was characterized with synchrotron powder XRD. The synchrotron XRD pattern for Li_2FeS_2 is shown in Figure 4.1a along with the Rietveld refinement and resulting difference curve. The refinement is a three-phase fit to Li_2FeS_2, < 2 wt% Li_2S, and < 3 wt% Li_2FeOS. The remaining reflections of low intensity do not correspond to any reasonable impurities, precursors, or decomposition products

from reaction with the silica tube or exposure to air. The Li_2FeS_2 structure can be described by alternating layers of edge-sharing octahedral Li and edge-sharing tetrahedral mixed Fe/Li. The anion sublattice forms a hexagonal framework of sulfide anions. This structure is consistent with the structure reported by Dahn and coworkers and is shown projected down the b-axis as an inset in Figure 4.1a.[120] The lattice parameters of Li_2FeS_2 are a = 3.902 Å and c = 6.296 Å, in good agreement with those reported by Batchelor *et al.*[120]

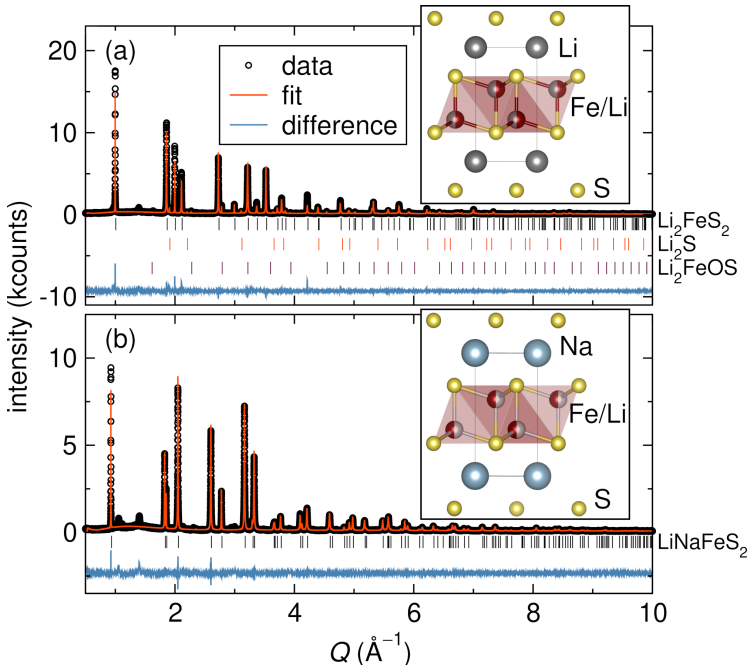

Figure 4.1: Synchrotron powder X-ray diffraction of (a) Li_2FeS_2 and (b) $LiNaFeS_2$. The Rietveld refinement and resulting difference trace are shown for each material. The refinement in (a) is a three-phase fit to Li_2FeS_2, < 2 wt% Li_2S and < 3 wt% Li_2FeOS, while the refinement in (b) is a fit to a single $LiNaFeS_2$ phase. The tick marks identify the locations of the Bragg reflections of the phases included in the fits.

The XRD of $LiNaFeS_2$ along with the Rietveld refinement and resulting difference curve is shown in Figure 4.1b. The structure is well described by the same space group as Li_2FeS_2 ($P\bar{3}m1$) with Na atoms replacing the octahedral Li sites and expanding the lattice, similar to other materials in the same structure type (e.g. $NaCuMS_2$ where M = Mn, Fe, Co, Zn).[130] The fit shown in Figure 4.1b is a single-phase fit yielding lattice parameters of a = 3.959 Åand c = 6.785 Å, indicating a lattice expansion of *ca.* 9% by volume to accommodate the Na atoms. Similar to the Li_2FeS_2 pattern, several additional reflections are found at low intensity that are

not ascribable to any reasonable impurities, but they are also different from those found in Li_2FeS_2.

In both Li_2FeS_2 and $LiNaFeS_2$, Fe occupies the tetrahedral site. We attempted to refine the XRD data with Fe in the octahedral site or with mixed occupancy with the octahedral site, which resulted in incorrect intensity profiles for the observed reflections. The XRD data were refined as a 1:1 occupancy of Li and Fe on the tetrahedral site, suggesting that the tetrahedral site is mixed with no evidence of ordering. The Fe edge XAS (see Section 4.2) provides further evidence for tetrahedral Fe. Furthermore, Fe was definitively reported to be tetrahedrally coordinated by Dahn and coworkers using single-crystal diffraction[120] after suggestions from infrared spectra and Mössbauer data.[122, 127]

Electrochemical Characterization

The two isostructural materials were electrochemically characterized to evaluate their ability to support reversible redox processes. Both materials were cycled in half-cells with Li metal anodes and Li^+ electrolytes. The galvanostatic discharge and charge curves for Li_2FeS_2 and $LiNaFeS_2$ are shown in Figure 4.2. The first charge curve (corresponding to removal of Li^+ from the lattice) for Li_2FeS_2, shows several inflections in the early part of the curve at *ca.* 0.5 mol e^- followed by a long plateau accounting for *ca.* 1 mol e^-. The discharge curve does not mirror the charge curve and shows a single plateau with a sloping region below *ca.* 2.1 V. The dissimilarity between the charge and discharge curve could indicate that the charge processes are irreversible causing the material to follow a different mechanistic pathway upon reduction. The second charge, however, is nearly identical to the first suggesting a similar oxidation mechanism and reversible behavior. The reversibility of the first charge curve is a very different behavior than is observed in the Li-rich oxides, which show different curves along with a significant capacity drop after the first cycle.[24, 25] For Li_2FeS_2, the features in both the charge and discharge curves are reversible despite the dissimilarity in the shapes with a slight capacity fade over cycling.

Compared to the first charge of Li_2FeS_2, the charge curve of $LiNaFeS_2$ initially shows a flatter initial plateau at slightly higher potentials up to 0.5 mol e^- followed by a more sloping high voltage plateau accounting for *ca.* 1 mol e^-. The shape of the discharge curve is similar to that of Li_2FeS_2. The curves are measured in Li^+ electrolytes and, therefore, the discharge curve likely corresponds to incorporation

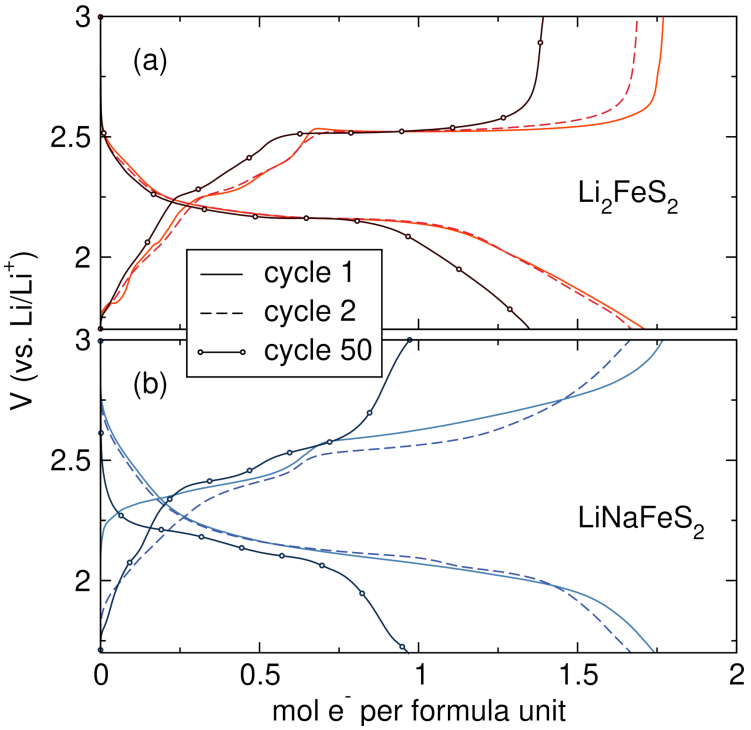

Figure 4.2: Galvanostatic cycling of (a) Li_2FeS_2 and (b) $LiNaFeS_2$ at C/10 based on 1 e^- per formula unit.

of Li^+ as the activity of Li^+ is much higher in the electrolyte compared to Na^+. The second oxidation curve resembles the features observed in the Li_2FeS_2 curve below 2.5 V suggesting that the material formed after the first discharge is acting similarly to Li_2FeS_2. The plateau at *ca.* 2.5 V on charge remains more sloping compared to the plateau in Li_2FeS_2. The change in shape of the voltage profile on charge is maintained in subsequent cycles, which can be observed in the cycle 50 trace.

The capacity in Figure 4.2 is shown in mol of e^- to facilitate direct comparison between Li_2FeS_2 and $LiNaFeS_2$. The moles of alkali extracted upon oxidation for both materials is much greater than one confirming that both structures can undergo multielectron redox. We note that some excess capacity in Li_2FeS_2 could be attributed to the Li_2S impurity. Assuming full oxidation of the Li_2S, only 0.15 mol e^- ($\leq$ 30 mAh g^{-1}) can be attributed to the impurity. The reversibility of the multielectron redox is very good with average first cycle Coulombic efficiencies of 98% for both Li_2FeS_2 and $LiNaFeS_2$.

To probe the shape of the profiles at near-equilibrium conditions, galvanostatic intermittent titration (GITT) was measured on both materials. The GITT traces for Li_2FeS_2 are shown in Figure 4.3a overlaid with the trace obtained at C/10 (based on

one electron).The near-equilibrium voltages measured for Li_2FeS_2 reasonably trace the observed profile at C/10. The overpotentials, approximated by the difference between the potential with applied current and that at open circuit, are much smaller in the initial oxidation processes of Li_2FeS_2 compared with those measured in the 2.5 V plateau. The low overpotential combined with the sloping profile associated with the oxidation process could indicate intercalation-like behavior with relatively fast kinetics. The 2.5 V plateau shows larger overpotentials that could originate from the slower kinetics associated with a two-phase reaction. Experimental[125] and computational[131] studies have suggested that deintercalation of 0.5 Li equivalents causes a phase change, which could correspond to a change in conductivity and cause the larger overpotentials in GITT. The GITT trace of the second charge shows very similar results as shown in Figure 4.3c,d.

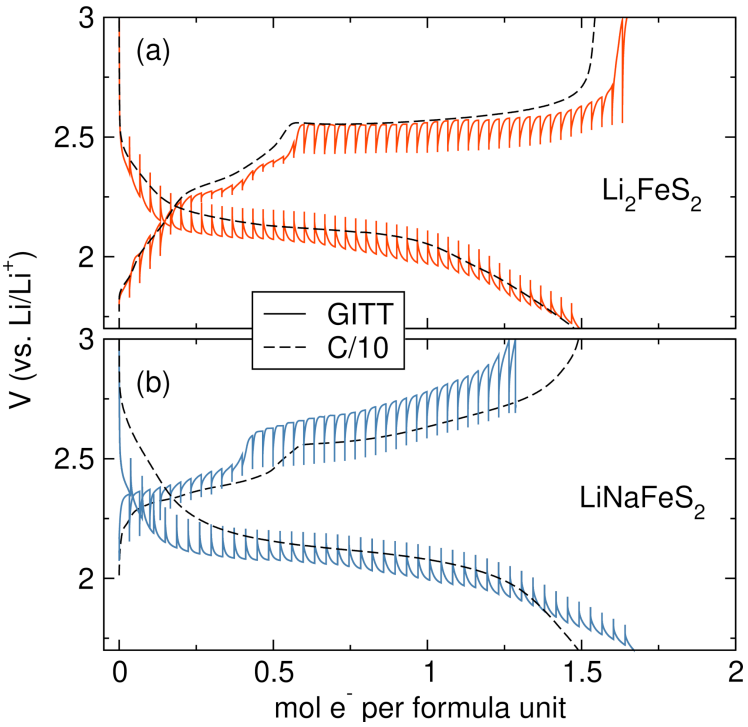

Figure 4.3: GITT curves of the first cycle of (a) Li_2FeS_2 and (b) $LiNaFeS_2$ shown with representative C/10 traces. GITT was obtained at C/10 based on 1 e^- per formula unit for 20 min separated by 4 h rest periods at OCV.

The GITT profile of $LiNaFeS_2$ shows different behavior than Li_2FeS_2. The GITT traces for $LiNaFeS_2$ are shown in Figure 4.3b. The initial oxidation processes show larger overpotentials and the 2.5 V plateau also shows larger overpotentials compared to Li_2FeS_2. The near-equilibrium voltages in the GITT trace track the sloping shape of the second plateau, suggesting that the sloped behavior is indicative of the

oxidation mechanism and is not a feature imposed by sluggish kinetics. Interestingly, the second plateau retains the sloping shape above 2.5 V in the second charge profile of $LiNaFeS_2$, contrary to the flat plateau in Li_2FeS_2. The overpotential of the initial oxidation process, however, drops substantially and appears more similar to the Li_2FeS_2 trace, likely due to the deintercalation of Li^+ as a result of lithiation during first discharge.

The GITT data of the discharge profiles are also shown in Figure 4.3. In Li_2FeS_2, the polarization decreases as the voltage profile begins to slope downwards after the plateau on discharge; however, the disparity is not as distinct as in the case of charging. A similar trend is observed in $LiNaFeS_2$.

The materials were cycled to determine the capacity fade as a function of cycle number. The discharge and charge capacity over 100 cycles are shown in Figure 4.4a. The error bars indicate the standard deviation of at least three replicate cells. Li_2FeS_2 shows a low capacity fade of *ca.* 0.5% per cycle over the first 10 cycles and 0.4% per cycle thereafter, despite little attempt to optimize electrode engineering. The shape of the voltage profile for Li_2FeS_2 is maintained upon cycling suggesting that the capacity loss is not occurring preferentially from any one part of the curve. The cycling data of $LiNaFeS_2$, however, show a much faster drop in capacity over the first several cycles corresponding to *ca.* 2% per cycle over the first 10 cycles and 0.8% per cycle thereafter.

Rate capability experiments further demonstrate the unique electrochemical behavior between the two materials. Figure 4.4b shows the capacity as a function of rate with error bars indicating the standard deviation between at least three replicate cells. The rate capability of $LiNaFeS_2$ is worse than that of Li_2FeS_2. $LiNaFeS_2$ deviates significantly from Li_2FeS_2 at C/2 and 1C. Upon comparing the shapes of the profiles at different rates, the sloping oxidation profile in Li_2FeS_2 and in cycles 2 onward in $LiNaFeS_2$ exhibits little to no change in voltage up to a rate of C/2 due to the small overpotentials associated with this oxidation process as measured by GITT. The discharge plateau in both materials, however, systematically drops in voltage with increasing rate due to the kinetic limitations associated with the reduction. A comparison of the evolution of the profiles as a function of C rate can be found in Figure 4.4c,d.

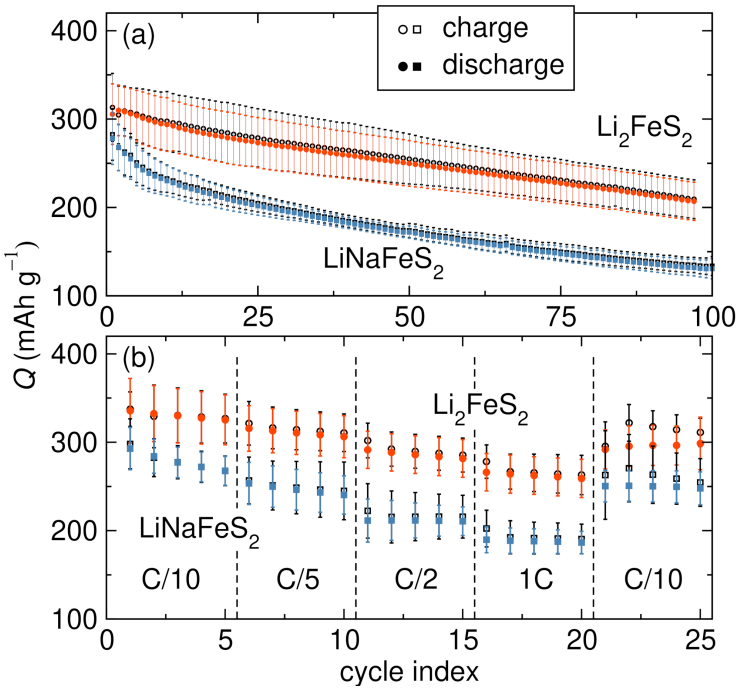

Figure 4.4: (a) Comparison of long term cycling performance of Li_2FeS_2 and $LiNaFeS_2$ at C/10 based on 1 e^- per formula unit. (b) Galvanostatic cycling of Li_2FeS_2 and $LiNaFeS_2$ at various rates (indicated). In both (a) and (b), the average of three replicate cells is shown along with error bars indicating the standard deviation. The voltage profiles of (c) Li_2FeS_2 and (d) $LiNaFeS_2$ cycled at different rates as summarized in (b).

Characterization of the Redox Processes

Both Li_2FeS_2 and $LiNaFeS_2$ reversibly cycle > one electron per transition metal. The excess capacity could originate either from multielectron oxidation of the Fe, oxidation of the S, or some combination thereof. To understand the redox processes in the sulfide systems, we pursued a variety of characterization techniques to ascribe oxidation states and local environments at various SOCs. The materials were probed *ex situ* in four conditions: (1) as-prepared, (2) charged to 2.5 V, (3) fully charged to 3 V, and (4) fully charged then fully discharged to 1.7 V. The approximate stoichiometry at each SOC is as follows: (1) $(LiA)_2FeS_2$, (2) $(LiA)_{1.25}FeS_2$, (3) $(LiA)_{0.25}FeS_2$, and (4) $(LiA)_2FeS_2$ where A = Li or Na.

To probe the activity of Fe during oxidation, Fe K-edge XAS was measured at the four SOCs for both Li_2FeS_2 and $LiNaFeS_2$. The pre- and near-edge data for Li_2FeS_2 and $LiNaFeS_2$ are plotted in Figure 4.5a and b, respectively. The Fe K-edge in general shows two prominent features: a pre-edge feature denoted as *a* ascribed to the weakly allowed Fe 1s to Fe 3d transition near 7113 eV, which is very sensitive

to local changes in symmetry, and the K-edge denoted as C, which is sensitive to changes in oxidation state. Upon oxidation to 2.5 V, the rising edge denoted as *b* shifts to higher energy in both materials. The position of the rising edge is more easily observed in the first derivative of the near-edge region, shown in Figure 4.5c and d. The rising edge shifts by 1 eV from 7117.2 eV to 7118.2 eV in Li_2FeS_2 and $LiNaFeS_2$ indicating oxidation of Fe^{2+}. Concurrently, the intensity of the pre-edge feature increases indicating a less distorted tetrahedral environment. Previous work by Kowalska *et al.* on dinuclear Fe complexes where Fe is in the 2+ or 3+ oxidation state in a tetrahedral environment with bridging S atoms agrees well with our results with a pre-edge feature at 7112-7113 eV and the rising edge at *ca.* 7117 eV for Fe^{2+} and a positive shift to *ca.* 7119 eV for Fe^{3+}.[132]

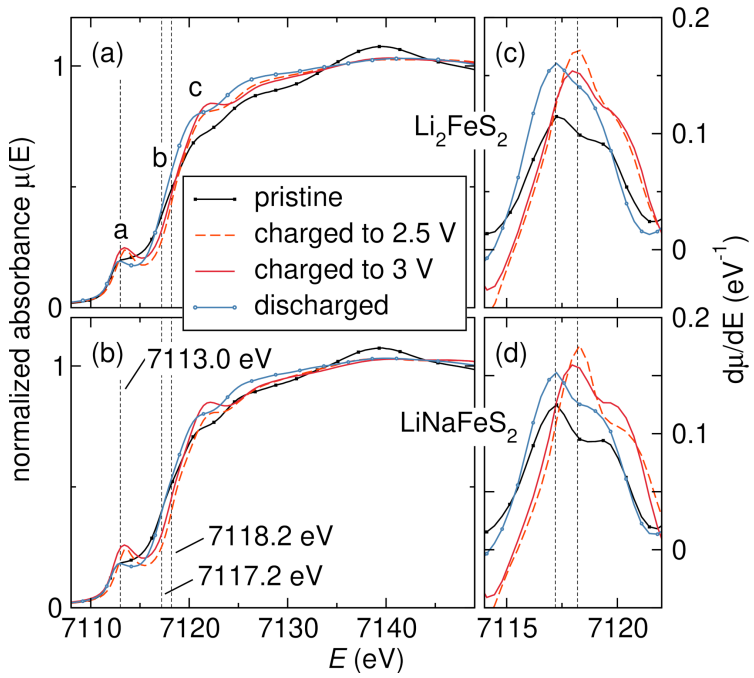

Figure 4.5: *Ex situ* Fe K-edge XANES of (a) Li_2FeS_2 and (b) $LiNaFeS_2$ composite electrodes at various states of charge. The first derivative of the rising edge for (c) Li_2FeS_2 and (d) $LiNaFeS_2$ allows for clear observation of the rising edge position. The dashed lines indicate the positions of the pre-edge features, *a*, at 7113 eV and the rising edges, *b*, 7117.2 eV and 7118.2 eV. The K-edge is labeled as C.

We next discuss the behavior of the Fe K-edge between 2.5 V and 3 V, corresponding to the plateau in Li_2FeS_2 and the sloping plateau in $LiNaFeS_2$. The shape of the pre-edge feature *a* and the XAS overall does not change in this region for either material. The position of the rising edge *b* remains at 7118.2 eV, as seen in Figure 4.5c and d, and the pre-edge feature *a* intensity does not change much indicating that Fe plays a

minimal role in the high voltage oxidation processes that correspond to essentially a one electron oxidation.

The Fe K-edge XAS of the discharged samples show significant changes compared to that of the oxidized materials. The pre-edge feature *a* decreases in intensity closely resembling the pristine materials for Li_2FeS_2 and $LiNaFeS_2$. The rising edge *b* similarly shifts back to 7117.2 eV after reduction, suggesting the Fe^{2+} oxidation is reversible. The intensity of the near-edge C, however, remains higher compared to the pristine material with small changes in shape which could indicate that the local structure does not mimic that of the pristine materials. Interestingly, the Fe K-edge XAS shows nearly identical behavior for all four SOCs between Li_2FeS_2 and $LiNaFeS_2$ despite the dissimilarities in the galvanostatic charging profiles.

The shift in the Fe K-edge data suggests that Fe is participating in oxidation below 2.5 V but no shift is observed upon subsequent oxidation to 3 V. To determine if S is also redox active, S K-edge XAS was measured on the same set of samples. S K-edge XAS has been used extensively to study the oxidation state of S and the degree of covalency of the Fe-S bond in similar materials, such as FeS and FeS_2, and metalloproteins.[133, 134] The pre- and near-edge data at all four SOCs for Li_2FeS_2 and $LiNaFeS_2$ are plotted in Figure 4.6. First, we discuss the spectrum of the pristine materials. The S K-edge spectra of both pristine materials show a strong pre-edge feature, *a*, that arises when S is covalently bound to a transition metal. The pre-edge feature *a* is assigned to the S 1s to Fe 3d transition, and the intensity of the pre-edge is a direct probe of the covalency of the Fe−S bond[135] due to more mixing of S 3s and 3p states with the Fe 3d.[136] The pre-edge feature is located at *ca.* 2469 eV in both pristine materials, which is on par with the pre-edge feature in tetrahedral FeS (2469.9 eV).[137] Both the pre-edge location (*ca.* 2469 eV) and uniform, narrow shape in the initial spectra align well with the expected signature for a sulfide (i.e. S^{2-}) moiety in both materials.[138–142]

Upon charging to 2.5 V, the intensity of the pre-edge feature *a* increases significantly. The increase in intensity is associated with better mixing of the S 3s and 2p with the unoccupied Fe 3d states, leading to a more covalent Fe-S bond. The enhanced covalency is correlated with the shift in the Fe K-edge, suggesting that the first oxidation process involves oxidation of bands with both Fe and S character. Concurrently, a decrease in the Fe-S bond is observed in the Fe EXAFS data due to an increase in the covalency of the Fe-S bond suggesting that oxidation involves electrons in nominally antibonding orbitals (*vide infra*).

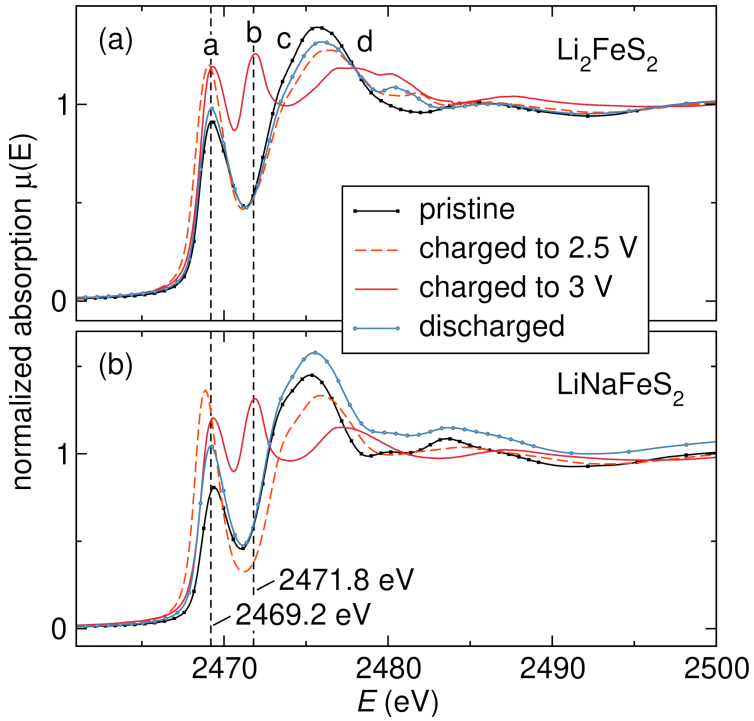

Figure 4.6: *Ex situ* S K-edge XANES of (a) Li_2FeS_2 and (b) $LiNaFeS_2$ composite electrodes at various states of charge. The pre-edge feature, a, is observed at 2473.0 eV along with the K-edge features, b-d, at higher energies.

Upon full charge to 3 V, a new pre-edge feature appears at a higher energy (c.a. 2472 eV) than the sulfide feature suggesting a new transition associated with oxidized S (relative to S^{2-}). A feature of similar shape and at the same energy (*ca.* 2475 eV) is observed in reference spectra of pyrite-FeS_2, which contains persulfide dumbbells of formal oxidation state S_2^{2-}.[139, 143, 144] We therefore suggest that the new feature in the S K-edge XANES is indicative of oxidized S. Evidence of S-S bond formation yielding a persulfide, S_2^{2-}, has been previously observed by IR spectroscopy as a result of chemical oxidation when $1 \leq x \leq 2$ in $Li_{2-x}FeS_2$.[122] We will therefore refer to the oxidized S moieties as persulfides. Contrary to pyrite FeS_2, though, charged $Li_{2-x}FeS_2$ contains both sulfide and persulfide features in the XAS.

The persistence of sulfide character in Li_xFeS_2 ($x \approx 0.5$) agrees well with the measured capacity between 2.5 V and 3 V of *ca.* $x = 1$, or 1 e^{-1} per formula unit. Full oxidation of the sulfide to persulfides would require a 2 e^- oxidation per formula unit. Because the charge passed galvanostatically above 2.5 V is *ca.* 1 e^{-1} per formula unit and the evolution of the persulfide features in the XAS is limited to above 2.5 V, we suggest that the formal charge state of S in the material can therefore be approximated as $S^{2-}(S_2^{2-})_{1/2}$.

Upon discharging $Li_{0.5}FeS_2$, S XAS features closely resemble those in the pristine material. The strong pre-edge feature at 2472 eV indicative of persulfides is no longer present, suggesting that sulfide oxidation to persulfide is reversible. We note that the galvanostatic profile of the second charge cycle overlays well with the first with a high Coulombic efficiency of *ca.* 98% on the first cycle confirming the reversibility of the anion redox.

The same trends are observed in $LiNaFeS_2$, as shown in Figure 4.6b. A strong pre-edge feature at 2472 eV appears in $LiNaFeS_2$ charged to 3 V. Upon discharging, the feature is absent. The combination of the Fe and S K-edge XAS for both materials suggests that the oxidation below 2.5 V can be ascribed to an oxidation of the covalent Fe-S bond while oxidation processes above 2.5 V can be ascribed to oxidation of S^{2-} to S_2^{2-}.

The Fe and S K-edge XAS provide strong evidence for anion redox in Li_2FeS_2 and $LiNaFeS_2$. However, spectroscopically, both materials behave similarly, and the spectroscopy does not explain the deviation in cycling behavior between the two. To further understand the bulk structural transformations, we performed *operando* XRD during galvanostatic cycling. Figure 4.7a and b shows the charge and discharge curve along with the *operando* diffraction of Li_2FeS_2. The strongest reflection, associated with the (001), is highlighted and encapsulates observed changes across the entire Q range. Uniaxial compression of the cell causes some preferential orientation of the plate-like crystals, increasing the intensity of the (001) and (002) reflections compared to the computed powder pattern.

Upon oxidation up to 2.5 V, the position of the (001) reflection shifts to higher Q corresponding to a contraction of the lattice. New reflections are not observed in the initial oxidation region and the intensity of reflections in the parent material slightly decrease. Contraction of the lattice and persistence of the reflections in the parent material are classic indications of solid-solution intercalation chemistry, by which the resulting material after removal of Li^+ is crystallographically related to the parent material. The contraction is not purely monotonic, however, possibly suggesting some ordering during the first oxidation step, which would explain the small steps in the oxidation curve. High-resolution synchrotron XRD data coupled to neutron diffraction are required to accurately determine the phases in the first oxidation region and will be the subject of future work.

Above 2.5 V, the (001) reflection continues to shift to higher Q suggesting further contraction of the lattice. The intensity of the (001) reflection significantly decreases

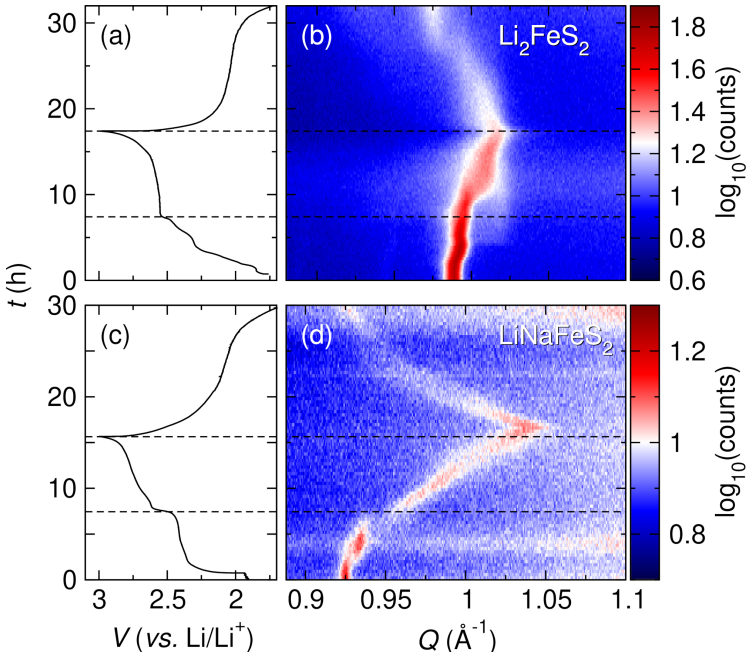

Figure 4.7: (a) Galvanostatic charge and discharge curve of Li_2FeS_2 obtained during *operando* XRD and (b) the corresponding diffraction patterns with a focus on the (001) reflection. (c) Galvanostatic charge and discharge curve of $LiNaFeS_2$ obtained during *operando* XRD and (d) the corresponding diffraction patterns with a focus on the (001) reflection. The capacity obtained on charge in this cell was 334 mAh g^{-1} (or *ca.* 1.7 electrons) for Li_2FeS_2 and 268 mAh g^{-1} (or *ca.* 1.5 electrons) for $LiNaFeS_2$, consistent with the other cell geometries in this work. The cells were allowed to rest at open circuit for the first two scans (thus the voltage is constant for the first *ca.* 1 h).

above 2.5 V due to loss of long-range order which corresponds to a loss in intensity of the other Bragg peaks in the diffraction patterns. The position of the peak maximum is tracked as a function of oxidation and the maximum abruptly shifts to a new position around 11 h suggesting that the broadening of the (001) reflection is due to the gradual appearance of a new reflection at higher Q. Such behavior is consistent with a two-phase mechanism and corresponds well with the flat plateau in the charge profile. The other reflections have lower intensity but show similar shifts.

After charging to 3 V, the cell is discharged to 1.7 V. Upon reduction, the visible reflections shift to lower Q indicating lattice expansion. The (001) again jumps abruptly to a lower Q value suggesting a two-phase mechanism during discharge. The long-range order of the starting material, however, is not recovered as indicated by the loss of diffraction intensity even after complete discharge, which is rather

surprising due to the similarity in shape and charge between the first and second cycles shown in Figure 4.2.

Figure 4.7c and d show the galvanostatic charge and discharge curve and the *operando* XRD for the first cycle of $LiNaFeS_2$. Upon oxidation to 2.5 V, the (001) reflection shifts to higher Q corresponding to lattice contraction, similar to Li_2FeS_2. The original peak fades during the first oxidation region gradually giving rise to a peak at higher Q suggesting a two-phase mechanism, corresponding well with the flat charge plateau. New reflections evolve on the shoulder of the parent material at slightly higher Q suggesting nucleation of a new but crystallographically related phase. The Q shift is larger for $LiNaFeS_2$, which could indicate that Na^+ is deintercalated at these potentials causing a greater change in the lattice parameter, compared to smaller Li^+.

Upon oxidation above 2.5 V in $LiNaFeS_2$, the evolution of the Bragg reflections is again different from that in Li_2FeS_2. The new reflection continues to shift monotonically to higher Q. The intensity of the reflection drops significantly due to loss in long-range order. The only crystallographic reflection remaining at the end of charge is in the range where we would expect the (001) reflection, suggesting that the layers remain somewhat intact. The lattice contraction incurred during the charge of $LiNaFeS_2$ is significantly greater than that for Li_2FeS_2, which could have implications on reversibility.

The (001) reflection shifts to lower Q as the material is discharged, corresponding to lattice expansion. The (001) peak is short lived during the discharge, however, indicating that long-range order continues to be lost during reduction. Because of the low intensity of the (001) reflection during discharge and loss of other reflections in the diffraction patterns, it is difficult to comment on the mechanism. We note, however, that the reflection shifts to a Q range in which the (001) is observed in pristine $LiNaFeS_2$ suggesting that some Na remain in the layers keeping the unit cell expanded relative to Li_2FeS_2.

Both Li_2FeS_2 and $LiNaFeS_2$ suffer a loss of long-range order during charge that is not recovered upon discharge. Therefore, a more local structure probe is needed to understand the redox mechanisms. To evaluate the Fe site specifically, we turned to *ex situ* Fe K-edge EXAFS analysis. Fe-specific correlations are observed by analyzing oscillations in the extended X-ray absorption fine structure at energies > 50 eV above the absorption edge. The Fourier transform of the data results in a histogram of correlations that can be fit with defined scattering paths to determine

the bond lengths and coordination numbers associated with the first and second coordination shells. The EXAFS data for Li_2FeS_2 and $LiNaFeS_2$ at various states of charge can be found in Figure 4.8a,b.

Figure 4.8c and d show the bond lengths and coordination numbers (N) for the first coordination shell of Fe in Li_2FeS_2 and $LiNaFeS_2$ at various states of charge. The first coordination shell is associated with direct single scattering Fe−S paths only. Upon charging the materials to 2.5 V, the Fe−S bond length decreases by 0.04 Å and 0.08 Å in Li_2FeS_2 and $LiNaFeS_2$, respectively. The decrease in Fe−S bond lengths corresponds to the overall lattice contraction observed in the diffraction. The decrease in Fe−S bond lengths also agrees well with the increases in covalency of the Fe−S bond observed in the Fe and S K-edge XANES. The coordination number for both materials starts around four as Fe occupies the tetrahedral site. Oxidation causes a decrease in the coordination number which could be due to Fe distorting further toward the base of the tetrahedron. The lower coordination number indicates that Fe is not migrating to the octahedral sites as Li^+ or Na^+ is removed. Interestingly, upon further oxidation to 3 V, the Fe−S bond lengths and the coordination numbers in both materials do not change significantly suggesting that the sulfide oxidation observed in the S K-edge spectroscopy does not affect the Fe local structure.

Upon discharging to 1.7 V, the Fe-S correlation length increases to 2.31 Å and 2.32 Å in Li_2FeS_2 and $LiNaFeS_2$, respectively, indicating that the Fe-S contraction is reversible upon reduction. Although the Fe-S bond length increases, the coordination number remains lower than the pristine material after discharge, suggesting that the discharged material does not completely recover the original structure.

Figure 4.8e and f show the bond lengths and coordination numbers for the second coordination shell of Fe in Li_2FeS_2 and $LiNaFeS_2$ at various states of charge. The second coordination shell is made up of Fe-Fe correlations between neighboring tetrahedral sites, again only taking into account direct single scattering paths. The tetrahedral sites in both materials have mixed occupancy Fe and Li; however, the scattering power of Li is very low so we assume the second shell correlations observed in the EXAFS data are primarily neighboring Fe_{Td}-Fe_{Td}. Initially, the Fe_{Td}-Fe_{Td} correlation lengths are much shorter in Li_2FeS_2 compared to $LiNaFeS_2$ due to the expanded unit cell of the $LiNaFeS_2$. Upon oxidation to 2.5 V, the Fe_{Td}-Fe_{Td} correlation lengths converge to similar values of 2.76 Å and 2.77 Å in Li_2FeS_2 and $LiNaFeS_2$, respectively, suggesting similar local environments around Fe. After

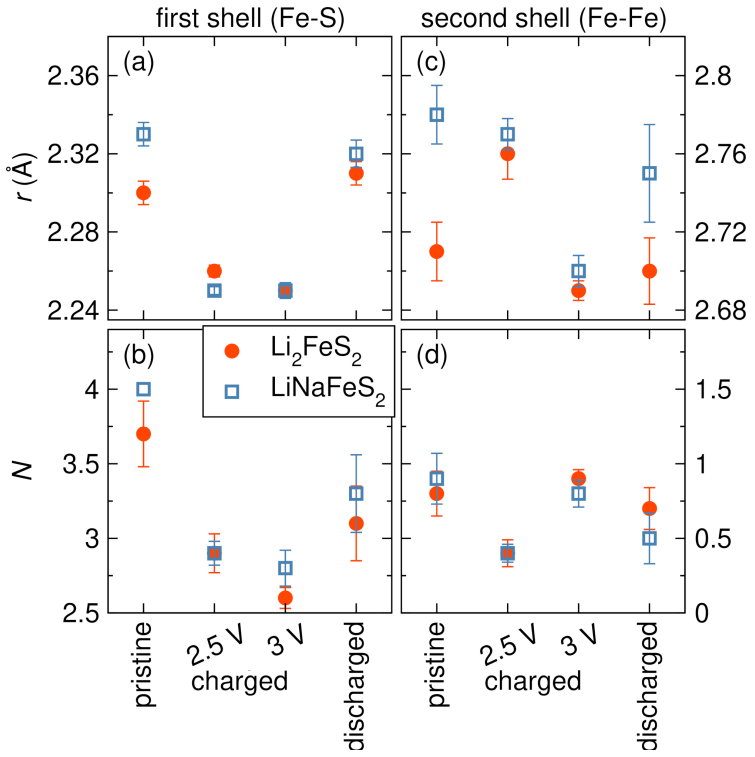

Figure 4.8: k^3-weighted EXAFS data at the Fe K-edge of (a) Li_2FeS_2 and (b) $LiNaFeS_2$ at various states of charge. The first shell (c) bond lengths and (d) coordination numbers, N, along with the second shell (e) bond lengths and (f) coordination numbers obtained from fitting the Fe EXAFS data. First shell correlations can be ascribed to Fe-S and second shell correlations are dominated by Fe-Fe.

fully charging to 3 V, both materials exhibit a sharp decrease in the Fe_{Td}-Fe_{Td} correlation length to around 2.70 Å once again indicating similar behavior during the flat plateau herein attributed primarily to sulfide oxidation to persulfide. The decrease could be explained by Fe becoming more centered in the tetrahedra as a result of alkali removal, which is supported by the increase in magnitude of the pre-edge in the Fe K-edge XANES. Upon discharge, both materials return to a similar value as that observed in the pristine materials.

Discussion of the Oxidation Mechanism

Both Li_2FeS_2 and $LiNaFeS_2$ achieve reversible, multielectron oxidation through oxidation of both cationic and anionic electronic states. To gain insight into the effect of the electronic structure on the oxidation mechanism, the partial density of states (pDOS) was calculated with DFT. Figure 4.9a shows the calculated density of states for the ordered form of Li_2FeS_2. The compound is predicted to adopt a high spin configuration, with one spin channel completely filled (spin up, positive

DOS) and the other spin channel (spin down, negative DOS) only partially filled. Figure 4.9a shows that while many of the states have both Fe-d and S-p character, those states at and immediately below the Fermi level are primarily of Fe-d character suggesting that initial Li extraction from Li_2FeS_2 will be accompanied by electron removal from Fe-d states, as observed in the Fe K-edge XAS data.

The pDOS was also calculated for the oxidized structure at a stoichiometry of $Li_{1.5}FeS_2$, just before anion oxidation. The *operando* XRD data suggest deintercalation through a solid-solution and thus the structure is modeled closely to that of Li_2FeS_2 but with Li vacancies. Extensive calculations of the energies of different Li-vacancy orderings reveal that the most stable structure contains only tetrahedral vacancies. IR spectroscopy of chemically oxidized Li_2FeS_2 has also suggested that Li is removed from the tetrahedral site.[122] Thus, Figure 4.9b shows the calculated density of states of $Li_{1.5}FeS_2$ with only tetrahedral vacancies. The pDOS of $Li_{1.5}FeS_2$ are qualitatively similar to those of Li_2FeS_2. Nevertheless, a comparison of the pDOS of Li_2FeS_2 and $Li_{1.5}FeS_2$ reveals a shift in the relative contribution of Fe and S states in the spin down channels. While the pDOS indicate that the electrons at the Fermi level occupy localized d-orbitals centered on Fe, their removal upon Li extraction from Li_2FeS_2 to form $Li_{1.5}FeS_2$ triggers a rehybridization between Fe-d and S-p states below the Fermi level. The removal of electrons from Fe-d states during Li-extraction should decrease the intrinsic energies of the remaining d-electronic states due to a reduction of on-site Coulomb repulsion, thereby allowing the remaining d-states to mix more covalently with the S p-states. The increase in covalency after oxidation is observed directly by the increase in the intensity of the pre-edge in the S K-edge XAS data. The increased contribution of S p-states to the states at the top of the spin down channel when going from Li_2FeS_2 to $Li_{1.5}FeS_2$ is evident in the charge density plots in Figure 4.9. The charge density plots for the spin down channels near the Fermi level in both Li_2FeS_2 and $Li_{1.5}FeS_2$ are shown in Figure 4.9c and d, respectively, allowing for the visualization of the localized density on the Fe in both cases. The charge density plots for the spin up channels are shown in Figure 4.9e and f showing the rehybridization of the electronic states to cause an increase in covalency in the oxidized structure.

Since the Fermi level of $Li_{1.5}FeS_2$ coincides with states that are primarily of Fe-d character, further topotactic Li removal from $Li_{1.5}FeS_2$ should proceed by means of an Fe-redox process. However, the plateau in the experimental charge voltage profile that starts at $x = 1.5$ and extends to approximately $x = 0.5$ signifies the

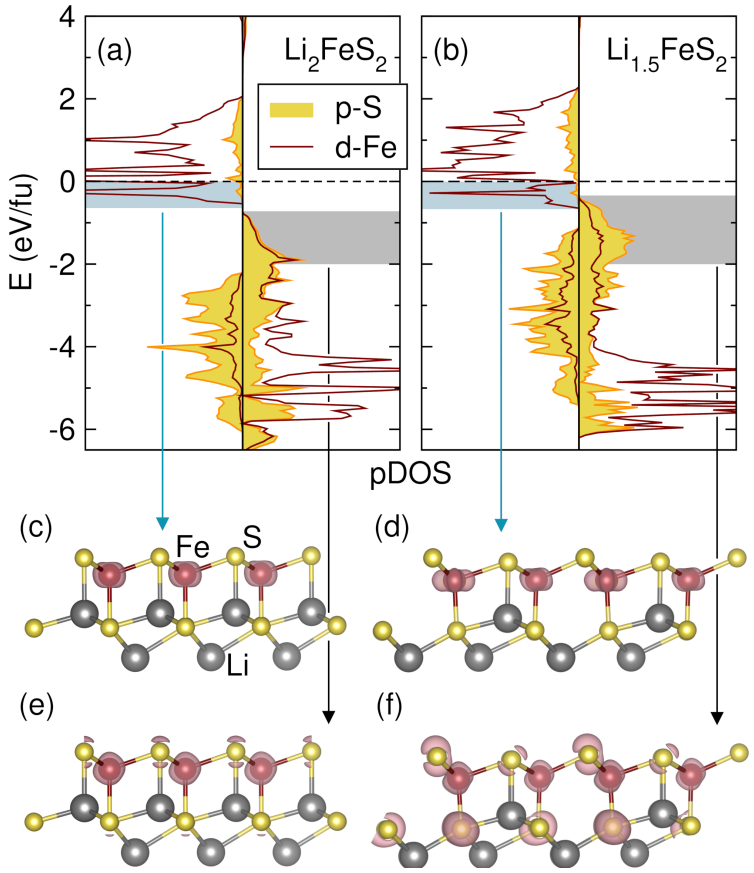

Figure 4.9: Calculated spin-polarized partial densities of states of (a) Li_2FeS_2 and (b) $Li_{1.5}FeS_2$ in which half of the tetrahedral Li sites are vacant. The charge density plots for the spin down electronic states near the Fermi level in (c) Li_2FeS_2 and (d) $Li_{1.5}FeS_2$. The charge density plots for the spin up electronic states near the Fermi level in (e) Li_2FeS_2 and (f) $Li_{1.5}FeS_2$. The electronic states in the pDOS are highlighted for all four cases in (a) and (b). While the Fermi level in both compounds cuts through states that are primarily of Fe-d character, the extraction of Li from Li_2FeS_2 to form $Li_{1.5}FeS_2$ results in a rehybridization between Fe-d and S-p states that leads to an increased participation of S states below the Fermi level. Calculations performed by F. Kaboudvand and A. Van der Ven.

occurrence of a two-phase reaction from $Li_{1.5}FeS_2$ to $Li_{0.5}FeS_2$ that undercuts the continued removal of Li through a topotactic reaction. While the structural changes accompanying this two-phase reaction remain difficult to characterize, the S K-edge XAS evidence of S oxidation in $Li_{0.5}FeS_2$ indicates that the redox reaction during the two-phase reaction has occurred at the S atoms. Efforts are ongoing to predict the most stable S dimer configurations in layered $Li_{0.5}FeS_2$.

The S K-edge data shown here confirms oxidation of the S anions and previous IR spectroscopy data suggest the formation of persulfides.[122] Determining exactly

where the persulfide bonds are forming in the oxidized structure is difficult, but here we hypothesize several possible structures. Prior to persulfide formation, roughly 0.5 equivalents of Li are removed from the structure. Figure 4.10a shows the delithiated structure with Li vacancies in the tetrahedral sites with no structural distortions from the fully lithated Li_2FeS_2 phase. Figure 4.10b shows a potential structure in which cooperative tilting of the rigid tetrahedral Fe subunits form persulfide moieties. Such cooperative tilting has been reported previously.[145, 146]

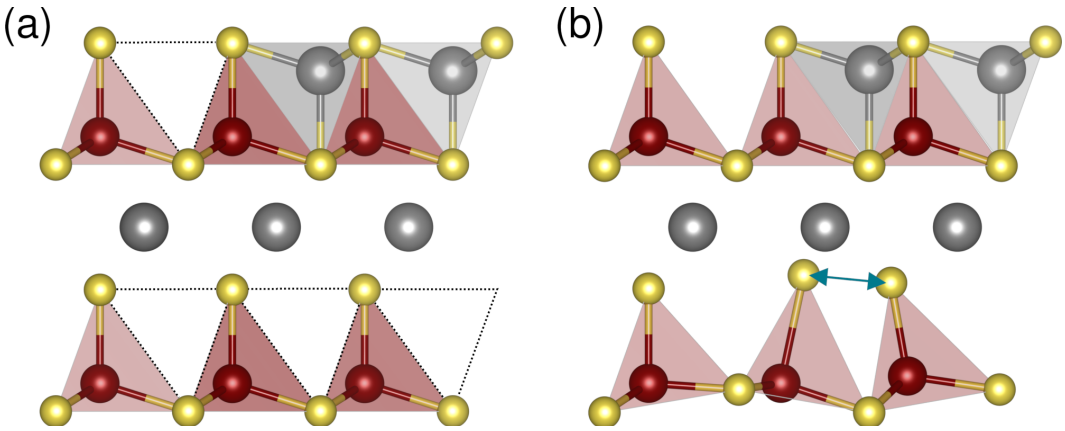

Figure 4.10: (a) Graphic representation of $Li_{2-x}FeS_2$ with tetrahedral Li vacancies and no structural distortions. (b) Graphic representation of hypothesized structural distortions that could occur in $Li_{2-x}FeS_2$ to result in persulfide moieties.

Clues to the location of the persulfide bond come from analyzing the EXAFS data. Based on the Fe K-edge EXAFS, the Fe−S correlation length does not change significantly between 2.5 and 3 V, which supports a mechanism of persulfide formation that does not greatly disrupt the FeS_4 tetrahedra. To maintain the average Fe-S correlation length after persulfide formation, the structure depicted in Figure 4.10 is thus possible. Furthermore, the corrugation in the corner sharing tetrahedral layer could occur in both layers upon further delithiation from $x > 0.5$ theoretically allowing for a total of one electron from anion oxidation, which is observed experimentally. After the one electron oxidation of the anions, the structure suggested in Figure 4.10b infers that half of the S atoms remain at the corners of two tetradedra. It would therefore be difficult to imagine how the structure could accommodate additional persulfide moieties. Thus, further anion redox would require either no structural change, i.e. a hole on S resulting in a formal S^{n-} where $n < 2$, or cause a significant phase change to resemble pyrite FeS_2 in which all S atoms are found as persulfides that link the Fe octahedra. Either scenario would likely incur a high energetic cost and thus results in incomplete oxidation of the S anions experimentally.

It is useful to compare the redox mechanisms of the alkali-rich iron sulfides with that of FeS_2, the stoichiometry of the fully delithiated material. FeS_2 has been studied extensively as a cathode for LIBs, with some similarities to Li_2FeS_2. Dahn and coworkers showed that reduction of the persulfide in pyrite FeS_2 is a kinetically controlled process.[126] At higher temperatures (i.e. $\geq$ 37 °C) or at exceptionally slow discharge rates (i.e. $\leq$ C/150), the formation of Li_2FeS_2 or similar material is possible, as evidenced by the similarity between the charge profile of FeS_2 discharged to two Li per Fe and that of Li_2FeS_2. At ambient temperature or faster rates, Li^+ diffusion within FeS_2 is limited such that full reduction to local domains of Li_2S and metallic Fe occurs at the same potential as persulfide reduction to Li_2FeS_2, and the two reactions cannot be distinguished from one another.[126, 147–151] Due to the extensive structural rearrangement upon initial reduction, pyrite FeS_2 cells are irreversible as neither FeS_2 nor a similar phase is reformed on charging.[111, 147, 149] Though pyrite FeS_2 cells boast high initial discharge capacities of 600 to 800 mAh g^{-1}, within 10 cycles even at exceptionally slow rates (C/40), the capacity decreases by over 50% to less than 300 mAh g^{-1}.[147] Extended cycling results in further capacity fade often to 100 mAh g^{-1} or less within tens of cycles. As is true with many conversion chemistries, nanostructured FeS_2, and related iron sulfides such as Fe_3S_4 and FeS, in intimate contact with the conducting matrix of the electrode results in better capacity retention.[152–154] In this study, however, bulk Li_2FeS_2 prepared in simple composite electrodes shows capacity retention rates of ≥99% per cycle (at C/10 based on one electron per Fe) over 100 cycles, highlighting the reversible nature of the chemistry compared to the irreversible conversion chemistry in FeS_2 materials. Li_2FeS_2 in the charged state (i.e. Li_xFeS_2) thus does not resemble pyrite-FeS_2. Aside from the difference in formal oxidation state of the constituents ($Fe^{2+/3+}$ and mixed S^{2-} and S_2^{2-} vs. $Fe^{2+}$and all S_2^{2-} in pyrite), structural differences enable high reversibility for Li_2FeS_2 by maintaining pathways for Li^+ migration.

4.3 Conclusions

Li_2FeS_2 and $LiNaFeS_2$ represent a set of isostructural materials capable of reversibly storing *ca.* 1.5 mol e^- per formula unit through both cation and anion redox. The oxidation mechanism for both materials is identical from a spectroscopic perspective. In the first region of the charge curve, formally Fe^{2+} is oxidized resulting in an increased covalency of the Fe-S bonds observed by the increase in the S K-edge pre-edge intensity and the shortening of the Fe-S bond in the EXAFS. Fe^{2+} oxidation is

observed by a shift in the position of the Fe K-edge rising edge. Transition metal oxidation only accounts for part of the curve, *ca.* 0.5 mol e^-. The next *ca.* 1 mol e^- is ascribed to oxidation of the sulfide anionic states, S^{2-}. The anion redox is clearly observed in the S K-edge XANES data by the appearance of a well-defined pre-edge feature and a shift in the near-edge position. Such oxidation has been previously ascribed to the formation of persulfides, S_2^{2-}. We hypothesize that the persulfide bonds are formed between corner sharing tetrahedra. Both cation and anion redox are reversible as the S K-edge and Fe K-edge return to closely mimic the spectra of the pristine material upon discharge. Structurally, however, the $LiNaFeS_2$ undergoes a much greater lattice contraction upon oxidation compared to Li_2FeS_2, which likely causes significant lattice strain over time limiting capacity retention. Further exploration of new materials with reversible, anion redox based on covalent metal-chalcogenide interactions will enable the development of next-generation Li ion batteries with increased capacity.

4.4 Experimental Methods

Materials Preparation. All materials and precursors were handled inside an Ar-filled glovebox (H_2O and O_2 < 1 ppm). Li_2FeS_2 was prepared by solid-state synthesis, similar to the method provided by Batchelor *et al.*[120] Namely, powders of Li_2S (Beantown Chemical, 99.9%), Fe (Acros Organics, 99.0%), and pyrite-FeS_2 (Sigma, 99.8%) were ground in stoichiometric quantities and pressed into pellets of 200-300 mg with a hand-operated arbor press. Pellets were placed inside carbon-coated silica ampoules, evacuated to ≤ 10 mTorr, and sealed with a methane-oxygen torch without exposure to air. The ampoule was heated at 5 °C min^{-1} to 500 °C with a dwell time of 12 h, then heated at 1 °C min^{-1}C to 900 °C followed by a dwell period of 16 h, during which the powders melt to form a molten reaction mixture. $LiNaFeS_2$ was prepared similarly but required lower temperatures for complete reaction. First, Na_2S was prepared from stoichoiometric Na (Acros Organics, rod, 99.8%, mechanically cleaned prior to use) and S (S_8 Acros Organics, > 99.5%) in separate alumina crucibles (almath) in an evacuated silica ampoule. The reactants were heated at 1 °C min^{-1} to 300 °C for 48 h and cooled ambiently to room temperature. The ground product was a fine powder slightly tan in color. The product was determined to be phase pure by XRD. Stiochiometric powders of Li_2S, Na_2S, Fe, and S were ground and pressed into pellets of up to 600 mg and subsequently sealed in evacuated silica ampoules. The pellet was heated in the ampoule at 2 °C min^{-1} to 500 °C for 96 h. After ambient cooling to room

temperature, the ampoules were opened inside the glovebox and the pellets were ground into fine, black powders for further characterization.

Electrochemical Characterization. *Electrode Fabrication*: Electrode slurries were prepared by suspending 50/40/10 (wt%) active material, conductive carbon (SuperP, Alfa Aesar, > 99%), and PVDF binder (MTI) in cyclopentanone (*ca.* 9 times by mass of total solids) (Acros Organics, > 99%) with a centrifugal mixer (Thinky USA). Electrodes were prepared by drop-casting the slurry on 1/2" diameter carbon-coated Al foil current collectors (MTI). The films were dried in a vacuum oven inside the glovebox at 100 °C for at least 12 h, yielding an active material loading of 1-3 mg on each electrode. Alternatively, to obtain higher mass loading, free-standing electrodes were prepared by hand grinding 60/20/20 (wt%) active material, carbon, and PTFE binder (Sigma, 1 μm powder) into a film and pressing into 3/8" diameter electrodes under *ca.* 1 ton of force to yield electrodes of 10-20 mg (total).

Electrochemical Testing: All electrochemical cells were assembled inside an Ar-filled glovebox (H_2O and O_2 < 1 ppm). All electrochemistry unless otherwise noted was performed in 2032 coin cells (MTI) with a Li foil anode (Sigma, 99.9%, 0.75 mm, mechanically cleaned immediately before cell assembly), polypropylene separator (Celgard 2400), *ca.* 4 drops of LP100 electrolyte (55±9 mg), and a working electrode of 50 wt% active material as described above. The LP100 electrolyte was prepared as a 1 M solution of $LiPF_6$ (Oakwood Chemical, Battery Grade) in a 1:1:3 (by volume) mixture of ethylene carbonate, dimethyl carbonate(DMC), and propylene carbonate (PC) (all Sigma, ≥ 99%). The solution was prepared in a dried HDPE bottle by mixing of the carbonates and addition of the salt. Electrolyte was not used for more than two weeks before a new solution was prepared. The liquid carbonates (DMC and PC) were stored over activated molecular sieves (3 Å, Beantown Chemical) prior to use. Both materials were charged (oxidized) at the rate indicated (based on 1 e^- per formula unit) to 3 V and discharged at the rate indicated to 1.7 V. In some cases, a lower oxidation cutoff potential (e.g. 2.5 V) was used as noted. All voltages are *vs.* Li/Li^+. All electrochemical experiments were performed with either a VMP3 mutli-channel potentiostat (Bio-Logic) or BCS 805 battery cycler (Bio-Logic). The current in the GITT experiments was C/10 based on one electron per formula unit for 20 min separated by 4 h rest periods.

Structural Characterization. *Powder X-ray Diffraction*: High-resolution synchrotron powder X-ray diffraction (XRD) was collected on samples sealed under

vacuum in 0.7 mm (O.D.) glass capillaries (to prevent air-exposure) placed inside of polyimide capillaries. The samples were measured on beamline 11-BM-B (λ = 0.412781 Å) at the Advanced Photon Source at Argonne National Laboratory.[155] The diffraction patterns were fit with the Rietveld method using the General Structure Analysis System II (GSAS-II),[75] and visualization of the crystal structures was aided by VESTA.[76]

Operando XRD was performed on a Bruker D8 Advance diffractometer with a Cu source using a previously reported cell geometry.[156] The free-standing electrodes were loaded into a modified stainless steel Swagelok cell with a Be window. The *operando* electrochemical cell comprised of a 1.2" (I.D.) stainless steel Swagelok union with a thin sheet of plastic wrapped around the interior of the cell to prevent the electrodes from shorting. The stack inside the cell included the Be window and current collector, the free-standing electrode (cathode), a glass-fiber separator (Whatman, GF/D), a Li foil anode, a spacer, a spring, and a stainless steel plunger that served as the other current collector. The cell was flooded with LP100 electrolyte and sealed around the plunger with PTFE ferrules. The cell was placed on the diffractometer stage such that the X-rays would directly access the cathode after penetrating the Be window. A VMP3 mutli-channel potentiostat (Bio-Logic) was used to perform the electrochemical experiments. The cell was cycled at C/10 based on one electron per formula unit. Powder patterns were collected continually starting from cell assembly (including a hold at open circuit of *ca.* 1 h), with each scan taking approximately 20 min.

X-ray Absorption Spectroscopy: Samples for *ex situ* X-ray absorption spectroscopy (XAS) were prepared in 1/2" diameter Nylon Swagelok cells with a Li foil anode, glass-fiber separator (Whatman, GF/D), *ca.* 10 drops of LP100 electrolyte (approx. 140 mg), and free-standing electrodes (prepared as described above). Electrodes were measured in the following states: pristine, charged to 2.5 V, fully charged to 3 V, and fully charged then fully discharged to 1.7 V. The active material used in the free-standing electrodes prepared for S K-edge XAS measurements was ball-milled prior to electrode fabrication to reduce the particle size (below *ca.* 10 μm) and limit self-absorption. After oxidizing or reducing the material galvanostatically to a defined cutoff, the samples were extracted, dried under vacuum for > 4 h, and diluted *ca.* 5:1 by mass with boron nitride (Alfa Aesar, 99.5%). All samples were measured *ex situ* from three sweeps in both fluorescence and transmission modes, where the data shown are the summed fluorescence data for each sample. Samples for Fe

and S K-edge XAS were measured at beamlines 4-1 and 4-3, respectively, at the Stanford Synchrotron Radiation Lightsource at SLAC National Accelerator Laboratory. Calibration, background correction, and data processing of X-ray absorption near edge structure (XANES) and EXAFS was performed using Athena.[77] All S K-edge XAS data were calibrated to a sodium thiosulfate standard that was repeatedly checked throughout experimentation to ensure a constant energy shift. The Fe K-edge data were calibrated to a collinear Fe foil present for each sample.

EXAFS Fitting: Extended X-ray absorption fine structure (EXAFS) data analysis and fitting were performed with the Athena and Artemis software programs from the IFEFFIT suite.[77, 157] Normalized EXAFS oscillations as a function of the photoelectron wavenumber (χ(k)) were obtained and fit in a k window of 2.9-3.1 to 11.2-11.7 $Å^{-1}$ (sample dependent) with dk = 2 for the Fe K-edge. For the S K-edge, a k window of 2.5 to 7.7 $Å^{-1}$ with dk = 1 was used for the Fourier transform. The S K-edge data were not fit. Fe K-edge data were fit with two scattering shells in an R window of 1.1 to 2.7 Å. The first shell was attributed to Fe−S correlations, and the second shell was assumed to be dominated by Fe−Fe correlations. The number of S near-neighbors for Fe was fixed to four in pristine $LiNaFeS_2$, which was found to be phase pure and contain fully tetrahedral Fe by Rietveld analysis of synchrotron X-ray diffraction data. The amplitude reduction factor obtained from the fit of pristine $LiNaFeS_2$ was used to estimate the number of S and Fe neighbors within the first and second shell, respectively, for both materials at various states of charge.

DFT Calculations: Density functional theory (DFT) calculations using the SCAN parameterization[158] were performed with the Vienna ab intio Simulation Package (VASP).[159–162] The projector augmented wave (PAW) method was used with a plane wave energy cutoff of 520 eV. The core states were treated with the VASP PAW potentials labeled Li_sv, Fe, and S. k-point meshes were automatically generated with a 32 $Å^{-1}$ density along each reciprocal lattice vector. All atomic positions were fully relaxed.

Chapter 5

COMPLEX STRUCTURAL RESPONSE OF MULTIELECTRON CATHODE LI_2FES_2 TO MIXED CATION AND ANION OXIDATION

5.1 Abstract

In Chapter 4, detailed electrochemical and *ex situ* spectroscopic studies of Li_2FeS_2, which show reversible multielectron redox characterized by oxidation of Fe concurrent with an increase in covalency of the Fe–S bond followed by oxidation of sulfides to persulfide-like moieties, are reported. Here, the ramifications of anion redox, specifically anion-anion bond formation, on the local structure of Li_2FeS_2 is explored using *operando* X-ray total scattering pair distribution function (PDF) analysis in tandem with similar local probe EXAFS. Local structure analysis reveals evidence of S–S bond formation, complex structural rearrangement during the anion oxidation plateau, and an asymmetric structural evolution upon discharge (relithiation). Introduction of a high degree of structural heterogeneity on the first charge cycle is found to be irreversible, directing an alternative discharge pathway, though the resultant structure closely resembles the as-prepared crystalline material on a local level. Computations of the S K-edge XANES lends further support to the hypothesis of S–S bond formation detailed in Chapter 4. Combining the electrochemistry, spectroscopy, and local structure studies allows for a deeper understanding of the electronic and physical properties and processes governing reversible anion redox, promoting the determination of design rules for next-generation high-capacity battery technologies.

5.2 Introduction

As shown in Chapter 4, Li_2FeS_2 is capable of multielectron storage via a combined cation and anion redox mechanism. The charge profile is characterized by a sloping region with multiple inflection points and a long, flat plateau at higher voltages as shown in Figure 5.1.[163] XANES analysis at the Fe and S K-edges of composite electrodes cycled to various points along the voltage profile show that the sloping region is attributable primarily to $Fe^{2+/3+}$ oxidation while the plateau aligns with the oxidation of sulfides (S^{2-}) to persulfides (S_2^{2-}). The diffraction patterns show significant loss of long-range order during charging that is not recovered on the subsequent discharge (Figure 4.7), and the discharge profile is markedly different. Notably, the second cycle closely traces the first despite the loss of long-range order and the different discharge pathway (Figure 4.2). A preliminary investigation into the local structure around Fe is conducted by Fe K-edge XANES and EXAFS analysis, which indicate that S oxidation results in minimal changes to the coordination environment. To satisfy this condition, we hypothesize a mechanism of S–S bond formation where corner-sharing FeS_4 tetrahedra tilt with respect to each other to bring the apex S atoms close enough together as shown relative to the pristine structure in Figure 5.1b,c. The questions then arise from the results of Chapter 4: (1) What is the cause of the path hysteresis between charge and discharge? (2) Why/how does the second cycle trace the first despite significant structural disruption? (3) What is the true mechanism of S–S bond formation? In this work, we further investigate the structural perturbations that accompany S oxidation and, more specifically, S–S bond formation in Li_2FeS_2.

5.3 Results and Discussion

Local Structure Analysis by S K-edge EXAFS and X-ray Pair Distribution Function Analysis

Due to loss of long-range order, structural probes like XRD (as shown in Figure 4.7) do not yield detailed information on the structural ramifications of S oxidation. To fill this gap in understanding, we turn to probes of local structure. First, S K-edge EXAFS analysis is performed as shown in Figure 5.3a, and we focus on the first two coordination shells. Due to a lack of data in *k*-space, quantitative fitting of the EXAFS is not feasible and, instead, the features and changes are here discussed qualitatively. Further, the EXAFS data is not phase shift corrected, though the phase shift tends to be around 0.5 Å in most materials.[164] In as-prepared Li_2FeS_2, the EXAFS is characterized by S–Fe nearest neighbors, which range from 2.36 to

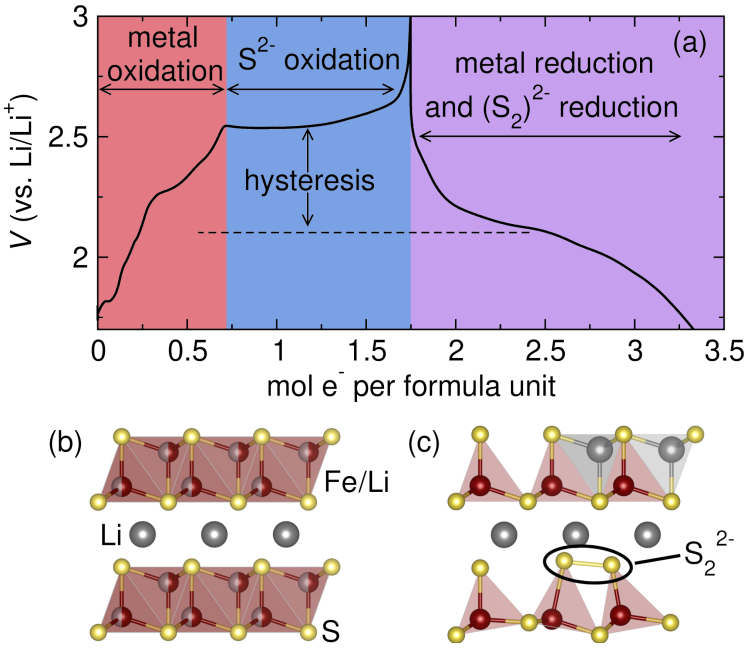

Figure 5.1: (a) First cycle galvanostatic charge and discharge of Li_2FeS_2 at a rate of C/10. Different regions are highlighted based on the charge compensation mechanism at that SOC, and the voltage hysteresis between charge and discharge is depicted. (b) The structure of pristine Li_2FeS_2. (c) The hypothesized S–S bond formation mechanism in Li_2FeS_2.

2.39 Å as depicted in Figure 5.3b. Upon charging to 2.5 V before the plateau, the S–Fe distance shortens slightly concomitant with a contraction of the lattice as Fe^{2+} is oxidized, which is also seen by XRD (Figure 4.7).[163] After fully charging to 3 V, significant changes to the first-shell feature are observed. A splitting into two more distinct features occurs along with a substantial shift to shorter correlation lengths, indicating additional contraction of the lattice or certain components of the lattice. To assign specific correlations to the features in the fully charged material, we turn to a structural model provided by theoretical calculations, keeping in mind that DFT methods tend to underestimate bond lengths.[165] Collaborators at the University of Birmingham and University of Cambridge, Prof. Andrew J. Morris and Dr. Angela F. Harper, employed plane-wave density functional theory (DFT) with CASTEP code[166, 167] to simulate the unit cell of Li_2FeS_2 in a partially (i.e. prior to S oxidation) and fully charged state as shown in Figure 5.2. The fully charged structure was obtained by perturbing the FeS_4 tetrahedra such that two S atoms were within 1.2 Å of each other, then the system was geometry optimized to relax the forces. The center of the low-R first-shell feature tracks well with an estimated S–Fe distance around 2.2 Å as predicted applying an estimated phase shift

correction of 0.5 Å. However, significant weight is still observed below this value suggesting non-negligible contributions from a shorter correlation, which supports formation of S–S bonds predicted to be around 2 Å as is consistent with other persulfide-containing materials.[168] The higher-R first-shell feature is attributed to S–Fe bonds that remain longer in domains of the materials where S is not oxidized, which will be expounded upon in Section 5.3. These values agree well with those in the relaxed structural model of the fully charged material as predicted by DFT and shown in Figure 5.3. Upon discharging, the first-shell feature resembles that of the as-prepared sample with only small differences, indicating largely reversible changes to the local structure around S on average.

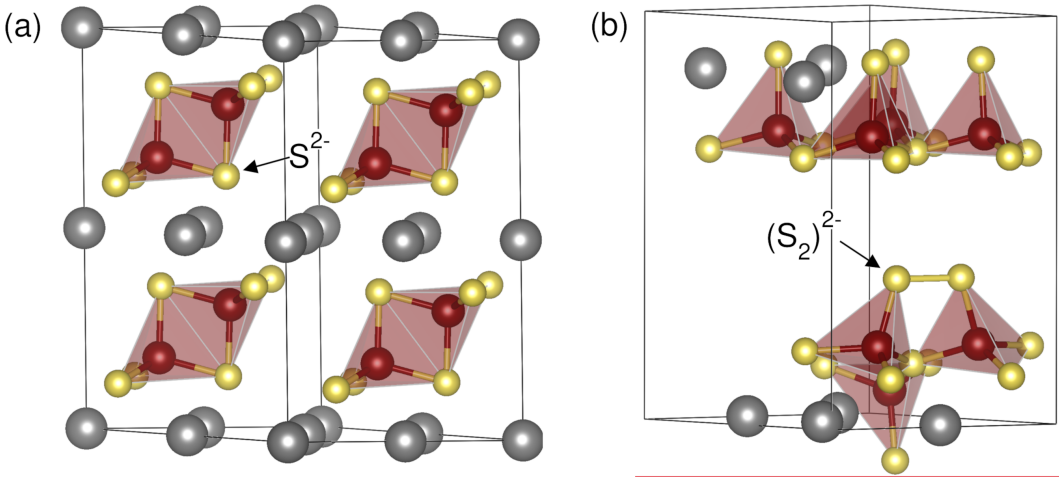

Figure 5.2: DFT-calculated structures of (a) partially charged (i.e. prior to S oxidation) and (b) fully charged Li_2FeS_2 from A. F. Harper (University of Cambridge) and A. J. Morris (University of Birmingham).

The second coordination shell encompasses several correlations: inter- and intralayer S-S and interlayer S-Fe distances as well as S-Fe-Fe multiple scattering paths. The most notable changes to the second-shell feature is a systematic decrease of the magnitude during charging, which points to an increase in disorder in the system with respect to environments around S.[23] In other words, this indicates a decrease in the instances of the corresponding second-shell scattering events, which points to a disordering of the system on a local level that significantly perturbs the parent structure. The system remains somewhat disordered on the two or more bond distance scale upon discharging as the magnitude does not recover to that of the as-prepared sample. The lack of significant changes to the correlation distance range covered by the second-shell feature suggests that the majority of, if not all, S–S bonds form within the Fe-containing layer and not between layers across Li

vacancies as reported in Chapter 4. If interlayer S–S bonds were to form, we would expect a notable decrease in the second-shell correlation distances as interlayer atomic distances decrease and scattering paths shorten, but this is not observed.

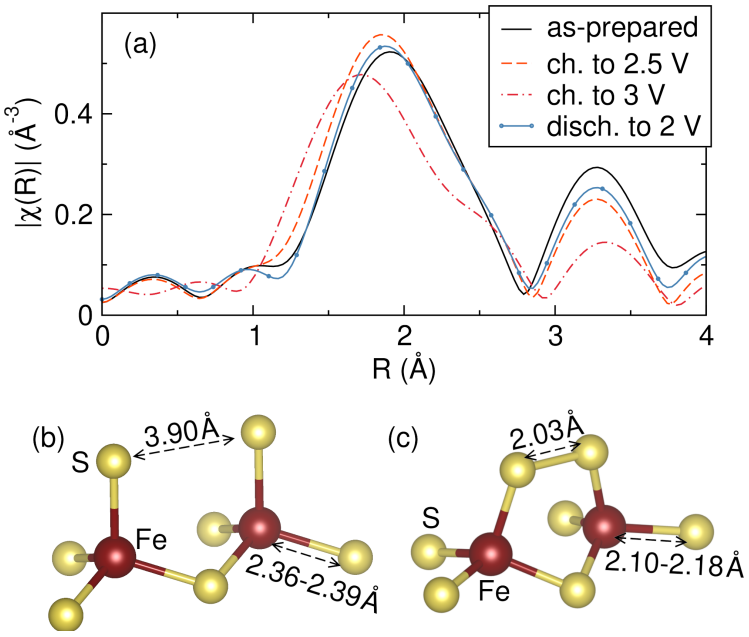

Figure 5.3: (a) *Ex situ* S K-edge EXAFS collected at various SOC of Li_2FeS_2 composite electrodes. EXAFS are not phase shift corrected. Depictions of corner-sharing FeS_4 tetrahedra with Fe–S and S–S distances in (a) as-prepared and (b) fully oxidized Li_2FeS_2. The oxidized structure is as calculated from DFT as described in Section 5.5.

Local and Mid-Range Structure Analysis by X-ray Pair Distribution Function Analysis

While EXAFS analysis provides useful information about the local structure, it is limited both to scattering events after absorption by a specific element and to relatively short distances. On the other hand, total scattering X-ray pair distribution function (PDF) uses high-energy X-rays and measures an ensemble of all scattering events in the material out to distances equivalent to a dozen bond lengths and more. To gain more insight into local structural changes, PDF analysis is performed on *ex situ* samples of Li_2FeS_2 at various SOC as shown in Figure 5.4. Due to having an accurate structural representation of the as-prepared sample from synchrotron XRD (Figure 4.1), the PDF is able to be fit. Figure 5.4a shows the PDF and fit showing good agreement, which continues past 20 Å indicating a highly crystalline structure. Here, only the low-r region is shown as we are primarily concerned with understanding local structural changes on the order of several bond lengths.

Figure 5.4b plots the calculated PDF of all component scattering events, providing a key for tracking how the changes in PDF correspond to real structural changes in the material.

The PDF of all *ex situ* samples are shown in Figure 5.4c. First, upon oxidation to 2.5 V, or removal of approximately 0.7 eq. of Li^+ per formula unit before the plateau, a contraction is immediately observed in the Fe–S bond length (Li_{T_d}–S bonds are disregarded as Li^+ is being removed) represented by a shift in the peak at 2.34 Å. The feature centered at 2.75 Å in the as-prepared sample, primarily representing intralayer Fe-Fe distances with contributions from Li_{O_h}-S scattering, broadens slightly upon removal of 0.7 eq. of Li^+ but does not shift meaningfully. Peak width, or real-space resolution (Δr), is also related to Q_{max} (maximum value of the amplitude of the scattering vector, where $Q = 4\pi sin\theta/\lambda$), which is an experimental parameter determined by the X-ray source and experiment setup.[169] The real-space resolution is inversely proportional to the Q_{max} and can be approximated as π/Q_{max} except when $Q_{max} > \pi/\sqrt{\langle u^2 \rangle}$, where $\sqrt{\langle u^2 \rangle}$ is the root-mean-squared atomic displacement. This limitation arises from the fact that local thermal vibrations will cause interatomic distances to be effectively smeared out over a slightly wider range in real space, broadening the peaks observed.[169] Therefore, peak broadening here suggests an increase in disorder, or decrease in long-range order, to the Fe network in the tetrahedral layer as the lattice contracts during Fe oxidation, but it is important to keep in mind that broadening effects result from atomic vibrations as well. The feature at 3.87 Å represents nearest neighbor S-S distances and second nearest neighbor Fe-Fe distances, which correspond to those of corner-sharing FeS_4 tetrahedra. Upon charging, the feature shifts to lower r and maintains its shape, which indicates a shortening of both S-S and Fe-Fe distances commensurate with an overall lattice contraction. The feature at 4.59 Å primarily represents next nearest Fe-S distances and behaves similarly to the feature at 3.87 Å in that an initial contraction is observed upon charging. The contraction is characterized by a broadened feature. This points to some Fe-S distances, which are all nearly identical in the as-prepared material, shortening more than others. The PDF looks nearly identical after removal of a full eq. of Li^+, which suggests the more disruptive structural changes do not begin at the start of the plateau but instead require a certain degree of delithiation to be triggered. This is discussed further in Section 5.3.

After charging to the start of the plateau, the low-r Fe/Li–S feature does not shift further even at full charge corroborating the results from fitting of the Fe EXAFS that

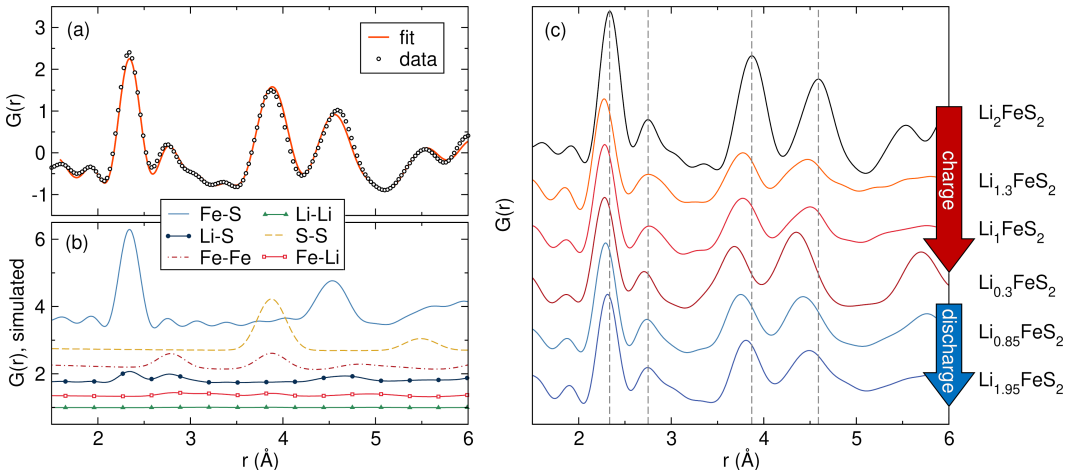

Figure 5.4: (a) X-ray total scattering PDF of as-prepared Li_2FeS_2 with fit and (b) calculated PDF of all possible scattering permutations between two atoms weighted by X-ray scattering cross section. (c) *Ex situ* PDF of Li_2FeS_2 at various SOCs during the first charge/discharge cycle with several dashed lines marking peak positions in the as-prepared sample as guides for the eye.

show minimal distortions to the FeS_4 tetrahedra during S oxidation.[163] The initial contraction in the Fe–S bond length is also consistent with the S K-edge EXAFS from this work and the *operando* XRD as reported previously.[163] Upon fully charging to $Li_{0.3}FeS_2$, several features sharpen and shift to slightly lower r. The implications of a higher degree of order at full charge is discussed further in Section 5.3. Specifically, the feature corresponding to S-S and Fe-Fe distances shifts further to lower r. These S-S distances represent the tetrahedral edges of Li^+ vacancies along which S–S bonds are thought to form. When fully charged, the feature coalesces to again form a singular feature indicating a more normal distribution of second nearest neighbor Fe-S distances. Notably, a new feature around 2 Å is not observed as reported for S–S bonds previously for a similar material, disordered rocksalt Li_2TiS_3,[115] but it is possible the feature is either too low in magnitude to be seen above the background features of the Fourier transform or hidden under the intense features at low r.

During discharge, the structural pathway appears to be different than that during charging, agreeing with the differences in the electrochemical profile. At approximately half depth of discharge, all previously mentioned features have shifted back towards the original values in as-prepared Li_2FeS_2. At full depth of discharge, however, most of the features have not fully shifted back to the original values, indicating permanent changes to the structure on a local level.

Discussion

The goals of this work are: (1) investigate the feasibility of the existing hypothesis for the formation of S–S bonds, (2) better understand the structure of oxidized Li_2FeS_2, and (3) glean structural causes for the hysteresis observed between the charge and discharge pathways. From S K-edge XANES, we know that Li_2FeS_2 exhibits S oxidation and the formation of persulfide moities, and we know that this process does not significantly distort FeS_4 tetrahedra from Fe K-edge EXAFS analysis.[163] From theoretical calculations of the S K-edge XANES spectrum of the proposed oxidized structure, a mechanism of coordinated tilting of corner-sharing FeS_4 tetrahedra is energetically possible in this system, and perhaps likely given the reproduction of the second pre-edge feature observed experimentally. A qualitative analysis of the S K-edge EXAFS of a fully charged sample provides evidence of correlations involving S that are substantially shorter than the Fe–S bond lengths, which we attribute to the S–S bonds. However, a feature at higher R within the first coordination shell is maintained, which we now explain with an updated hypothesis of the ramifications of S oxidation to the short- and long-range order of Li_2FeS_2.

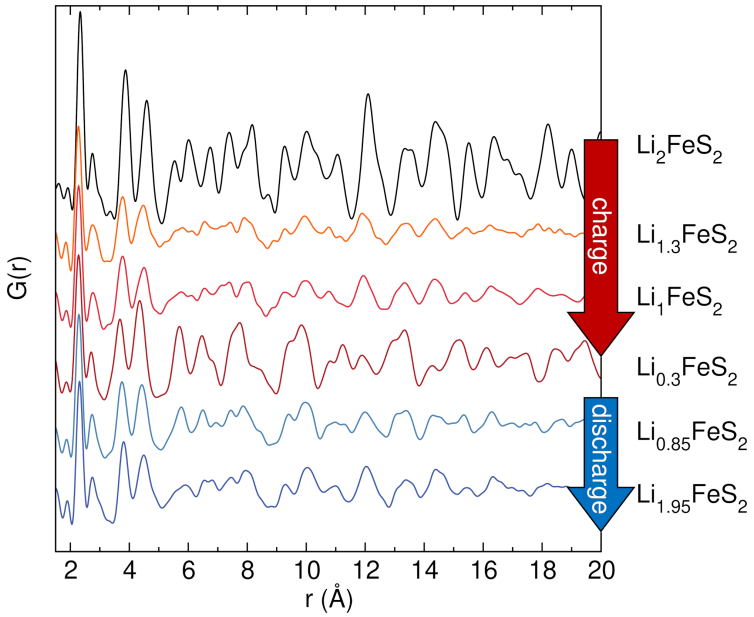

Figure 5.5: Extended r-range of *ex situ* X-ray PDF of Li_2FeS_2 at various SOCs during the first charge/discharge cycle to highlight permanent loss of long-range crystallinity.

Removal of approximately 1 eq. of Li^+ is compensated by oxidation of S, which is half of the S available. Therefore, half of the S atoms in the structure are assumed to be part of a persulfide moiety, leaving the other half to remain as reduced

sulfides. The formation of S–S bonds during oxidation necessitates significant distortions to the local structure, and, presumably, this affects the regions of the crystal structure adjacent to persulfide moieties as well. It is worth remembering that the tetrahedral sites are split sites and are equally as likely to be occupied by Li as by Fe, meaning there are likely Fe-rich and Fe-poor regions in the as-prepared material. The hypothesized method of S–S formation requires corner-sharing connectivity of FeS_4 tetrahedra and Li^+ vacancies, so in Fe-rich regions it follows that S–S bonds are unable to form unless Fe is mobile within the structure. This may be possible as shown by the Fe occupying a tetrahedral site in the octahedral layer in the relaxed oxidized structure shown in Figure 5.2 but is not proven concretely one way or the other by experimental means. Given this information, we extend the hypothesis by asserting that S oxidation and formation of S–S bonds introduces significant structural heterogeneity to the sample on a local level. For example, there may be regions of the material that do not have oxidized S and therefore closely resemble the structure of the material before any S oxidation takes place, while other regions have many S–S bonds that induce local distortions, which may provide further insight into the 1 e^- per S limitation discussed in Chapter 4. The energetic penalty to completely disorder the bulk of the material to accommodate more S–S bonds may enforce this upper boundary to the redox capabilities. This type of structural heterogeneity across the material explains the loss of long-range order exhibited by *operando* XRD as well as the two-phase coexistence shown again by XRD and corroborated by the electrochemistry and entropic potential measurements.[163] This hypothesis is also consistent with the X-ray PDF. As shown in Figure 5.5, crystallinity over mid-range and long-range distances is lost immediately upon oxidation. The disorder is maintained after 1 eq. of Li^+ is removed, but, interestingly, it appears to partially return as full charge, which indicates a relaxation of the highly delithiated structure. This is consistent with the entropic potential measurements and *operando* XRD that suggest the structural change occurs not at the beginning of the plateau in the electrochemical profile but somewhere in the middle. Relaxation of the structure at a high degree of delithiation into a more ordered arrangement is likely a result of widespread S oxidation and S–S bond formation throughout the structure.

The introduction of widespread structural heterogeneity during the first charge may also be the cause for the material proceeding through a different pathway upon discharging. As shown in Figure 5.5, the features in the PDF of the partially and fully discharged samples closely resemble those in the as-prepared sample but with much lower magnitude. This is indicative of increased disorder but a structure that,

on a local level, is structurally very similar to the starting material. It appears that forming S–S bonds and disrupting the long-range order on the first charge is an irreversible process, which explains the coulombic efficiency being the worst on the first cycle as shown in Figure 5.6. Kinetic overpotentials as shown by GITT (Figure 4.3) are higher during discharge as it is more difficult to relithiate regions of the structure where many S–S bonds have formed as vacant tetrahedral sites are blocked. With enough extra energy (i.e. voltage), the Li^+ can be pushed back into the structure, though it remains disordered on a long-range level, and this is the origin of the voltage hysteresis observed (Figure 5.1). Furthermore, a preliminary experiment with cryomilled Li_2FeS_2 is performed and the cell shows worse capacity retention than as-prepared Li_2FeS_2 (Figure 5.6), suggesting that introducing defects before cycling does not circumvent the loss of long-range order and prevent the first cycle capacity fade. This method has been shown to improve capacity retention in structurally analogous $LiNaFeS_2$,[170] but it appears the issues facing Li_2FeS_2 are somewhat unique.

Despite the irreversible structural distortions after the first charge, the second cycle closely mirrors the first. This is unlike similar oxide-based materials where the voltage profile after the first charge is irreversibly changed.[14, 15] The higher reversibility of Li_2FeS_2 is certainly related to the propensity of S to form stable S–S bonds within a solid lattice as opposed to O, for which the thermodynamic driving force to form O_2 gas is overwhelming.

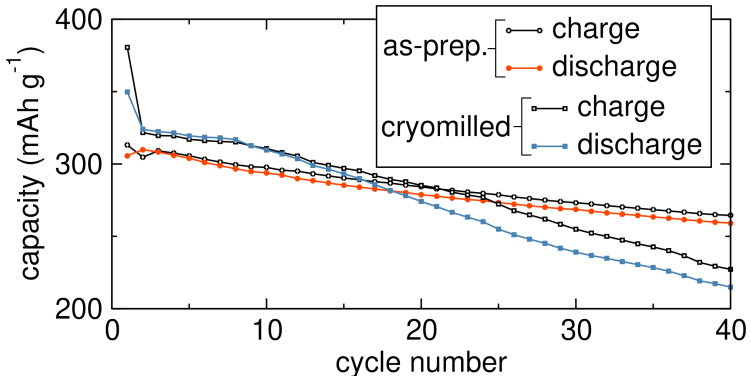

Figure 5.6: Cycling stability comparison between as-prepared and cryomilled Li_2FeS_2. Cells cycled galvanostatically at C/10. As-prepared data adapted from Figure 4.4a and *J. Am. Chem. Soc.* **2020**, *142*, 6737–6749. Copyright 2020 American Chemical Society.

5.4 Conclusions

In conclusion, the oxidation mechanism of Li_2FeS_2 is highly complex from a structural perspective. The tetrahedral tilting mechanism of S–S bond formation as reported in Chapter 4 and by Hansen *et al.*[163] is consistent with the results described herein and predicted to be stable computationally but is not explicitly proven through experiment. Instead, evidence of the irreversible introduction of significant structural heterogeneity is found, making detailed characterization of the structure of the oxidized material difficult. Entropic potential measurements reveal a configurational change occurs later in the high-voltage plateau that does not manifest in the electrochemical profile. reviously conducted *operando* XRD[163] and the X-ray PDF results in this work. S K-edge EXAFS analysis indicates the presence of short S-related correlations that are attributed to S–S bonds. The structural heterogeneity induced by S–S bond formation is irreversible, but the structure is able to regain a configuration that resembles as-prepared Li_2FeS_2 locally but is disordered on a long-range level. By preliminary experiments with cryomilled Li_2FeS_2, introducing defects into the material artificially does not improve cycling stability. As such, it will likely be difficult to engineer Li_2FeS_2 and similar materials to avoid this type of long-range structural disruption if the anion redox mechanism requires bond forming reactions. Nevertheless, the improved reversibility of sulfides with respect to oxides provide an exciting avenue for further research and development of high capacity cathode materials based on anion redox, which will be discussed at length in Chapter 7.

5.5 Experimental Methods

Computational Methods. All DFT calculations were performed using the plane-wave pseudopotential code CASTEP v19.11[167] at the PBE level of theory[171] using the CASTEP on-the-fly HARD set of pseudopotentials. These pseudopotentials are generated using a smaller cut-off radius, and therefore require a larger set of plane waves, which provides more accurate results for the subsequent XAS calculations (not described in this thesis). A kinetic energy cut-off of 1000 eV and k-point spacing less than 2π*0.03 $Å^{-1}$ was used.

To model the $LiFeS_2$ structure, first, the pristine Li_2FeS_2 structure was used, and half of the Li atoms were removed, resulting in a model with Fe atoms occupying edge-shared tetrahedral positions between Li layers. Then, the structure was geometry optimized using the same plane wave kinetic energy cut-off and k-point parameters as previously mentioned to obtain a structure that had forces relaxed to within

0.05 eVÅ^{-1}. To model the formation of persulfide bonds in the material, Li atoms were removed until the cell reached a stoichiometry of $LiFeS_2$ with Fe atoms now occupying the corner-sharing positions to match the proposed atom arrangement as described in Chapter 4 and in Hansen *et al.*.[163] Two S atoms in adjacent FeS_4 tetrahedra were brought artificially close together to encourage persulfide formation after optimization (within 1.9 Å of each other). Following geometry optimization, these atoms were 2.03 Å apart, which is within the range of S–S bond lengths found in many solid-state materials.[168]

Extended X-ray Absorption Fine Structure. Samples for *ex situ* X-ray absorption spectroscopy (XAS) were prepared as described in Section 4.4. All samples were measured *ex situ* from three sweeps in fluorescence. Samples S K-edge XAS were measured at beamline 4-3 at the Stanford Synchrotron Radiation Lightsource at SLAC National Accelerator Laboratory. Calibration, background correction, and data processing of X-ray absorption near edge structure (XANES) and EXAFS was performed using Athena.[77] All S K-edge XAS data were calibrated to a sodium thiosulfate standard that was repeatedly checked throughout experimentation to ensure a constant energy shift.

X-ray Total Scattering Pair Distribution Function Analysis. Samples for *ex situ* PDF measurements were prepared in 2032 coin cells with a Li foil anode, glass-fiber separator (Whatman, GF/D), 12 drops of electrolyte (approx. 170 mg), and a composite electrode (3:1:1 by mass of Li_2FeS_2:Super P carbon (Alfa Aesar, ≥99%):polytetrafluoroethylene (PTFE, Sigma Aldrich)). The composite mixture was ground to homogeneity with a mortar and pestle, and pressed into pellets of 0.25" diameter with a hand driven arbor press. Electrodes were cycled galvanostatically to various states of charge using predetermined voltage cutoffs on the first cycle charge and discharge. The coin cells were disassembled in an Ar glovebox and electrodes were then removed, washed with dimethyl carbonate, and dried under vacuum. Samples were sealed under an Ar atmosphere in polyimide capillaries.

PDF experiments were carried out at the 28-ID-1 beamline at NSLS-II at Brookhaven National Laboratory using the rapid acquisition PDF method (RAPDF) [172] during the beamtime from 11/23/2020 to 11/24/2020. A 2D Perkin Elmer amorphous silicon detector was placed 210 mm behind the samples, which were loaded in 1 mm OD glass capillaries. The incident wavelength of the x-rays was 0.1665 Å. The detector exposure time was 300 s. Calibration of the experimental setup was done using Nickel as a calibrant.

Raw data were summed and corrected for polarization effects before being integrated along arcs of constant angle to produce 1D powder diffraction patterns using the program pyFAI [173]. Correction was then made to the data and normalization was carried out to obtain the total scattering structure function, $F(Q)$, which was Fourier transformed to obtain the PDF using PDFgetX3 [174] within xPDFsuite [175]. The maximum momentum transfer Q_{max} for Fourier transformation is 21.5 Å. The modeling was carried out using Diffpy-CMI [176].

Description of the PDF Method (contributed by S. Tao of Columbia University).

The PDF method is a total scattering technique for determining local order in nanostructured materials.[177] The technique does not require periodicity, so it is well suited for studying nanoscale features in a variety of materials.[178, 179] The experimental PDF, denoted $G(r)$, is the truncated Fourier transform of the total scattering structure function, $F(Q) = Q[S(Q) - 1]$:[180]

$$G(r) = \frac{2}{\pi} \int_{Q_{\min}}^{21.5} F(Q) \sin(Qr)\, Q, \tag{5.1}$$

where Q is the magnitude of the scattering momentum. The structure function, $S(Q)$, is extracted from the Bragg and diffuse components of x-ray, neutron or electron powder diffraction intensity. For elastic scattering, $Q = 4\pi \sin(\theta)/\lambda$, where λ is the scattering wavelength and 2θ is the scattering angle. In practice, values of $Q_{\min}$ and 21.5 are determined by the experimental setup and 21.5 is often reduced below the experimental maximum to eliminate noisy data from the PDF since the signal to noise ratio becomes unfavorable in the high-Q region.

Once the experimental PDFs are determined they can be analyzed directly or through modeling. A powerful approach is simply to compare experimentally determined PDFs from samples under study and from known control samples.[181] A great deal can be learned simply from visual inspections and by taking differences to look for residual signals. Numerical tools that compare the likeness, or degree of correlation, between two curves also give insight.[181, 182] The Pearson correlation coefficient is one such tool.[182]

The PDF gives the scaled probability of finding two atoms in a material a distance r apart and is related to the density of atom pairs in the material.[177] For a macroscopic scatterer, $G(r)$ can be calculated from a known structure model according

to

$$G(r) = 4\pi r \left[\rho(r) - \rho_0\right], \tag{5.2}$$
$$\rho(r) = \frac{1}{4\pi r^2 N} \sum_i \sum_{j \neq i} \frac{b_i b_j}{\langle b \rangle^2} \delta(r - r_{ij}).$$

Here, ρ_0 is the atomic number density of the material and $\rho(r)$ is the atomic pair density, which is the mean weighted density of neighbor atoms at distance r from an atom at the origin. The sums in $\rho(r)$ run over all atoms in the sample, b_i is the scattering factor of atom i, $\langle b \rangle$ is the average scattering factor and r_{ij} is the distance between atoms i and j.

In practice, we use Grfromrhor to fit the PDF generated from a structure model to a PDF determined from experiment. For this purpose, the delta functions in Grfromrhor are Gaussian-broadened and the equation is modified to account for experimental effects. PDF modeling, where it is carried out, is performed by adjusting the parameters of the structure model, such as the lattice constants, atom positions and anisotropic atomic displacement parameters, to maximize the agreement between the theoretical and an experimental PDF. This procedure is implemented, for example, in PDFGUI [183] and Diffpy-CMI. [176]

Chapter 6

CONTROLLING COVALENCY AND ANION REDOX POTENTIALS THROUGH ANION SUBSTITUTION IN LI-RICH CHALCOGENIDES

Adapted from: Martinolich, A. J.; Zak, J. J.; Agyeman-Budu, D. N.; Kim, S. S.; Bashian, N. H.; Irshad, A.; Narayan, S. R.; Melot, B. C.; Nelson Weker, J.; See, K. A. Controlling Covalency and Anion Redox Potentials through Anion Substitution in Li-Rich Chalcogenides. *Chem. Mater.* **2021**, *33*, 378–391.

Chapter Abstract

Development of next-generation battery technologies is imperative in the pursuit of a clean energy future. Toward that end, battery chemistries capable of multielectron redox processes are at the forefront of studies on Li-based systems to increase the gravimetric capacity of the cathode. Multielectron processes rely either on the iterative redox of transition metal cations in the cathode or redox involving both the transition metal cations and the anionic framework. Targeting coupled cation and anion redox to achieve multielectron charge storage is difficult, however, because the structure-property relationships that govern reversibility are poorly understood. In an effort to develop fundamental understanding of anion redox, we have developed a materials family that displays tunable anion redox over a range of potentials that are dependent on a systematic modification of the stoichiometry. We report anion redox in the chalcogenide solid solution $Li_2FeS_{2-y}Se_y$, wherein the mixing of the sulfide and selenide anions yields a controllable shift in the high voltage oxidation plateau. Electrochemical measurements indicate that reversible multielectron redox occurs across the solid solution. X-ray absorption spectroscopy supports the oxidation of both iron and selenium at high states of charge, while Raman spectroscopy indicates the formation of Se–Se dimers in Li_2FeSe_2 upon Li deintercalation, providing insight into the charge mechanism of the Li-rich iron chalcogenides. Anion substitution presents direct control over the functional properties of multielectron redox materials for next generation battery technologies.

6.1 Introduction

As discussed in Chapter 2, Li-rich oxide cathodes for LIBs invoke O oxidation that occurs at high voltages outside the electrochemical stability window of the organic carbonate electrolyte. As a result, although apparent gravimetric capacities indicate multielectron redox, there are several other parasitic reactions that could contribute to the observed current including irreversible O_2 gas release and oxidative decomposition of the electrolyte. Recently, irreversible degradation reactions were shown to contribute significantly to the observed capacity in layered oxides such as $LiNi_{0.6}Mn_{0.2}Co_{0.2}O_2$ and Li_2MnO_3 cycled to high voltages.[23, 52] Sulfides oxidize at a lower voltage than oxides due to their higher energy frontier orbitals and therefore present an opportunity to study anion redox while avoiding the difficulties of characterizing a system in the presence of multiple side reactions. Recent studies have centered around Li-rich titanium sulfides.[114–116, 118] Notably, Fe substitution into $Li_{1.33}Ti_{0.67}S_2$ yields reversible S oxidation concurrent with Fe oxidation as indicated by various X-ray spectroscopic techniques at the S $L_{2,3}$-edge and K-edge.[118] The original Li-rich sulfide material, Li_2FeS_2, was first synthesized by Sharma *et al.* in 1976.[119] Subsequent studies focused on the electrochemistry[124–126] and characterization of the chemically oxidized species.[122, 124, 127] We recently reported the mechanism of reversible, multielectron redox based on both Fe and S oxidation in the alkali-rich materials Li_2FeS_2 and $LiNaFeS_2$.[163] Fe and S K-edge XAS studies show oxidation of Fe^{2+} to mixed $Fe^{2+/3+}$ from Li_2FeS_2 to $Li_{\approx 1.5}FeS_2$ followed by oxidation of S^{2-} to $(S_2)^{2-}$ from $Li_{\approx 1.5}FeS_2$ to $Li_{\approx 0.5}FeS_2$. The Fe^{2+} oxidation causes the electronic structure of the material to change resulting in increased Fe–S covalency, pushing the S 2p states closer to the Fermi level and enabling anion oxidation.[163] The redox mechanism is electrochemically and spectroscopically reversible, but changes in the local and bulk structure evolve as the material is cycled, leading to capacity fade over time.[163]

Li_2FeS_2 has therefore proven to be an excellent model system to study anion redox. Here, we aim to develop additional structure-property relationships by chemically controlling the anion redox processes in the Li_2FeS_2 family through anion substitution. In previous work on Li-rich oxides, the degree of covalency between the transition metal and chalcogen has been cited as a primary driving force enabling reversible anion redox, and the focus has been on modulating covalency through changing the transition metal to 4d and 5d metals with more diffuse bands.[25–27, 184] Here, we modulate the anionic redox characteristics through systematic chemical substitution of the anion framework in which we substitute S with Se.

By tuning the anion p bands to directly control the degree of covalency, structure-property relationships that enable reversible anion redox are elucidated. Thus, we report the preparation, structural, and electrochemical characterization of Li_2FeSe_2 as well as the anionic solid solution $Li_2FeS_{2-y}Se_y$. Substituting Se for S has a clear, direct influence over the reversible redox processes observed upon charge and discharge. Fe and Se K-edge XAS show an increase in covalency upon anionic substitution and reversible Se anion redox. The results herein provide direct evidence of tunable anion redox in a Li-rich cathode material, supporting the design of materials for next-generation energy storage technologies.

6.2 Results and Discussion

Structural Characterization

Li_2FeSe_2 was prepared using traditional solid state methods from Li_2Se, $FeSe_2$, and Fe. The structure and XRD pattern with quantitative Rietveld refinement are shown in Figure 6.1. Ying *et al.* previously reported the existence of Li_2FeSe_2 but without any quantitative structural characterization.[185] Li_2FeSe_2 is isostructural to the Li-rich sulfide Li_2FeS_2. The material crystallizes with a trigonal unit cell in the space group $P\bar{3}m1$. The structure consists of a close packed lattice of selenide anions coordinating alternating layers of octahedral and tetrahedral cations (Figure 6.1a). The octahedral sites are fully occupied by Li, whereas the occupancy of the tetrahedral site is 50% Li and 50% Fe.

Since Li_2FeSe_2 is isostructural to Li_2FeS_2, we sought to form a solid solution between the two chalcogenides. Li_2FeS_2 and Li_2FeSe_2 were mixed in stoichiometric quantities and annealed in evacuated carbon coated silica ampoules to form the mixed anion members of the solid solution, $Li_2FeS_{2-y}Se_y$ ($0 \leq y \leq 2$). XRD patterns with quantitative Rietveld refinements of representative materials are shown in Figure 6.2a. Strong reflections corresponding to the (00l) planes are observed across the solid solution as evidence of preferred orientation stemming from preferred crystallite growth along the layers. The preferred orientiation results in differences in relative intensity of the other reflections, for example the reflection in Li_2FeS_2 at 43.5 2θ shifts to lower 2θ as the larger Se anion is substituted for S, and decreases in intensity relative to the (002) reflection. However, the reflection does not completely disappear, supporting that the entire solid solution forms with the no change in space group or symmetry. The refined lattice parameters for all materials are shown in Figure 6.2b. The entire stoichiometric range exhibits Vegard's Law behavior, where the lattice parameters increase linearly as Se is substituted onto the anion site for

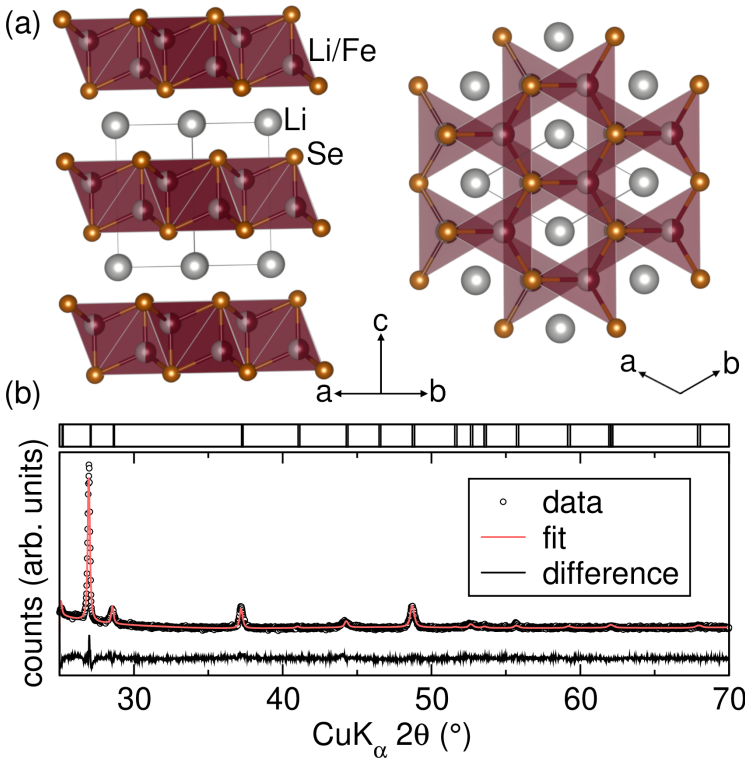

Figure 6.1: (a) The structure of Li_2FeSe_2 consists of a close packed arrangement of Se anions coordinating alternating layers of octahedral Li and tetrahedral mixed Li and Fe. (b) XRD of Li_2FeSe_2 and quantitative fit using the Rietveld method, indicating the formation of a pure crystalline phase.

Table 6.1: Rietveld refinement parameters of synthesized materials across the $Li_2FeS_{2-y}Se_y$ solid solution. Analysis performed by A. J. Martinolich.

y	*a* (Å)	c (Å)	Li_a position (*x*, *y*, *z*)	Li_b/Fe position (*x*, *y*, *z*)	S/Se position (*x*, *y*, *z*)
0.2	3.917(1)	6.3248(5)	0, 0, 0	1/3, 2/3, 0.337(2)	2/3, 1/3, 0.26(2)
0.6	3.925(2)	6.3949(7)	0, 0, 0	1/3, 2/3, 0.35(8)	2/3, 1/3, 0.255(4)
1	3.997(2)	6.4625(5)	0, 0, 0	1/3, 2/3, 0.408(6)	2/3, 1/3, 0.224(1)
1.4	4.018(2)	6.5205(5)	0, 0, 0	1/3, 2/3, 0.407(3)	2/3, 1/3, 0.234(2)
1.8	4.056(4)	6.5762(5)	0, 0, 0	1/3, 2/3, 0.409(1)	2/3, 1/3, 0.227(5)
2	4.058(2)	6.5892(5)	0, 0, 0	1/3, 2/3, 0.380(2)	2/3, 1/3, 0.255(1)

S, indicating the formation of a solid solution. More detailed information from the Rietveld refinements is shown in Table 6.1.

Electrochemical Characterization

The Li-rich solid solution was studied using CV and galvanostatic cycling to probe the influence of anion substitution on the electrochemistry and charge storage mechanisms. The CVs of the solid solutions are shown in Figure 6.3. The sulfide end

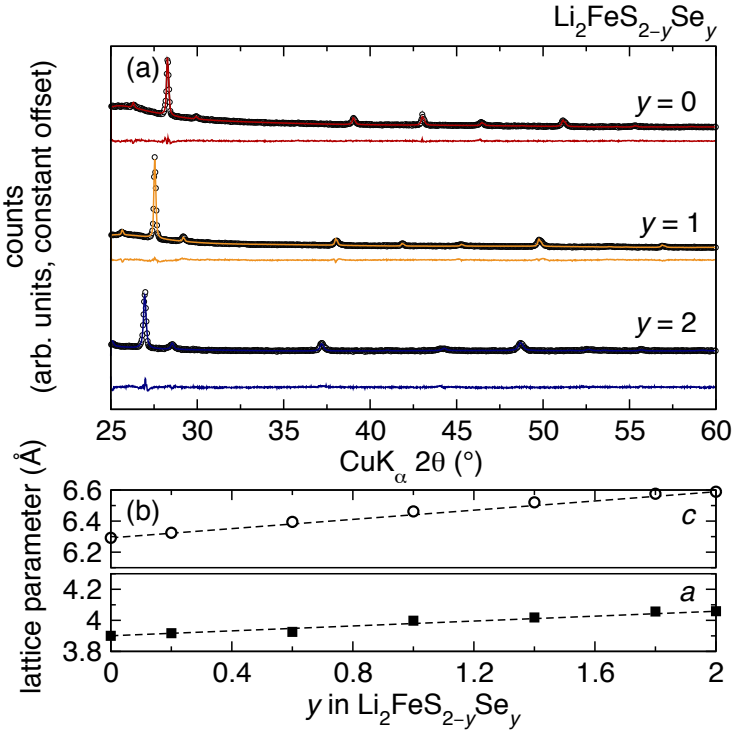

Figure 6.2: (a) Selected XRD patterns and quantitative Rietveld refinements to a single phase of the solid solution $Li_2FeS_{2-y}Se_y$. The reflections shift to lower 2θ upon selenium substitution, indicating an increase in the lattice parameters. (b) The refined lattice parameters C and *a* plotted as a function of anion substitution show a linear trend with stoichiometry following Vegard's Law which indicates formation of the solid solution across all stoichiometries. The error in the refined lattice parameters are smaller than the plotted symbols, 0.003 Å or less. Dashed lines serve as a guide to the eye.

member Li_2FeS_2 exhibits multiple anodic waves on the first cycle between 2.2 V and and 2.85 V, the most prominent of which is centered at 2.72 V vs. Li/Li^+. All further potentials are referenced to a Li foil counter/reference electrode unless otherwise noted. Upon the reverse sweep, a single cathodic wave is observed at 1.95 V. The second cycle yields less defined waves before the major anodic wave, which shifts to slightly higher potentials, while the single cathodic wave shifts to slightly lower potentials.

The redox properties change significantly upon substitution of Se for S in $Li_2FeS_{2-y}Se_y$. While multiple small anodic waves are observed across all values of *y*, the major anodic wave shifts to lower potentials as the Se content increases suggesting that the anion contributes to the oxidation mechanism. In fact, the major anodic wave in Li_2FeS_2 is correlated to anion oxidation of S^{2-} to $(S_2)^{2-}$.[163] Because the potential

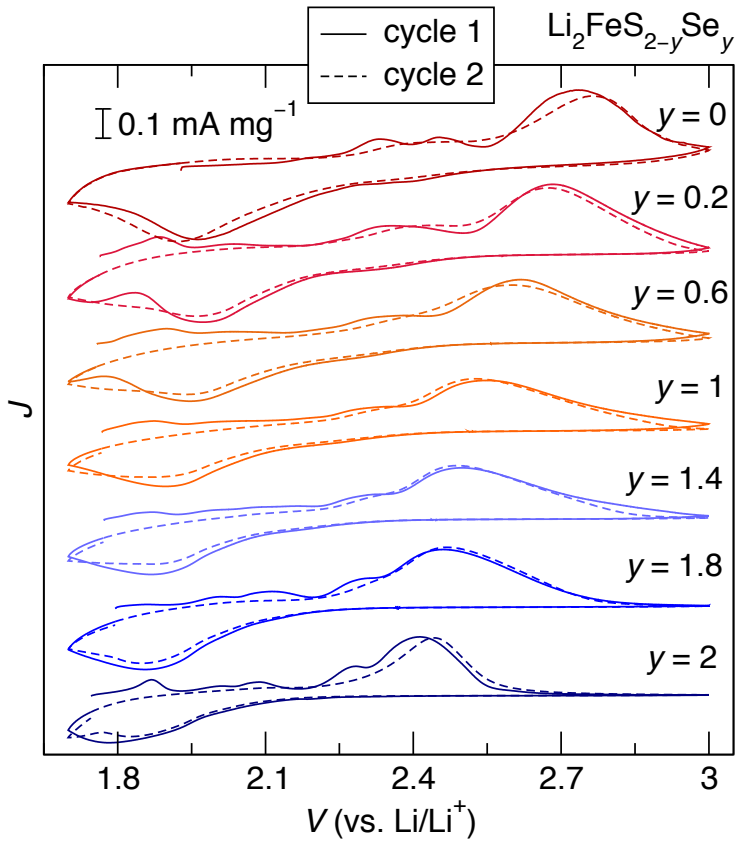

Figure 6.3: Cyclic voltammetry of $Li_2FeS_{2-y}Se_y$ collected at a scan rate of 0.1 mV/s. The predominant oxidation wave shifts by approximately 300 meV upon full substitution of Se for S, indicating the influence of anion substitution on the redox properties of the material.

shifts as a function of Se content, we suggest that as Se is substituted on the S site, contribution of the Se 4p orbital to the density of states raises the energy of the frontier states and thus lowers the potential of anion oxidation. We note that the entire wave shifts and discrete waves due to S^{2-} oxidation and Se^{2-} oxidation are not observed in the mixed anion materials, suggesting complete mixing of the anions in the lattice. Interestingly, the cathodic sweep is very similar across all stoichiometries of the solid solution with only a slight shift to more negative potentials at $y>1$. The small features in the positive sweep are less defined in the second cycle, while the large anodic wave is observed at approximately the same potential, indicating that the reversibility of the electrochemistry is maintained.

Galvanostatic cycling measurements were performed to understand the influence of the anion substitution on the electrochemical energy storage properties of the material. The first galvanostatic charge and discharge profiles of all members of

the solid solution are shown in Figure 6.4. The capacities are normalized to the equivalents of Li that are (de)intercalated from the active material. Greater than one equivalent of Li can be reversibly cycled in the material across the solid solution, indicating multielectron redox.

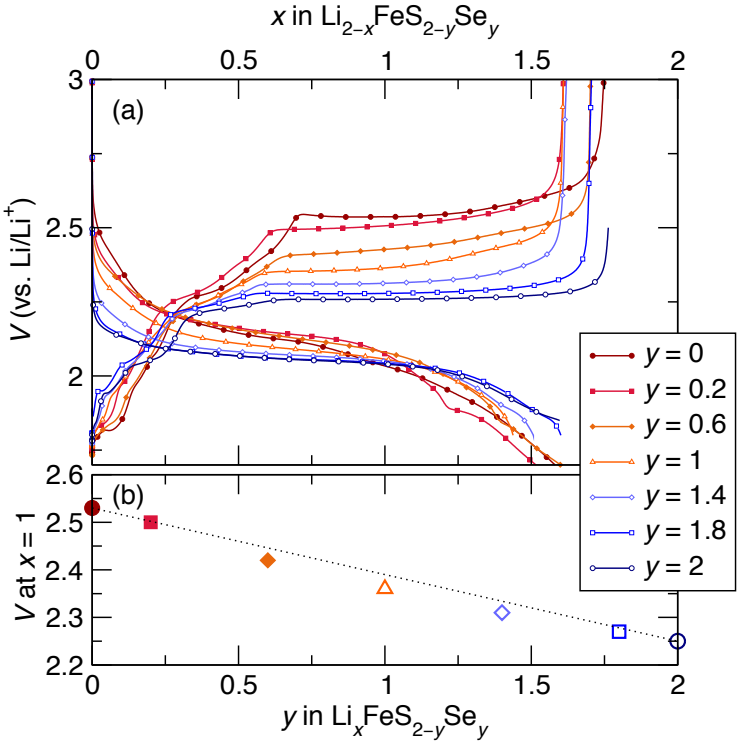

Figure 6.4: (a) The first charge and discharge profiles of $Li_2FeS_{2-y}Se_y$ at a rate of C/10 based on 1 e^- per formula unit. Greater than one equivalent of Li is reversibly stored for all stoichiometries, indicating the presence of multielectron redox across the solid solution. (b) The voltage after the deintercalation of one equivalent of Li plotted versus the anion content, indicating direct correlation between anion content and charge voltage.

The voltage charge curves are significantly affected by the chalcogenide substitution. Similar to the previously reported Li_2FeS_2, the solid solution maintains two distinct regions in the charge curve: a sloping region with multiple inflections followed by a long, flat plateau. Our previous work indicates that the sloping region corresponds to $Fe^{2+/3+}$ redox and the long plateau is related to S^{2-}/S_2^{2-} redox, which is supported by Fe and S K-edge X-ray absorption spectroscopy.[163] At low states of charge ($x \leq 0.5$ in $Li_{2-x}FeS_{2-y}Se_y$), the Se-rich members of the solid solution exhibit a slightly higher voltage than the S-rich members. Beyond $x = 0.5$, the voltage decreases as Se content increases. While the sulfide-rich ($y \leq 1$) materials continue to show sloping charge curves until $x \approx 0.75$, the selenide rich ($y > 1$) materials

exhibit a much flatter charge curve from $x \approx 0.5$ onwards. At higher states of charge, all materials exhibit a flat charge curve.

The plateau at high states of charge consistently shifts to lower voltages as the Se content increases. The voltage dependence on the anion substitution can be visualized by plotting the voltage at a given Li content ($x = 1$) versus Se content (Figure 6.4b). The voltage of the plateau shows a linear dependence with Se content, indicating the direct control over the redox properties afforded through anion substitution on an isostructural lattice. Introduction of Se 4p states at the expense of S 3p states provides a density of redox active, anionic electronic states at higher energy, which are then oxidized at a lower voltage. The constant shift of the plateau indicates that the S and Se states are mixing rather than oxidizing independently. Considering the contribution of sulfide oxidation in this region of the curve for the $y = 0$ end member, the systematic shift with increasing Se content indicates that the Se/S ratio is directly controlling the voltage of anion redox, along with the multielectron capacity exhibited across the solid solution. If the S and the Se were electronically isolated, two separate plateaus would be expected at the voltages of the end members. The systematic shift of the single plateau represents the first time that anion redox has been directly manipulated through anion substitution, rather than indirectly inferred via the substitution of redox-inactive cations to drive redox onto the supporting anions, which is common in the study of anion redox in oxide-based cathode materials.

While the voltage of the charge plateau shows a controllable trend upon anion substitution, the discharge curves are less affected. All materials in the solid solution show a single, partially sloping discharge plateau with high capacity and good Coulombic efficiency. The discharge curves for the S-rich materials ($y \leq 1$) are slightly more sloping, while the Se-rich materials exhibit a flatter plateau. The sloping region of the discharge curves for $y = 0.2$ and $y = 0.6$ are at slightly higher potentials than for Li_2FeS_2. The voltage of the discharge curve then shifts down as the Se content increases. The shifts as Se is substituted for S may be derived from the increased metallic character of the materials, as would be expected for a selenide over a sulfide due to the less localized bands and greater orbital overlap.

The voltage of the charge plateau is dependent on Se content. The Se content, however, could simultaneously affect both the oxidation potential and the electronic conductivity of the material, both of which could shift the voltage of the plateau. Higher conductivity would lead to lower overpotential which could cause

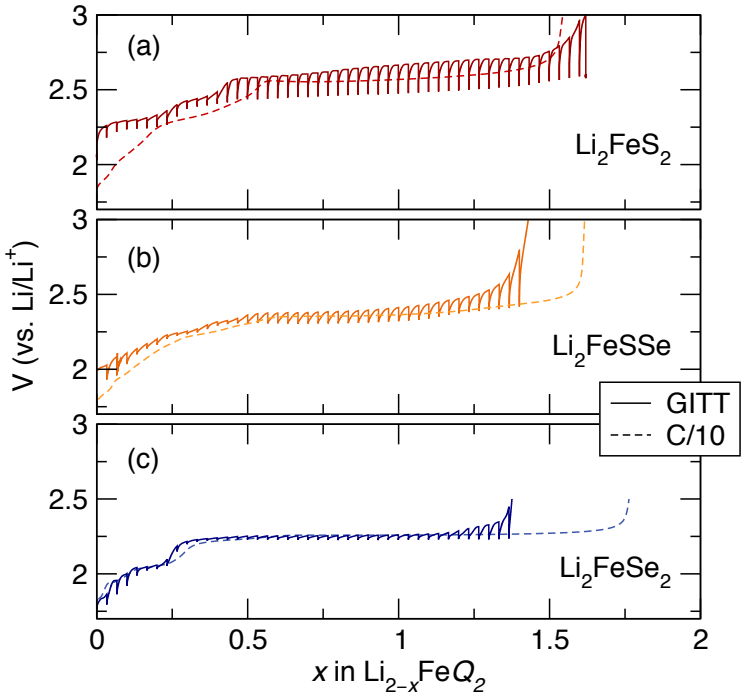

Figure 6.5: GITT curves upon charging (a) Li_2FeS_2 (b) Li_2FeSSe and (c) Li_2FeSe_2. As Se is substituted for S, both the polarization and the equilibrium voltage decreases. The GITT curve of Li_2FeS_2 is adapted adapted from Hansen, C. J.; Zak, J. A.; Martinolich, A. J.; Ko, J.; Bashian, N.; Kaboudvand, F.; Van der Ven, A.; Melot, B.; Nelson Weker, J.; See, K. A. *J. Am. Chem. Soc.* **2020**, *142*, 6737–6749, Copyright 2020 ACS Publications.

the plateau to shift to lower potentials. To determine if increased electronic conductivity causes the plateau shift by reducing polarization, GITT was measured on Li_2FeS_2, Li_2FeSSe, and Li_2FeSe_2. GITT allows us to measure the overpotentials by comparing the differences in the potential upon applied current and that at equilibrium, or very close to it, throughout the charge curve.

The GITT of Li_2FeS_2 along with the C/10 trace are shown in Figure 6.5a. The overpotentials are low in the initial sloping region of the curve, between 100 mV and 200 mV. The overpotentials increases to approx. 250 mV during the charge plateau at higher states of charge, wherein the anion redox occurs. The greater polarization may relate to the necessity for partial structural rearrangement and bond formation between sulfide anions during this process.[163] Substituting Se for S drastically affects the overpotentials and equilibrium potential. The GITT curves for Li_2FeSSe and Li_2FeSe_2 are shown in Figure 6.5b and c, respectively. In the mixed anion material, the overpotential is between 50 mV-100 mV and remains in that range until near the end of the charge curve. In the case of the selenide, the

initial polarization is approx. 50 mV-100 mV, but in contrast to the S-containing materials, the polarization clearly decreases at the onset of the flat charge plateau, with polarization of approximately 30 mV until the highest states of charge are reached. The equilibrium voltage difference between the sulfide and the selenide are clearly present, indicating the direct impact of the anion on the oxidation potential and electronic structure.

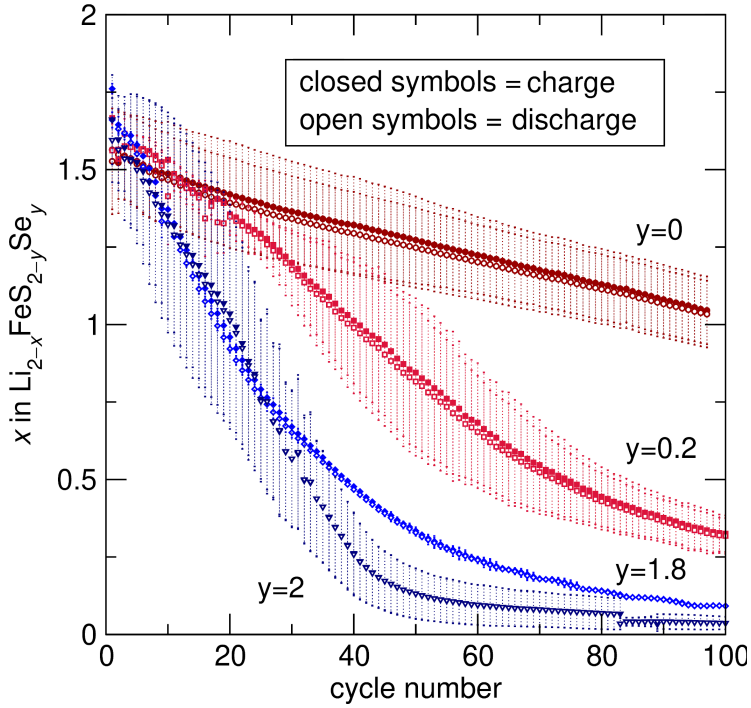

Figure 6.6: Capacity at a C/10 rate based on 1 e^- per formula unit as a function of cycle number for the solid solution $Li_2FeS_{2-y}Se_y$. Substitution of Se for S results in much greater capacity fade, with the selenium end member showing nearly complete loss of capacity after 75 cycles. Error bars represent the standard deviation of three replicate cells. The cycling data for Li_2FeS_2 was adapted from adapted from Hansen, C. J.; Zak, J. A.; Martinolich, A. J.; Ko, J.; Bashian, N.; Kaboudvand, F.; Van der Ven, A.; Melot, B.; Nelson Weker, J.; See, K. A. *J. Am. Chem. Soc.* **2020**, *142*, 6737–6749, Copyright 2020 ACS Publications.

To determine the effect of anion substitution on the capacity retention, four members of the solid solution $Li_2FeS_{2-y}Se_y$ were cycled galvanostatically in a half cell. The average capacities of at least three replicate cells along with the standard deviation represented by error bars are shown in Figure 6.6. While the sulfide exhibits good capacity retention over time,[163] substituting Se for S yields greater capacity fade after extended cycling with more Se-rich materials showing greater capacity fade. $Li_2FeS_{1.8}Se_{0.2}$ shows a similar trend in capacity fade over the first 20 cycles to the S

end member, after which, however, the fade accelerates resulting in an 80% capacity loss over 100 cycles. The Se-rich materials $Li_2FeS_{0.2}Se_{1.8}$ and Li_2FeSe_2 exhibit rapid capacity loss from the beginning of cycling, with 50% loss in capacity after 25 cycles and nearly complete capacity loss after 100 cycles. We hypothesize that the poorer capacity retention of the selenide compared to the sulfide is due to differences in the structural behavior upon charging (see Section 6.2).

Operando XRD

To probe changes to the bulk crystal structure of Li_2FeSe_2 upon electrochemical cycling, *operando* XRD was collected for the first two charge/discharge cycles (Figure 6.7). The material exhibits evidence of preferred orientation, with strong reflections in the (00*l*) direction and attenuated signals from other crystallographic directions. Thus, we focused on changes in the (002) reflection, representative of the expansion and contraction along the C direction, orthogonal to the layers of edge sharing tetrahedra in Li_2FeSe_2 (Figure 6.1).

The charge and discharge curves measured during *operando* XRD are shown along with a contour plot of the diffraction patterns in (Figure 6.7). Prior to beginning the initial charge, the cell was measured at open circuit voltage for one hour. The (002) reflection is observed at a *d* spacing of 3.25 Å and the (101) reflection is observed at 3.095 Å with much lower intensity. Upon charging, the (002) reflection begins to shift from 3.25 Å to lower *d* spacing as Li is deintercalated from Li_2FeSe_2, indicating a contraction of the lattice along the C direction. The (002) reflection shifts by approximately 0.01 Å at the earliest states of charging. A new reflection appears at approx. $Li_{1.85}FeSe_2$ with a *d* spacing of 3.16 Å, indicating the formation of a second phase. The reflection of the second phase shifts rapidly to smaller *d* spacing as the material is charged before remaining approximately constant and growing in intensity at 3.095 Å, which overwhelms the intensity from the (101) reflection of the parent phase. After the formation and shift of the second phase, the behavior appears classically two-phase, wherein the signal from the parent Li_2FeSe_2 at 3.24 Å decreases in intensity as the intensity of the new reflection at 3.095 Å increases and reaches maximum intensity at the end of charge. At the end of charge, the reflection from the parent phase shifts rapidly to near the position of the second phase at approx. 3.10 Å. The two-phase behavior is supported by the flat plateau at 2.25 V in the galvanostatic charge profile after the sloping region.

The structural changes to Li_2FeSe_2 are partially reversible upon discharge. The

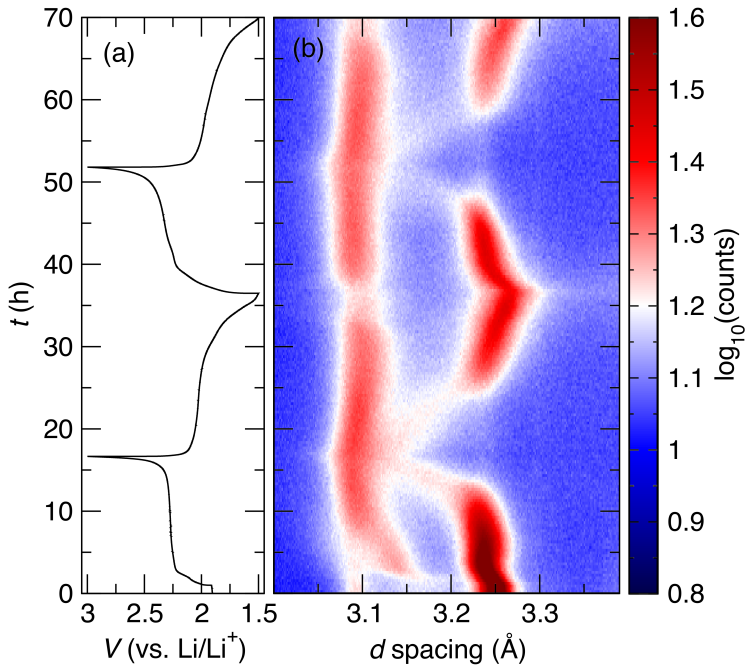

Figure 6.7: (a) Galvanostatic charge and discharge curves of the first two cycles of Li_2FeSe_2 during *operando* XRD and (b) the corresponding diffraction patterns focused on the strong (002) reflection at 3.25 Å. The material exhibits irreversible structural changes that are retained during the second cycle as evidenced by the maintenance of the reflection centered around 3.1 Å corresponding to the new phase.

reflection at 3.10 Å from the parent phase rapidly shifts back to 3.23 Å at the earliest stages of lithiation, then continues to shift slowly and increase in intensity as discharge continues. The reflection is approximately 3.25 Å at the end of discharge, indicating the reformation of the parent Li_2FeSe_2 phase. The intensity of the reflection at 3.10 Å decreases as the discharge continues, indicating conversion of the second phase formed during oxidation. However, at the end of discharge, the peak related to the second phase at 3.095 Å is still present, indicating incomplete reversibility of the structural transformations that take place upon charge. The incomplete lithiation of the new phase upon discharge is consistent with the Coulombic efficiency of the first cycle of approximately 90% (Figure 6.4a). The retention of the second, oxidized phase even at the end of the first discharge may lead to the capacity fade observed over many cycles (Figure 6.6). Over multiple cycles it is likely that more of the second phase becomes irreversibly oxidized, leading to capacity fade.

The second charge and discharge perform largely the same as the first cycle. One important distinction is that since the oxidized phase with the smaller *d* spacing

remains present in the electrode after the first discharge, there is no observation of its nucleation or initial contraction. Instead, the reduced, parent phase slightly shifts to smaller *d* spacings and decreases in intensity while the oxidized phase remains unchanged. At the end of the second charge, the reduced phase again rapidly shifts to 3.10 Å, mirroring the behavior of the first charge. The second discharge is comparable to the first, wherein the oxidized phase loses intensity at the expense of the reduced parent phase, with no major changes in the *d* spacings of either phase after the reduced phase is reformed. The clear, two-phase charge/discharge mechanism of Li_2FeSe_2 indicates the formation of a distinct second phase, which we hypothesize contains oxidized species of both Fe and Se enabled through the highly covalent Fe–Se interactions in the material.

Electrochemical Impedance Spectroscopy

The formation and retention of the second phase after the first charge of Li_2FeSe_2 is also reflected in intermittent electrochemical impedance spectroscopy (EIS) measurements used to further probe the nature of the second phase formed during charge and compare the data with that obtained from the more reversible Li_2FeS_2 material. The structural behavior of Li_2FeSe_2 upon electrochemical cycling differs from that of Li_2FeS_2. While both materials exhibit two-phase behavior at high states of charge, the behavior of the parent phase at the end of the charge cycles represents a rapid 5% contraction. Comparatively, the sulfide contracts by less than 3%[163] over the entire course of charging. The greater and more rapid structural changes that occur upon cycling between the parent and deintercalated phases of Li_2FeSe_2 may lead to the rapid capacity fade observed over time (Figure 6.6). Selected Nyquist plots and associated charge transfer resistances, R_{ct}, during charge and discharge of both the sulfide and the selenide are shown in Figure 6.8. The charge transfer resistance of both Li_2FeS_2 and Li_2FeSe_2 increase as the materials are oxidized. Upon discharging, however, the materials exhibit different behavior. The charge transfer resistance of the sulfide decreases close to the initial value of the as-prepared material, which is supported by the reversible electrochemistry on the second charge and minimal structural changes apart from increased disorder with cycling.[163] However, the charge transfer resistance of the selenide does not decrease upon discharge. We hypothesize that the impedance remains high due to the presence of the second phase after discharge observed in the *operando* XRD that forms during charge, and the irreversibility of this phase causes capacity fade over time.

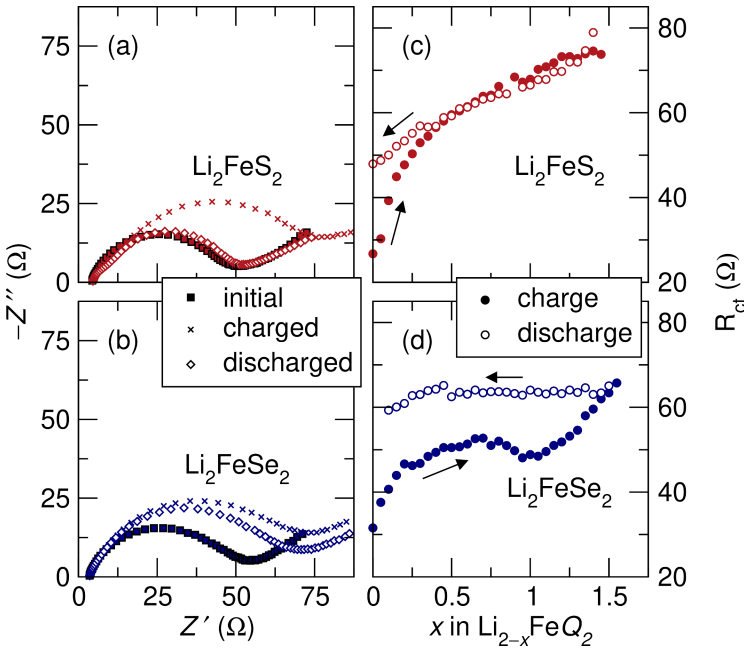

Figure 6.8: Selected Nyquist plots obtained by intermittent EIS measurements during charge and discharge of (a) Li_2FeS_2 and (b) Li_2FeSe_2. The Nyquist plots are fit with a modified Randles circuit consisted of a resistor (R_s) in series with an RQ circuit comprised of a constant phase element (Q_1) in parallel with a resistor (R_{ct}) and constant phase element (Q_2) in series. The R_{ct} values obtained from the fits plotted as a function of discharge and charge for (c) Li_2FeS_2 and (d) Li_2FeSe_2. While the charge transfer resistance of both materials increases upon charging, only the resistance of the sulfide decreases again upon discharge, suggesting formation of a new high-impedance phase in Li_2FeSe_2.

X-ray Absorption Spectroscopy

We have shown in Li_2FeS_2 that delithiation is compensated by both Fe and S oxidation[163]. The similarities in the electrochemistry when substituting Se for S suggests anion redox is occurring in the Se-containing phases, as well. However, electrochemistry is not a direct probe of anion redox and, as such, we sought spectroscopic evidence to directly probe the behavior of both Fe and Se in Li_2FeSe_2 and a mixed anion phase. We executed Fe and Se K-edge XAS measurements of Li_2FeSe_2 and Li_2FeSSe at various states of charge to monitor the oxidation state of both the cationic and anionic species upon electrochemical cycling. Samples were charged and discharged to various inflection points in the galvanostatic profile and measured *ex situ* to ascertain what redox centers contribute to each feature observed. Li_2FeSe_2 was cycled to the following conditions: as-prepared (Li_2FeSe_2), charged to 2.2 V ($Li_{1.65}FeSe_2$), charged to 2.25 V ($Li_{1.4}FeSe_2$), fully charged to 2.5 V ($Li_{0.25}FeSe_2$), and fully charged then fully discharged to 1.85 V ($Li_{1.85}FeSe_2$). The Fe K-edge

spectra of Li_2FeSe_2 at the indicated states of charge are shown in Figure 6.9a. The pristine material exhibits the following features: two pre-edge features denoted collectively as *a* at approximately 7111 and 7113 eV, the rising edge denoted as *b* centered at 7116.9 eV, the K-edge denoted as C, and the near-edge scattering region denoted as *d*. The rising edge position is in agreement with reports of Fe^{2+} in a tetrahedral Se environment in Mn- and Cu-substituted β-FeSe ($M_xFe_{1-x}Se_\delta$).[186] Compared to Li_2FeS_2,[163] the rising edge *b* is at slightly lower energy (7116.9 eV compared to 7117.3 eV), which indicates a more covalent interaction between the Fe^{2+} centers and the Se^{2-} anions reflecting the predicable higher degree of overlap of the Se 2p band with the Fe d bands. The higher degree of covalency is further supported by the lower intensity of the pre-edge features *a* relative to that in the sulfide analog. The Fe K pre-edge corresponds to a Fe 1s to 3d transition and the character of this transition is dictated largely by the crystal field with more covalent interactions indicating a stronger crystal field.[40] Due to the larger radius of Se^{2-} compared to S^{2-},[187] the $FeSe_4$ tetrahedra in Li_2FeSe_2 are more distorted in the c direction than the FeS_4 tetrahedra in Li_2FeS_2. The greater distortion contributes to the lower pre-edge intensity observed in Li_2FeSe_2. We observe splitting of the pre-edge feature as two distinct pre-edge features suggesting multiple available excited states, consistent with a high spin configuration of tetrahedral Fe^{2+} that results in holes in orbitals of nominal e_g and t_2 symmetry. The multiplet splitting is distinguishable in Li_2FeSe_2 and not in Li_2FeS_2 due to the wider crystal field splitting caused by the more distorted tetrahedral geometry in Li_2FeSe_2. Insights into local structure can also be gleaned from the near-edge features and oscillations above the edge, which are due to scattering events with near neighbors.

Now we consider how the Fe K-edge changes upon oxidation. The oxidation state of Fe is indicated by the position of the rising edge *b*. The rising edge position is easily observed as the peak in the first derivative of the K-edge spectrum shown in Figure 6.9b and c. The rising edge position shifts continuously to higher energy at each state of charge indicating continuous oxidation. When charged to 2.2 V, the rising edge shifts approx. 0.4 eV from 7116.9 eV indicating partial oxidation of Fe^{2+} to Fe^{3+}. After further charging to 2.25 V, the position of the rising edge shifts only slightly (approx. 0.1 eV), however, minimal charge is passed between 2.2 V and 2.25 V (approx. 0.18 e^- per formula unit) so a significant edge shift is not expected. Upon fully charging to 2.5 V, the rising edge shifts another approx. 0.3 eV for a total shift of 0.8 eV, supporting further oxidation of some Fe^{2+} to Fe^{3+}. The continuous shift of the rising edge indicates ongoing contributions to the redox

from mixed bands with Fe states, a phenomenon not observed in Li_2FeS_2 where the Fe rising edge only shifts at early states of charge before the long plateau at 2.5 V.[163] The Fe–Se interaction is more covalent than the Fe–S interaction and therefore Fe contributes to redox in a more continuous, less discrete manner in Li_2FeSe_2 than it does in Li_2FeS_2. Upon discharge, the rising edge shifts back to 7116.9 eV (Figure 6.9c) indicating reversible redox from highly covalent bands in Li_2FeSe_2.

The Fe K-edge spectra of Li_2FeSe_2 at different charge states also show marked differences in the pre-edge and near-edge regions. Upon charging to 2.2 V (i.e. after the sloping region), the pre-edge features *a* shift to slightly higher energy indicating oxidation of Fe^{2+}. The pre-edge features increases in intensity upon oxidation which can indicate an increase in covalency due to more Se p character mixing with the Fe d states and/or a more symmetric tetrahedral environment due to decreased centrosymmetry leading to a dipole-partially allowed transition by d-p mixing. It is likely that both are contributing in the case of Li_2FeSe_2 as an increase in Fe–Se covalency is expected upon Fe oxidation[163], and the more intense scattering feature *d* centered around 7138 eV supports a more symmetric tetrahedral environment around Fe, i.e. the four Fe–Se distances are approximately equal leading to less destructive interference among scattered photoelectrons. The decrease in the K-edge intensity, C, also indicates a higher degree of covalency due to the Se character in the Fe p states increasing, thereby lessening the number of available 1s to 4p transitions. After further charging to 2.25 V, after the first small plateau of the charge curve, the pre-edge and near-edge do not change significantly, suggesting that the additional short plateau does not correspond to significant changes to the local environment around Fe. Interestingly, at the end of charge (2.5 V), the pre-edge and near-edge features decrease in intensity, suggesting a decrease in local tetrahedral symmetry around the Fe center at high states of charge. Upon discharge, the pre-edge and near-edge features remains slightly higher in intensity and the edge intensity is lower than in the pristine material, indicating some irreversible changes in local symmetry at the Fe centers. Additionally, the maintained pre-edge intensity throughout cycling demonstrates that Fe remains in a tetrahedral coordination environment. If the Fe migrated to an octahedral site between the tetrahedral layers, for example, the pre-edge intensity would decrease due to the resulting centrosymmetry and lack of d-p hybridization.

To summarize, Fe is contributing to the redox throughout the charging process,

which is different than what we observed in Li_2FeS_2 where the Fe edge only shifts prior to the plateau at 2.5 V associated with anion redox.[163] The continuous shift in Li_2FeSe_2 is due to the more covalent Fe–Se interactions that allow oxidation to occur from bands with Fe character throughout the charge curve. The irreversible changes observed in the Fe K-edge data after discharge in Li_2FeSe_2 do not affect the Coulombic efficiency, which remains relatively high averaging around 99.2% over 100 cycles, suggesting that, while it may play a role in long-term capacity fade, local structural changes do not preclude near complete relithiation.

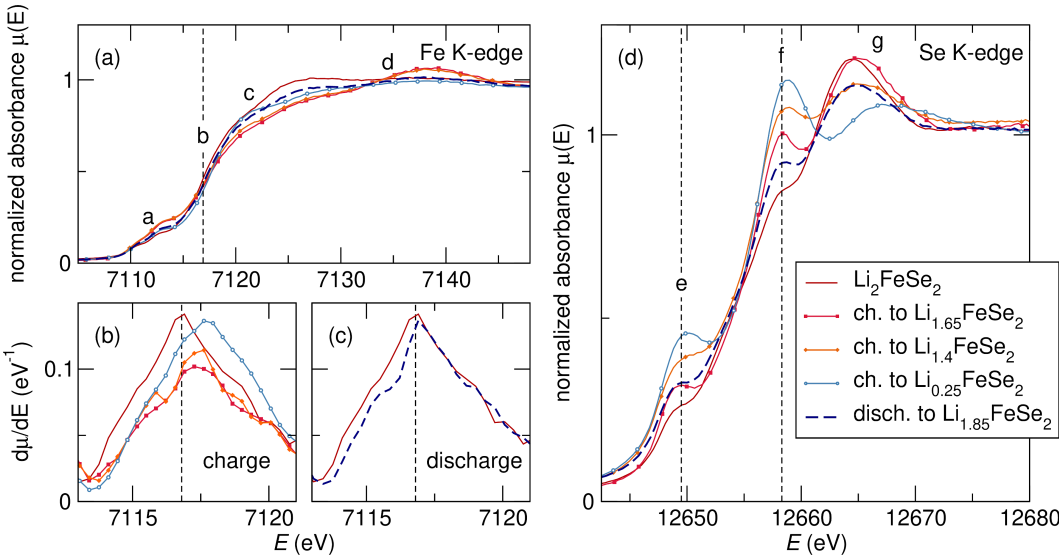

Figure 6.9: *(a) Ex situ* Fe K-edge XANES of Li_2FeSe_2 at various states of charge: Li_2FeSe_2 (as-prepared), $Li_{1.65}FeSe_2$ (charged to 2.2 V), $Li_{1.4}FeSe_2$ (charged to 2.25 V), $Li_{0.25}FeSe_2$ (charged to 2.5 V), and $Li_{1.85}FeSe_2$ (fully charged then discharged to 1.85 V). The first derivative of the Fe rising K-edge upon (b) oxidation and (c) reduction compared to the pristine material allows for clear observation of the rising edge position. In the Fe K-edge spectra, the pre-edge features at approx. 7111 and 7113 eV are labeled as *a*, the rising edge is marked by a dashed line at 7116.9 eV and labeled as *b*. The K-edge is labeled as C, and the near-edge scattering region is labeled as *d*. (d) *Ex situ* Se K-edge XANES of Li_2FeSe_2 at various states of charge. In the Se K-edge spectra, the pre-edge feature is labeled as *e*, the edge feature as *f*, and the near-edge scattering feature as *g*.

Although the Fe K-edge shifts continuously throughout the charge, it is unlikely that the multielectron oxidation is sustained completely by the Fe since that would implicate some Fe^{4+}. Fe^{4+} is unlikely as nearly all known Fe^{4+} species utilize biomimetic (i.e. oxo, nitrido, and imido) and/or macrocycling ligand frameworks to stabilize the high-valent Fe.[188] There are no known reports of Fe^{4+} in a S or Se coordination sphere. We therefore hypothesize that Se redox contributes to the

charge storage mechanism, similar to the S redox observed in Li_2FeS_2.[163] To probe the anionic contributions to the multielectron redox properties of Li_2FeSe_2, Se K-edge XAS spectra were collected at the same states of charge and are shown in Figure 6.9d. The pristine material exhibits several features: the pre-edge feature labeled as *e* ascribed to Se 1s to 3d transitions (approx. 12649.5 eV), the edge feature labeled as *f* ascribed to Se 1s to 4p transitions (rising edge centered at approx. 12654 eV), and the near-edge features labeled *g* ascribed to scattering events around Se.[189] Here, the rising edge is difficult to define due to the close proximity of the pre-edge, edge, and scattering features. As such, changes in the peaks themselves will be analyzed preferentially. Specifically, variation to the intensity and position of the edge peak indicate changes in covalency and oxidation state as the bands with Se 4p character are oxidized and reduced.

Immediately upon charging, both the pre-edge and edge features increase in intensity throughout the entire oxidation process, indicating a steady increase in Fe–Se covalency as more Se p character mixes with the Fe d states. An increase in the edge intensity also indicates Se oxidation due to the number of available 1s to 4p transitions increasing as the population of the valence 4p states decreases. Both features also shift to higher energy (approx. 0.5 eV) throughout charging, suggesting oxidation of Se. An analogous shift in the edge position and increase in the edge intensity has been observed in Se K-edge data comparing Se (Se^0), $FeSe_2$ (Se_2^{2-}), and FeSe (Se^{2-}).[190] The observed behavior in Li_2FeSe_2 deviates from that in Li_2FeS_2 in which the cationic and anionic redox is more decoupled from the cationic contributions; that is, the sloping region early in the galvanostatic charge profile is primarily Fe^{2+} oxidation and the long plateau at 2.5 V is primarily sulfide to persulfide oxidation.[163] Here, Se is contributing more directly to the redox throughout charging due to the Fe–Se interaction being significantly more covalent than the Fe–S interaction in Li_2FeS_2.

While the Fe K-edge spectra of Li_2FeSe_2 charged to 2.2 V and 2.25 V look nearly identical apart from a very small edge shift, the Fe and Se K-edge spectra together provide clear evidence of both cation and anion redox. The Se K-edge exhibits clear increases in both the pre-edge and edge intensity in addition to a shift to higher energy of both features. The concomitant shift in both the Fe and Se K-edge spectra support highly covalent Fe–Se interactions in Li_2FeSe_2, which is consistent with the increased mixing of the Fe d and Se p states. The near-edge scattering feature at 12665 eV in the pristine structure does not change significantly at 2.2 V, but loses

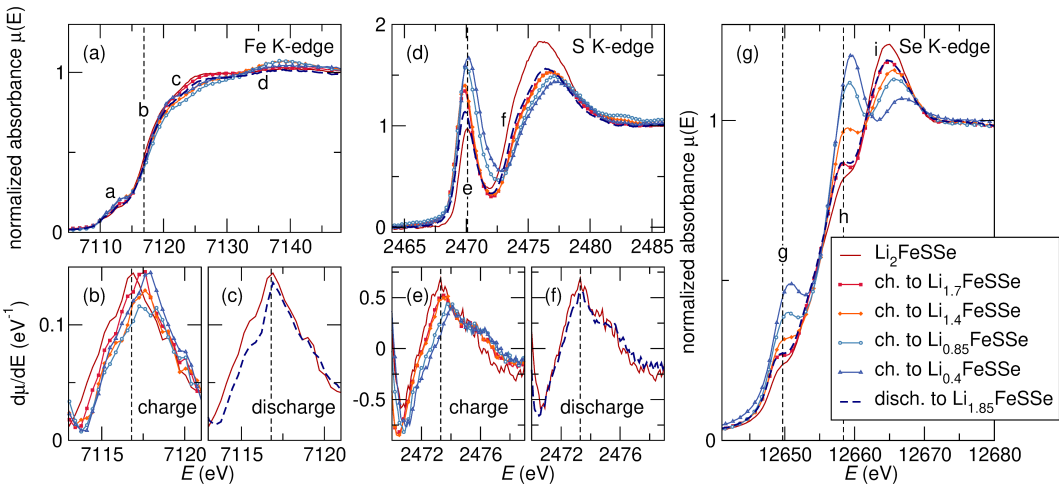

Figure 6.10: (a) *Ex situ* Fe K-edge XANES of Li_2FeSSe at various states of charge : Li_2FeSSe (as-prepared), $Li_{1.7}FeSSe$ (charged to 2.2 V), $Li_{1.4}FeSSe$ (charged to 2.34 V), $Li_{0.85}FeSSe$ (charged to 2.38 V), $Li_{0.4}FeSSe$ (charged to 3 V), and $Li_{1.85}FeSSe$ (fully charged then discharged to 1.8 V). The first derivative of the Fe rising K-edge upon (b) oxidation and (c) reduction compared to the pristine material allows for clear observation of the rising edge position. In the Fe K-edge spectra, the pre-edge features at approx. 7111 and 7113 eV are labeled as *a*, the rising edge is marked by a dashed line at 7117 eV and labeled as *b*. The K-edge is labeled as C, and the near-edge scattering region is labeled as *d*. (d) *Ex situ* S K-edge XANES of Li_2FeSSe at various states of charge. The first derivative of the rising S K-edge upon (e) oxidation and (f) reduction compared to the pristine material shows clear shifts in the edge position. In the S K-edge spectra, the pre-edge feature is labeled as *e* and the rising edge feature as *f*. (g) *Ex situ* Se K-edge XANES of Li_2FeSSe at various states of charge. In the Se K-edge spectra, the pre-edge feature is labeled as *g*, the edge feature *h*, and the near-edge scattering feature *i*.

intensity at 2.25 V, suggesting increased disorder around Se. Then, at 2.5 V, the scattering feature loses intensity further and shifts to higher energy, which indicates significant changes to the local structure around Se. Upon discharge, the Se K-edge spectrum shifts back to resemble the material charged to 2.2 V rather than the pristine material. The near-edge scattering feature also returns to the same energy as the pristine sample, but the intensity is not recovered. In fact, the scattering feature closely resembles that of the 2.25 V sample, but the edge peak intensity is almost as low as the pristine sample, which means the electronic structure of Se is nearly recovered but the local structure is not. Such behavior supports partial reversibility of anionic redox but some irreversible structural changes in the material. The partial irreversibility is consistent with the Fe K-edge data, together indicating a change in the local structure upon electrochemical cycling.

To understand the effect of chalcogen substitution on the charge storage mechanism, Fe, S, and Se K-edge XAS was collected on Li_2FeSSe at various states of charge. The Fe K-edge data is shown in Figure 6.10a-c. Li_2FeSSe was cycled to the following conditions: (1) as-prepared (Li_2FeSSe), (2) charged to 2.2 V ($Li_{1.7}FeSSe$), (3) charged to 2.34 V ($Li_{1.4}FeSSe$), (4) charged to 2.38 V ($Li_{0.85}FeSSe$), fully charged to 3 V ($Li_{0.4}FeSSe$), and (5) fully charged then fully discharged to 1.8 V ($Li_{1.85}FeSSe$). The characteristics of the Fe edge are comparable to those observed in Li_2FeSe_2. In the pristine material, a small pre-edge feature, *a*, is observed before the edge, *b*, centered at 7117.0 eV (Figure 6.10a). The edge shift is again evaluated by plotting the first derivative of the spectrum and it shifts to 7118.0 eV as the material is charged, indicating oxidation of the Fe (Figure 6.10b). The intensity of the pre-edge feature, *a*, increases as the material is charged, suggesting an increase in Fe–*Q* (*Q* = S, Se) covalency and/or an increase in symmetry at the tetrahedrally coordinated Fe. At the most charged state, the Fe pre-edge remains at its highest intensity, which is in contrast to the Li_2FeSe_2, and suggests that the mixed anions in the material aid in stabilizing the local coordination at high states of charge. Upon discharge, the Fe edge shifts back to 7117.0 eV and the pre-edge intensity decreases, indicating reversibility in the Fe-based charge storage in Li_2FeSSe. Li_2FeSSe shows greater spectroscopic reversibility and also greater capacity retention in the cycling data.

The anion-based redox in Li_2FeSSe is examined at various states of charge using S and Se K-edge XAS (Figure 6.10d-g). The S K-edge XANES spectra exhibit a sharp, intense pre-edge feature, *e*, and a K-edge feature, *f*, similar to that observed in Li_2FeS_2.[163] The pre-edge is related to a 1s to 3p transition in S that has a significant component of Fe 3d antibonding character.[191] As such, the pre-edge feature provides a handle by which to ascertain the degree of Fe–S covalency in the system. It is therefore clear from the continuously increasing pre-edge intensity that the Fe–S covalency is increasing with oxidation, suggesting a continuous rehybridization (i.e. mixing of cation and anion states) of the band structure during charging. The pre-edge position shifts slightly during cycling, which is related to changes in the local crystal field. It is useful at this point to note the features observed in the S K-edge spectra of Li_2FeS_2 during cycling. Upon oxidation of Li_2FeS_2, a new pre-edge feature appears at higher energy associated with the formation of persulfide S–S dimers,[163] spectroscopically similar to pyrite FeS_2.[192, 193] The pre-edge feature appears in addition to the pre-edge associated with reduced sulfide (the formal oxidation state of S in oxidized Li_2FeS_2 can be thought of as mixed persulfide, S_2^{2-}, and sulfide, S^{2-}), suggesting that the new pre-edge feature arises

due to electronically isolated persulfide states. Interestingly, we do not observe that new pre-edge feature upon oxidation of Li_2FeSSe even at full charge. In FeS_2, the transition has been described previously as an excitation of core 1s electrons into bands with mixed e_g (Fe) and antibonding σ^* (S) character.[193] We suggest that the lack of a new pre-edge feature in Li_2FeSSe is due to the higher degree of covalency in Li_2FeSSe compared to Li_2FeS_2, i.e. the cation and anion bands are more mixed near the Fermi level and therefore oxidation is not occurring to the same degree from isolated persulfide-related bands. Importantly, the rising edge, *f*, continuously shifts to higher energy upon charging, which indicates ongoing S oxidation. The shift is shown clearly in the first derivative plot in Figure 6.10e. The continuous shifting of the edge is contrary to that observed in Li_2FeS_2 in which the edge shifts only after the 2.5 V plateau.[163] The continuous shift in Li_2FeSSe again suggests a higher degree of covalency upon substituting Se onto the S site. Upon discharging (i.e. relithiating) Li_2FeSSe, the rising edge shifts to lower energy, indicating reduction of S. However, it does not shift back to the original position, which suggests some irreversible changes. Additionally, the pre-edge feature of the discharged material is more intense than in the as-prepared sample, meaning the level of Fe–S covalency remains greater and Fe remains in a tetrahedral coordination environment. The observation that the discharged material does not completely recover the original structure aligns with the results on Li_2FeSe_2 by *operando* XRD (Figure 6.7) that show the irreversible formation of a new phase.

We next discuss the XANES at the Se K-edge. Compared to the spectrum of the as-prepared Li_2FeSe_2, the Se K-edge in Li_2FeSSe is shifted to higher energy by approximately 0.5 eV, suggesting that the presence of S in the material yields less electron density on the Se, even before oxidation. As such, the Fe–Se interaction is less covalent in the presence of S. The more ionic nature of the Fe–Se bond is supported by the shorter average bond length in Li_2FeSSe when compared to Li_2FeSe_2 (2.45 Å vs. 2.51 Å) as elucidated by the quantitative Rietveld refinement of the XRD data. We note, however, that the bond length from the XRD reflects the average structure and thus includes both the Fe–S and Fe–Se bond lengths as the material has mixed S/Se occupancy on the anion site. Upon charging to 2.2 V, the Se pre-edge and edge features grow in intensity and shift to higher energies, indicating that the electronic structure of Se is changing even at early states of charge. That is, even at early states of charge, the bands close to the Fermi level have significant Fe and Se character allowing for Se oxidation. The shift in the pre-edge and edge features continues as the material is oxidized, with the edge reaching a maximum

of 12656.4 eV at the highest state of charge. Like in Li_2FeSe_2, the pre-edge and edge features more closely resemble the spectrum of the sample charged to 2.2 V than the as-prepared sample, again indicating some irreversible change to the local structure.

The pre-edge and edge features shift by approximately 1 eV in Li_2FeSSe *vs.* 0.5 eV in Li_2FeSe_2, indicating that the presence of S leads to a more oxidized state on the Se anions. To explain the discrepancy, we hypothesize that at a 1:1 ratio of S to Se, it is possible to form S–Se heterodimers in addition to S–S and Se–Se dimers as both S and Se are oxidized. Due to the greater electronegativity of S, the S–Se bond will be polarized as more electron density is localized on S, leading to a nominally more oxidized state on Se (formally $Se^{1-\delta}$).

Raman Spectroscopy

As has been observed in pyrite FeS_2[139, 143, 144] and delithiated Li_2FeS_2[163], the S K-edge has a unique pre-edge feature associated with persulfides allowing for a diagnostic tool to probe persulfide formation. The Se K-edge, however, does not show an analogous pre-edge feature when perselenides are present, for example in the Se K-edge spectrum of marcasite-$FeSe_2$.[190] Therefore, although the Se K-edge data suggests oxidation of Se, it is unclear if oxidation causes Se–Se bond formation. Se–Se dimers, however, exhibit a distinct vibrational mode assigned to Se–Se stretches in the Raman spectrum of $FeSe_2$ at 217 cm^{-1}.[194] Therefore, to probe the formation of Se–Se dimers in Li_2FeSe_2, *in situ* Raman spectroscopy measurements were performed to probe changes to local bonding environments. The Raman spectrum of pristine Li_2FeSe_2 shown in Figure 6.11a shows several sharp vibrational modes at low frequency (255, 187, 125, 91 cm^{-1}). The same modes are visible in the spectrum of the cathode measured at OCV (Figure 6.11b) though with much lower intensity due to signal attenuation through the electrolyte and decreased Li_2FeSe_2 sample due to the composite nature of the cathode. Upon charging galvanostatically (Figure 6.11c), the intensity of Raman scattering increases dramatically across the spectral width. The increase in intensity may be due to slight enhancement by surface plasmons due to the conductive nature of Li_2FeSe_2 and the applied current[195] or the oxidation and removal of a surface layer attenuating signal on the pristine electrode. In addition to the intensity increase, the modes at 255, 187, and 125 cm^{-1} noticeably shift to higher frequency, which indicates stiffening of the modes consistent with oxidation. Importantly, a new mode appears at 219 cm^{-1} and grows in intensity with respect to the other modes as a function

of oxidation. The new mode is assigned to Se–Se stretching based on literature assignments of the modes in $FeSe_2$.[194] The new mode could be due to Se–Se dimers formed in the material itself or new phases that resemble $FeSe_2$. We note that the strongest mode in $FeSe_2$ at approximately 180 cm^{-1} is not observed in the oxidized sample either due to the overlap with intense modes from pristine Li_2FeSe_2 or the dissimilar phase of the oxidized material compared to $FeSe_2$. The new mode at 219 cm^{-1} gains intensity immediately upon charging, supporting the conclusion from Se K-edge XAS that the anions are contributing to the oxidation throughout charging. The mode loses some intensity upon discharging but does not completely disappear at full depth of discharge, suggesting that the formation of Se–Se dimers is not entirely reversible. It is possible that there are Se–Se bonds in the new high-impedance phase that is irreversibly formed during oxidation as indicated by *operando* XRD and EIS measurements. Regardless, the new mode provides evidence for an oxidation mechanism in which Se–Se dimers are formed, which are expected to form due to the spectroscopic evidence of persulfides in Li_2FeS_2 and the inherent chemical similarities in S and Se.

Discussion

The charge storage mechanism of $Li_2Fe\mathit{Q}_2$ is influenced by the identity and substitution of the anion Q. Upon Se substitution for S, the major oxidation and reduction features shift to lower potentials, and the shift is most significant at later states of charge where anion redox contributions are more substantial. The GITT measurements show that the shift in potential is inherent to the electronic structure of the material, and not just a change in kinetic overpotentials, confirming the participation of Se in the redox mechanism. The voltage shifts due to participation of Se bands during oxidation and *in situ* Raman spectroscopy data support the formation of Se–Se dimers, just as S–S dimers form upon oxidation of Li_2FeS_2.[122, 163] The oxidation potential of the solid solution trends with anion substitution, suggesting that oxidation occurs from bands with both Se and S character. The relative contribution of metal oxidation vs. anion oxidation is also affected by anion substitution. Counter to the discrete, sequential oxidation of Fe^{2+} and S^{2-} in the sulfide endmember, Se substitution leads to a more covalent Fe–anion interaction that results in both Fe^{2+} and anion (S^{2-} and Se^{2-}) oxidation throughout the charging profile. We note that the charge states indicated here are simply formal oxidation states to facilitate bookkeeping of the oxidation states and do not represent the actual charge on each atom.

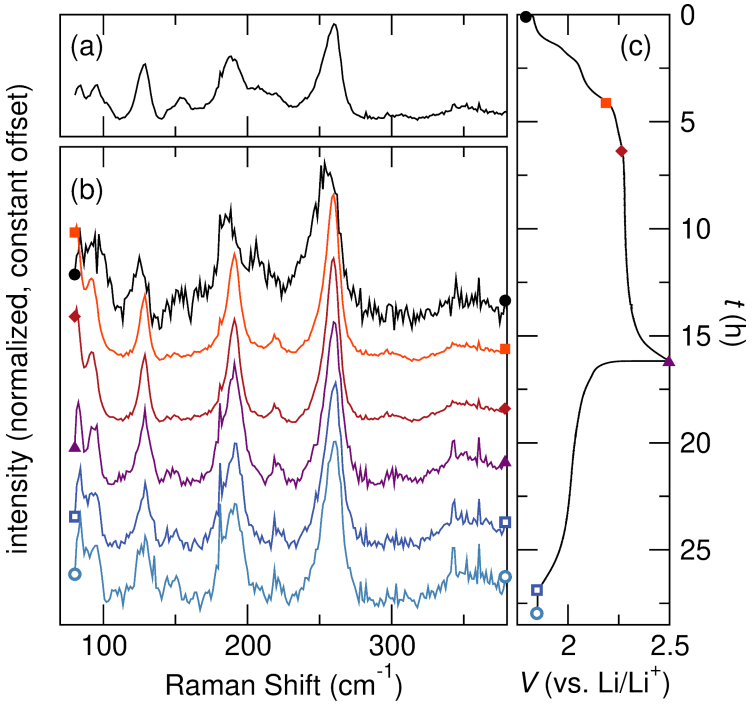

Figure 6.11: (a) *Ex situ* Raman spectroscopy of pristine Li_2FeSe_2. (b) *In situ* Raman spectroscopy of Li_2FeSe_2 and (c) the correlated charge/discharge curve measured at C/10 based on 1 e^-. A new vibrational mode appears at 219 cm^{-1} appears upon charging. The new mode is at the same frequency as Se–Se stretches in $FeSe_2$ supporting the hypothesis that perselenide moieties are formed throughout the oxidation process as Se and Fe are both oxidized to compensate for Li^+ removal.

To discuss the influence of anion substitution on the relative contributions of cation vs. anion redox in these materials, we compare the K-edge shifts for Fe, S, and Se during oxidation and reduction of Li_2FeSe_2 and Li_2FeSSe (Figure 6.12). Both materials show a shift in the edge position of both Fe and Se throughout charge, and Li_2FeSSe shows an analogous shift in the S edge position. At the earliest states of charge, however, the Fe K-edge shifts more than the S and/or Se K-edge in both cases suggesting a greater contribution from Fe-rich bands at lower potentials. The Se edge begins to shift more than the Fe edge as the long plateau is approached in both cases. In the case of Li_2FeSe_2, the Fe and Se K-edges shift by approximately the same amount. The mixed material, however, shows a greater contribution from Se compared to Fe in the last part of the charge curve. The mixed material is less covalent and thus the decreased rehybridization reduces the contribution from the metal center at high states of charge, similar to the decoupled Fe and S oxidation in Li_2FeS_2. The S K-edge does not show the same shift as Se, which may point to the mixed anion states having more Se than S character due to Se states being of

higher energy relative to those of S. The shift in the Se edge could also be affected by the formation of S–Se dimers in which the more electronegative S atom draws charge away from the Se. Overall, the Fe K-edge shift is greater in Li_2FeSSe than Li_2FeSe_2 due to the greater covalency in the latter, where the charge storage is more shared between the cations and anions and leads to formally less oxidized Fe centers at high states of charge.

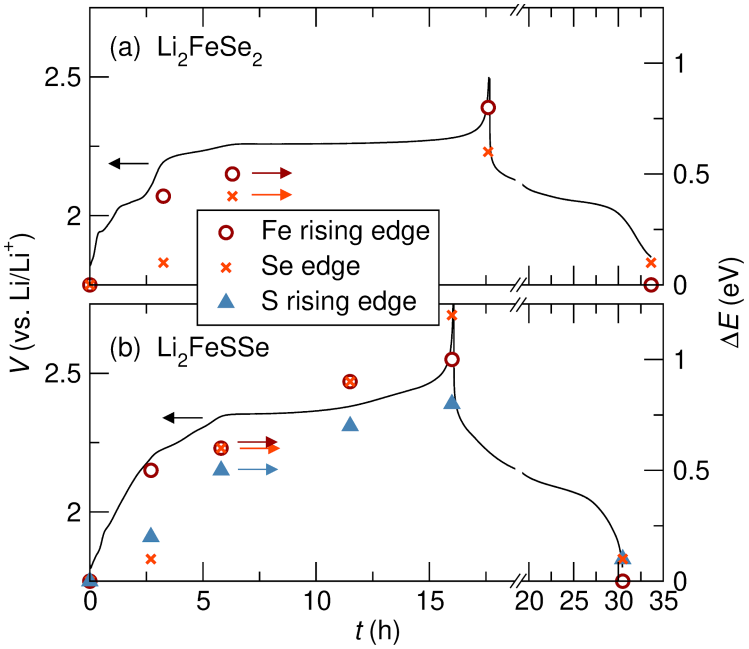

Figure 6.12: The metal and chalcogen K-edge positions overlaid on the charge and discharge curves for (a) Li_2FeSe_2 and (b) Li_2FeSSe. The edge shift is greater upon charge in the mixed anion material.

Fe, S, and Se K-edge XAS of the discharged samples of both Li_2FeSe_2 and Li_2FeSSe show near complete recovery of the pre-edge and edge positions. The near-edge scattering features, however, show partial reversibility that provides evidence that reversible anion redox is accompanied by irreversible local structural changes. The change in local structure is likely a result of the second phase that is observed in the *operando* XRD and corroborated by intermittent EIS measurements that showed the persistence of a higher charge-transfer resistance in Li_2FeSe_2 after the first charge. The concurrent oxidation of Fe and Se coincides with rapid phase separation, rather than a pseudo-continuous contraction of the lattice upon charging as observed in Li_2FeS_2. We hypothesize that the structural changes are the cause of capacity fade in Li_2FeSe_2.

6.3 Conclusions

Li_2FeSe_2 and the solid solution $Li_2FeS_{2-y}Se_y$ exhibit reversible multielectron storage capacity enabled by both cation and anion redox. The oxidation potential can be systematically tuned between the sulfide and selenide end members, indicating that the anions are well mixed as a solid solution and the electronic structure is composed of bands of mixed Se and S character. Fe, S, and Se K-edge XAS studies indicate that oxidation affects the electronic structure of all three components (i.e. Fe, S, and Se) throughout the charge profile, which is in contrast to Li_2FeS_2 that shows Fe oxidation followed sequentially by S oxidation.[163] The anion oxidation of the selenide end member results in the formation of Se–Se dimers as evidenced by *in situ* Raman spectroscopy, similar to the S–S dimers formed Li_2FeS_2.[163] Using information gleaned from the Fe, S, and Se K-edge spectra, we suggest that the mixed anion materials form mixtures of S–S, S–Se, and Se–Se dimers upon mixed anion oxidation, which agrees well with the systematic shift in the oxidation potential observed in the electrochemistry. The discovery of tunable anion redox provides the ability to study the influence of metal-anion covalency on the multielectron redox mechanisms at play in Li-rich systems.

The high degree of covalency in Li_2FeSe_2 enables continuous oxidation of both Fe and Se throughout the charge. Covalent metal-anion bonds are often implicated in the multielectron oxide literature as a desirable property with the aim of stabilizing anion redox. We observe that the more covalent Fe-Se material shows anion redox earlier in the charging profile. The reversibility of the redox, however, is worse in the selenide compared to the sulfide and interestingly trends with stoichiometry with more Se causing systematically poorer capacity retention. The loss in capacity retention is likely due to the structural changes that occur upon cycling. The selenide forms a high impedance second phase upon oxidation that never completely reverts to the initial material during reduction. Therefore, our results indicate that while increased covalency increases the propensity of anion redox at lower voltages, the structural changes incurred through anion-anion bonding have the potential to be deleterious to material performance. As such, addressing metal-anion covalency alone is not enough to guarantee increased charge storage capabilities. Instead, developing holistic understanding of the changes to both electronic and bulk structure upon charging and discharging is necessary to design next-generation multielectron storage materials.

6.4 Experimental Methods

Materials Preparation. The Li-rich selenide Li_2FeSe_2 was prepared in an evacuated vitreous silica ampoule from Li_2Se, $FeSe_2$ (preparations discussed below), and Fe (Acros Organics, 99%) in stoichiometric quantities. To prevent corrosion of the reaction vessel, the inside of the silica ampoule was coated with carbon. The reactants were heated to 500 ℃ at 5 ℃ min^{-1}, allowed to react for 12 h, heated to 1000 ℃ at 1 ℃ min^{-1}, allowed to react for 24 h, at which point the reaction was quenched in a water bath. The product formed as a black polycrystalline ingot. The product is air and water sensitive and was kept under inert conditions for all processing and manipulations.

Li_2FeS_2 was prepared according to our previously reported protocol.[163] Li_2S (Beantown Chemical, 99.9%), FeS_2 (Acros Organics, 99.0%), and Fe (Acros Organics, 99%) were combined in stoichiometric quantities, sealed in a C-coated silica ampoule under vacuum, and heated at 5 ℃ min^{-1} to 500 ℃, allowed to dwell for 12 h, heated to 900 ℃ at 1 ℃ min^{-1}, and allowed to dwell for 16 h before cooling to room temperature. The material was collected, stored, and manipulated in an Ar-filled glove box.

The solid solution $Li_2FeS_{2-y}Se_y$ was prepared from stoichiometric quantities of the end members. Powders of the reactants were ground together in an Ar-filled glove box, pelleted, and sealed in C-coated silica ampoule. The reactions were heated at 5 ℃ min^{-1} to 900 ℃ and allowed to dwell for 24 h before cooling to room temperature.

Li_2Se was prepared from Li metal (Alfa Aesar, 99%) and Se powder (Acros Organics, 99.5+%) in a sealed silica ampoule. To prevent rapid, uncontrolled reaction between the the chalcogen and the alkali metal, each reactant was contained in an individual alumina crucible within the tube. The crucible containing the chalcogen was placed on top of the crucible containing the alkali and the tube was sealed and kept upright. The reaction vessel was heated at 1 ℃ min^{-1} to 400 ℃ and allowed to dwell at temperature for 12 h before cooling to room temperature. The Li_2Se product was collected from the crucible originally containing the Li in an Ar filled glove box.

$FeSe_2$ was prepared from a stoichiometric mixture of Fe powder (Acros Organics, 99%) and Se powder (Acros Organics, 99.5+%). The elements were ground together until homogeneous, densified into a pellet, and heated at 10 ℃ min^{-1} to 700 ℃, allowed to dwell for 12 h, then cooled to 550 ℃ at 1 ℃ min^{-1} and allowed to dwell for 24 h.

Material Analysis. Powder X-ray diffraction patterns were collected on a Panalytical X'Pert Pro Diffractometer equipped with a CuKα X-ray source. To prevent oxidation of the material during the measurement, the powders were mounted on a glass slide and covered with polyimide tape. The diffraction patterns were fit by the Rietveld method using GSAS-II.[75] Crystal structures were visualized using Vesta.[76]

Electrochemical Studies. The materials were combined in composite electrodes at a ratio of 3:1:1 by mass of active material:polytetrafluoroethylene (PTFE, Sigma Aldrich) : Super P carbon (Alfa Aesar, ≥99%). The composite mixture was ground to homogeneity with a mortar and pestle, and pressed into pellets of 0.25" diameter with a hand driven arbor press. Electrochemical measurements were collected in 2032 coin cells with dried 18 mm diameter glass fiber separators (Whatman GF/D), polished Li metal counter/reference electrodes, and 11 drops of electrolyte (approx. 156 mg). All potentials hereafter are in reference to the Li metal counter/reference electrode potential which is taken to be approximately equal to Li/Li^+ . The electrolyte was prepared as a 1 M solution of $LiPF_6$ (Sigma Aldrich, ≥99.99%) in a 1:1:3 mixture by volume of ethylene carbonate (Sigma Aldrich, >99%), propylene carbonate (Sigma Aldrich, >99%), and dimethyl carbonate (Sigma Aldrich, >99%). Galvanostatic cycling data was collected at a rate of C/10 based on 1 e^- per formula unit, unless otherwise noted. Cyclic voltammetry data was collected at a rate of 0.1 mV/s unless otherwise noted. Galvanostatic intermittent titration technique data was collected at a rate of C/10 based on 1 e^- per formula unit for 20 min followed by a 4 h open circuit hold step. All electrochemical measurements were collected using a Biologic BCS 805 battery cycler unless otherwise noted.

Electrochemical Impedance Spectroscopy. Electrochemical impedance spectroscopy (EIS) measurements were carried out using a VersaStat MC electrochemical workstation. Impedance was measured in the frequency range of 100 kHz to 50 mHz with a sinusoidal excitation voltage of 5 mV (peak to peak). The cells were incrementally charged or discharged at a rate of C/10 (based on 1 e^- per formula unit) in steps of $0.1x$ (where x is mol of Li), and the voltage of the cell was allowed to relax to an equilibrium value after each charge/discharge step. The EIS measurements were then carried out under open circuit conditions at ambient temperature. The resulting spectra were analyzed using ZSimpWin software. A modified Randles equivalent circuit model was used in the analysis. The simulated impedance plots agreed well with the actual impedance spectra, with less than 5% error for each circuit element.

The Nyquist plots exhibited a depressed semicircular loop in the high frequency region (100 kHz to 1 Hz) and a prominent tail at low frequencies (below 1 Hz) characteristic of mass transfer-related processes. Accordingly, a modified Randles circuit was used for analyzing the impedance response. The modified Randles circuit consisted of a resistor (R_s) in series with an RQ circuit comprised of a constant phase element (Q_1) in parallel with a resistor (R_{ct}) and constant phase element (Q_2) in series. The full circuit can be represented as $R_s[Q_1[R_{ct}\ Q_2]]$. Here, R_s and R_{ct} denote the uncompensated series resistance and charge transfer resistances, respectively. The constant phase elements Q_1 and Q_2 represent the double layer capacitance and the mass transfer process, respectively. The constant phase element (CPE) was used instead of the ideal capacitor to account for the distributed capacitance arising from the nature of the porous electrode. The CPE has impedance similar to a capacitor, but with a phase angle of less than 90 degrees. The impedance of CPE is defined as, $Z_{CPE} = 1/[Q_0(j\omega)^n]$, where ω is the angular frequency and n is a constant number between 0 and 1. Thus, when n = 1, the CPE becomes a capacitor and the imaginary component of the Warburg element when n = 0.5. The values for n were close to 0.8 for Q_1 and 0.45 for Q_2 in the present study.

X-ray Absorption Spectroscopy. Samples for *ex situ* X-ray absorption spectroscopy (XAS) were prepared in 2032 coin cells with a Li foil anode, glass-fiber separator (Whatman, GF/D), 12 drops of electrolyte (approx. 170 mg), and a composite electrode with the active material of interest (prepared as described above). Electrodes were galvanostatically cycled to various states of charge using predetermined voltage cutoffs. The coin cells were disassembled under inert conditions, electrodes were then removed, washed with dimethyl carbonate, and dried under vacuum for > 2 h. Samples were sealed under an Ar atmosphere in the Al sample holder with either polyimide tape (Fe and Se) or polypropylene film (S). Fe and Se K-edge XAS was collected at beamline 4-1 and S K-edge XAS was collected at beamline 4-3 at the Stanford Synchrotron Radiation Lightsource at SLAC National Accelerator Laboratory. Samples were measured at the Fe and Se K-edges from one or two sweeps (depending on sample quality) in both fluorescence and transmission modes, where the data shown are the summed fluorescence data for each sample. Samples were measured at the S K-edge from four sweeps in fluorescence mode. Calibration, background correction, and data processing of X-ray absorption near edge structure (XANES) was performed using Athena.[77] The Fe K-edge data and Se K-edge data were calibrated to a collinear Fe foil or Se standard, respectively, present for

each sample. S K-edge data was calibrated to a sodium thiosulfate standard that was checked repeatedly throughout experimentation to ensure a constant energy shift. Data quality and collection in a limited window in k-space precluded EXAFS analysis.

Operando XRD Studies. XRD measurements were performed using a Bruker D8 diffractometer with a Co K_α source (λ_1 = 1.78897 Å, λ_2 = 1.79285 Å), equipped with a Lynxeye XE-T detector. A modified Swagelok cell, with a Be window serving as a current collector, allowed for diffraction patterns to be collected during electrochemical cycling. XRD scans were performed in a Bragg-Brentano geometry over a range of 25° to 40° 2θ with a total scan time of 20 minutes. Scans were continuously repeated throughout the duration of electrochemical cycling. Two electrode *operando* cells were assembled in an Ar-filled glovebox using Li metal as a combined counter and reference electrode and Whatman GF/D borosilicate glass fiber sheets as the separator. 1 M $LiPF_6$ in ethylene carbonate and dimethylcarbonate (1:1 v/v) was used as the electrolyte. Working electrodes were prepared by blending active material with Super P (Alfa Aesar, ≥99%) and PTFE (Sigma Aldrich) in a ratio of 70:15:15 (wt.%), respectively, and pressing under uniaxial pressure.

In Situ Raman Spectroscop. Raman spectra were collected on a Horiba XploRA One confocal Raman microscope. All spectra were collected with a 785 nm diode laser, a grating with groove density 1200 gr mm^{-1}, and 1% laser power (≈0.52 mW) to minimize laser damage to the samples. The hole and slit were fixed at 500 and 200 μm, respectively. The laser was focused using a 50× (numerical aperture 0.50) objective, which yielded a nominal lateral resolution of ca. 785 nm and axial resolution of ca. 6.28 μm. *In situ* measurements were performed by focusing the laser on the front-side of the cathode in a custom spectroelectrochemical cell (Figure 2.7) with a nylon body, stainless steel current collectors, and a borosilicate glass cover slip window (0.17-0.25 mm thickness). The cell stack was assembled with a free-standing electrode prepared in an 8:1:1 ratio by mass of active material:polytetrafluoroethylene (PTFE, Sigma Aldrich) : Super P carbon (Alfa Aesar, ≥99%), a Whatman GF/D glass fiber separator with a 3/32" hole punched out, a polished Li foil anode with a 5/32" hole punched out, and 6 drops (94 ± 2 mg) of electrolyte. The electrolyte was the same composition as that used for the cycling experiments diluted by a factor of 10 to yield 0.1 M $LiPF_6$ to limit interference from fluorescence. Spectra were collected with a 10 s acquisition time and 360 accumulations after optimizing the focus for each spectrum. Spectra were collected while

the cell was cycled galvanostatically at C/10 based on 1 e^- and the electrochemical program was paused for each collection.

Chapter 7

AN EXPLORATION OF SULFUR REDOX IN LITHIUM BATTERY CATHODES

Adapted from: Zak, J. J.; Kim, S. S.; Laskowski, F. A. L.; See, K. A. An Exploration of Sulfur Redox in Lithium Battery Cathodes. *J. Am. Chem. Soc.* **2022**, *144*, 10119—10132.

Chapter Abstract

Secondary Li-ion batteries have enabled a world of portable electronics and electrification of personal and commercial transportation. However, the charge storage capacity of conventional intercalation cathodes is reaching the theoretical limit set by the stoichiometry of Li in the fully lithiated structure. Increasing the Li:transition metal ratio and consequently involving structural anions in the charge compensation, a mechanism termed anion redox, is a viable method to improve storage capacities. Although anion redox has recently become the front-runner as a next-generation storage mechanism, the concept has been around for quite some time. In this perspective, we explore the contribution of anions in charge compensation mechanisms ranging from intercalation to conversion and the hybrid mechanisms between. We focus our attention on the redox of S because the voltage required to reach S redox lies within the electrolyte stability window, which removes the convoluting factors caused by the side reactions that plague the oxides. We highlight examples of S redox in cathode materials exhibiting varying degrees of anion involvement with a particular focus on the structural effects. We call attention to those with intermediate anion contribution to redox and the hybrid intercalation- and conversion-type structural mechanism at play that takes advantage of the positives of both mechanistic types to increase storage capacity while maintaining good reversibility. The hybrid mechanisms often invoke the formation of persulfides, and so a survey of binary and ternary materials containing persulfide moieties is presented to provide context for materials that show thermodynamically stable persuflide moieties.

7.1 Introduction

Although multielectron behavior has been observed in some oxides, detailed mechanistic understanding remains elusive. Anion redox may explain the observed multielectron storage, but the community has yet to agree on the charge storage mechanism. Multielectron storage in oxides has been attributed to high valent metals,[196] trapped molecular O_2,[48] reversible formation of peroxo-like oxidized O species,[25, 26, 102] and decomposition reactions.[23, 52, 53] Developing mechanistic understanding is difficult in oxide systems where high operating voltages cause electrolyte decomposition and other degradation reactions.[23, 41, 197] The challenges are magnified when studying anion redox because the high voltages required to access the O 2p states coincide with side reactions that convolute electrochemical and spectroscopic data. Even if anion redox is responsible for the observed capacities, the issues associated with studying anion redox in oxides make it difficult to develop structure-property relationships. Furthermore, many of the multielectron oxides use 4d and 5d metals which are generally less abundant and heavier than the 3d metals. Thus, we aim to discuss anion redox in sulfides to not only develop clear structure-property relationships but also to realize multielectron materials using 3d metals.

Relative to oxide systems, sulfides are ideal for studying anion redox and developing structure-property relationships. Coupled cation-anion redox was first predicted in Li-rich metal sulfides like Li_2FeS_2 in the late 1980s.[122, 198] Sulfides present several advantages over oxides: they are softer, more polarizable and are stable in a wide variety of structures. Sulfides intrinsically operate at lower voltages than oxides, which removes barriers associated with electrolyte decomposition, degradation reactions, and gas release. The energetics of the S valence states allow it to form relatively covalent metal-anion bonds with the more abundant, less expensive 3d transition metals. For these reasons, Li-rich sulfides may be the key to understanding and designing reversible anion redox behavior in next-generation cathodes. Despite the promise, some challenges still remain. The low voltage of sulfide oxidation limits energy density and sulfides are traditionally air-sensitive. Li-rich sulfides exhibit hysteresis between the charge and discharge curves. Additionally, poor stability of the oxidized structure may be a concern for some materials.

A fundamental understanding of S redox could provide the insight necessary to understand anion redox in multielectron materials. Here, we discuss S redox in

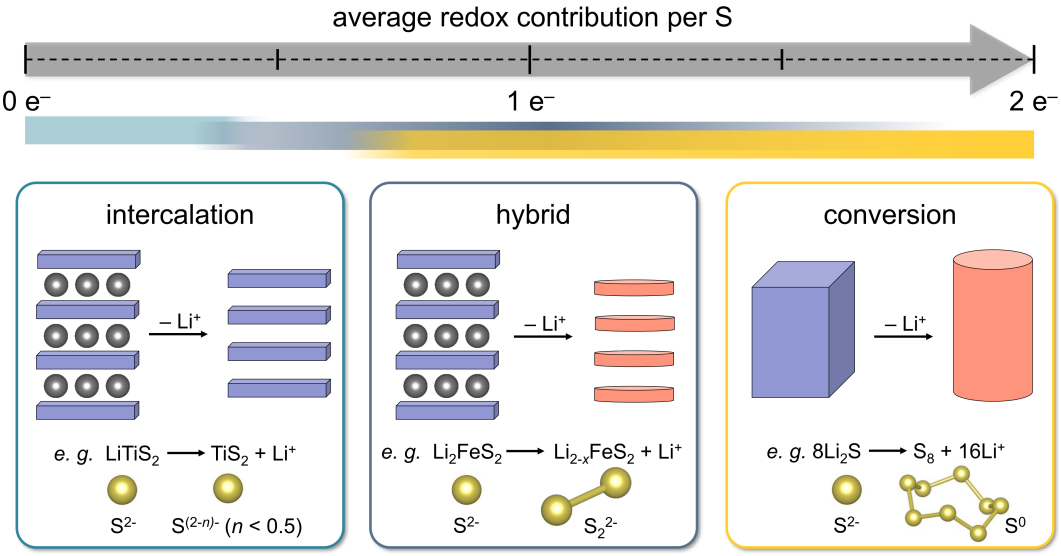

Figure 7.1: The degree to which S participates in charge compensation can vary widely depending on the material, thermodynamics (voltage), and kinetics (current). The structural response to the anion redox defines the charge storage mechanism and the range of structural responses can be binned into three categories: intercalation, hybrid, and conversion. As more charge is compensated by the S, the mechanism shifts from an intercalation mechanism to a hybrid mechanism to finally a conversion mechanism. Each mechanism spans over a range of potential S redox contributions with variation attributed to different materials families. Combinations of these mechanisms can be observed in a single material.

materials ranging from intercalation materials with minimal anion redox contributions to materials with coupled cation-anion redox to conversion materials that only utilize the anions. Anion redox can be thought of as a sliding scale ranging from conventional intercalation chemistry at one extreme to conversion chemistry at the other. Hybrid mechanisms that couple anion and cation redox occupy the continuum between the extremes (Figure 7.1). The mechanism depends both on the extent to which the anion is participating in charge compensation and the structural changes incurred through mobile ion insertion/removal. The mechanism also depends on the thermodyanmic factors (voltage) and kinetic factors (current). Several mechanisms can be observed in a single material, and shifting between mechanisms can be as simple as changing the rate. We develop a holistic picture of S anion redox by considering its consequences on both the electronic and physical structure, within the continuum. We explore several case studies for each mechanism and discuss how the materials respond to anion redox. Specifically for hybrid mechanisms, the formation of persulfides is often invoked as the key structural response that stabilizes sulfide oxidation. Thus, we conclude the perspective with overarching trends

and observations from a survey of binary and ternary persulfides to discuss the thermodynamic structures that accommodate persulfides. By considering patterns that dictate the presence persulfides in thermodynamically stable phases, we hope to inform future directions for materials that support reversible anion redox behavior.

7.2 Intercalation Chemistry: Minimal Anion Contributions and Structural Changes

We begin our discussion with an example of a charge storage mechanism with minimal anion redox contributions: intercalation chemistry. Intercalation involves the incorporation of a mobile species, in this case a cation, into a host material. The incorporation of the ion causes minimal structural changes and the resulting material remains related to that of the original material by one or more crystallographically equivalent orientational relationships. Thus, the process is considered a topotactic reaction.[199] Upon (de)intercalation of Li^+ in materials like LCO, NMC, and NCA, the lattice responds by simple expansion and contraction. Such changes are minimally disruptive to the structure; for example, the volume change in LCO with Li^+ (de)intercalation is ~3%,[200] which results in highly stable cycling. In addition to physical structural responses, incorporation of cations causes changes to the electronic structure. As cations are intercalated, the material is reduced to satisfy charge compensation.

The canonical example of intercalation in sulfides is TiS_2, discovered in the 1970s by Whittingham.[105, 106] TiS_2 adopts a layered structure with layers of edge-sharing TiS_6 octahedra separated by a 2.8 Å van der Waals gap. Up to one full equivalent of Li^+ can be intercalated into the octahedral sites within the van der Waals gaps to form $LiTiS_2$. Upon Li^+ interaclation, the material is reduced and the charge compensation is often simply described with formal oxidation states: reduction of Ti^{4+} to Ti^{3+}. Li^+ can then be removed via the same mechanism resulting in formal oxidation of Ti^{3+} and minimal structural deformation. Typical discharge and charge curves of TiS_2 are shown in Figure 7.2a. When cycled between 1.4 V and 3 V vs. Li/Li^+ (all subsequent voltages will be referenced to the Li/Li^+ couple), the electrochemistry of TiS_2 is highly reversible with the sloping voltage profile indicative of a single-phase mechanism.[111, 201, 202] The shape of the voltage profile is determined by kinetic and thermodynamic factors, but thermodynamic factors tend to dominate in materials that have small overpotentials, like TiS_2. Incremental insertion of Li^+ leads to a thermodynamic mixture of Li_xTiS_2, resulting in the voltage decreasing steadily as a function of increasing x.

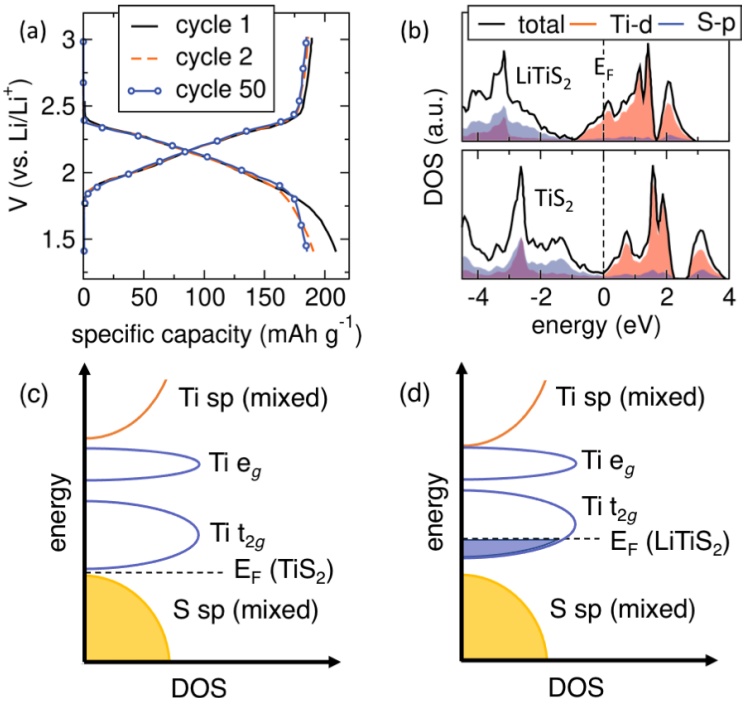

Figure 7.2: (a) Galvanostatic cycling of TiS_2 reveals a highly reversible, gently sloping charge and dsicharge profile. (b) The partial density of states calculation for $LiTiS_2$ and TiS_2 shows mostly Ti character near the Fermi level (E_F). Both (a) and (b) are adapted in part with permission from Ref. 26. Copyright 2018 American Chemical Society. Graphical representations of density of states near the Fermi level in (c) TiS_2 and (d) $LiTiS_2$, respectively, with assignments and relative energy shifts. The Ti t_{2g} states fill as the material is reduced. Relative changes in relevant band positions from Moreau *et al.*[1].

Although Ti plays a majority role in charge compensation, the Ti-S bond has covalent character and thus the charge compensation is somewhat shared by the S. Covalent interactions are most often considered as the classical electron pair bond; that is, the bond is characterized by the overlap of charge distributions of antiparallel electron spin between neutral atoms.[203] Ionic solids, on the other hand, consist of charged species strongly bound by electrostatic interaction. In most materials, the bonding is more complex and involves a balance of attractive and repulsive forces that sum to the lattice energy of a crystal. There exists a continuum between a perfectly ionic and perfectly covalent crystal, and most materials exist somewhere between the two. Electronegativity and size (i.e. polarizability) of cations and anions in a crystal are good proxies for determining the extent of ionic vs. covalent character in the bonding. Experimentally determining covalency requires techniques that probe mixing of the electronic states of the cation and anion such as XAS, X-ray emission spectroscopy (XES), and resonant inelastic X-ray scattering (RIXS). XAS is one

of the more widely employed techniques due to the wealth of information that can be gained. The K-edge position is indicative of oxidation state while shakedown transitions and pre-edge features probe transitions to valence states and are thus reporters of covalency. The intensity of the features below the edge is closely related to metal-ligand d-p mixing.[40] Metal L-edge XAS is also a precise probe of covalency. The dipole-allowed p to d transition causes the total integrated intensity to be proportional to the 3d character in unoccupied valence orbitals.[40] Mixing of cation and anion bands can also be calculated computationally with density functional theory (DFT) and visualized with a partial density of states diagram.

The aforementioned techniques can thus be used to evaluate the degree of covalency in TiS_2 and correlate the covalency with the charge compensation mechanism. We will begin by discussing the XAS data. Of course, Ti participates in charge compensation with clear evidence in the Ti L- and K-edge data,[1, 202, 204] however, we will focus our discussion on the participation of S. Wu *et al.* reported *ex situ* XAS spectra at the S K-edge collected for Li_xTiS_2 (x = 0, 0.4, 0.8, 1) and observe a systematic decrease in the two near-edge features corresponding to t_{2g} and e_g band-like mixed Ti 3d-S 3p states, indicating that the mixed states are filled as the material is reduced.[204, 205] A broad feature above the edge attributed to S 3p states mixed with Ti 4s and 4p states systematically shifts to lower energies and increases in intensity primarily due to backscattering effects from higher coordination number of S in $LiTiS_2$ (six in $LiTiS_2$ compared to three in TiS_2). *Operando* S K-edge XAS by Zhang *et al.* provides finer detail to the same experiment and corroborates the trends.[201] All of the observed changes indicate that the electronic structure of S changes upon redox.

Calculated band structures corroborate the experimental findings and aid in visualizing the cationic and anionic contributions to the valence states. The partial density of states diagrams for TiS_2 and $LiTiS_2$ calculated by Zhang *et al.* are shown in Figure 7.2b.[201] The bands near the Fermi level in TiS_2 contain both Ti and S character and predict that, upon reduction of TiS_2, the first electron would occupy the Ti 3d states that are antibonding with S 3p states.[1, 201, 204, 205] Said another way, S 3p states are mixing with d^0 Ti^{4+} states similar to a ligand-to-metal charge transfer that is often invoked in molecular metal complexes. Upon discharging to $LiTiS_2$ (reduction), the partial density of states shows Ti states dominate, indicating a decrease in covalency.[201] The change is represented graphically in Figure 7.2c and d with relative energy shifts from Moreau *et al.*[1] Zhang *et al.* performed

Bader charge analysis, which calculates the charge on each atom, and predict that one Ti and two S gain 0.089 and 0.384 electrons, respectively, for each intercalated Li^+, further indicating S contribution to charge compensation.[201]

Next, we discuss the implications of the (de)lithiation reactions on the structure of TiS_2. The physical response has been explored on a bulk level with X-ray diffraction (XRD)[206–209] and on a local level with EXAFS analysis[201, 202]. On the bulk scale, TiS_2 undergoes a volume expansion of approximately 11% upon Li^+ insertion.[210] *Operando* XRD experiments show that the expansion and subsequent contraction of the lattice as Li^+ is inserted and removed is reversible, indicating no permanent bulk structural deformations.[209] However, on a local level, EXAFS above the Ti K-edge reveals permanent changes in the second coordination shell (i.e. Ti-Ti correlations) despite completely reversible changes to the first-shell Ti-S correlations.[201, 202] With respect to S, there is only a slight lengthening of the Ti–S bond upon reduction (lithiation) and, with no change in coordination number observed for Ti, it follows that the S sublattice undergoes little to no change beyond expansion. Figure 7.3 shows the structure of $LiTiS_2$ vs. the fully delthiated TiS_2. The original atom positions in $LiTiS_2$ are shown as black circles overlaid on the TiS_2 to highlight the minimal structure change despite removal of a full equivalent of Li^+.

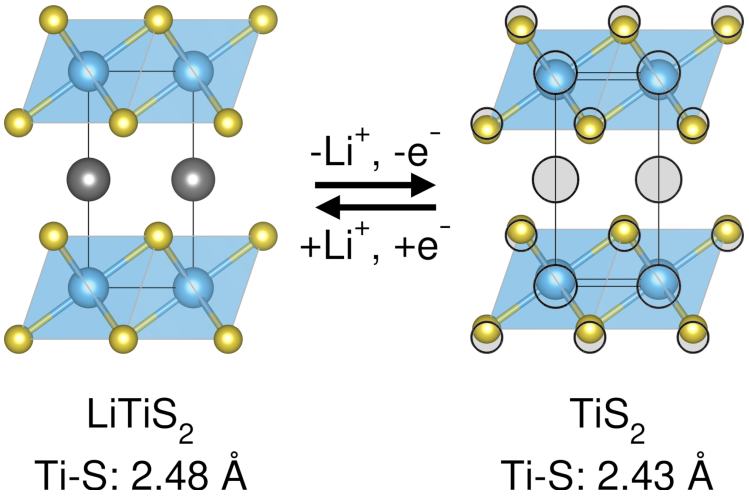

Figure 7.3: Conversion between $LiTiS_2$ and TiS_2 causes minimal changes to the structure. Upon delithiation, the c lattice parameter decreases and the Ti-S bond slightly compresses. The original atom positions of $LiTiS_2$ are overlaid in black on the TiS_2 structure to facilitate comparison.

The mechanism becomes significantly more complicated when TiS_2 is discharged (reduced) below 1.4 V. Zhang *et al.* report a new plateau at 0.45 V when TiS_2 is

discharged to 0.05 V.[201] The plateau is attributed to the reduction of Ti cations to Ti^0 and the formation of Li_2S. However, despite the precedence for this type of mechanism in metal oxides like Fe_2O_3[211] and Co_3O_4[212], there is limited evidence in the TiS_2 system. Any obvious spectral signatures of Li_2S in the S K-edge XAS are missing and XRD studies only show signs of Li_2S at intermediate states of charge.[201, 213] Several studies suggest the possibility of Li^+ inserting into the structure in tetrahedral sites, which have also been predicted to be more stable.[201, 214–216] Regardless, Zhang *et al.* show in the *operando* S K-edge XAS that there are irreversible changes to all spectral features after a single discharge to 0.05 V. The irreversibility is likely structural in nature. Slow Li^+ diffusion kinetics during oxidation of the discharge products may also contribute.

In summary, charge compensation in the canonical intercalation material TiS_2 is somewhat shared between Ti and S due to mixed bands with Ti d and S p character near the Fermi level. However, the contributions from S are small and the layered TiS_2 structure is thermodynamically stable resulting in minimal impact to the S sublattice upon delithation, despite the undercoordinated S in TiS_2. Cycling in a sufficiently anodic voltage range is highly reversible with minimal structural changes, limited mostly to a slight Ti–S bond lengthening. Thus, anions can participate in the charge compensation processes of intercalation reactions that come with minimal structure changes and a high degree of reversibility. Along the continuum depicted in Figure 7.1, intercalation reactions lie at the far left where redox contributions from the anion are small along with the corresponding structural changes.

7.3 Extensive Structure Change: Conversion

Next we consider charge storage mechanisms where charge compensation is entirely accounted for by the anion: conversion chemistry. We consider the (de)lithiation of elemental S, which is most commonly studied as the S_8 allotrope.[217, 218] When S_8 is reduced, substantial structural rearrangement occurs in which all the original S-S bonds are broken and new Li-S bonds are formed to yield Li_2S. Conversion-type mechanisms have also been reported in binary metal sulfides in which Li_2S is formed along with the associated reduced metal, but we will first focus our attention on S_8 to explore the role of S in conversion-type materials without convolution from other components like transition metals. Li-S systems are of interest due to the high theoretical capacity (1672 mAh g^{-1} for S_8 vs. 274 mAh g^{-1} for LCO) and the widespread abundance of S.[219, 220] S_8 is a molecular crystal composed of eight-membered, puckered rings in an orthorhombic unit cell where the average

intra-ring S-S bond is 2.04 Å and the shortest inter-ring distances are around 3.7 Å (Figure 7.4). S adopts the eight-membered ring structure in part due to the atomic size that disfavors short double bonds due to poor orbital overlap. This concept is referred to as the double bond rule, which states that elements with a principal quantum number (n) greater than 2 for the valence electrons form single-bonded structures instead of double bonds.[221] S forms strong single bonds with itself (215 kJ mol^{-1})[222] and, as such, catenates into structures like S_8.

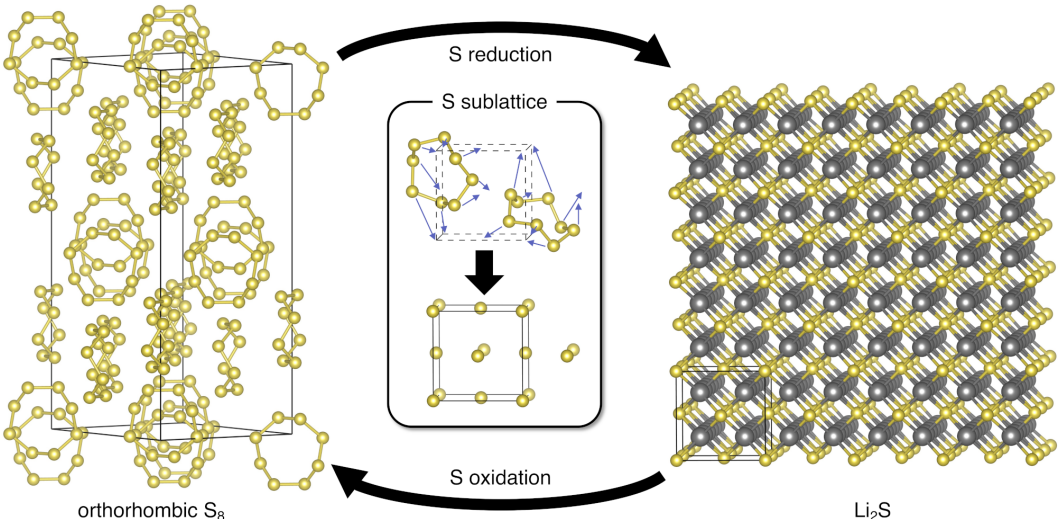

Figure 7.4: The charge storage mechanism in a Li–S battery involves conversion of orthorhombic S_8 to Li_2S and back, necessitating a large structural rearrangement. The S_8 and Li_2S structures are shown to-scale and contain the same number of S atoms to highlight the differences between the two materials. Although the mechanism for conversion in the solid-state is not known, we highlight some possible translation vectors for each S atom to convert from S sublattice in S_8 to that in Li_2S.

Upon electrochemical insertion of Li^+, S_8 is eventually converted to Li_2S, which requires a 2 electron reduction per S atom. Li_2S has a cubic unit cell with an FCC S sublattice and no S connectivity; the shortest S-S distance is 4.1 Å. The conversion from S_8 to Li_2S therefore requires a substantial structural rearrangement. Figure 7.4 shows the S_8 structure to Li_2S with a constant number of S atoms to compare the atom positions and volume. Reduction to Li_2S causes up to 80% volume change and a significant rearrangement of the S sublattice.[223]

The structural changes produce various problems in Li-S cells, including slow kinetics, diminished electrode integrity, and decreased active material accessibility.[224] A liquid electrolyte can overcome some of these issues by allowing for a solution-mediated pathway from S_8 to Li_2S via various soluble Li polysulfide intermediates.

In liquid electrolytes, S_8 is first electrochemically reduced to break the ring structure, leaving the terminal sulfides available to coordinate Li^+.[225] The resulting Li polysulfide species are soluble and can be further reduced to shorter-chain polysulfides and eventually to solid Li_2S. However, soluble intermediates shuttle to the Li anode where they are chemically reduced, resulting in poor Coulombic efficiency and active material loss.[226, 227] Because of the multiple phases formed during discharge, the discharge profile exhibits two characteristic plateaus. Here, however, to focus on direct solid-state conversion mechanisms, we will only touch on systems with inorganic solid-state electrolytes (SSEs) that preclude the formation and transport of polysulfide intermediates.

Solid-state reduction of S_8 is characterized by a single, gently sloping voltage profile in the galvanostatic discharge data shown in Figure 7.5a.[223, 228–231] The lack of distinct features and relatively flat plateaus in the electrochemical profile can indicate two-phase behavior. In the case of all-solid-state Li-S cells, *ex situ* XRD and XAS suggest that the discharge curve represents the conversion of S_8 directly to Li_2S.[232, 233] Direct conversion requires breaking of relatively strong S–S bonds and rearrangement to form a close-packed FCC sublattice. Although the mechanism for the solid-state transformation of S_8 to Li_2S is not known, we show the smallest possible translation vectors required to convert S_8 to Li_2S in Figure 7.4. Given slow Li^+ diffusion kinetics in the solid-state and poor electronic conductivity, kinetics tend to be sluggish. As such, particle morphology, especially size, plays an essential role in addressing the kinetic limitations of the S_8 to Li_2S (and the reverse) conversion reaction.[234, 235] Transient polysulfide intermediates could alleviate kinetic limitations, but they are likely to be non-crystalline phases that would require extensive spectroscopic characterization for detection. Solid-state, crystalline lithium polysulfides are not thermodynamically stable, including the widely suggested Li_2S_2 intermediate which lies approx. 70 meV off the convex hull.[236] In-depth spectroscopic studies of the redox mechanisms in all-solid-state Li-S cells have not been done, but the insight gained from such a study would be immensely useful in understanding solid state S redox.

Conversion-type mechanisms in binary metal sulfides exhibit similar characteristics to the reduction of S_8. For example, pyrite FeS_2 ($Pa\bar{3}$) consists of a FCC lattice of Fe^{2+} octahedrally coordinated by persulfides, S_2^{2-}, which connect adjacent corner-sharing polyhedra. This type of structure is markedly different from previously discussed binary metal sulfide, TiS_2, which adopts a layered structure and high-

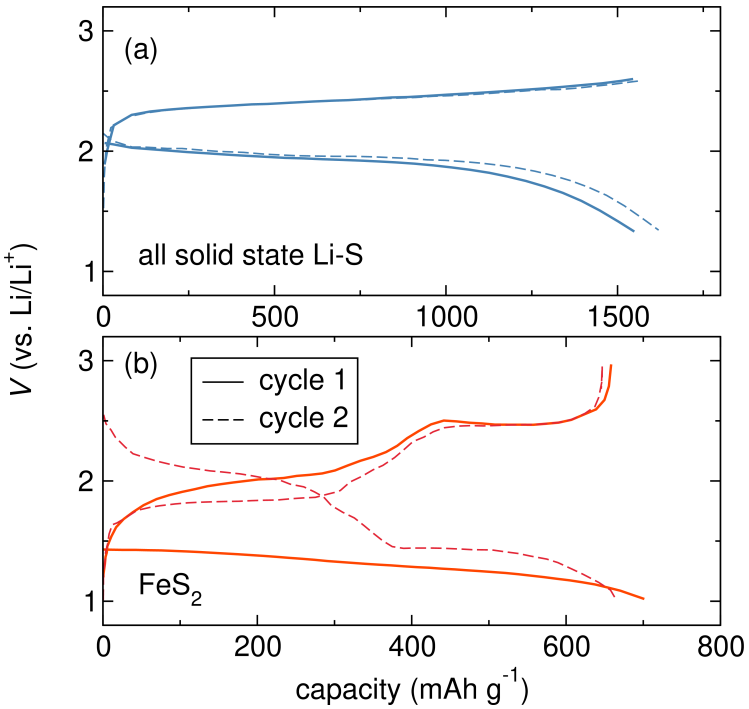

Figure 7.5: Galvanostatic cycling of (a) S_8 in an all solid state setup (Li | Li_3PS_4 | S_8) at a C/20 rate and (b) FeS_2 in a traditional liquid electrolyte cell (Li | 1 M $LiPF_6$ in 1:1 EC/DMC | FeS_2) at a C/40 rate. In both cases, cells are discharged (reduced) first and undergo a conversion-type reaction. Upon charging, the Li-S cell undergoes the same conversion reaction in reverse whereas FeS_2 exhibits a hybrid-type mechanism. Li-S data are adapted from Ref. 56. Copyright 2015 The Electrochemical Society. Reproduced by permission of IOP Publishing. All rights reserved. FeS_2 data are adapted in part with permission from Ref. 64. Copyright 2017 American Chemical Society.

valent Ti^{4+} coordinated exclusively by sulfide anions (S^{2-}). Reduction of pyrite FeS_2 yields a high capacity of 893 mAh g^{-1} based on a 4 e^- transfer assuming complete conversion of Fe^{2+} to Fe^0 and persulfide (S_2^{2-}) to sulfide (S^{2-}). Figure 7.5b shows a representative example of the first two cycles of FeS_2. The first discharge is characterized by a long plateau below 1.5 V that involves either a one-step reaction or a multi-step reaction depending on the discharge rate and temperature. Regardless of the step count, the flat plateau indicates a two-phase mechanism. Although multiple intermediate species have been proposed, including several in the ternary Li-Fe-S phase space, the final product at the end of first discharge is Fe and Li_2S.[126, 147, 237–241] With a key difference, this mechanism mirrors that of S_8, which is converted to Li_2S as well, and thus experiences a similarly disruptive structural rearrangement as a consequence of S reduction. The main difference is of course the presence of Fe, which changes the reduction pathway. The potential

at which FeS_2 converts to Fe and Li_2S is approximately 500 mV lower than that observed in an all-solid-state Li-S cell.[147]

The first charge cycle for pyrite FeS_2 exhibits more complex behavior compared to S_8-Li_2S conversion. Multiple mechanisms have been proposed. Based on *in situ* XRD and ^{57}Fe M*ö*ssbauer, Fong *et al.* proposed that Li_2FeS_2 is formed as an intermediate species during the first plateau at 1.7 V, followed by disproportionation to nonstoichiometric pyrrhotite, FeS_y, and elemental S.[126] Butala *et al.* observed a conversion from Fe and Li_2S to an intermediate ternary local structure during the lower plateau from *ex situ* Fe K-edge XAS and *operando* PDF. A shift in the low-r peaks was observed by PDF for the subsequent plateau, suggesting the expansion and contraction of bond lengths associated with an intercalation-type mechanism.[147] Zou *et al.* proposed that instead of the formation of a ternary intermediate, layered mackinawite FeS is formed during the first plateau, followed by Li_2S oxidation to elemental S, based on *ex situ* XRD and TEM.[241] The conclusions from Zou *et al.* are supported by the electrochemical behavior of the all-solid-state Li-S cell. During the first charge (after initial discharge), Li_2S is oxidized to S_8 (i.e. S^{2-} to S^0) around 2.5 V. Zou *et al.* calculated that the upper plateau around 2.5 V is due to the same process. The result underlines the difficulty of oxidizing S^{2-} in Li_2S, a highly stable material, back to a binary metal persulfide of a different structure. While the conversion would necessitate only partial oxidation, it also requires significant structural reorganization. Instead, the S^{2-} either remains S^{2-} as in FeS or is oxidized all the way to elemental S_8. It follows that the second discharge curve differs from the first, further confirming that pyrite FeS_2 is not recovered at the end of charge.

Although FeS_2 is not recovered at the end of charge, Fe and Li_2S are recovered as discharge products upon cycling. Butala *et al.* showed that the PDF of discharged cycles four and five can be fit with a combination of hexagonal close-packed Fe and Li_2S with larger diameter clusters than early cycles. The result suggests that Fe clusters grow with subsequent discharges.[147] As for subsequent charge cycles, PDF profiles of charge products resemble that of the first cycle, indicating that the same products are recovered.[147] Additionally, each cycle exhibits high Coulombic efficiency, indicating reversible oxidation of Fe and Li_2S. However, absence of pyrite FeS_2 suggests a different mechanism on the first discharge that is not repeated thereafter. In short, FeS_2 undergoes a complex multi-phase mechanism upon the first discharge and is converted to Fe and Li_2S, which is comparable to the mechanism in Li-S systems. Even in FeS_2 systems, the shuttle effect of polysulfides (S_n^{2-}) as

well as Fe dissolution are thought to have an adverse effect on the electrochemical performance.[241–243]

The electronic structure of FeS_2 reveals insights about the effect of metal-anion covalency on anion redox. In the pDOS of FeS_2, the states right below the Fermi level mostly consist of Fe d character (t_{2g}), with little hybridization with the S p states.[192, 244] Above the Fermi level, a stronger hybridization between Fe 3d (e_g) and S 3p states is observed. The calculations agree with the pioneering works of Rouxel that suggested lowering d levels along a period will eventually lead to energetic overlap. As the metal d states overlap with the anion p states, the d levels will be filled at the expense of the sp valence band associated with the anion.[198] The presence of hybridized anion p states near the Fermi level suggests that anion redox can be accessed without subjecting the material to extreme conditions such as high voltages or drastic structural changes.

To summarize, the conversion mechanism using anion redox could yield gravimetric capacities an order of magnitude higher than current commercialized Li-ion cathodes. However, for the conversion of S_8 to Li_2S several factors preclude highly reversible and stable cycling. A primary issue is the slow kinetics associated with the difficulty of converting between structurally dissimilar S_8 and Li_2S. Solution-mediated pathways are more kinetically favorable but incur challenges related to the polysulfide shuttle effect. Forcing solid-state conversion with SSEs results in volume changes that can lead to diminished ionic transport, electronic transport, and interfacial contact issues over time.[245] Pyrite FeS_2 also realizes a high gravimetric capacity accompanied by large structural changes that prove detrimental to long-term efficacy. Conversion mechanisms based on S redox therefore present a foil to the intercalation systems involving S electronic states, discussed in the previous section. Intercalation materials like TiS_2 are highly reversible due to the minimal changes in structure during cycling but are intrinsically limited in capacity. Conversely, conversion materials have high theoretical capacity but large structural changes diminish long-term cyclability. Thus, conversion materials lie on the far right side of the anion redox continuum shown in Figure 2.1 in which maximal charge is stored by the anion and significant structural changes are incurred. In the following section, we will discuss a "hybrid-type" mechanism that incorporates elements of both intercalation and conversion based around S redox, which results in high capacities and good reversibility.

7.4 Intermediate Structure Change: Hybrid Mechanisms

Charge storage mechanisms that lie between conversion and intercalation may offer opportunities for high capacity storage coupled with minimal, or at least reversible, structural changes. The intercalation-type material TiS_2 shows reversible electrochemistry with minimal structural change but with a limited capacity of one electron per transition metal. On the other end of the spectrum, the conversion-type material S_8 can be reduced to Li_2S yielding large capacities but the extensive structural reorganization inhibits reversibility. How can we take advantage of the benefits of both mechanisms while mitigating the drawbacks? Combining mechanistic elements from both intercalation and conversion into a hybrid-type mechanism allows for a middle ground to be achieved. A material that exhibits the reversibility of intercalation chemistry while surpassing the intercalation capacity limit would be transformative for next-generation LIB cathodes. While this limit can be broken by targeting multielectron storage on a single metal, we will focus on mechanisms that employ the electronic states of the anions in the charge compensation mechanism. Because the anion is involved, there is likely to be some structural response to the oxidation. The degree to which the structural response resembles intercalation or conversion depends largely on the system and experimental conditions. The degree to which, and how, S redox is involved also depends on these metrics and understanding the implications of anion redox on the structure is the key to achieving reversible, high capacity, multielectron storage.

To avoid the massive structural rearrangements associated with substantial charge compensation provided by the anion in conversion mechanisms, we can instead target an intermediate regime in which the anion participates in charge compensation but is not fully oxidized. By leveraging only partial oxidation of the anion, perhaps we can achieve more reversible, but still high capacity, storage. To explore the concept of partial anion oxidation, we must first begin with lithiated metal sulfides that contain greater than one mol equivalent of Li^+ relative to the transition metal. These so-called Li-rich metal sulfides allow for the possibility of multielectron oxidation (relative to the transition metal). In Li-rich structures, removal of more than one equivalent of Li^+ requires charge compensation by traditional transition metal redox with additional compensation via anion redox, assuming the metal is only capable of less than one electron redox.

Several Li-rich metal sulfides have been reported and many have Ti in a layered structure, likely due to position of the Ti 3d states relative to the S 3p states. One

recently studied Li-rich sulfide is Li_2TiS_3, but it proves to be electrochemically inactive due to the d^0 Ti^{4+} and apparent inability to access S states.[117, 118] Efforts to activate anion redox have focused on adjusting the band positions of the metal with respect to the S, which can be accomplished by substituting a different metal on the Ti site. Li *et al.* reported the Li-rich sulfide $Li_{1.2}Ti_{0.6}Co_{0.2}S_2$ with appreciable capacity from anion oxidation despite having the same C2/*m* structure as Li_2TiS_3.[117] Charge-density difference maps from DFT showed that the S is the primary contributor during the first oxidation, especially S atoms proximal to Co sites. Co is suggested to change the electronics to stabilize holes on S over oxidation of the metals.

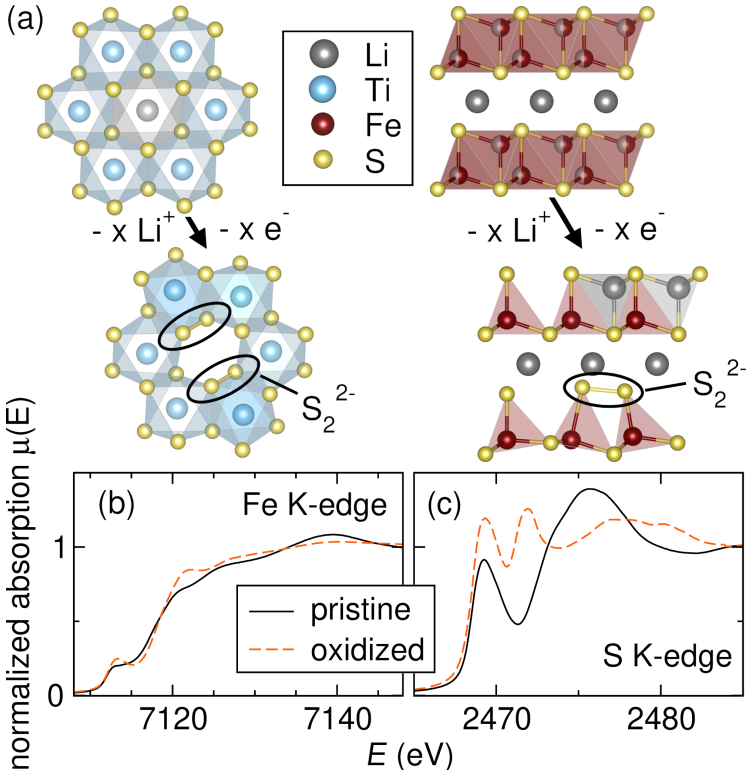

Figure 7.6: The oxidation of S^{2-} could result in the formation of S–S bonds to form a persulfide, S_2^{2-}. The location of the S–S bond will likely vary between different phases. (a) For instance, oxidation of Li_2TiS_3 (left) is suggested to form persulfides, S_2^{2-}, along the octahedral edge. Reproduced from *J. Am. Chem. Soc* **2021**, *143*, 1908–1916. Copyright 2021 American Chemical Society. Oxidation of Li_2FeS_2 (right) causes minimal changes in the Fe local structure and thus the S–S bond is hypothesized to form due to tilting of the corner sharing Fe tetrahedra. X-ray absorption at the (b) Fe and (c) S K-edge of Li_2FeS_2. Reproduced from *J. Am. Chem. Soc.* **2020**, *142*, 6737–6749. Copyright 2020 American Chemical Society.

Anion redox can also be activated through structural manipulations that alter the

electronic interaction between the metal and anion bands. Saha *et al.* reported a family of materials that utilizes chemical substitution to activate anion redox by synthesizing rock-salt Fe-substitued Li_2TiS_3, written as $Li_{1.33-2y/3}Ti_{0.67-y/3}Fe_yS_2$.[118] Here, Fe is formally in the 2+ oxidation state, providing partially filled bands with d character closer in energy to the S 3p states than the 3d states of Ti. As a result, Fe^{2+} is oxidized to Fe^{3+} at early states of charge followed by oxidiation of S^{2-} at higher states of charge as evidenced by spectroscopic characterization. It is worth noting that the authors do not invoke persulfide formation, and instead use S^{n-} to represent partially oxidized S. By *operando* XRD, the discharge pathway differs from the charge pathway but the original structure is regained after a full cycle. However, in all reported systems with Ti^{4+}, Ti^{4+} reduction to Ti^{3+} is invoked upon discharge, which leads to different charge compensation mechanisms and a voltage drop for oxidation in subsequent cycles. Nagarajan *et al.* reported an analogous system using Fe substitution in Li_2SnS_3 instead of Li_2TiS_3. The results are similar in that both Fe and S redox are observed, except in this case the Sn^{4+} remains redox inactive.[246] Structural manipulations can also be accomplished with the introduction of Ti^{3+}. Flamary *et al.* mixed $LiTiS_2$ ($P\bar{3}m$, O1 stacking) and Li_2TiS_3 (C2/m, O3 stacking) to yield a material in the $R\bar{3}m$ space group with both Ti^{3+} and Ti^{4+}.[114] The electrochemical behavior of the synthesized $Li(Li_xTi_{1-x})S_2$ ($0.17 \leq x \leq 0.33$) materials is similar to that of the Fe-substituted system detailed above. Ti^{3+} is first oxidized to Ti^{4+} then S^{2-} is oxidized at higher states of charge. Here, the authors do invoke persulfide formation based on XPS analysis. Li_2TiS_3 can additionally be activated by introducing defects. Mechanochemically prepared Li_2TiS_3 is suggested to form a cation disordered cubic rocksalt phase that can be oxidized,[115, 116] although the stoichiometry of the as-prepared phase is not probed. Oxidation is suggested to involve the sulfide anions resulting in the formation of S–S bonds along the edge of the TiS_6 octahedra near Li^+ vacancies.[115] The S–S bond is predicted by AIMD and the PDF data suggests a new correlation near 2.0 Å which corresponds with the predicted bond length.[115] Kitchaev et al. also predict with DFT that as Li_2TiS_3 is oxidized, a S–S bond will form along the octahedral edge. Their predicted delithiated structure is shown on the left in Figure 7.6a with two persulfides per vacancy.[247] The most direct evidence of a S–S bond is found in the Na literature, and although the Na systems are outside the scope of the perspective, this particular study is worth noting. The S K-edge EXAFS of oxidized $NaCr_{2/3}Ti_{1/3}S_2$ shows a shoulder on the short side of the first shell correlation peak which is suggested to arise due to S–S bond formation.[248]

The rock salt-type structures are suggested to accomodate reversible formation of a S–S bond. To compare, we next turn back to the Li-Fe-S ternary phase space to explore a different structure type. We remind the reader that the reversibilty issues plaguing pyrite FeS_2 revolve around the inability to recover the pyrite structure after initial reduction and to accommodate Li^+ without a large structural change. However, in Li-FeS_2 cells, Li_2FeS_2 with various structures has been proposed as a ternary intermediate, [126, 237] based on the Li-Fe-S ternary isothermal phase diagram at 450 ℃ and ^{57}Fe M*ö*ssbauer.[151, 249, 250] Li_2FeS_2 has also been prepared by solid-state synthesis methods and its structure has been extensively studied.[120, 122, 124, 127] Li_2FeS_2 adopts the $P\bar{3}m1$ space group and crystallizes as a layered material, in which layers of edge-sharing octahedral Li are separated by layers of edge-sharing tetrahedral mixed Fe/Li,[120] as shown in Figure 7.7b. Early reports the electrochemistry of Li_2FeS_2 revealed reversible cycling behavior in an intermediate voltage range between 1.45 and 2.45 V.[123] Fong *et al.* recently demonstrated that the delithiated phase differs from that of pyrite or marcasite FeS_2 and more closely resembles pristine Li_2FeS_2, suggesting that elements of the structure are maintained during cycling.[126] This result also highlights one of the reasons FeS_2 is not formed when cycling Li_2FeS_2. The S sublattices are different; that is, the formally S^- of the persulfide anions in FeS_2 do not adopt the close-packed configuration that the S^{2-} anions in Li_2FeS_2 do. The difference in the S sublattices is visualized in Figure 7.7. The anion sublattice in layered Li_2TiS_3 as described above also adopts a close-packed configuration, and, analogous to Li_2FeS_2, TiS_2 is not observed upon delithiation. As such, Li_2FeS_2 presents an interesting system to explore S redox in a material with structural motifs reminiscent of intercalation-type materials. Recently, Hansen *et al.* studied Li_2FeS_2 extensively and characterized the charge transfer mechanism.[163]

Electrochemical and spectroscopic characterization of Li_2FeS_2 reveals both intercalation and conversion characteristics. As shown in Figure 7.8a, the charge profile of Li_2FeS_2 exhibits an initial sloping region characteristic of intercalation-like behavior followed by a long plateau indicating a transition to two-phase behavior at approx. 2.5 V. Li_2FeS_2, whose theoretical capacity is 400 mAh g^{-1} based on full delithation, exhibits a capacity of 350 mAh g^{-1}, indicating multielectron transfer. Charge compensation in the initial sloping region is associated with $Fe^{2+/3+}$ oxidation, which is supported by the shift in the rising Fe K-edge to a higher energy as shown in Figure 7.6b.[163] In the subsequent plateau, a new pre-edge feature appears in the S K-edge spectrum as shown in Figure 7.6c that matches the pre-edge fea-

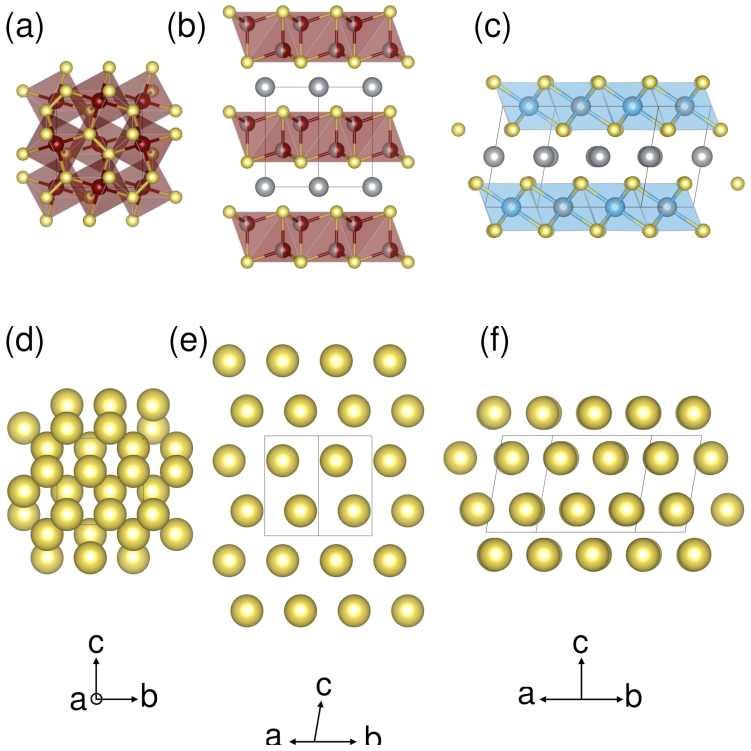

Figure 7.7: The structures of (a) pyrite FeS_2, (b) Li_2FeS_2, (c) Li_2TiS_3, and (d–f) their corresponding anion sublattices shown as space-filling models. Spacing-filling models show that Li_2FeS_2 and Li_2TiS_3 anions are close packed while those of FeS_2 are not.

ture associated with persulfides in pyrite FeS_2, suggesting S oxidation to persulfides ($(S_2)^{2-}$).[163] Interestingly, the position of the Fe K-edge does not shift in the plateau region, suggesting that oxidation occurs in a discrete fashion with S following Fe. The subsequent discharge curve somewhat mirrors the charge curve with a plateau at 2.2 V and a sloping region below 2.2 V. The difference in the charge/discharge profiles suggests a different redox pathway as opposed to a simple reversal of the charge process. Nonetheless, the Fe and S K-edges of discharged Li_2FeS_2 resemble those of the pristine material, suggesting that Fe and S are reversibly reduced to the pristine states at the end of discharge.[163] It is important to note that the lower voltage cutoff here is limited to 1.7 V, thereby preventing reduction to Fe and Li_2S, which, based on cycling of FeS_2, is not fully reversible.[147]

The unusual electrochemical behavior suggests topotactic deintercalation of Li^+ in the initial stages compensated primarily by oxidation of Fe^{2+}. The following flat plateau indicates a transition from a single-phase intercalation-like mechanism to a two-phase mechanism during which S^{2-} is oxidized to S_2^{2-}. pDOS calculations

show that the bands near the Fermi level are dominated by Fe d states initially but become more covalent with S p states as Li^+ is removed, which eventually manifests as a transition from Fe to S oxidation.[163] Assuming the plateau is solely anion redox, approximately 50% of the S^{2-} is oxidized to S_2^{2-}. Unlike in FeS_2, elemental S_8 is not observed spectroscopically or in the *operando* XRD. Only a 3% contraction along the C direction is observed by *operando* XRD.[163] Therefore, it follows that persulfide formation results in minimal long-range structural transformations and the parent layered structure is largely maintained. Persulfides may distort the structure locally, and the EXAFS analysis suggests a possible mechanism of tetrahedral tilting as shown in Figure 7.6b. However, upon discharging the original structure reforms, indicating persulfide formation is reversible and minimally disruptive. The same cannot often be said for Li-rich oxides. One of the best performing examples, Li_2RuO_3, adopts a layered structure similar to Li_2TiS_3 and is able to cycle over 1.5 eq. of Li per formula unit as shown on the right in Figure 7.8a. During the first charge, several plateau features are observed, including one around 4.2 V that is attributed to oxidation of O^{2-}.[24, 25, 251] The character of the oxidized O is debated, with hypotheses including localized holes on O,[44] formation of peroxo-like moieties,[26] and trapped molecular O_2.[48] Regardless of the mechanism, which may be material dependent, in all cases the first charge cycle looks significantly different than the discharge and subsequent cycles. The change in shape is also accompanied by a significant drop in capacity - 13 % in the case of Li_2RuO_3. As such, the complex nature of the oxidation mechanism and inherent partial irreversibility in oxides motivates interest in the reversible anion redox observed in some sulfides.

The reversibility of Li-rich metal sulfides is intrinsically linked to the oxidation mechanism, specifically the electronic and structural nature of anion oxidation. As alluded to earlier in this section, Li^+ vacancies have been purported to facilitate S–S bond formation during the oxidation of S^{2-} in several materials systems. Ab initio molecular dynamics simulations by Sakuda *et al.* probed the structural response to delithation of disordered cation rocksalt phase of Li_2TiS_3.[115] S atoms adjacent to more than one Li^+ vacancy preferentially formed S–S bonds.[115] Flamary *et al.* also hypothesize about the importance of vacancies in forming S–S dimers, rationalizing it through a reductive coupling mechanism.[114] That is, S^{2-} is oxidized to S^-, which is short-lived due to Ti-S covalency and rapidly reduces Ti^{4+} to Ti^{3+} forming S_2^{2-} moieties preferentially along the octahedral edges of Ti surrounding Li^+ vacancies. However, neither experimental nor computational evidence for this hypothesis is given. Kitchaev *et al.* filled the computational evidence gap by performing DFT

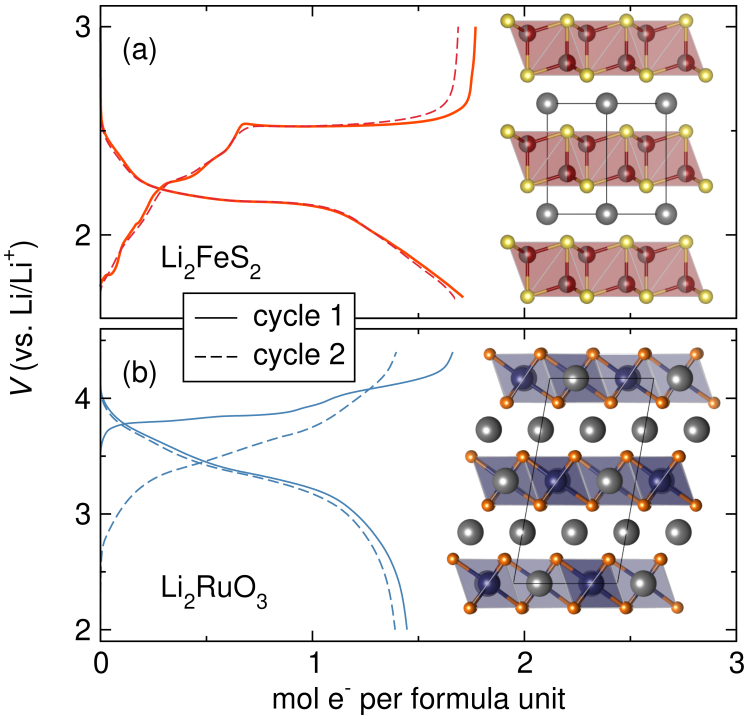

Figure 7.8: Galvanostatic cycling of (a) Li_2FeS_2 and (b) Li_2RuO_3, which both exhibit multielectron storage based on cation and anion redox contributions. The cycling behavior of Li_2FeS_2 is much more reversible than that in Li_2RuO_3. Li_2FeS_2 electrochemistry adapted from *J. Am. Chem. Soc.* **2020**, *142*, 6737–6749. Copyright 2020 American Chemical Society.

calculations on oxidized Li_2TiS_3 with both the Ti^{3+} and Fe^{2+} substitutions finding that both preferentially formed persulfide moieties along metal octahedral edges adjacent to Li^+ vacancies.[247] The importance of vacancies carries to other structure types as well. In Li_2FeS_2, we hypothesize that the formation of vacancies upon oxidation cause formerly edge-sharing tetrahedra to become corner-sharing. The now corner-sharing tetrahedra can then tilt to form a S–S bond during oxidation without changing the first coordination shell of the Fe, which does not change much according to the EXAFS data.[163] Although the S–S bond is not being formed along a polyhedral edge, this type of structural persulfide formation mechanism also requires the presence of Li^+ vacancies.

The high reversibility of Li_2FeS_2 provides insights about design rules for multielectron cathode materials. First, the oxidation of Fe to compensate for initial Li^+ removal via intercalation plays two roles: (1) it allows for rehybridization of the Fe d and S p bands resulting in increased covalency and S p states closer to the Fermi level, and (2) it creates vacancies in the lattice that provide space and degrees of free-

dom for the distortions necessary to bring adjacent S atoms close enough together to form persulfides. By this mechanism, the oxidation of S^{2-} is limited such that the layered structural framework is largely maintained. Furthermore, by limiting the lower voltage cutoff, there is no over-reduction to Li_2S. Notably, Li-Li_2FeS_2 cells polarize during oxidation upon delithation of approximately 1.8 eq. of Li without any signs of over-oxidation to elemental S, indicating the integrity of the layered structure even at high degrees of delithation. Fe maintains its coordination number during cycling without migrating to an octahedral environment.[163] Unlike Li-rich oxide materials in which the metal–O bond breaks prior to the formation of peroxo-like species, S is able to make S–S bonds without breaking the metal–S bond. The retained metal–anion bond mitigates the metal migration that produces densification and capacity loss in oxides.[56, 57] Minimal phase change also signifies that there is little volume expansion of the active material, ensuring electrical contact for continued cycling and simple synthesis without the need for nanostructuring. By avoiding a full conversion to a completely different species while accessing extra e^- transfer via S redox, the hybrid mechanism can significantly increase capacities of cathode materials.

From studying the mechanism of Li_2FeS_2 in comparison with that of FeS_2, we highlight the importance of a structural framework that can accommodate persulfide formation while avoiding conversion to Li_2S or S_8. The formation of a S–S bond necessitates degrees of freedom on the local scale to allow distortions that lead to persulfide formation. Therefore, we recognize the importance of understanding structural motifs that accommodate persulfide formation.

7.5 Persulfide Survey

Persulfide formation is hypothesized to be a mechanism by which sulfides are oxidized in multielectron anion redox materials with high reversibility. Therefore, it is prudent to understand what structural motifs and environments support persulfide formation. The most reversible electrochemical cycling will occur between materials that are thermodynamically stable (e.g. TiS_2 and $LiTiS_2$). As such, we compiled a list of solid-state binary (*-S) and ternary (*-*-S) phases that contain persulfide moieties in thermodynamically stable structures. Alkali, alkaline earth, and transition metals as well as metalloids and lanthanides were all considered. Structures predicted with DFT from Materials Project[252] were cross-referenced with experimentally reported structures from the Inorganic Crystal Structure Database (ICSD)[253, 254]. Only materials that were synthesized and characterized are in-

cluded in the survey. A summary of the survey results for both binary and ternary sulfides is shown in Figure 7.9. Here, a subset of materials and structures are discussed to identify trends, but the full lists of binary and ternary materials containing persulfides from the survey can be found in the publication from which this chapter is adapted.

Only two persulfides exist in groups 1 and 2 that can be synthesized at ambient pressure: Na_2S_2 and BaS_2. Na_2S_2 is isostructrual to Li_2O_2 with alternating layers of octahedrally coordinated Na and trigonal bipyramidal Na with persulfides along *c*.[255] BaS_2 has eight-coordinate Ba with persulfides along two polyhedral edges per Ba.[256] With there being so few stable persulfides in these groups, it is difficult to pull out trends. However, the transition metals provide a much richer phase space. Group 3 has no binary persulfides or compounds of the form MS_2 because the elements only have one d electron and are not stable in a 4+ oxidation state. All elements in Groups 4 and 5, apart from V, form compounds with MS_3 stoichiomtery in the $ZrSe_3$ or $NbSe_3$ structure type consisting of high-coordinate metals with several persulfides along polyhedral edges.[257, 258] V forms persulfides in VS_4 with eight-coordinate V and four persulfides per metal.[259] Group 6 does not form any persulfides. Upon reaching Group 7, a significant change to the stable S-rich materials is observed. Mn,[260] Fe,[261] Ru,[262] Os,[263] Co,[261] and Rh[264] all form stable phases of the form MS_2 with space group $Pa\bar{3}$, the pyrite structure. The pyrite structure consists of corner-sharing MS_6 octahedra and all S exists as part of a persulfide. As a result, the metals are in the 2+ oxidation state. This is at odds with materials like TiS_2, VS_2, and others from earlier groups that adopt a $P\bar{3}m$ structure with layers of edge-sharing MS_2 octahedra separated by van der Waals gaps. The $P\bar{3}m$ structures contain no persulfides and the metals are in the 4+ oxidation state. The phenomenon has been called the "layered-to-pyrite" transition and is due to greater overlap of metal d and anion sp bands moving across the period from left to right.[198] Later group metals like Rh and Ir also form compounds with persulfides where the metal is in the 3+ oxidation state (e.g. Rh_3S_4[265] and Ir_3S_8[266]). Interestingly, these materials have similar connectivity to the pyrite structure with some corner-sharing octahedra that are connected by persulfides. Ir_3S_8 is a defect pyrite structure with ordered vacancies. Moving into Groups 10, 11, and 12, materials with the pyrite structure can be found for Ni, Cu, Zn, and Cd but have only been successfully synthesized at high pressure.[261]

In the survey, no post-transition metal or metalloid binary persulfides were found

synthesized at ambient pressure. Additionally, there are some lanthanides that have persulfides and they are generally of the form LS_2[267] or $LS_{1.9}$[268] with the lanthanide most commonly in the 3+ oxidation state. The structure of these lanthanide materials is always high-coordinate lanthanide (most often nine-coordinate) with one or two persulfide edges and a combination of face- and edge-sharing connectivity.

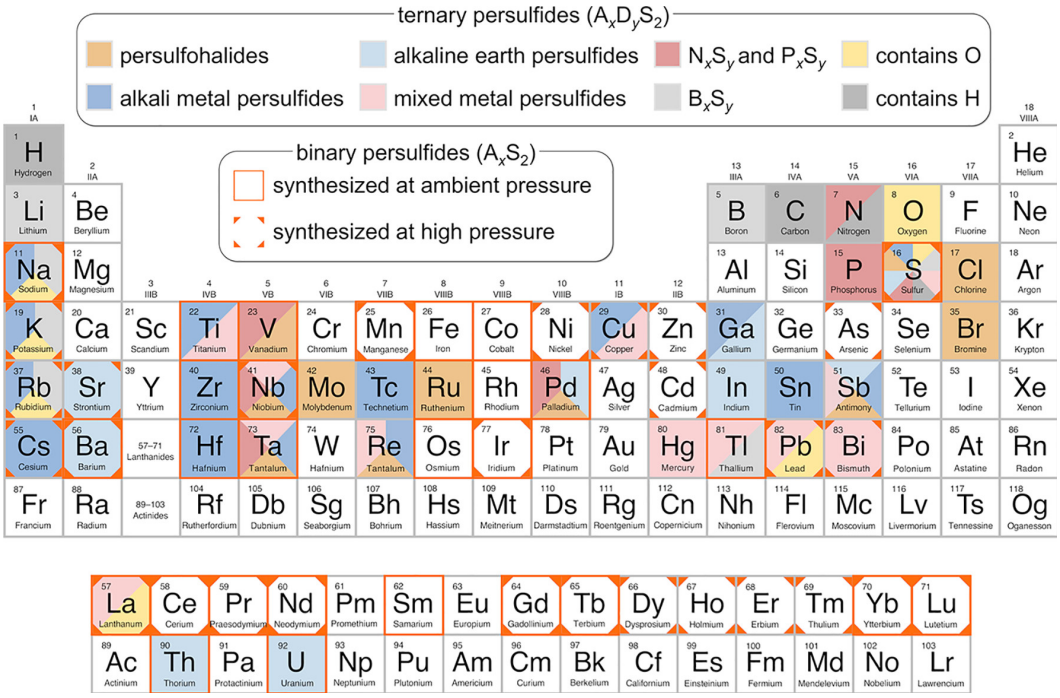

Figure 7.9: Elements that constitute reported binary and ternary sulfide phases containing persulfide S_2^{2-} moieties. Solid and dashed purple borders represent binary phases synthesized at ambient pressure and high pressure, respectively. Binary materials that form with stable persulfides at ambient pressure are good starting points for further investigation into electrode materials that can best accommodate reversible anion redox. Fill colors indicate compositional categories for ternary materials. The composition of a ternary persulfide depends on the electronic structure, size, and favorable coordination environments of each constituent ion.

From the results of the survey of binary S-containing materials, several trends are observed. When the cation is a transition metal, the metal-anion interactions dictate the electronic structure and thereby the physical structure in which the material crystallizes. A notable example is the layered-to-pyrite transition, which is most starkly observed in MS_2 phases going across the period of 3d transition metals.[198] If the metal d states overlap sufficiently with the S p states, the S is oxidized preferentially over the metal, which stays in a lower oxidation state. In this case, nearly all binary transition metal persulfides have octahedrally coordinated metals with some degree of corner-sharing connectivity and persulfides joining adjacent

polyhedra with primary examples being the pyrite and marcasite structures. We note that the materials still contain metal-anion bonds. If the metal d-S p overlap is not sufficient, the metals are stable in a more highly oxidized state and with the S present as sulfide (S^{2-}). This is observed in materials that adopt a layered structure like TiS_2. Moving to 4d and 5d transition metals and to different metal:anion ratios, this trend has exceptions in which metals adopt a higher order, irregular, and unsymmetrical coordination environment with the persulfides along polyhedral edges instead of connecting adjacent polyhedra. Several persulfide-containing phases are stable with cations that are not transition metals but structural trends within the families are not obvious.

We also surveyed ternary systems. The survey returned 103 unique materials, of which 71 contain persulfides. Here, a persulfide is defined as a S–S dimer where neither S atom is a part of a polyanion or a longer polysulfide chain. Contrary to the binary survey, a majority (48) of the ternaries with persulfides include an alkali or alkaline earth metal. Notably, only one phase contains Li, $Li_2B_2S_5$, which has an unusual structure in which persulfides are found as part of five-membered B_2S_3 rings connecting layers of distorted edge-sharing LiS_4 tetrahedra.[269] There are similar materials with Na ($Na_2B_2S_5$[269]) and K ($K_2B_2S_7$[270]), but as the the cation gets larger moving down the group, the alkali metal cation coordination number increases. In $Na_2B_2S_5$, the Na cations adopt a distorted octahedral geometry, and, in $K_2B_2S_7$, the K cations are able to accommodate an 8-coordinate environment and include additional persulfides along polyhedral edges. The theme of larger cations resulting in high-coordinate environments to accommodate persulfides continues with Rb and Cs, and the number of reported compounds increases going down the group as well. Most are of the form $A_xM_yS_z$ where A is an alkali metal and M is either a 4d[271, 272] or 5d[273] transition metal (with the exception of Ti) or a later group post-transition metal or metalloid (i.e. Ga,[274] Sn,[275] Sb[276]). The few materials with alkaline earth metals have distorted 8-coordinate Sr or Ba with persulfides again along polyhedral edges.[277, 278] Beyond Groups 1 and 2, there are several stable ternary transition metal sulfide halides–such as $V_4S_9Br_4$,[279] MoS_2Cl_3,[280] and NbS_2Br_2[281]–that adopt structures with similar bonding motifs consisting of high-coordinate metals in small clusters linked in two-dimensional layers. Additional ternary transition metal sulfides that have persulfide moieties include late-group post-transition metals and metalloids like Tl,[282] Sb,[283] and Bi,[284] which adopt high-coordinate environments with S. Very few ternary lanthanides with S–S dimers as defined here have been reported with the only examples being LaSO,[285]

in which the anions separate into distinct layers, and La_2CuS_4.[286] In both cases, La adopts an 8-coordinate environment with S.

Among ternary materials, the survey shows that a consistent structural feature of stable persulfides is high-coordinate environments of one or more component with S, leading to S–S dimers forming along polyhedral edges. Of course, the cation size is a significant factor that determines the type of coordination environments a particular atom is likely to adopt. Therefore, it makes sense that most of the ternary materials found through this survey have at least one late-group, large element that is able to accommodate high-order and unusual coordination environments. This trend is also observed in the survey of the binaries as detailed above, apart from those that form in the pyrite or marcasite MS_2 structures. It follows, then, that perhaps the pyrite and marcasite transition metal sulfides are to be regarded as more of an exception to the rule that thermodynamically stable S–S dimers require high-coordinate atoms and tend to result in unusual and low-symmetry structures.

7.6 Sulfide Oxidation vs. Oxide Oxidation

Now that we have explored anion redox in metal sulfides, we can compare their structural response to that in the analogous Li-rich oxides. Li-rich oxides have been a focus of research in the battery field for over a decade due to high capacities and operating voltages. Multielectron redox has been observed in several materials with the most reversible being in the Li_2MO_3 family where M is a 4d or 5d metal, sometimes with 3d metals and metalloids added for stability.[24, 25, 27, 287] Oxidation of lattice O is invoked in these systems and a mechanism of peroxide formation has been suggested based on experimental and computational results. However, the available evidence is convoluted by complex and competing decomposition reactions. The difficulty of studying anion redox in oxides is one of the reasons sulfides provide a rich opportunity to understand the structure-property relationships that govern reversible anion redox behavior. Oxidation of sulfides is easier to control than oxides as S_8 is a solid and O_2 is a gas, which is released from the lattice causing densification around O vacancies, metal over-reduction, pressure buildup in the cell, and significant capacity fade.[23, 56, 57, 60] This difference is due to the fact that valence electrons in S have a principal quantum number of 3 and there are vacant d orbitals that can be used in bonding, which results in the formation of molecular crystals like S_8. Conversely, O may only form sp hybridized bonds, which is why multi-atom forms of O only include gases like O_2 and O_3. Another advantage is that sulfide oxidation to persulfides also occurs at a lower voltage

than oxide oxidation and is therefore not convoluted by electrolyte decomposition reactions. Furthermore, many commonly used electrolytes like $LiPF_6$ in organic carbonates do not contain S, so even if there was electrolyte decomposition on the cathode, element-specific characterization techniques would be unaffected. Finally, there are very few binary transition metal peroxides with the most common being in Group 12 (ZnO_2, CdO_2, HgO_2). As such, if peroxides are forming in Li-rich metal oxides, the fully delithiated end member will not be stable. This also holds true for LCO and isostructural oxides. In LCO, if greater than half an equivalent of Li^+ is removed, there are several monoclinic phase transformations because layered CoO_2 is not a stable phase.[288] In the case of sulfides, there are many stable binary persulfides as mentioned above, suggesting a richer phase space for potential anion redox materials.

7.7 Conclusions and Outlook

Sulfur anion redox has been studied for decades and presents a viable method to significantly increase charge storage capacity in cathode materials. The response of the structure to anion redox plays a significant role in determining cycling stability and overall reversibility of the cathode materials. In general, the more the anion is contributing to the charge compensation processes, the more the structure will respond. In the case of lithiation of TiS_2, S contributes minimally to the charge compensation and thus oxidation incurs only a slight structure change upon formation of $LiTiS_2$ leading to highly reversible cycling. In the case of conversion-type mechanisms like that of S_8, S is the sole contributor to the charge compensation causing dramatic structural reorganization, kinetic bottlenecks, and poor reversibility. A hybrid-type mechanism that employs elements of both intercalation and conversion partially reaps the benefits of both while mitigating the pitfalls. Specifically, a material that couples the intercalation chemistry associated with redox on a transition metal with the minimal bond forming and breaking reactions associated with anion redox is desirable. The bond forming and breaking reactions must be reigned in to maintain the skeleton of the original material, thereby preventing the substantial disruptive rearrangements associated with conversion chemistry.

To take advantage of the high capacities afforded by anion redox, the redox reactions must be reversible. In the best case scenario, the charge and discharge pathways are symmetric, as is the case for TiS_2, which limits processes that cause capacity fade. However, reaction path hysteresis, when the charge pathway differs from the discharge pathway, does not always result in reduced cyclability. For instance, in

the case of Li_2FeS_2, even though the reaction paths for oxidation and reduction are not identical, the structure of the discharged material closely resembles the pristine structure leading to charge curves on the second cycle that is nearly identical to the first.[163] The framework of Li_2FeS_2 is maintained enough during charge that it can reform during discharge. This is not the case for FeS_2, which does not go through a Li_2FeS_2 intermediate upon discharge, depending on the rate.[241] The kinetic control over the reaction pathway is a consequence of the bond forming and breaking reactions that are hallmarks of sulfide oxidation, or persulfide reduction. Therefore, starting with an oxidized material and lithiating does not always yield the same results as delithiating a chemically similar material. As such, it is important to begin with a structural framework that can accommodate both the sulfide and persulfide structural motifs.

In an ideal case, the sulfide and persulfide end-members are both thermodynamically stable phases. Per our survey of binary and ternary materials with S–S dimers, we found only a limited number of stable materials with oxidized S in this form. Nevertheless, the stable persulfide-containing materials provide potential starting points for structural frameworks that may support reversible anion redox. We note, however, that it may be beneficial to leave some alkali in the material upon oxidation to help preserve the framework. In the case of Li_2FeS_2, full electrochemical oxidation to FeS_2 cannot be achieved due to the kinetic overpotentials required to convert the phase. Thus, Li_2FeS_2 has a built-in mechanism that prevents substantial structural rearrangement, but this is not true if one were to start with FeS_2.

When considering materials that start lithiated, we suggest it is important to consider how the formation of vacancies might play a role in enabling persulfide formation. Oxidization of sulfides to persulfide requires a rehybridization of the S 3p orbitals, and thus those p orbitals cannot be tied up in a metal-S bond or a Li-S bond. It is likely that the vacancies allow for the rehybridization and also provide structural flexibility that is needed to form the S–S bond.

Further important considerations when selecting candidate materials are the oxidation state of the transition metal and the structure. Leveraging transition metal redox and finding a structure that accommodates a large alkali content are critical. The cost and availability as well as the mass of the components should be assessed to minimize cost and maximize gravimetric capacity and energy density. In this context, the fact that many stable persulfides form in high-coordinate environments supported by heavy elements is limiting. There are still, though, several candidate

materials that meet these qualifications.

As the field moves forward investigating anion redox, we hope more researchers will continue to place emphasis on not just understanding the changes to the electronic structure (e.g. oxidation state, metal-anion covalency, band structure) but also the changes to the physical structural in response to anion redox. We highlight the importance of *operando* characterization to view changes in real time and under operating conditions. Although *ex situ* measurements are valuable, the physical structure of a partially delithiated material can change significantly as the structure relaxes into an equilibrium state different than the structure while cycling.

Of course, several challenges remain in the field of anion redox in sulfides. We still do not fully understand the structure of the oxidized materials because long range order is often lost. Carefully evaluating the materials with local structure probes will prove to be an exciting area. Recent advances in modeling spectroscopic signatures as they relate to structure, for instance in XAS, will also prove to be a useful tool. Although we focus on the formation of persulfides as a result of sulfide oxidation, stabilizing holes on S without a rehybridization is another way in which anion redox may be leveraged. Such a mechanism is likely when S is participating minimally in charge storage, but the more the p states are depopulated, the more likely the p orbitals will rehybridize to form S–S bonds.

An additional challenge is the voltage associated with anion redox of S. The S 3p states lie at a much higher energy compared to O 2p, and thus the voltage for oxidation and reduction is low. Most anion redox in sulfides occurs near 2.5 V vs. Li/Li^+ and it is crucial to increase the voltage. We caution that overpotentials may appear to increase the voltage, but we must engineer the crystal chemistry and structure to increase the thermodynamic potential. We hope the field will take interest in answering the above questions to uncover the secrets of anion redox and move towards engineering better performing, high-capacity cathodes for next-generation LIBs.

7.8 Experimental Methods

Li_2RuO_3 Synthesis and Electrochemistry. *Synthesis*: Li_2RuO_3 was synthesized according to the procedure outlined by Sathiya *et al.*[25] Li_2CO_3 (Sigma-Aldrich, 99+%) and RuO_2 (Acros Organics, 99.5%, anhydrous) were ground in stoichiometric quantities (with a 10% by weight excess of Li_2CO_3 to counter Li loss at high temperatures) and pressed into pellets with a hand-operated arbor press. Pellets

were heated in alumina crucibles in air at 2 °C min^{-1} to 800 °C with a dwell time of 6 h and cooled ambiently to room temperature. The powder was then heated at 2 °C min^{-1} to 900 °C for 12 h and 1100 °C for 12 h with intermediate grinding steps.

Electrochemistry: Slurries for laminate electrodes were prepared by suspending 80/10/10 (wt%) active material, conductive carbon (SuperP, Alfa Aesar, > 99%), and PVDF binder (MTI) in *N*-methyl-2-pyrrolidone (approximately 2 times by mass of total solids) (Sigma-Aldrich, 99.5%) with a centrifugal mixer (Thinky USA). Laminates were prepared by doctor blading onto carbon-coated Al foil (MTI) at a 20 μm thickness. The films were dried in air overnight and 1/2" diameter electrodes were punched from the film. The electrodes were dried in a vacuum oven at 110 °C for at least 12 h, yielding an active material loading of 4-6 mg.

Galvanostatic cycling experiments were performed in 2032 coin cells with a Li foil counter, Celgard 2400 separator, and 1 M $LiPF_6$ in 1:1:3 (v/v) ethylene carbonate/propylene carbonate/dimethyl carbonate (all Sigma, > 99%, anhydrous) electrolyte at a rate of C/10 based on 1 electron per formula unit.

Persulfide Survey Search Procedure. The structure survey was accomplished in Python 3.8.5 running on Ubuntu (version 20.04.2 LTS). All S-containing structures were initially queried from the Material's Project repository using the Pymatgen library (version 2020.8.3) and its MPRester class. Structures with E_{hull} values greater than 0 eV were excluded. Each structure was then converted to an Atoms object using the Atomic Simulation Environment (ASE version 3.19.1) and its AseAtomsAdaptor class. The get_all_neighbors() method was employed to screen for structures where the closest S-S distance was no greater than 2.25 angstroms. Structures that met the 2.25 angstrom cutoff were exported as .cif files and manually examined in Vesta. Structures were cross-referenced with the ICSD to include only experimentally reported phases.

Bibliography

[1] Moreau, P.; Ouvrard, G.; Gressier, P.; Ganal, P.; Rouxel, J. Electronic Structures and Charge Transfer in Lithium and Mercury Intercalated Titanium Disulfides. *J. Phys. Chem. Solids* **1996**, *57*, 1117–1122.

[2] Jay, A.; Reidmiller, D.; Avery, C.; Barrie, D.; DeAngelo, B.; Dave, A.; Dzaugis, M.; Kolian, M.; Lewis, K.; Reeves, K.; Winner, D. Impacts, Risks, and Adaptation in the United States: Fourth National Climate Assessment. *U.S. Global Change Research Program* **2018**, *2*, 33–71.

[3] Yang, Z.; Zhang, J.; Kintner-Meyer, M. C. W.; Lu, X.; Choi, D.; Lemmon, J. P.; Liu, J. Electrochemical Energy Storage for Green Grid. *Chem. Rev.* **2011**, *111*, 3577–3613.

[4] Mongird, K.; Viswanathan, V.; Alam, J.; Vartanian, C.; Baxter, R.; Sprenkle, V. *2020 Grid Energy Storage Technology Cost and Performance Assessment*; 2020.

[5] Olabi, A. G.; Onumaegbu, C.; Wilberforce, T.; Ramadan, M.; Abdelkareem, M. A.; Al – Alami, A. H. Critical Review of Energy Storage Systems. *Energy* **2021**, *214*, 118987.

[6] Choi, D.; Shamim, N.; Crawford, A.; Huang, Q.; Vartanian, C. K.; Viswanathan, V. V.; Paiss, M. D.; Alam, M. J. E.; Reed, D. M.; Sprenkle, V. L. Li-Ion Battery Technology for Grid Application. *J. Power Sources* **2021**, *511*, 230419.

[7] Tian, Y.; Zeng, G.; Rutt, A.; Shi, T.; Kim, H.; Wang, J.; Koettgen, J.; Sun, Y.; Ouyang, B.; Chen, T.; Lun, Z.; Rong, Z.; Persson, K.; Ceder, G. Promises and Challenges of Next-Generation "Beyond Li-ion" Batteries for Electric Vehicles and Grid Decarbonization. *Chem. Rev.* **2021**, *121*, 1623–1669.

[8] Stecca, M.; Elizondo, L. R.; Soeiro, T. B.; Bauer, P.; Palensky, P. A Comprehensive Review of the Integration of Battery Energy Storage Systems Into Distribution Networks. *IEEE Open J. Ind. Electron. Soc.* **2020**, *1*, 46–65.

[9] Mizushima, K.; Jones, P. C.; Wiseman, P. J.; Goodenough, J. B. Li_xCoO_2 (0<x<-1): A new cathode material for batteries of high energy density. *Mater. Res. Bull.* **1980**, *15*, 783–789.

[10] Shaju, K. M.; Bruce, P. G. Macroporous Li(Ni1/3Co1/3Mn1/3)O2: A High-Power and High-Energy Cathode for Rechargeable Lithium Batteries. *Adv. Mater.* **2006**, *18*, 2330–2334.

[11] Chen, C. H.; Liu, J.; Stoll, M. E.; Henriksen, G.; Vissers, D. R.; Amine, K. Aluminum-Doped Lithium Nickel Cobalt Oxide Electrodes for High-Power Lithium-Ion Batteries. *J. Power Sources* **2004**, *128*, 278–285.

[12] Nitta, N.; Wu, F.; Lee, J. T.; Yushin, G. Li-Ion Battery Materials: Present and Future. *Mater. Today* **2015**, *18*, 252–264.

[13] Yamada, A.; Chung, S. C.; Hinokuma, K. Optimized LiFePO4 for Lithium Battery Cathodes. *J. Electrochem. Soc.* **2001**, *148*, A224.

[14] Assat, G.; Tarascon, J.-M. Fundamental Understanding and Practical Challenges of Anionic Redox Activity in Li-ion Batteries. *Nat. Energy* **2018**, *3*, 373–386.

[15] Rozier, P.; Tarascon, J. M. Review—Li-Rich Layered Oxide Cathodes for Next-Generation Li-Ion Batteries: Chances and Challenges. *J. Electrochem. Soc.* **2015**, *162*, A2490–A2499.

[16] Grimaud, A.; Hong, W. T.; Shao-Horn, Y.; Tarascon, J.-M. Anionic Redox Processes for Electrochemical Devices. *Nat. Mater.* **2016**, *15*, 121–126.

[17] Li, B.; Xia, D. Anionic Redox in Rechargeable Lithium Batteries. *Adv. Mater.* **2017**, *29*, 1701054.

[18] Hu, S.; Pillai, A. S.; Liang, G.; Pang, W. K.; Wang, H.; Li, Q.; Guo, Z. Li-Rich Layered Oxides and Their Practical Challenges: Recent Progress and Perspectives. *Electrochem. Energ. Rev.* **2019**, *2*, 277–311.

[19] Yang, J.; Niu, Y.; Wang, X.; Xu, M. A Review on the Electrochemical Reaction of Li-rich Layered Oxide Materials. *Inorg. Chem. Front.* **2021**, *8*, 4300–4312.

[20] M. Thackeray, M.; Kang, S.-H.; S. Johnson, C.; T. Vaughey, J.; Benedek, R.; A. Hackney, S. Li_2MnO_3-Stabilized $LiMO_2$ (M = Mn, Ni, Co) Electrodes for Lithium-Ion Batteries. *J. Mater. Chem.* **2007**, *17*, 3112–3125.

[21] Thackeray, M. M. Manganese Oxides for Lithium Batteries. *Prog. Solid State Chem.* **1997**, *25*, 1–71.

[22] Robertson, A. D.; Bruce, P. G. Mechanism of Electrochemical Activity in Li_2MnO_3. *Chem. Mater.* **2003**, *15*, 1984–1992.

[23] Rana, J.; Papp, J. K.; Lebens-Higgins, Z.; Zuba, M.; Kaufman, L. A.; Goel, A.; Schmuch, R.; Winter, M.; Whittingham, M. S.; Yang, W.; McCloskey, B. D.; Piper, L. F. J. Quantifying the Capacity Contributions during Activation of Li_2MnO_3. *ACS Energy Lett.* **2020**, *5*, 634–641.

[24] Sathiya, M.; Ramesha, K.; Rousse, G.; Foix, D.; Gonbeau, D.; Prakash, A. S.; Doublet, M. L.; Hemalatha, K.; Tarascon, J.-M. High Performance $Li_2Ru_{1-y}Mn_yO_3$ ($0.2 \leq y \leq 0.8$) Cathode Materials for Rechargeable Lithium-Ion Batteries: Their Understanding. *Chem. Mater.* **2013**, *25*, 1121–1131.

[25] Sathiya, M.; Rousse, G.; Ramesha, K.; Laisa, C. P.; Vezin, H.; Sougrati, M. T.; Doublet, M.-L.; Foix, D.; Gonbeau, D.; Walker, W.; Prakash, A. S.; Hassine, M. B.; Dupont, L.; Tarascon, J.-M. Reversible Anionic Redox Chemistry in High-Capacity Layered-Oxide Electrodes. *Nat. Mater.* **2013**, *12*, 827.

[26] McCalla, E.; Abakumov, A. M.; Saubanère, M.; Foix, D.; Berg, E. J.; Rousse, G.; Doublet, M.-L.; Gonbeau, D.; Novák, P.; Van Tendeloo, G.; Dominko, R.; Tarascon, J.-M. Visualization of O-O Peroxo-like Dimers in High-Capacity Layered Oxides for Li-ion Batteries. *Science* **2015**, *350*, 1516–1521.

[27] Pearce, P. E.; Perez, A. J.; Rousse, G.; Saubanère, M.; Batuk, D.; Foix, D.; McCalla, E.; Abakumov, A. M.; Tendeloo, G. V.; Doublet, M.-L.; Tarascon, J.-M. Evidence for Anionic Redox Activity in a Tridimensional-Ordered Li-rich Positive Electrode β-Li_2IrO_3. *Nat. Mater.* **2017**, *16*, 580.

[28] James, A. C. W. P.; Goodenough, J. B. Structure and Bonding in Lithium Ruthenate, Li_2RuO_3. *J. Solid State Chem.* **1988**, *74*, 287–294.

[29] Li, B.; Shao, R.; Yan, H.; An, L.; Zhang, B.; Wei, H.; Ma, J.; Xia, D.; Han, X. Understanding the Stability for Li-Rich Layered Oxide Li_2RuO_3 Cathode. *Adv. Funct. Mater.* **2016**, *26*, 1330–1337.

[30] Sathiya, M.; Abakumov, A. M.; Foix, D.; Rousse, G.; Ramesha, K.; Saubanère, M.; Doublet, M. L.; Vezin, H.; Laisa, C. P.; Prakash, A. S.; Gonbeau, D.; VanTendeloo, G.; Tarascon, J.-M. Origin of Voltage Decay in High-Capacity Layered Oxide Electrodes. *Nat. Mater.* **2015**, *14*, 230–238.

[31] Lyu, Y.; Hu, E.; Xiao, D.; Wang, Y.; Yu, X.; Xu, G.; Ehrlich, S. N.; Amine, K.; Gu, L.; Yang, X.-Q.; Li, H. Correlations between Transition-Metal Chemistry, Local Structure, and Global Structure in $Li_2Ru_{0.5}Mn_{0.5}O_3$ Investigated in a Wide Voltage Window. *Chem. Mater.* **2017**, *29*, 9053–9065.

[32] Kobayashi, H.; Kanno, R.; Kawamoto, Y.; Tabuchi, M.; Nakamura, O. Physical Properties of the De-Lithiated $Li_{2-x}RuO_3$ with the Layered Structure. *Solid State Ion.* **1996**, *86–88*, 859–863.

[33] Chen, Y.-C.; Huo, M.; Liu, Y.; Chen, T.; Leng, C.-C.; Li, Q.; Sun, Z.-L.; Song, L.-J. Structural, Electrical, and Lithium Ion Dynamics of Li_2MnO_3 from Density Functional Theory. *Chinese Phys. Lett.* **2015**, *32*, 017102.

[34] Boulineau, A.; Croguennec, L.; Delmas, C.; Weill, F. Reinvestigation of Li_2MnO_3 Structure: Electron Diffraction and High Resolution TEM. *Chem. Mater.* **2009**, *21*, 4216–4222.

[35] Boulineau, A.; Croguennec, L.; Delmas, C.; Weill, F. Structure of Li_2MnO_3 with Different Degrees of Defects. *Solid State Ion.* **2010**, *180*, 1652–1659.

[36] Wang, Y.; Gu, H.-T.; Song, J.-H.; Feng, Z.-H.; Zhou, X.-B.; Zhou, Y.-N.; Wang, K.; Xie, J.-Y. Suppressing Mn Reduction of Li-Rich Mn-Based Cathodes by F-Doping for Advanced Lithium-Ion Batteries. *J. Phys. Chem. C* **2018**, *122*, 27836–27842.

[37] J. Carroll, K.; Qian, D.; Fell, C.; Calvin, S.; M. Veith, G.; Chi, M.; Baggetto, L.; Shirley Meng, Y. Probing the Electrode/Electrolyte Interface in the Lithium Excess Layered Oxide $Li_{1.2}Ni_{0.2}Mn_{0.6}O_2$. *Phys. Chem. Chem. Phys.* **2013**, *15*, 11128–11138.

[38] Shimoda, K.; Minato, T.; Nakanishi, K.; Komatsu, H.; Matsunaga, T.; Tanida, H.; Arai, H.; Ukyo, Y.; Uchimoto, Y.; Ogumi, Z. Oxidation Behaviour of Lattice Oxygen in Li-rich Manganese-Based Layered Oxide Studied by Hard X-ray Photoelectron Spectroscopy. *J. Mater. Chem. A* **2016**, *4*, 5909–5916.

[39] Xu, J.; Sun, M.; Qiao, R.; Renfrew, S. E.; Ma, L.; Wu, T.; Hwang, S.; Nordlund, D.; Su, D.; Amine, K.; Lu, J.; McCloskey, B. D.; Yang, W.; Tong, W. Elucidating Anionic Oxygen Activity in Lithium-Rich Layered Oxides. *Nat. Commun.* **2018**, *9*, 947.

[40] Baker, M. L.; Mara, M. W.; Yan, J. J.; Hodgson, K. O.; Hedman, B.; Solomon, E. I. K- and L-edge X-ray Absorption Spectroscopy (XAS) and Resonant Inelastic X-ray Scattering (RIXS) Determination of Differential Orbital Covalency (DOC) of Transition Metal Sites. *Coord. Chem. Rev.* **2017**, *345*, 182–208.

[41] Renfrew, S. E.; McCloskey, B. D. Residual Lithium Carbonate Predominantly Accounts for First Cycle CO_2 and CO Outgassing of Li-Stoichiometric and Li-Rich Layered Transition-Metal Oxides. *J. Am. Chem. Soc.* **2017**, *139*, 17853–17860.

[42] Qiu, B.; Zhang, M.; Wu, L.; Wang, J.; Xia, Y.; Qian, D.; Liu, H.; Hy, S.; Chen, Y.; An, K.; Zhu, Y.; Liu, Z.; Meng, Y. S. Gas–Solid Interfacial Modification of Oxygen Activity in Layered Oxide Cathodes for Lithium-Ion Batteries. *Nat. Commun.* **2016**, *7*, 12108.

[43] Liang, Y.; Prendergast, D. Quantum Many-Body Effects in x-Ray Spectra Efficiently Computed Using a Basic Graph Algorithm. *Phys. Rev. B* **2018**, *97*, 205127.

[44] Luo, K.; Roberts, M. R.; Hao, R.; Guerrini, N.; Pickup, D. M.; Liu, Y.-S.; Edström, K.; Guo, J.; Chadwick, A. V.; Duda, L. C.; Bruce, P. G. Charge-Compensation in 3d-Transition-Metal-Oxide Intercalation Cathodes through the Generation of Localized Electron Holes on Oxygen. *Nature Chemistry* **2016**, *8*, 684.

[45] Gent, W. E. et al. Coupling between Oxygen Redox and Cation Migration Explains Unusual Electrochemistry in Lithium-Rich Layered Oxides. *Nat Commun* **2017**, *8*, 2091.

[46] Lebens-Higgins, Z. W.; Vinckeviciute, J.; Wu, J.; Faenza, N. V.; Li, Y.; Sallis, S.; Pereira, N.; Meng, Y. S.; Amatucci, G. G.; Der Ven, A. V.; Yang, W.; Piper, L. F. J. Distinction between Intrinsic and X-ray-Induced Oxidized Oxygen States in Li-Rich 3d Layered Oxides and LiAlO2. *J. Phys. Chem. C* **2019**, *123*, 13201–13207.

[47] House, R. A.; Marie, J.-J.; Park, J.; Rees, G. J.; Agrestini, S.; Nag, A.; Garcia-Fernandez, M.; Zhou, K.-J.; Bruce, P. G. Covalency Does Not Suppress O2 Formation in 4d and 5d Li-rich O-redox Cathodes. *Nat Commun* **2021**, *12*, 2975.

[48] House, R. A.; Rees, G. J.; Pérez-Osorio, M. A.; Marie, J.-J.; Boivin, E.; Robertson, A. W.; Nag, A.; Garcia-Fernandez, M.; Zhou, K.-J.; Bruce, P. G. First-Cycle Voltage Hysteresis in Li-rich 3 d Cathodes Associated with Molecular O_2 Trapped in the Bulk. *Nat. Energy* **2020**, *5*, 777–785.

[49] House, R. A.; Maitra, U.; Pérez-Osorio, M. A.; Lozano, J. G.; Jin, L.; Somerville, J. W.; Duda, L. C.; Nag, A.; Walters, A.; Zhou, K.-J.; Roberts, M. R.; Bruce, P. G. Superstructure Control of First-Cycle Voltage Hysteresis in Oxygen-Redox Cathodes. *Nature* **2020**, *577*, 502–508.

[50] Armstrong, A. R.; Holzapfel, M.; Novák, P.; Johnson, C. S.; Kang, S.-H.; Thackeray, M. M.; Bruce, P. G. Demonstrating Oxygen Loss and Associated Structural Reorganization in the Lithium Battery Cathode $Li[Ni_{0.2}Li_{0.2}Mn_{0.6}]O_2$. *J. Am. Chem. Soc.* **2006**, *128*, 8694–8698.

[51] McCalla, E. et al. Reversible Li-Intercalation through Oxygen Reactivity in Li-Rich Li-Fe-Te Oxide Materials. *J. Electrochem. Soc.* **2015**, *162*, A1341–A1351.

[52] Renfrew, S. E.; McCloskey, B. D. Quantification of Surface Oxygen Depletion and Solid Carbonate Evolution on the First Cycle of $LiNi_{0.6}Mn_{0.2}Co_{0.2}O_2$ Electrodes. *ACS Appl. Energy Mater.* **2019**, *2*, 3762–3772.

[53] Kaufman, L. A.; McCloskey, B. D. Surface Lithium Carbonate Influences Electrolyte Degradation via Reactive Oxygen Attack in Lithium-Excess Cathode Materials. *Chem. Mater.* **2021**, *33*, 4170–4176.

[54] Qiao, R.; Chuang, Y.-D.; Yan, S.; Yang, W. Soft X-Ray Irradiation Effects of Li_2O_2, Li_2CO_3 and Li_2O Revealed by Absorption Spectroscopy. *PLOS ONE* **2012**, *7*, e49182.

[55] Risthaus, T.; Zhou, D.; Cao, X.; He, X.; Qiu, B.; Wang, J.; Zhang, L.; Liu, Z.; Paillard, E.; Schumacher, G.; Winter, M.; Li, J. A High-Capacity P2

$Na_{2/3}Ni_{1/3}Mn_{2/3}O_2$ Cathode Material for Sodium Ion Batteries with Oxygen Activity. *J. Power Sources* **2018**, *395*, 16–24.

[56] Gu, M.; Belharouak, I.; Zheng, J.; Wu, H.; Xiao, J.; Genc, A.; Amine, K.; Thevuthasan, S.; Baer, D. R.; Zhang, J.-G.; Browning, N. D.; Liu, J.; Wang, C. Formation of the Spinel Phase in the Layered Composite Cathode Used in Li-Ion Batteries. *ACS Nano* **2013**, *7*, 760–767.

[57] Bak, S.-M.; Hu, E.; Zhou, Y.; Yu, X.; Senanayake, S. D.; Cho, S.-J.; Kim, K.-B.; Chung, K. Y.; Yang, X.-Q.; Nam, K.-W. Structural Changes and Thermal Stability of Charged $LiNi_xMn_yCo_zO_2$ Cathode Materials Studied by Combined In Situ Time-Resolved XRD and Mass Spectroscopy. *ACS Appl. Mater. Interfaces* **2014**, *6*, 22594–22601.

[58] Foix, D.; Sathiya, M.; McCalla, E.; Tarascon, J.-M.; Gonbeau, D. X-Ray Photoemission Spectroscopy Study of Cationic and Anionic Redox Processes in High-Capacity Li-Ion Battery Layered-Oxide Electrodes. *J. Phys. Chem. C* **2016**, *120*, 862–874.

[59] Dahéron, L.; Dedryvère, R.; Martinez, H.; Ménétrier, M.; Denage, C.; Delmas, C.; Gonbeau, D. Electron Transfer Mechanisms upon Lithium Deintercalation from $LiCoO_2$ to CoO_2 Investigated by XPS. *Chem. Mater.* **2008**, *20*, 583–590.

[60] Lebens-Higgins, Z. W.; Chung, H.; Zuba, M. J.; Rana, J.; Li, Y.; Faenza, N. V.; Pereira, N.; McCloskey, B. D.; Rodolakis, F.; Yang, W.; Whittingham, M. S.; Amatucci, G. G.; Meng, Y. S.; Lee, T.-L.; Piper, L. F. J. How Bulk Sensitive Is Hard X-ray Photoelectron Spectroscopy: Accounting for the Cathode–Electrolyte Interface When Addressing Oxygen Redox. *J. Phys. Chem. Lett.* **2020**, *11*, 2106–2112.

[61] Reed, J.; Ceder, G.; Ven, A. V. D. Layered-to-Spinel Phase Transition in Li_xMnO_2. *Electrochem. Solid-State Lett.* **2001**, *4*, A78.

[62] Jarvis, K.; Wang, C.-C.; Varela, M.; Unocic, R. R.; Manthiram, A.; Ferreira, P. J. Surface Reconstruction in Li-Rich Layered Oxides of Li-Ion Batteries. *Chem. Mater.* **2017**, *29*, 7668–7674.

[63] Boulineau, A.; Simonin, L.; Colin, J.-F.; Bourbon, C.; Patoux, S. First Evidence of Manganese–Nickel Segregation and Densification upon Cycling in Li-Rich Layered Oxides for Lithium Batteries. *Nano Lett.* **2013**, *13*, 3857–3863.

[64] Koga, H.; Croguennec, L.; Ménétrier, M.; Mannessiez, P.; Weill, F.; Delmas, C. Different Oxygen Redox Participation for Bulk and Surface: A Possible Global Explanation for the Cycling Mechanism of $Li_{1.20}Mn_{0.54}Co_{0.13}Ni_{0.13}O_2$. *J. Power Sources* **2013**, *236*, 250–258.

[65] Zuo, W.; Luo, M.; Liu, X.; Wu, J.; Liu, H.; Li, J.; Winter, M.; Fu, R.; Yang, W.; Yang, Y. Li-Rich Cathodes for Rechargeable Li-based Batteries: Reaction Mechanisms and Advanced Characterization Techniques. *Energy & Environ. Sci.* **2020**, *13*, 4450–4497.

[66] Chen, J. et al. Pseudo-Bonding and Electric-Field Harmony for Li-Rich Mn-Based Oxide Cathode. *Adv. Funct. Mater.* **2020**, *30*, 2004302.

[67] Zhu, Z.; Gao, R.; Waluyo, I.; Dong, Y.; Hunt, A.; Lee, J.; Li, J. Stabilized Co-Free Li-Rich Oxide Cathode Particles with An Artificial Surface Prereconstruction. *Adv. Energy Mater.* **2020**, *10*, 2001120.

[68] Wang, C.; Xing, L.; Vatamanu, J.; Chen, Z.; Lan, G.; Li, W.; Xu, K. Overlooked Electrolyte Destabilization by Manganese (II) in Lithium-Ion Batteries. *Nat. Commun.* **2019**, *10*, 3423.

[69] Wang, X.; Nakamura, H.; Yoshio, M. Capacity Fading Mechanism for Oxygen Defect Spinel as a 4 V Cathode Material in Li-ion Batteries. *J. Power Sources* **2002**, *110*, 19–26.

[70] Xia, Y.; Zhou, Y.; Yoshio, M. Capacity Fading on Cycling of 4 V Li / $LiMn_2O_4$ Cells. *J. Electrochem. Soc.* **1997**, *144*, 2593.

[71] Benedek, R.; Iddir, H. Simulation of First-Charge Oxygen-Dimerization and Mn-Migration in Li-Rich Layered Oxides $xLi_2MnO_3 \cdot (1 - x)LiMO_2$ and Implications for Voltage Fade. *J. Phys. Chem. C* **2017**, *121*, 6492–6499.

[72] Yu, D. Y. W.; Yanagida, K. Structural Analysis of Li_2MnO_3 and Related Li-Mn-O Materials. *J. Electrochem. Soc.* **2011**, *158*, A1015–A1022.

[73] Ponosov, Y. S.; Komleva, E. V.; Streltsov, S. V. Phonon Anomalies near the Magnetostructural Transition in Li_2RuO_3: Raman Spectroscopy and Density Functional Theory Studies. *Phys. Rev. B* **2019**, *100*, 134310.

[74] Toby, B. H. EXPGUI, a Graphical User Interface for GSAS. *J. Appl. Cryst.* **2001**, *34*, 210–213.

[75] Toby, B. H.; Von Dreele, R. B. GSAS-II: The Genesis of a Modern Open-Source All Purpose Crystallography Software Package. *J. Appl. Cryst.* **2013**, *46*, 544–549.

[76] Momma, K.; Izumi, F. VESTA 3 for Three-Dimensional Visualization of Crystal, Volumetric and Morphology Data. *J. Appl. Cryst.* **2011**, *44*, 1272–1276.

[77] Ravel, B.; Newville, M. ATHENA, ARTEMIS, HEPHAESTUS: Data Analysis for X-ray Absorption Spectroscopy Using IFEFFIT. *J. Synchrotron Rad.* **2005**, *12*, 537–541.

[78] McCloskey, B. D.; Valery, A.; Luntz, A. C.; Gowda, S. R.; Wallraff, G. M.; Garcia, J. M.; Mori, T.; Krupp, L. E. Combining Accurate O_2 and Li_2O_2 Assays to Separate Discharge and Charge Stability Limitations in Nonaqueous Li–O_2 Batteries. *J. Phys. Chem. Lett.* **2013**, *4*, 2989–2993.

[79] McCloskey, B. D.; Bethune, D. S.; Shelby, R. M.; Girishkumar, G.; Luntz, A. C. Solvents' Critical Role in Nonaqueous Lithium–Oxygen Battery Electrochemistry. *J. Phys. Chem. Lett.* **2011**, *2*, 1161–1166.

[80] McCloskey, B. D.; Speidel, A.; Scheffler, R.; Miller, D. C.; Viswanathan, V.; Hummelshøj, J. S.; Nørskov, J. K.; Luntz, A. C. Twin Problems of Interfacial Carbonate Formation in Nonaqueous Li–O_2 Batteries. *J. Phys. Chem. Lett.* **2012**, *3*, 997–1001.

[81] Li, Q.; Chen, J.; Fan, L.; Kong, X.; Lu, Y. Progress in Electrolytes for Rechargeable Li-based Batteries and Beyond. *Green Energy Environ.* **2016**, *1*, 18–42.

[82] An, S. J.; Li, J.; Daniel, C.; Mohanty, D.; Nagpure, S.; Wood, D. L. The State of Understanding of the Lithium-Ion-Battery Graphite Solid Electrolyte Interphase (SEI) and Its Relationship to Formation Cycling. *Carbon* **2016**, *105*, 52–76.

[83] Zhuo, Z.; Dai, K.; Wu, J.; Zhang, L.; Tamura, N.; Chuang, Y.-d.; Feng, J.; Guo, J.; Shen, Z.-x.; Liu, G.; Pan, F.; Yang, W. Distinct Oxygen Redox Activities in Li_2MO_3 (M = Mn, Ru, Ir). *ACS Energy Lett.* **2021**, *6*, 3417–3424.

[84] Meazah Haregewoin, A.; Sorsa Wotango, A.; Hwang, B.-J. Electrolyte Additives for Lithium Ion Battery Electrodes: Progress and Perspectives. *Energy Environ. Sci.* **2016**, *9*, 1955–1988.

[85] Wang, H.; Li, X.; Li, F.; Liu, X.; Yang, S.; Ma, J. Formation and Modification of Cathode Electrolyte Interphase: A Mini Review. *Electrochem. Commun.* **2021**, *122*, 106870.

[86] Kepp, K. P. A Quantitative Scale of Oxophilicity and Thiophilicity. *Inorg. Chem.* **2016**, *55*, 9461–9470.

[87] Carrasco, J.; Lopez, N.; Illas, F.; Freund, H.-J. Bulk and Surface Oxygen Vacancy Formation and Diffusion in Single Crystals, Ultrathin Films, and Metal Grown Oxide Structures. *J. Chem. Phys.* **2006**, *125*, 074711.

[88] Johnson, R. A. Surface Stresses and Vacancies. *Surf. Sci.* **1996**, *355*, 241–247.

[89] Hirai, S.; Morita, K.; Yasuoka, K.; Shibuya, T.; Tojo, Y.; Kamihara, Y.; Miura, A.; Suzuki, H.; Ohno, T.; Matsuda, T.; Yagi, S. Oxygen Vacancy-Originated Highly Active Electrocatalysts for the Oxygen Evolution Reaction. *J. Mater. Chem. A* **2018**, *6*, 15102–15109.

[90] Li, M.; Liu, J.; Xu, Y.; Qian, G. Phosphate Adsorption on Metal Oxides and Metal Hydroxides: A Comparative Review. *Environ. Rev.* **2016**, *24*, 319–332.

[91] Taminato, S.; Hirayama, M.; Suzuki, K.; Kim, K.; Tamura, K.; Kanno, R. Reversible Structural Changes and High-Rate Capability of Li_3PO_4-Modified Li_2RuO_3 for Lithium-Rich Layered Rocksalt Oxide Cathodes. *J. Phys. Chem. C* **2018**, *122*, 16607–16612.

[92] Xu, H. Y.; Xie, S.; Wang, Q. Y.; Yao, X. L.; Wang, Q. S.; Chen, C. H. Electrolyte Additive Trimethyl Phosphite for Improving Electrochemical Performance and Thermal Stability of $LiCoO_2$ Cathode. *Electrochim. Acta* **2006**, *52*, 636–642.

[93] Zhou, Z.; Ma, Y.; Wang, L.; Zuo, P.; Cheng, X.; Du, C.; Yin, G.; Gao, Y. Triphenyl Phosphite as an Electrolyte Additive to Improve the Cyclic Stability of Lithium-Rich Layered Oxide Cathode for Lithium-Ion Batteries. *Electrochim. Acta* **2016**, *216*, 44–50.

[94] Han, J.-G.; Lee, S. J.; Lee, J.; Kim, J.-S.; Lee, K. T.; Choi, N.-S. Tunable and Robust Phosphite-Derived Surface Film to Protect Lithium-Rich Cathodes in Lithium-Ion Batteries. *ACS Appl. Mater. Interfaces* **2015**, *7*, 8319–8329.

[95] Lux, S. F.; Chevalier, J.; Lucas, I. T.; Kostecki, R. HF Formation in $LiPF_6$-Based Organic Carbonate Electrolytes. *ECS Electrochem. Lett.* **2013**, *2*, A121.

[96] He, M.; Su, C.-C.; Peebles, C.; Feng, Z.; Connell, J. G.; Liao, C.; Wang, Y.; Shkrob, I. A.; Zhang, Z. Mechanistic Insight in the Function of Phosphite Additives for Protection of $LiNi_{0.5}Co_{0.2}Mn_{0.3}O_2$ Cathode in High Voltage Li-Ion Cells. *ACS Appl. Mater. Interfaces* **2016**, *8*, 11450–11458.

[97] Lee, D. J.; Im, D.; Ryu, Y.-G.; Lee, S.; Yoon, J.; Lee, J.; Choi, W.; Jung, I.; Lee, S.; Doo, S.-G. Phosphorus Derivatives as Electrolyte Additives for Lithium-Ion Battery: The Removal of O_2 Generated from Lithium-Rich Layered Oxide Cathode. *J. Power Sources* **2013**, *243*, 831–835.

[98] Li, Z. D.; Zhang, Y. C.; Xiang, H. F.; Ma, X. H.; Yuan, Q. F.; Wang, Q. S.; Chen, C. H. Trimethyl Phosphite as an Electrolyte Additive for High-Voltage Lithium-Ion Batteries Using Lithium-Rich Layered Oxide Cathode. *J. Power Sources* **2013**, *240*, 471–475.

[99] Kobayashi, H.; Kanno, R.; Kawamoto, Y.; Tabuchi, M.; Nakamura, O.; Takano, M. Structure and Lithium Deintercalation of Li_{2-x}RuO3. *Solid State Ion.* **1995**, *82*, 25–31.

[100] House, R. A.; Jin, L.; Maitra, U.; Tsuruta, K.; Somerville, J. W.; Förstermann, D. P.; Massel, F.; Duda, L.; Roberts, M. R.; Bruce, P. G. Lithium Manganese Oxyfluoride as a New Cathode Material Exhibiting Oxygen Redox. *Energy Environ. Sci.* **2018**, *11*, 926–932.

[101] Yao, Z.; Kim, S.; He, J.; Hegde, V. I.; Wolverton, C. Interplay of Cation and Anion Redox in $Li_4Mn_2O_5$ Cathode Material and Prediction of Improved $Li_4(Mn,M)_2O_5$ Electrodes for Li-ion Batteries. *Sci. Adv.* **2018**, *4*, eaao6754.

[102] Li, X.; Qiao, Y.; Guo, S.; Xu, Z.; Zhu, H.; Zhang, X.; Yuan, Y.; He, P.; Ishida, M.; Zhou, H. Direct Visualization of the Reversible O^{2-}/O^{-} Redox Process in Li-Rich Cathode Materials. *Adv. Mater.* **2018**, *30*, 1705197.

[103] McCalla, E.; Sougrati, M. T.; Rousse, G.; Berg, E. J.; Abakumov, A.; Recham, N.; Ramesha, K.; Sathiya, M.; Dominko, R.; Van Tendeloo, G.; Novák, P.; Tarascon, J.-M. Understanding the Roles of Anionic Redox and Oxygen Release during Electrochemical Cycling of Lithium-Rich Layered Li_4FeSbO_6. *J. Am. Chem. Soc.* **2015**, *137*, 4804–4814.

[104] Shen, S. et al. Tuning Electrochemical Properties of Li-Rich Layered Oxide Cathodes by Adjusting Co/Ni Ratios and Mechanism Investigation Using in Situ X-ray Diffraction and Online Continuous Flow Differential Electrochemical Mass Spectrometry. *ACS Appl. Mater. Interfaces* **2018**, *10*, 12666–12677.

[105] Whittingham, M. S. Electrical Energy Storage and Intercalation Chemistry. *Science* **1976**, *192*, 1126–1127.

[106] Whittingham, M. S. Electrointercalation in Transition-Metal Disulphides. *J. Chem. Soc., Chem. Commun.* **1974**, 328–329.

[107] Whittingham, M. S.; Gamble, F. R. The Lithium Intercalates of the Transition Metal Dichalcogenides. *Mater. Res. Bull.* **1975**, *10*, 363–371.

[108] Murphy, D. W.; Di Salvo, F. J.; Hull, G. W.; Waszczak, J. V. Convenient Preparation and Physical Properties of Lithium Intercalation Compounds of Group 4B and 5B Layered Transition Metal Dichalcogenides. *Inorg. Chem.* **1976**, *15*, 17–21.

[109] Murphy, D. W.; Carides, J. N.; Di Salvo, F. J.; Cros, C.; Waszczak, J. V. Cathodes for Nonaqueous Lithium Batteries Based on VS_2. *Mater. Res. Bull.* **1977**, *12*, 825–830.

[110] Thompson, A. H. Lithium Ordering in Li_xTiS_2. *Phys. Rev. Lett.* **1978**, *40*, 1511–1514.

[111] Whittingham, M. S. Chemistry of Intercalation Compounds: Metal Guests in Chalcogenide Hosts. *Prog. Solid State Chem.* **1978**, *12*, 41–99.

[112] Whittingham, M. S. The Electrochemical Characteristics of VSe_2 in Lithium Cells. *Mater. Res. Bull.* **1978**, *13*, 959–965.

[113] Chang, K.; Chen, W. L-Cysteine-Assisted Synthesis of Layered MoS_2/Graphene Composites with Excellent Electrochemical Performances for Lithium Ion Batteries. *ACS Nano* **2011**, *5*, 4720–4728.

[114] Flamary-Mespoulie, F.; Boulineau, A.; Martinez, H.; Suchomel, M. R.; Delmas, C.; Pecquenard, B.; Le Cras, F. Lithium-Rich Layered Titanium Sulfides: Cobalt- and Nickel-free High Capacity Cathode Materials for Lithium-Ion Batteries. *Energy Storage Mater.* **2020**, *26*, 213–222.

[115] Sakuda, A.; Ohara, K.; Kawaguchi, T.; Fukuda, K.; Nakanishi, K.; Arai, H.; Uchimoto, Y.; Ohta, T.; Matsubara, E.; Ogumi, Z.; Kuratani, K.; Kobayashi, H.; Shikano, M.; Takeuchi, T.; Sakaebe, H. A Reversible Rocksalt to Amorphous Phase Transition Involving Anion Redox. *Sci. Rep.* **2018**, *8*, 15086.

[116] Sakuda, A.; Takeuchi, T.; Okamura, K.; Kobayashi, H.; Sakaebe, H.; Tatsumi, K.; Ogumi, Z. Rock-Salt-Type Lithium Metal Sulphides as Novel Positive-Electrode Materials. *Sci. Rep.* **2014**, *4*, 4883.

[117] Li, B.; Jiang, N.; Huang, W.; Yan, H.; Zuo, Y.; Xia, D. Thermodynamic Activation of Charge Transfer in Anionic Redox Process for Li-Ion Batteries. *Adv. Funct. Mater.* **2018**, *28*, 1704864.

[118] Saha, S.; Assat, G.; Sougrati, M. T.; Foix, D.; Li, H.; Vergnet, J.; Turi, S.; Ha, Y.; Yang, W.; Cabana, J.; Rousse, G.; Abakumov, A. M.; Tarascon, J.-M. Exploring the Bottlenecks of Anionic Redox in Li-rich Layered Sulfides. *Nat. Energy* **2019**, *4*, 977–987.

[119] Sharma, R. A. Equilibrium Phases Between Lithium Sulfide and Iron Sulfides. *J. Electrochem. Soc.* **1976**, *123*, 448.

[120] Batchelor, R. J.; Einstein, F. W. B.; Jones, C. H. W.; Fong, R.; Dahn, J. R. Crystal Structure of Li_2FeS_2. *Phys. Rev. B* **1988**, *37*, 3699–3702.

[121] Le Mehaute, A.; Brec, R.; Dugast, A.; Rouxel, J. The Li_xFeS_2 Electrochemical System. *Solid State Ion.* **1981**, *3–4*, 185–189.

[122] Gard, P.; Sourisseau, C.; Ouvrard, G.; Brec, R. Infrared Study of Lithium Intercalated Phases in the Li_xFeS_2 System ($0 \leq x \; leq \; 2$). Characterization of a New Iron Disulfide. *Solid State Ion.* **1986**, *20*, 231–238.

[123] Brec, R.; Prouzet, E.; Ouvrard, G. Redox Processes in the Li_xFeS2/Li Electrochemical System Studied through Crystal, Mössbauer, and EXAFS Analyses. *J. Power Sources* **1989**, *26*, 325–332.

[124] Brec, R.; Dugast, A.; Le Mehauté, A. Chemical and Electrochemical Study of the Li_xFeS2 Cathodic System ($0 \leq x \leq 2$). *Mater. Res. Bull.* **1980**, *15*, 619–625.

[125] Dugast, A.; Brec, R.; Ouvrard, G.; Rouxel, J. Li_2FeS_2, a Cathodic Material for Lithium Secondary Battery. *Solid State Ion.* **1981**, *5*, 375–378.

[126] Fong, R.; Dahn, J. R.; Jones, C. H. W. Electrochemistry of Pyrite-Based Cathodes for Ambient Temperature Lithium Batteries. *J. Electrochem. Soc.* **1989**, *136*, 3206.

[127] Blandeau, L.; Ouvrard, G.; Calage, Y.; Brec, R.; Rouxel, J. Transition-Metal Dichalcogenides from Disintercalation Processes. Crystal Structure Determination and M*ö*ssbauer Study of Li_2FeS_2 and Its Disintercalates Li_xFeS_2(0.2 *leq* x *leq* 2). *J. Phys. C: Solid State Phys.* **1987**, *20*, 4271–4281.

[128] Barker, J.; Kendrick, E. The Electrochemical Insertion and Safety Properties of the Low-Cost Li-ion Active Material, Li_2FeS_2. *J. Power Sources* **2011**, *196*, 6960–6963.

[129] Ritchie, A. G.; Bowles, P. G.; Scattergood, D. P. Lithium-Ion/Iron Sulphide Rechargeable Batteries. *J. Power Sources* **2004**, *136*, 276–280.

[130] Oledzka, M.; Ramanujachary, K. V.; Greenblatt, M. New Low-Dimensional Quaternary Sulfides $NaCuMS_2$ (M = Mn, Fe, Co, and Zn) with the $CaAl_2Si_2$-Type Structure: Synthesis and Properties. *Chem. Mater.* **1998**, *10*, 322–328.

[131] Honda, A.; Higai, S.; Wada, N.; Sakabe, Y. First-Principles Calculations for Structural Phase Transition of Li_xFeS_2. *J. Phys. Chem. Solids* **2008**, *69*, 1353–1355.

[132] Kowalska, J. K.; Hahn, A. W.; Albers, A.; Schiewer, C. E.; Bjornsson, R.; Lima, F. A.; Meyer, F.; DeBeer, S. X-Ray Absorption and Emission Spectroscopic Studies of $[LFe2S2]_n$ Model Complexes: Implications for the Experimental Evaluation of Redox States in Iron–Sulfur Clusters. *Inorg. Chem.* **2016**, *55*, 4485–4497.

[133] Glaser, T.; Hedman, B.; Hodgson, K. O.; Solomon, E. I. Ligand K-Edge X-ray Absorption Spectroscopy: A Direct Probe of Ligand-Metal Covalency. *Acc. Chem. Res.* **2000**, *33*, 859–868.

[134] Solomon, E. I.; Hedman, B.; Hodgson, K. O.; Dey, A.; Szilagyi, R. K. Ligand K-edge X-ray Absorption Spectroscopy: Covalency of Ligand–Metal Bonds. *Coord. Chem. Rev.* **2005**, *249*, 97–129.

[135] Dey, A.; Jiang, Y.; Ortiz de Montellano, P.; Hodgson, K. O.; Hedman, B.; Solomon, E. I. S K-edge XAS and DFT Calculations on Cytochrome P450: Covalent and Ionic Contributions to the Cysteine-Fe Bond and Their Contribution to Reactivity. *J. Am. Chem. Soc.* **2009**, *131*, 7869–7878.

[136] Li, D.; Bancroft, G. M.; Kasrai, M.; Fleet, M. E.; Feng, X.; Tan, K. S K- and L-edge X-ray Absorption Spectroscopy of Metal Sulfides and Sulfates; Applications in Mineralogy and Geochemistry. *Canad. Mineral.* **1995**, *33*, 949–960.

[137] Farrell, S. P.; Fleet, M. E.; Stekhin, I. E.; Kravtsova, A.; Soldatov, A. V.; Liu, X. Evolution of Local Electronic Structure in Alabandite and Niningerite Solid Solutions [(Mn,Fe)S, (Mg,Mn)S, (Mg,Fe)S] Using Sulfur K- and L-edge XANES Spectroscopy. *Am. Mineral.* **2002**, *87*, 1321–1332.

[138] Farrell, S. P.; Fleet, M. E. Sulfur K-edge XANES Study of Local Electronic Structure in Ternary Monosulfide Solid Solution [(Fe, Co, Ni)$_{0.923}$S]. *Phys. Chem. Min.* **2001**, *28*, 17–27.

[139] Bostick, B. C.; Fendorf, S. Arsenite Sorption on Troilite (FeS) and Pyrite (FeS_2). *Geochim. Cosmochim. Acta* **2003**, *67*, 909–921.

[140] George, G. N.; Gorbaty, M. L. Sulfur K-edge x-Ray Absorption Spectroscopy of Petroleum Asphaltenes and Model Compounds. *J. Am. Chem. Soc.* **1989**, *111*, 3182–3186.

[141] Wu, Z. Y.; Ouvrard, G.; Moreau, P.; Natoli, C. R. Interpretation of Preedge Features in the Ti and S K-Edge X-Ray-Absorption near-Edge Spectrain the Layered Disulfides TiS_2 and TaS_2. *Phys. Rev. B* **1997**, *55*, 9508–9513.

[142] Mijovilovich, A.; Pettersson, L. G. M.; de Groot, F. M. F.; Weckhuysen, B. M. Functional Groups and Sulfur K-Edge XANES Spectra: Divalent Sulfur and Disulfides. *J. Phys. Chem. A* **2010**, *114*, 9523–9528.

[143] Kitajou, A.; Yamaguchi, J.; Hara, S.; Okada, S. Discharge/Charge Reaction Mechanism of a Pyrite-Type FeS_2 Cathode for Sodium Secondary Batteries. *J. Power Sources* **2014**, *247*, 391–395.

[144] Liu, H.-c.; Xia, J.-l.; Nie, Z.-y.; Ma, Y.-l.; Ma, C.-y.; Zheng, L.; Hong, C.-h.; Zhao, Y.-d. Iron L-Edge and Sulfur K-Edge XANES Spectroscopy Analysis of Pyrite Leached by Acidianus Manzaensis. *T. Nonferr. Metal. Soc.* **2015**, *25*, 2407–2414.

[145] Bashian, N. H.; Zhou, S.; Zuba, M.; Ganose, A. M.; Stiles, J. W.; Ee, A.; Ashby, D. S.; Scanlon, D. O.; Piper, L. F. J.; Dunn, B.; Melot, B. C. Correlated Polyhedral Rotations in the Absence of Polarons during Electrochemical Insertion of Lithium in ReO_3. *ACS Energy Lett.* **2018**, *3*, 2513–2519.

[146] Zhou, S.; Barim, G.; Morgan, B. J.; Melot, B. C.; Brutchey, R. L. Influence of Rotational Distortions on Li^+- and Na^+-Intercalation in Anti-NASICON $Fe_2(MoO_4)_3$. *Chem. Mater.* **2016**, *28*, 4492–4500.

[147] Butala, M. M.; Mayo, M.; Doan-Nguyen, V. V. T.; Lumley, M. A.; Göbel, C.; Wiaderek, K. M.; Borkiewicz, O. J.; Chapman, K. W.; Chupas, P. J.; Balasubramanian, M.; Laurita, G.; Britto, S.; Morris, A. J.; Grey, C. P.; Seshadri, R. Local Structure Evolution and Modes of Charge Storage in Secondary Li–FeS_2 Cells. *Chem. Mater.* **2017**, *29*, 3070–3082.

[148] Clark, M. B. In *Lithium Batteries*; Gabano, J. P., Ed.; Academic Press: London, 1983; pp 115–136.

[149] Zhang, S. S.; Tran, D. T. Electrochemical Verification of the Redox Mechanism of FeS_2 in a Rechargeable Lithium Battery. *Electrochim. Acta* **2015**, *176*, 784–789.

[150] Ardel, G.; Golodnitsky, D.; Freedman, K.; Peled, E.; Appetecchi, G. B.; Romagnoli, P.; Scrosati, B. Rechargeable Lithium/Hybrid-Electrolyte/Pyrite Battery. *J. Power Sources* **2002**, *110*, 152–162.

[151] Jones, C. H. W.; Kovacs, P. E.; Sharma, R. D.; McMillan, R. S. An Iron-57 Mössbauer Study of the Intermediates Formed in the Reduction of Iron Disulfide in the Lithium/Iron Disulfide Battery System. *J. Phys. Chem.* **1991**, *95*, 774–779.

[152] Paolella, A.; George, C.; Povia, M.; Zhang, Y.; Krahne, R.; Gich, M.; Genovese, A.; Falqui, A.; Longobardi, M.; Guardia, P.; Pellegrino, T.; Manna, L. Charge Transport and Electrochemical Properties of Colloidal Greigite (Fe_3S_4) Nanoplatelets. *Chem. Mater.*, **2011**, *23*, 3762–3768.

[153] Xu, L.; Hu, Y.; Zhang, H.; Jiang, H.; Li, C. Confined Synthesis of FeS_2 Nanoparticles Encapsulated in Carbon Nanotube Hybrids for Ultrastable Lithium-Ion Batteries. *ACS Sustainable Chem. Eng.* **2016**, *4*, 4251–4255.

[154] Fei, L.; Lin, Q.; Yuan, B.; Chen, G.; Xie, P.; Li, Y.; Xu, Y.; Deng, S.; Smirnov, S.; Luo, H. Reduced Graphene Oxide Wrapped FeS Nanocomposite for Lithium-Ion Battery Anode with Improved Performance. *ACS Appl. Mater. Interfaces* **2013**, *5*, 5330–5335.

[155] Wang, J.; Toby, B. H.; Lee, P. L.; Ribaud, L.; Antao, S. M.; Kurtz, C.; Ramanathan, M.; Von Dreele, R. B.; Beno, M. A. A Dedicated Powder Diffraction Beamline at the Advanced Photon Source: Commissioning and Early Operational Results. *Rev. Sci. Instrum.* **2008**, *79*, 085105.

[156] Leriche, J. B.; Hamelet, S.; Shu, J.; Morcrette, M.; Masquelier, C.; Ouvrard, G.; Zerrouki, M.; Soudan, P.; Belin, S.; Elkaïm, E.; Baudelet, F. An Electrochemical Cell for Operando Study of Lithium Batteries Using Synchrotron Radiation. *J. Electrochem. Soc.* **2010**, *157*, A606.

[157] Newville, M. *IFEFFIT* : Interactive XAFS Analysis and *FEFF* Fitting. *J. Synchrotron Rad.* **2001**, *8*, 322–324.

[158] Sun, J.; Ruzsinszky, A.; Perdew, J. P. Strongly Constrained and Appropriately Normed Semilocal Density Functional. *Phys. Rev. Lett.* **2015**, *115*, 036402.

[159] Kresse, G.; Hafner, J. Ab Initio Molecular Dynamics for Liquid Metals. *Phys. Rev. B* **1993**, *47*, 558–561.

[160] Kresse, G.; Hafner, J. Ab Initio Molecular-Dynamics Simulation of the Liquid-Metal–Amorphous-Semiconductor Transition in Germanium. *Phys. Rev. B* **1994**, *49*, 14251–14269.

[161] Kresse, G.; Furthmüller, J. Efficiency of Ab-Initio Total Energy Calculations for Metals and Semiconductors Using a Plane-Wave Basis Set. *Comput. Mater. Sci.* **1996**, *6*, 15–50.

[162] Kresse, G.; Furthmüller, J. Efficient Iterative Schemes for Ab Initio Total-Energy Calculations Using a Plane-Wave Basis Set. *Phys. Rev. B* **1996**, *54*, 11169–11186.

[163] Hansen, C. J.; Zak, J. J.; Martinolich, A. J.; Ko, J. S.; Bashian, N. H.; Kaboudvand, F.; Van der Ven, A.; Melot, B. C.; Nelson Weker, J.; See, K. A. Multielectron, Cation and Anion Redox in Lithium-Rich Iron Sulfide Cathodes. *J. Am. Chem. Soc.* **2020**, *142*, 6737–6749.

[164] Newville, M. Fundamentals of XAFS. *Rev. Mineral. Geochem.* **2014**, *78*, 33–74.

[165] Yanagisawa, S.; Tsuneda, T.; Hirao, K. An Investigation of Density Functionals: The First-Row Transition Metal Dimer Calculations. *J. Chem. Phys.* **2000**, *112*, 545–553.

[166] Segall, M. D.; Lindan, P. J. D.; Probert, M. J.; Pickard, C. J.; Hasnip, P. J.; Clark, S. J.; Payne, M. C. First-Principles Simulation: Ideas, Illustrations and the CASTEP Code. *J. Phys.: Condens. Matter* **2002**, *14*, 2717–2744.

[167] Clark, S. J.; Segall, M. D.; Pickard, C. J.; Hasnip, P. J.; Probert, M. I. J.; Refson, K.; Payne, M. C. First Principles Methods Using CASTEP. *Z. Krist. - Cryst. Mater.* **2005**, *220*, 567–570.

[168] Zak, J. J.; Kim, S. S.; Laskowski, F. A. L.; See, K. A. An Exploration of Sulfur Redox in Lithium Battery Cathodes. *J. Am. Chem. Soc.* **2022**, *144*, 10119–10132.

[169] Dinnebier, R. E.; Leineweber, A.; Evans, J. S. O. *11. Total Scattering Methods*; De Gruyter, 2018; pp 253–268.

[170] Kim, S. S.; Agyeman-Budu, D. N.; Zak, J. J.; Dawson, A.; Yan, Q.; Cában-Acevedo, M.; Wiaderek, K. M.; Yakovenko, A. A.; Yao, Y.; Irshad, A.; Narayan, S. R.; Luo, J.; Nelson Weker, J.; Tolbert, S. H.; See, K. A. Promoting Reversibility of Multielectron Redox in Alkali-Rich Sulfide Cathodes through Cryomilling. *Chem. Mater.* **2022**, *34*, 3236–3245.

[171] Perdew, J. P.; Burke, K.; Ernzerhof, M. Generalized Gradient Approximation Made Simple. *Phys. Rev. Lett.* **1996**, *77*, 3865–3868.

[172] Chupas, P. J.; Qiu, X.; Hanson, J. C.; Lee, P. L.; Grey, C. P.; Billinge, S. J. L. Rapid-Acquisition Pair Distribution Function (RA-PDF) Analysis. *J. Appl. Cryst.* **2003**, *36*, 1342–1347.

[173] Kieffer, J.; Wright, J. P. PyFAI: A Python Library for High Performance Azimuthal Integration on GPU. *Powder Diffraction* **2013**, *28*, S339–S350.

[174] Juhás, P.; Davis, T.; Farrow, C. L.; Billinge, S. J. L. PDFgetX3: A Rapid and Highly Automatable Program for Processing Powder Diffraction Data into Total Scattering Pair Distribution Functions. *J. Appl. Cryst.* **2013**, *46*, 560–566.

[175] Yang, X.; Juhas, P.; Farrow, C. L.; Billinge, S. J. L. xPDFsuite: An End-to-End Software Solution for High Throughput Pair Distribution Function Transformation, Visualization and Analysis. *arXiv* **2015**, 1402.3163.

[176] Juhás, P.; Farrow, C. L.; Yang, X.; Knox, K. R.; Billinge, S. J. L. Complex Modeling: A Strategy and Software Program for Combining Multiple Information Sources to Solve Ill Posed Structure and Nanostructure Inverse Problems. *Acta Cryst. A* **2015**, *71*, 562–568.

[177] Egami, T.; Billinge, S. J. L. *Underneath the Bragg Peaks: Structural Analysis of Complex Materials*; Newnes, 2012.

[178] Billinge, S. J. L. Nanoscale Structural Order from the Atomic Pair Distribution Function (PDF): There's Plenty of Room in the Middle. *J. Solid State Chem.* **2008**, *181*, 1695–1700.

[179] Billinge, S. J. L.; Kanatzidis, M. G. Beyond Crystallography: The Study of Disorder, Nanocrystallinity and Crystallographically Challenged Materials with Pair Distribution Functions. *Chem. Commun.* **2004**, 749–760.

[180] Farrow, C. L.; Billinge, S. J. L. Relationship between the Atomic Pair Distribution Function and Small-Angle Scattering: Implications for Modeling of Nanoparticles. *Acta Cryst. A* **2009**, *65*, 232–239.

[181] Billinge, S. J. L.; Dykhne, T.; Juhás, P.; Božin, E.; Taylor, R.; Florence, A. J.; Shankland, K. Characterisation of Amorphous and Nanocrystalline Molecular Materials by Total Scattering. *CrystEngComm* **2010**, *12*, 1366–1368.

[182] Dykhne, T.; Taylor, R.; Florence, A.; Billinge, S. J. L. Data Requirements for the Reliable Use of Atomic Pair Distribution Functions in Amorphous Pharmaceutical Fingerprinting. *Pharm. Res.* **2011**, *28*, 1041–1048.

[183] Farrow, C. L.; Juhas, P.; Liu, J. W.; Bryndin, D.; Božin, E. S.; Bloch, J.; Proffen, T.; Billinge, S. J. L. PDFfit2 and PDFgui: Computer Programs for Studying Nanostructure in Crystals. *J. Phys.: Condens. Matter* **2007**, *19*, 335219.

[184] Sathiya, M.; Leriche, J.-B.; Salager, E.; Gourier, D.; Tarascon, J.-M.; Vezin, H. Electron Paramagnetic Resonance Imaging for Real-Time Monitoring of Li-ion Batteries. *Nat. Commun.* **2015**, *6*, 6276.

[185] Ying, T.; Gu, Y.; Chen, X.; Wang, X.; Jin, S.; Zhao, L.; Zhang, W.; Chen, X. Anderson Localization of Electrons in Single Crystals: $Li_xFe_7Se_8$. *Sci. Adv.* **2016**, *2*, e1501283.

[186] Huang, T.-W.; Chen, T.-K.; Yeh, K.-W.; Ke, C.-T.; Chen, C. L.; Huang, Y.-L.; Hsu, F.-C.; Wu, M.-K.; Wu, P. M.; Avdeev, M.; Studer, A. J. Doping-driven structural phase transition and loss of superconductivity in $M_xFe_{1-x}Se_\delta$ (M= Mn, Cu). *Phys. Rev. B* **2010**, *82*, 104502.

[187] Shannon, R. D. Revised Effective Ionic Radii and Systematic Studies of Interatomic Distances in Halides and Chalcogenides. *Acta Cryst. A* **1976**, *32*, 751–767.

[188] Tomyn, S.; Shylin, S. I.; Bykov, D.; Ksenofontov, V.; Gumienna-Kontecka, E.; Bon, V.; Fritsky, I. O. Indefinitely Stable Iron(IV) Cage Complexes Formed in Water by Air Oxidation. *Nat. Commun.* **2017**, *8*, 14099.

[189] Joseph, B.; Iadecola, A.; Saini, N.; Simonelli, L.; Mizuguchi, Y.; Takano, Y.; Mizokawa, T. A study of the electronic structure of $FeSe_{1-x}Te_x$ chalcogenides by Fe and Se K-edge X-ray absorption near edge structure measurements. *J. Phys.-Condens. Mat.* **2010**, *22*, 485702.

[190] Scheinost, A. C.; Charlet, L. Selenite Reduction by Mackinawite, Magnetite, and Siderite: XAS Characterization of Nanosized Redox Products. *Environ. Sci. Technol.* **2008**, *42*, 1984–1989.

[191] Rose, K.; Shadle, S. E.; Eidsness, M. K.; Kurtz, D. M.; Scott, R. A.; Hedman, B.; Hodgson, K. O.; Solomon, E. I. Investigation of Iron-Sulfur Covalency in Rubredoxins and a Model System Using Sulfur K-Edge X-ray Absorption Spectroscopy. *J. Am. Chem. Soc.* **1998**, *120*, 10743–10747.

[192] Womes, M.; Karnatak, R. C.; Esteva, J. M.; Lefebvre, I.; Allan, G.; Olivierfourcades, J.; Jumas, J. C. ELECTRONIC STRUCTURES OF FeS AND FeS2: X-RAY ABSORPTION SPECTROSCOPY AND BAND STRUCTURE CALCULATIONS. *J. Phys. Chem. Solids* **1997**, *58*, 345–352.

[193] Sugiura, C. Sulfur K X-ray Absorption Spectra of FeS, FeS_2, and Fe_2S_3. *J. Chem. Phys.* **1981**, *74*, 215–217.

[194] Yuan, B.; Luan, W.; Tu, S.-t. One-step synthesis of cubic FeS_2 and flower-like $FeSe_2$ particles by a solvothermal reduction process. *Dalton Trans.* **2012**, *41*, 772–776.

[195] Kanipe, K. N.; Chidester, P. P. F.; Stucky, G. D.; Meinhart, C. D.; Moskovits, M. Properly Structured, Any Material Can Produce Intense Surface Enhanced Raman Spectra. *J. Phys. Chem. C* **2017**, *121*, 14269–14273.

[196] Radin, M. D.; Vinckeviciute, J.; Seshadri, R.; der Ven, A. V. Manganese Oxidation as the Origin of the Anomalous Capacity of Mn-containing Li-excess Cathode Materials. *Nat Energy* **2019**, *4*, 639–646.

[197] Hu, E.; Yu, X.; Lin, R.; Bi, X.; Lu, J.; Bak, S.; Nam, K.-W.; Xin, H. L.; Jaye, C.; Fischer, D. A.; Amine, K.; Yang, X.-Q. Evolution of Redox Couples in Li- and Mn-rich Cathode Materials and Mitigation of Voltage Fade by Reducing Oxygen Release. *Nat. Energy* **2018**, *3*, 690–698.

[198] Rouxel, J. Anion–Cation Redox Competition and the Formation of New Compounds in Highly Covalent Systems. *Chem.–Eur. J.* **1996**, *2*, 1053–1059.

[199] *IUPAC. Compendium of Chemical Terminology*, 2nd ed. (the "Gold Book"); Compiled by A. D. McNaught and A. Wilkinson. Blackwell Scientific Publications: Oxford, 1997. Online version (2019-) created by S. J. Chalk. ISBN 0-9678550-9-8. https://goldbook.iupac.org/ (accessed Nov 2021).

[200] Liu, Q.; Su, X.; Lei, D.; Qin, Y.; Wen, J.; Guo, F.; Wu, Y. A.; Rong, Y.; Kou, R.; Xiao, X.; Aguesse, F.; Bareño, J.; Ren, Y.; Lu, W.; Li, Y. Approaching the Capacity Limit of Lithium Cobalt Oxide in Lithium Ion Batteries via Lanthanum and Aluminium Doping. *Nat. Energy* **2018**, *3*, 936–943.

[201] Zhang, L.; Sun, D.; Kang, J.; Wang, H.-T.; Hsieh, S.-H.; Pong, W.-F.; Bechtel, H. A.; Feng, J.; Wang, L.-W.; Cairns, E. J.; Guo, J. Tracking the Chemical and Structural Evolution of the TiS_2 Electrode in the Lithium-Ion Cell Using Operando X-Ray Absorption Spectroscopy. *Nano Lett.* **2018**, *18*, 4506–4515.

[202] Lin, C.-H.; Topsakal, M.; Sun, K.; Bai, J.; Zhao, C.; Dooryhee, E.; Northrup, P.; Gan, H.; Lu, D.; Stavitski, E.; Chen-Wiegart, Y.-c. K. Operando Structural and Chemical Evolutions of TiS_2 in Na-Ion Batteries. *J. Mater. Chem. A* **2020**, *8*, 12339–12350.

[203] Kittel, C. *Introduction to Solid State Physics.* 5th ed.; John Wiley & Sons, Inc.: New York, **1976**

[204] Wu, Z. Y.; Lemoigno, F.; Gressier, P.; Ouvrard, G.; Moreau, P.; Rouxel, J.; Natoli, C. R. Experimental and Theoretical Studies of the Electronic Structure of Ti_2. *Phys. Rev. B* **1996**, *54*, R11009–R11013.

[205] Wu, Z. Y.; Ouvrard, G.; Lemaux, S.; Moreau, P.; Gressier, P.; Lemoigno, F.; Rouxel, J. Sulfur K-Edge X-Ray-Absorption Study of the Charge Transfer upon Lithium Intercalation into Titanium Disulfide. *Phys. Rev. Lett.* **1996**, *77*, 2101–2104.

[206] Chianelli, R. R.; Scanlon, J. C.; Rao, B. M. L. In Situ Studies of Electrode Reactions: The Mechanism of Lithium Intercalation in TiS_2. *J. Solid State Chem.* **1979**, *29*, 323–337.

[207] Dahn, J. R.; Py, M. A.; Haering, R. R. In Situ X-Ray Diffraction Experiments on Lithium Intercalation Compounds. *Can. J. Phys.* **1982**, *60*, 307–313.

[208] Liu, X.-C.; Yang, Y.; Wu, J.; Liu, M.; Zhou, S. P.; Levin, B. D. A.; Zhou, X.-D.; Cong, H.; Muller, D. A.; Ajayan, P. M.; Abruña, H. D.; Ke, F.-S. Dynamic Hosts for High-Performance Li–S Batteries Studied by Cryogenic Transmission Electron Microscopy and in Situ X-Ray Diffraction. *ACS Energy Lett.* **2018**, *3*, 1325–1330.

[209] Houdeville, R. G.; Black, A. P.; Ponrouch, A.; Palacín, M. R.; Fauth, F. Operando Synchrotron X-Ray Diffraction Studies on TiS_2: The Effect of Propylene Carbonate on Reduction Mechanism. *J. Electrochem. Soc.* **2021**, *168*, 030514.

[210] Sinha, S.; Murphy, D. W. Lithium Intercalation in Cubic TiS_2. *Solid State Ionics* **1986**, *20*, 81–84.

[211] Chen, M.; Zhao, E.; Yan, Q.; Hu, Z.; Xiao, X.; Chen, D. The Effect of Crystal Face of Fe_2O_3 on the Electrochemical Performance for Lithium-Ion Batteries. *Sci. Rep.* **2016**, *6*, 29381.

[212] Buršík, J.; Soroka, M.; Kužel, R.; Mika, F. Growth and Characterization of Thin Oriented Co_3O_4(111) Films Obtained by Decomposition of Layered Cobaltates Na_xCoO_2. *J. Solid State Chem.* **2015**, *227*, 17–24.

[213] Chen Shi-Yu, W. Z.-X. Characterization of TiS_2 as an Anode Material for Lithium Ion Batteries. *Acta Phys. -Chim. Sin.* **2010**, *27*, 97–102.

[214] Kartick, B.; Srivastava, S. K.; Mahanty, S. TiS_2–MWCNT Hybrid as High Performance Anode in Lithium-Ion Battery. *J. Nanopart. Res.* **2013**, *15*, 1950.

[215] Van der Ven, A.; Bhattacharya, J.; Belak, A. A. Understanding Li Diffusion in Li-Intercalation Compounds. *Acc. Chem. Res.* **2013**, *46*, 1216–1225.

[216] Suslov, E. A.; Bushkova, O. V.; Sherstobitova, E. A.; Reznitskikh, O. G.; Titov, A. N. Lithium Intercalation into TiS_2 Cathode Material: Phase Equilibria in a Li–TiS2 System. *Ionics* **2016**, *22*, 503–514.

[217] Abrahams, S. C. The Crystal and Molecular Structure of Orthorhombic Sulfur. *Acta Cryst.* **1955**, *8*, 661–671.

[218] Rettig, S. J.; Trotter, J. Refinement of the Structure of Orthorhombic Sulfur, α-S_8. *Acta Cryst C* **1987**, *43*, 2260–2262.

[219] Gaultois, M. W.; Sparks, T. D.; Borg, C. K. H.; Seshadri, R.; Bonificio, W. D.; Clarke, D. R. Data-Driven Review of Thermoelectric Materials: Performance and Resource Considerations. *Chem. Mater.* **2013**, *25*, 2911–2920.

[220] Yaroshevsky, A. A. Abundances of Chemical Elements in the Earth's Crust. *Geochem. Int.* **2006**, *44*, 48–55.

[221] Jutzi, P. New Element-Carbon (p-p)π Bonds. *Angew. Chem. Int. Edit.* **1975**, *14*, 232–245.

[222] Flowers, P.; Theopold, K.; Langley, R.; Robinson, W. R. *Chemistry*; OpenStax: Houston, TX, 2015. https://openstax.org/details/books/chemistry-2e (accessed Nov 2021).

[223] Han, F.; Yue, J.; Fan, X.; Gao, T.; Luo, C.; Ma, Z.; Suo, L.; Wang, C. High-Performance All-Solid-State Lithium–Sulfur Battery Enabled by a Mixed-Conductive Li_2S Nanocomposite. *Nano Lett.* **2016**, *16*, 4521–4527.

[224] Kumar, R.; Liu, J.; Hwang, J.-Y.; Sun, Y.-K. Recent Research Trends in Li–S Batteries. *J. Mater. Chem. A* **2018**, *6*, 11582–11605.

[225] Mikhaylik, Y. V.; Akridge, J. R. Polysulfide Shuttle Study in the Li/S Battery System. *J. Electrochem. Soc.* **2004**, *151*, A1969.

[226] Coleman, J. R.; Bates, M. W. In *Research and Development in Non-Mechanical Electrical Power Sources*; Collins, D. H., Ed.; Pergamon, 1970; pp 289–302.

[227] Zhang, S.; Ueno, K.; Dokko, K.; Watanabe, M. Recent Advances in Electrolytes for Lithium–Sulfur Batteries. *Adv. Energy Mater.* **2015**, *5*, 1500117.

[228] Nagao, M.; Hayashi, A.; Tatsumisago, M. Fabrication of Favorable Interface between Sulfide Solid Electrolyte and Li Metal Electrode for Bulk-Type Solid-State Li/S Battery. *Electrochem. Commun.* **2012**, *22*, 177–180.

[229] Yamada, T.; Ito, S.; Omoda, R.; Watanabe, T.; Aihara, Y.; Agostini, M.; Ulissi, U.; Hassoun, J.; Scrosati, B. All Solid-State Lithium–Sulfur Battery Using a Glass-Type P_2S_5–Li_2S Electrolyte: Benefits on Anode Kinetics. *J. Electrochem. Soc.* **2015**, *162*, A646.

[230] Wang, S.; Zhang, Y.; Zhang, X.; Liu, T.; Lin, Y.-H.; Shen, Y.; Li, L.; Nan, C.-W. High-Conductivity Argyrodite Li_6PS_5Cl Solid Electrolytes Prepared via Optimized Sintering Processes for All-Solid-State Lithium–Sulfur Batteries. *ACS Appl. Mater. Interfaces* **2018**, *10*, 42279–42285.

[231] Zhang, Q.; Huang, N.; Huang, Z.; Cai, L.; Wu, J.; Yao, X. CNTs@S Composite as Cathode for All-Solid-State Lithium-Sulfur Batteries with Ultralong Cycle Life. *J. Energy Chem.* **2020**, *40*, 151–155.

[232] Nagao, M.; Hayashi, A.; Tatsumisago, M.; Ichinose, T.; Ozaki, T.; Togawa, Y.; Mori, S. Li_2S Nanocomposites Underlying High-Capacity and Cycling Stability in All-Solid-State Lithium–Sulfur Batteries. *J. Power Sources* **2015**, *274*, 471–476.

[233] Takeuchi, T.; Kageyama, H.; Nakanishi, K.; Tabuchi, M.; Sakaebe, H.; Ohta, T.; Senoh, H.; Sakai, T.; Tatsumi, K. All-Solid-State Lithium Secondary Battery with Li_2S – C Composite Positive Electrode Prepared by Spark-Plasma-Sintering Process. *J. Electrochem. Soc.* **2010**, *157*, A1196.

[234] Fang, R.; Zhao, S.; Sun, Z.; Wang, D.-W.; Cheng, H.-M.; Li, F. More Reliable Lithium-Sulfur Batteries: Status, Solutions and Prospects. *Adv. Mater.* **2017**, *29*, 1606823.

[235] Pan, H.; Cheng, Z.; He, P.; Zhou, H. A Review of Solid-State Lithium–Sulfur Battery: Ion Transport and Polysulfide Chemistry. *Energy Fuels* **2020**, *34*, 11942–11961.

[236] See, K. A.; Leskes, M.; Griffin, J. M.; Britto, S.; Matthews, P. D.; Emly, A.; Van der Ven, A.; Wright, D. S.; Morris, A. J.; Grey, C. P.; Seshadri, R. *Ab Initio* Structure Search and in Situ ^{7}Li NMR Studies of Discharge Products in the Li–S Battery System. *J. Am. Chem. Soc.* **2014**, *136*, 16368–16377.

[237] Iwakura, C.; Isobe, N.; Tamura, H. Initial Open Circuit Voltages and Discharge Reaction Mechanisms in Non-Aqueous Electrolyte Li/FeS2 Cells. *Electrochim. Acta* **1983**, *28*, 277–283.

[238] Yersak, T. A.; Macpherson, H. A.; Kim, S. C.; Le, V.-D.; Kang, C. S.; Son, S.-B.; Kim, Y.-H.; Trevey, J. E.; Oh, K. H.; Stoldt, C.; Lee, S.-H. Solid State Enabled Reversible Four Electron Storage. *Adv. Energy Mater.* **2013**, *3*, 120–127.

[239] Shao-Horn, Y.; Osmialowski, S.; Horn, Q. C. Reinvestigation of Lithium Reaction Mechanisms in FeS_2 Pyrite at Ambient Temperature. *J. Electrochem. Soc.* **2002**, *149*, A1547.

[240] Zhang, S. S. The Redox Mechanism of FeS_2 in Non-Aqueous Electrolytes for Lithium and Sodium Batteries. *J. Mater. Chem. A* **2015**, *3*, 7689–7694.

[241] Zou, J.; Zhao, J.; Wang, B.; Chen, S.; Chen, P.; Ran, Q.; Li, L.; Wang, X.; Yao, J.; Li, H.; Huang, J.; Niu, X.; Wang, L. Unraveling the Reaction Mechanism of FeS_2 as a Li-Ion Battery Cathode. *ACS Appl. Mater. Interfaces* **2020**, *12*, 44850–44857.

[242] Xu, X.; Ying, H.; Zhang, S.; Meng, Z.; Yan, X.; Han, W.-Q. Biomass-Derived 3D Interconnected Porous Carbon-Encapsulated Nano-FeS2 for High-Performance Lithium-Ion Batteries. *ACS Appl. Energy Mater.* **2020**, *3*, 5589–5596.

[243] Sun, K.; Cama, C. A.; DeMayo, R. A.; Bock, D. C.; Tong, X.; Su, D.; Marschilok, A. C.; Takeuchi, K. J.; Takeuchi, E. S.; Gan, H. Interaction of FeS_2 and Sulfur in Li-S Battery System. *J. Electrochem. Soc.* **2016**, *164*, A6039.

[244] Hu, J.; Zhang, Y.; Law, M.; Wu, R. Increasing the Band Gap of Iron Pyrite by Alloying with Oxygen. *J. Am. Chem. Soc.* **2012**, *134*, 13216–13219.

[245] Yao, X.; Huang, N.; Han, F.; Zhang, Q.; Wan, H.; Mwizerwa, J. P.; Wang, C.; Xu, X. High-Performance All-Solid-State Lithium–Sulfur Batteries Enabled by Amorphous Sulfur-Coated Reduced Graphene Oxide Cathodes. *Adv. Energy Mater.* **2017**, *7*, 1602923.

[246] Nagarajan, S.; Hwang, S.; Balasubramanian, M.; Thangavel, N. K.; Arava, L. M. R. Mixed Cationic and Anionic Redox in Ni and Co Free Chalcogen-Based Cathode Chemistry for Li-Ion Batteries. *J. Am. Chem. Soc.* **2021**, *143*, 15732–15744.

[247] Kitchaev, D. A.; Vinckeviciute, J.; Van der Ven, A. Delocalized Metal–Oxygen π-Redox Is the Origin of Anomalous Nonhysteretic Capacity in Li-Ion and Na-Ion Cathode Materials. *J. Am. Chem. Soc.* **2021**, *143*, 1908–1916.

[248] Wang, T.; Ren, G-X.; Shadike, Z.; Yue, J.-L.; Cao, M.-H.; Zhang, J.-N.; Chen, M.-W.; Yang, X.-Q.; Bak, S.-M.; Northrup, P.; Liu, P.; Liu, X.-S.; Fu, Z.-W. Anionic redox reaction in layered $NaCr_{2/3}TI_{1/3}S_2$ through electron holes formation and dimerization of S-S. *Nat. Commun.* **2019**, *10*, 4458.

[249] Tomczuk, Z.; Tani, B.; Otto, N. C.; Roche, M. F.; Vissers, D. R. Phase Relationships in Positive Electrodes of High Temperature Li - Al / LiCl - KCl / FeS_2 Cells. *J. Electrochem. Soc.* **1982**, *129*, 925.

[250] Aselage, T. L.; Hellstrom, E. E. Multicomponent Phase Diagrams for Battery Applications: II . Oxygen Impurities in the Battery Cathode. *J. Electrochem. Soc.* **1987**, *134*, 1932.

[251] Yu, Y. et al. Revealing Electronic Signatures of Lattice Oxygen Redox in Lithium Ruthenates and Implications for High-Energy Li-Ion Battery Material Designs. *Chem. Mater.* **2019**, *31*, 7864–7876.

[252] Jain, A.; Ong, S. P.; Hautier, G.; Chen, W.; Richards, W. D.; Dacek, S.; Cholia, S.; Gunter, D.; Skinner, D.; Ceder, G.; Persson, K. A. Commentary: The Materials Project: A Materials Genome Approach to Accelerating Materials Innovation. *APL Mater.* **2013**, *1*, 011002.

[253] Bergerhoff, G.; Brown, I. D.; Allen, F. H. *Crystallographic Databases*; International Union of Crystallography: Chester, 1987..

[254] Belsky, A.; Hellenbrandt, M; Karen, V. L.; Luksch, P. New developments in the Inorganic Crystal Structure Database (ICSD): accessibility in support of materials research and design. *Acta Cryst. B* **2002**, *58*, 364–369.

[255] Böttcher, P.; Getzschmann, J.; Keller, R. Zur Kenntnis der Dialkalimetalldichalkogenide β-Na_2S_2, K_2S_2, α-Rb_2S_2, β-Rb_2S_2, K_2Se_2, Rb_2Se_2, α-K_2Te_2, β-K_2Te_2 und Rb_2Te_2. *Z. Anorg. Allg. Chem.* **1993**, *619*, 476–488.

[256] Kawada, I.; Kato, K.; Yamaoka, S. Barium Disulphide. *Acta Cryst. B* **1975**, *31*, 2905–2906.

[257] Furuseth, S.; Brattås, L.; Kjekshus, A. On the Crystal Structures of TiS_3, ZrS_3, $ZrSe_3$, $ZrTe_3$, HfS_3, and $HfSe_3$. *Acta Chem. Scand. A* **1975**, *29*, 623–631.

[258] Bloodgood, M. A.; Wei, P.; Aytan, E.; Bozhilov, K. N.; Balandin, A. A.; Salguero, T. T. Monoclinic Structures of Niobium Trisulfide. *APL Mater.* **2018**, *6*, 026602.

[259] Kozlova, M. N.; Mironov, Y. V.; Grayfer, E. D.; Smolentsev, A. I.; Zaikovskii, V. I.; Nebogatikova, N. A.; Podlipskaya, T. Y.; Fedorov, V. E. Synthesis, Crystal Structure, and Colloidal Dispersions of Vanadium Tetrasulfide (VS_4). *Chem.–Eur. J.* **2015**, *21*, 4639–4645.

[260] Tokuda, M.; Yoshiasa, A.; Mashimo, T.; Arima, H.; Hongu, H.; Tobase, T.; Nakatsuka, A.; Sugiyama, K. Crystal Structure Refinement of $MnTe_2$, $MnSe_2$, and MnS_2: Cation-Anion and Anion–Anion Bonding Distances in Pyrite-Type Structures. *Z. Krist.-Cryst. Mater.* **2019**, *234*, 371–377.

[261] Bither, T. A.; Bouchard, R. J.; Cloud, W. H.; Donohue, P. C.; Siemons, W. J. Transition Metal Pyrite Dichalcogenides. High-pressure Synthesis and Correlation of Properties. *Inorg. Chem.* **1968**, *7*, 2208–2220.

[262] Lutz, H. D.; Müller, B.; Schmidt, T.; Stingl, T. Structure Refinement of Pyrite-Type Ruthenium Disulfide, RuS_2, and Ruthenium Diselenide, $RuSe_2$. *Acta Cryst. C* **1990**, *46*, 2003–2005.

[263] Stingl, T.; Müller, B.; Lutz, H. D. Crystal Structure Refinement of Osmium(II) Disulfide, OsS_2. *Z. Kristallogr.* **1992**, *202*, 161–162.

[264] Thomassen, L. Über Kristallstrukturen einiger binärer Verbindungen der Platinmetalle II. *Z. Phys. Chem.* **1929**, *4B*, 277–287.

[265] Parthé, E.; Hohnke, E.; Hulliger, F. A New Structure Type with Octahedron Pairs for Rh_2S_3, Rh_2Se_3 and Ir_2S_3. *Acta Cryst.* **1967**, *23*, 832–840.

[266] Kjekshus, A.; Rakke, T.; Andresen, A., F. Pyrite-like Phases in the Rh–Te System. *Acta Chem. Scand. A* **1978**, *32*, 209–217.

[267] Schleid, T.; Lauxmann, P.; Bartschb, C.; Doert, T. Lanthanoiddisulfide – Synthesen Und Kristallstrukturen von α-CeS_2, α-NdS_2, β-LaS_2, β-CeS_2 Und β-PrS_2 / Rare Earth Metal Disulfides – Syntheses and Crystal Structures of α-CeS_2, α-NdS_2, β-LaS_2, β-CeS_2, and β-PrS2. *Z. Naturforsch. B* **2009**, *64*, 189–196.

[268] Doert, T.; Graf, C.; Lauxmann, P.; Schleid, T. $LaS_{1.9}$, $CeS_{1.9}$, $PrS_{1.9}$, $NdS_{1.9}$ Und $GdS_{1.9}$: Fünf Neue Lanthanoidpolysulfide – Synthese Und Kristallstrukturen Und Ihre Strukturbeziehung Zum ZrSSi-Typ. *Z. Anorg. Allg. Chem.* **2007**, *633*, 2719–2724.

[269] Jansen, C.; Küper, J.; Krebs, B. $Na_2B_2S_5$ and $Li_2B_2S_5$: Two Novel Perthioborates with Planar 1,2,4-Trithia-3,5-Diborolane Rings. *Z. Anorg. Allg. Chem.* **1995**, *621*, 1322–1329.

[270] Hammerschmidt, A.; Küper, J.; Stork, L.; Krebs, B. $Na_2B_2Se_7$, $K_2B_2S_7$ und $K_2B_2Se_7$: Drei Perchalkogenoborate mit neuem polymeren Anionengerüst. *Z. Anorg. Allg. Chem.* **1994**, *620*, 1898–1904.

[271] Rumpf, C.; Bensch, W. Synthesis and Crystal Structure of New Ternary Chalcogenides of Group IV Metals: K_2ZrS_4, Rb_2ZrS_4, and Rb_2HfS_4. *Z. Naturforsch. B* **2000**, *55*, 695–698.

[272] Klepp, K. O.; Gabi, G. Preparation and Crystal Structure of $Cs_4Nb_2S_{11}$. *Z. Naturforsch. B* **1998**, *53*, 1236–1238.

[273] Dürichen, P.; Bensch, W. New Compounds Containing the Complex Anion $[Ta_2S_{11}]^{4-}$; $A_4Ta_2S_{11}$ (A = Rb, Cs). *Acta Cryst. C* **1998**, *54*, 706–708.

[274] Devi, M. S.; Vidyasagar, K. Molten Flux Synthesis, Single Crystal X-ray Structure and Ion-Exchange Properties of the First Polythiogallate, $CsGaS_3$. *J. Chem. Soc., Dalton Trans.* **2002**, 4751–4754.

[275] Liao, J. H.; Varotsis, C.; Kanatzidis, M. G. Syntheses, Structures, and Properties of Six Novel Alkali Metal Tin Sulfides: $K_2Sn_2S_8$, α-$Rb_2Sn_2S_8$, β-$Rb_2Sn_2S_8$, $K_2Sn_2S_5$, $Cs_2Sn_2S_6$, and Cs_2SnS_{14}. *Inorg. Chem.* **1993**, *32*, 2453–2462.

[276] McCarthy, T. J.; Kanatzidis, M. G. Polysulfide Ligands in Solid-State Antimony Compounds. Isolation and Structural Characterization of $Cs_2Sb_4S_8$ and $CsSbS_6$. *Inorg. Chem.* **1994**, *33*, 1205–1211.

[277] Huster, J.; Bronger, W. Synthesis and Crystal Structure of $BaPd_2S_4$—a Sulphide-Disulphide Compound, $BaPd_2S_2(S_2)$. *J. Alloy. Compd.* **1995**, *224*, 190–193.

[278] Choi, K.-S.; Kanatzidis, M. G. Sulfosalts with Alkaline Earth Metals. Centrosymmetric vs Acentric Interplay in $Ba_3Sb_{4.66}S_{10}$ and $Ba_{2.62}Pb_{1.38}Sb_4S_{10}$ Based on the Ba/Pb/Sb Ratio. Phases Related to Arsenosulfide Minerals of

the Rathite Group and the Novel Polysulfide $Sr_6Sb_6S_{17}$. *Inorg. Chem.* **2000**, *39*, 5655–5662.

[279] Mironov, Y. V.; Yarovoi, S. S.; Naumov, D. Y.; Kozlova, S. G.; Ikorsky, V. N.; Kremer, R. K.; Simon, A.; Fedorov, V. E. $V_4S_9Br_4$: A Novel High-Spin Vanadium Cluster Thiobromide with Square-Planar Metal Core. *J. Phys. Chem. B* **2005**, *109*, 23804–23807.

[280] Marcoll, J.; Rabenau, A.; Mootz, D.; Wunderlich, H. The Crystal Structures of MoS_2Cl_3 and $Mo_3S_7C_{14}$ *Rev. Chem. Miner.* **1974**, *11*, 607

[281] Sokolov, M. N.; Rogachev, A. V.; Virovets, A. V.; Yarovoi, S. S.; Mironov, Y. V.; Fedin, V. P. Crystal Structure of Two Polymorphic Modifications of NbS_2Br_2 Niobium Thiobromide. *J. Struct. Chem.* **2013**, *54*, 451–453.

[282] Klepp, K. O. Darstellung Und Kristallstruktur von Tl_2TiS_4 : Ein Perthiotitanat(IV) Mit ∞^1-[TiS_4^{2-}]-Ketten Preparation and Crystal Structure of Tl_2TiS_4 : A Perthiotitanate(IV) with ∞^1-[TiS_4^{2-}]-Chains. *Z. Naturforsch. B* **1985**, *40*, 229–234.

[283] Srikrishnan, T.; Nowacki W. A Redetermination of the Crystal Structure of Livingstonite, $HgSb_4S_8$. *Z. Kristallogr.* **1975**, *141*, 174–192.

[284] The Structure of $Cu_4Bi_4S_9$ and Its Relation to the Structures of Covellite, CuS and Bismuthinite, Bi_2S_3. *Z. Kristallogr.* **1975**, *141*, 217–232.

[285] Wichelhaus, W. The Rare-Earth Oxide Disulfides $La_2O_2S_2$, $Pr_2O_2S_2$, and $Nd_2O_2S_2$. *Naturwissenschaften* **1978**, *65*, 593–594.

[286] Strobel, S.; Schleid, T. La_2CuS_4: A Lanthanum Copper Sulfide with Discrete Anion Triples $[S_3Cu\cdots S—S\cdots CuS_3]^{12-}$ Based on $La_4[Cu_2S_6(S_2)]$. *Angew. Chem. Int. Edit.* **2003**, *42*, 4911–4913.

[287] Jacquet, Q.; Iadecola, A.; Saubanère, M.; Lemarquis, L.; Berg, E. J.; Alves Dalla Corte, D.; Rousse, G.; Doublet, M.-L.; Tarascon, J.-M. Competition between Metal Dissolution and Gas Release in Li-Rich $Li_3Ru_yIr_{1-y}O_4$ Model Compounds Showing Anionic Redox. *Chem. Mater.* **2018**, *30*, 7682–7690.

[288] Amatucci, G. G.; Tarascon, J. M.; Klein, L. C. CoO_2, The End Member of the Li_xCoO_2 Solid Solution. *J. Electrochem. Soc.* **1996**, *143*, 1114.